

Christian Frederik Breitkreuz
Thermodynamic Properties of Formaldehyde Solutions and Poly(oxymethylene) dimethyl ether (OME) Production
Scientific Report Series Volume 41
2023

Scientific Report Series
Laboratory of Engineering Thermodynamics (LTD)
University of Kaiserslautern
P.O. Box 3049
67653 Kaiserslautern
Germany

ISSN 2195-7606
ISBN 978-3-944433-34-9

© LTD all rights reserved

Thermodynamic Properties of Formaldehyde Solutions and Poly(oxymethylene) dimethyl ether (OME) Production

Dem Fachbereich Maschinenbau und Verfahrenstechnik
der Technischen Universität Kaiserslautern
zur Erlangung des akademischen Grades

Doktor-Ingenieur (Dr.-Ing.)

genehmigte

Dissertation

von

M.Sc. Christian Frederik Breitzkreuz
aus Bochum

Dekan: Prof. Dr. rer. nat. Roland Ulber

Berichterstatter: Prof. Dr.-Ing. Hans Hasse

Prof. Dr.-Ing. Jakob Burger

Tag der mündlichen Prüfung: 13.01.2023

D 386

Das ist wirklich ein spezialgelagerter Sonderfall

Justus Jonas

Danksagung

Diese Arbeit ist entstanden während meiner Zeit als wissenschaftlicher Mitarbeiter am Lehrstuhl für Thermodynamik der TU Kaiserslautern. Ich danke dem Lehrstuhlinhaber Herrn Prof. Hans Hasse für die Ermöglichung dieser Arbeit, seiner intensiven und sehr persönlichen Unterstützung in fachlichen Fragen, besonders auch in schwierigen Zeiten. Ich danke Herrn Prof. Günthner für die Übernahme des Vorsitzes der Prüfungskommission. Mein Dank gilt auch Herrn Prof. Jakob Burger, der die Arbeit nicht nur begutachtet, sondern mir auch stets fachlichen Input auf zahlreichen Projekttreffen gegeben hat.

Mein Dank gilt dem Bundesministerium für Bildung und Forschung, welches durch das Forschungsvorhaben „NAMOSYN“ wesentlich zur Finanzierung beigetragen hat.

Darüber hinaus danke ich zahlreichen Kollegen, oder eher Freunden am Lehrstuhl, ohne die die Arbeit so nie möglich gewesen wäre. Das wären Nicole, Julian, Kirsten, Dirk, Tanja, Berthold durch ihre Unterstützung bei allen experimentellen Arbeiten und Marlies, Ilona und Jennifer durch ihre Unterstützung bei allen organisatorischen Dingen. Des Weiteren danke ich ganz vielen wiss. Mitarbeitern für die Unterstützung sowohl bei der Arbeit als auch abseits der Arbeit durch die notwendige Ablenkung beim gemeinsamen Sport, den Partys, Brettspielen oder Spaziergängen (mit kleinen Anhängen). Ihr habt mir immer ein Gefühl von ein bisschen Heimat in der Fremde gegeben und meine Zeit am Lehrstuhl zu einer sehr schönen Zeit gemacht.

Danke an alle Studierenden, die als Hiwi oder für ihre Abschlussarbeiten unzählige Stunden mit Titrieren, Wiegen oder anderen Fleißarbeiten so viel beigetragen haben.

Ich danke meinen Eltern, dass sie so viel gegeben haben, immer in mich vertraut haben und mir so diesen Weg ermöglicht haben. Danke an meine großen Geschwister und Anhang, dass sie mir, vielleicht nicht immer bewusst, ein Vorbild waren und immer sein werden.

Danke an meine Mitstreiter aus Dortmund mit denen ich durch ein enges Band stets verbunden bin und die mich durch ein wenig Konkurrenz aber auch viel Vertrauen stets unterstützt haben.

Da sind noch so viele, die mich auf meinem Weg unterstützt haben, sei es schon vor Jahren oder auf den letzten Metern bis zur Vollendung dieser Arbeit und denen ich dankbar bin und ich hoffe sie alle wissen darum.

Abstract

Formaldehyde is an important intermediate in the chemical industry. In technical processes, formaldehyde is used in aqueous or methanolic solutions. In these, it is bound in oligomers that are formed in reversible reactions. These reactions and also the vapor-liquid equilibria of mixtures containing formaldehyde, water, and methanol have been thoroughly studied in the literature. This is, however, not the case for solid-liquid equilibria of these mixtures, even though the precipitation of solids poses important problems in many technical processes. Therefore, in the present thesis, a fundamental study on the formation of solid phases in the system (formaldehyde + water + methanol) was carried out. Based on the experiments, a physico-chemical model of the solid-liquid equilibrium was developed. Furthermore, also kinetic effects, which are important in practice, were described. The results enable, for the first time, to understand the solid formation in these mixtures, which previously was considered to be hard to predict.

The studies on the solid formation in formaldehyde-containing systems were carried out as a part of a project dealing with the production of poly(oxymethylene) dimethyl ethers (OME). OME are formaldehyde-based synthetic fuels that show cleaner combustion than fossil diesel. Different aspects of the OME production were studied. First, a conceptual design for a OME production process based on dimethyl ether (DME) was carried out based on process simulation. This study revealed that the DME route is principally attractive. However, basic data on the formation of OME from DME were missing, and had to be estimated for the conceptual design study. Therefore, in a second step an experimental study on the formation of OME from DME was carried out. In this reaction, trioxane, a cyclic trimer of formaldehyde is used as a water-free formaldehyde source. Trioxane is currently produced from aqueous formaldehyde solution in energy-intensive processes. Therefore, a new trioxane production process was developed in which trioxane is obtained from a crystallization step. In process simulations, the new process was compared to the best previously available process and was found to be promising.

While OME are excellent synthetic fuels, it is also attractive to use them in blends with hydrogenated vegetable oil (HVO), which is available on a large scale. However, blends of OME and HVO that are initially homogenous tend to demix after a while in technical applications. This phenomenon was poorly understood previously. Therefore, in this work, liquid-liquid equilibria in mixtures of individual components of the two fuels in combination with water were systematically studied and a corresponding model was developed.

Kurzfassung

Formaldehyd ist eine wichtige Chemikalie in der chemischen Industrie. In technischen Prozessen wird Formaldehyd in Form von wässrigen oder methanolischen Lösungen eingesetzt. In diesen ist er in Form von Oligomeren gebunden, die in reversiblen Reaktionen gebildet werden. Diese Reaktionen und auch die Dampf-Flüssig-Gleichgewichte in Mischungen aus Formaldehyd, Wasser und Methanol sind ausführlich in der Literatur beschrieben. Das ist jedoch nicht der Fall für die Fest-flüssig Gleichgewichte dieser Mischungen, obwohl die Feststoffbildung in zahlreichen technischen Prozessen ein Problem ist. Daher wurde in dieser Arbeit eine grundlegende Untersuchung zur Bildung einer festen Phase im System (Formaldehyd + Wasser + Methanol) durchgeführt. Basierend auf den Ergebnissen wurde ein physikalisch-chemisches Modell zur Beschreibung des Fest-flüssig Gleichgewichts entwickelt. Des Weiteren wurden auch technisch relevante kinetische Effekte beschrieben. So ist es zum ersten Mal möglich die Feststoffbildung zu beschreiben, was bisher als sehr komplex erachtet wurde.

Die Untersuchungen zur Feststoffbildung wurden im Rahmen eines Projekts zur Herstellung von Poly(oxymethylen)dimethylethern (OME) durchgeführt. OME sind auf Formaldehyd basierende synthetische Kraftstoffe, die eine sauberere Verbrennung als fossiler Diesel zeigen. In der Arbeit wurden verschiedene Aspekte der OME-Produktion untersucht. Zunächst wurde eine konzeptionelle Designstudie für die Herstellung von OME ausgehend von Dimethylether (DME) basierend auf Prozesssimulation durchgeführt. Diese Studie hat gezeigt, dass die DME-Route prinzipiell attraktiv ist. Jedoch fehlten wichtige Daten zur Bildung von OME aus DME, die daher für diese Studie abgeschätzt werden mussten. In einem zweiten Schritt wurde die Bildung von OME aus DME experimentell untersucht. Bei der Reaktion wird Trioxan als wasserfreie Formaldehydquelle eingesetzt. Bisher wird Trioxan in energieintensiven Prozessen ausgehend von wässrigen Formaldehydlösungen hergestellt. Daher wurde ein neuer Prozess zur Herstellung von Trioxan entwickelt bei dem das Trioxan durch Kristallisation gewonnen wird. Die Ergebnisse von Simulationen des neuen Prozesses im Vergleich mit dem aktuell besten verfügbaren Prozess sind vielversprechend.

Neben der reinen Verwendung von OME ist auch eine Nutzung in Blends mit hydriertem Pflanzenöl (HVO) sehr attraktiv, da dieses bereits in großen Mengen verfügbar ist. Jedoch neigen die zunächst homogenen Blends in der Anwendung zur Entmischung. Dieses Phänomen war bisher nicht erklärbar. Daher wurden in dieser Arbeit die Flüssig-flüssig Gleichgewichte in Mischungen aus einzelnen Komponenten der beiden Kraftstoffarten in Kombination mit Wasser systematisch untersucht und modelliert.

Contents

1	Introduction	1
2	Solid-liquid equilibria in formaldehyde-containing mixtures	5
2.1	Introduction.....	5
2.2	Literature data on the formation of solids in formaldehyde-containing mixtures.....	6
2.3	Chemical reactions in formaldehyde solutions.....	7
2.4	Experiments	9
2.4.1	Chemicals and sample preparation	9
2.4.2	Studies of the formation of solids	10
2.4.3	Chemical analysis	11
2.5	Modeling.....	12
2.5.1	Physico-chemical model of the solid-liquid equilibrium	12
2.5.1.1	Overview	12
2.5.1.2	Model equations and parameters.....	15
2.5.2	Kinetic model of the solid formation.....	17
2.6	Results and discussion.....	19
2.6.1	Overview	19
2.6.2	Introductory examples	19
2.6.3	Solid-liquid equilibria	22
2.6.3.1	System (formaldehyde + water)	22
2.6.3.2	Systems (formaldehyde + methanol) and (formaldehyde + water + methanol).....	25
2.6.3.3	System (formaldehyde + water + OME).....	29
2.6.3.4	System (formaldehyde + water + methanol + OME).....	34
2.6.4	Kinetics of the formation of formaldehyde-rich solid	38
2.6.4.1	Modeling of the kinetic experiments.....	39

2.6.4.2	Determination of the chain length p of the precipitating oligomer.	40
2.7	Conclusions	46
3	Chemical reactions in the OME synthesis from dimethyl ether	49
3.1	Introduction	49
3.2	Chemical reactions	50
3.3	Experiments	52
3.3.1	Overview	52
3.3.2	Apparatus	53
3.3.3	Chemicals and catalyst	54
3.3.4	Preparation of the OME mixture	55
3.3.5	NMR analysis	55
3.4	Model	56
3.4.1	Overview	56
3.4.2	Model equations	56
3.4.3	Implementation and parameterization	59
3.5	Results and discussion	60
3.5.1	Overview	60
3.5.2	Experimental concentration profiles	61
3.5.3	Modeling of the experimental results	63
3.5.4	Model parameters	65
3.5.4.1	Temperature dependence	68
3.6	Conclusions	70
4	Production processes for OME and trioxane	72
4.1	Trioxane production process	72
4.1.1	Introduction	72
4.1.2	Processes	74
4.1.2.1	New crystallization-based process	74
4.1.2.2	Pressure swing process	76
4.1.3	Solid-liquid equilibrium measurements	76
4.1.3.1	Overview	76

4.1.3.2	Chemicals and measurement method.....	78
4.1.3.3	Results	78
4.1.4	Modeling and simulation.....	80
4.1.4.1	Process model	80
4.1.4.2	Process specifications and optimization.....	81
4.1.5	Results and discussion	83
4.1.5.1	New crystallization-based process and comparison to the pressure swing process	83
4.1.5.2	Discussion of process alternatives	89
4.1.6	Conclusions	89
4.2	OME production process	90
4.2.1	Introduction	90
4.2.2	Process concept	90
4.2.3	Chemical model	91
4.2.3.1	Chemical reactions	91
4.2.3.2	Chemical equilibrium constants	91
4.2.4	Physical property model	94
4.2.4.1	Pure component properties	94
4.2.4.2	Vapor-liquid equilibrium	94
4.2.5	Process design	95
4.2.5.1	Implementation.....	95
4.2.5.2	∞/∞ model of the process.....	95
4.2.5.3	Design with an ∞/∞ model	95
4.2.5.4	Detailed process model	96
4.2.6	Discussion.....	100
4.2.7	Conclusion.....	100
5	Application of OME as fuel	101
5.1	Introduction.....	101
5.2	Experimental apparatus and procedure	103
5.2.1	Chemicals	103
5.2.2	Phase equilibrium measurements.....	103
5.2.3	Chemical analysis	104

5.3	Modeling.....	105
5.4	Results and discussion.....	106
5.4.1	Overview.....	106
5.4.2	Experiments in the system (OME + n-alkane + water).....	109
5.4.3	Modeling of the system (OME + n-alkane + water).....	114
5.4.4	Experiments with systems with more than three components.....	116
5.4.4.1	System (OME ₄ + n-hexadecane + toluene + water).....	116
5.4.4.2	Systems of the type (OME-mixture + n-alkane + water).....	118
5.5	Conclusions.....	121
6	Conclusions	123
	Literature	125
	Appendix	137
A	Supporting information for Chapter 2	137
A.1	Ion chromatography.....	137
A.2	Formation of further side components and their measurement.....	138
A.3	UNIFAC-based model for the calculation of the activity coefficient.....	138
A.4	Chemical equilibrium model.....	139
A.5	Coupling of the solubility constants for different values of <i>p</i>	140
A.6	Reaction kinetic model.....	140
A.7	New fit of the rate constant of the degradation of MG ₂	141
A.8	Experimental data for the systems (formaldehyde + water) and (formaldehyde + water + methanol).....	144
A.9	Experimental data for the systems (formaldehyde + water + OME) and (formaldehyde + water + methanol + OME).....	192
B	Supporting information for Chapter 3	219
B.1	Discussion of alternative reactions mechanisms of the OME formation.....	219
B.2	Operating procedures of the experiments.....	220
B.2.1	Type A experiments.....	220
B.2.2	Type B experiments.....	221
B.3	Peak assignment of the components in the NMR spectra.....	221

B.4	Pure component properties	225
B.5	PSRK equation of state	226
B.6	UNIFAC-based activity coefficient model	227
B.7	Experimental data	229
B.7.1	Experiments described in the main text.....	229
B.7.2	Experiment with zeolite catalyst	238
B.8	Comparison of the mechanisms for methyl formate formation	240
B.9	Activity-based and mole-fraction based equilibrium constants	240
C	Supporting information for Chapter 4	241
C.1	Supporting information for Chapter 4.1	241
C.1.1	Process Model	241
C.1.2	Enthalpy model	246
C.1.3	Crystallization-based trioxane process with a crystallization temperature of 303 K.....	250
C.2	Supporting information for Chapter 4.2.....	253
C.2.1	Details on the calculation of $K_{(xv)}$	253
C.2.2	Parameters of the used UNIFAC-based model	254
D	Supporting information for Chapter 5	254
D.1	NMR spectroscopy	254
D.2	Karl-Fischer titration	256
D.3	Interaction parameters of the UNIFAC-model.....	256
D.4	Isothermal flash calculation	257
D.5	Feed compositions	258
D.6	Modeling of the organic phase in the system (OME _n + n-alkane + water).....	259

1 Introduction

Formaldehyde (C_2HO) is one of the most important intermediates in the chemical industry. It is produced by the oxidation of methanol. In 2011 over 31 million tons were produced [1]. Due to its high reactivity, it is rarely used in monomeric form, but mostly in aqueous solutions or mixtures with short-chain alcohols, such as methanol. In these solutions, formaldehyde forms oligomers with water and alcohols in reversible reactions. In the solutions, most of the formaldehyde is bound chemically in the oligomers. As a consequence of the formation of the oligomers, formaldehyde solutions are always complex multi-component reactive mixtures. The reactions in these solutions are well-studied and a physico-chemical model of their properties has been established which describes the liquid properties and vapor-liquid equilibria with high precision [2–7].

However, there remains an important open problem in formaldehyde technology: the omnipresent threat of solid precipitation from these solutions. It is known, that the precipitates are formaldehyde oligomers, but the exact conditions under which they form are not known. Therefore, Chapter 2 of this thesis focuses on the study of the solid formation from formaldehyde mixtures.

The following parts of this thesis deal with the synthesis of interesting downstream products of formaldehyde, the poly(oxymethylene) dimethyl ethers (OME). OME are oligomers with the general structure $\text{CH}_3\text{O}(\text{CH}_2\text{O})_n\text{CH}_3$. As they have only C-O bonds in their backbone and no C-C bonds, they burn cleanly with only weak soot formation [8–11]. Moreover, OME have a low toxicity and as methanol can be produced from various renewable raw materials or directly from carbon dioxide and hydrogen it is sustainable too [12–14]. Therefore, they are the focus of current research on clean-burning synthetic fuels [12,13,15–17]. OME_n with n between 2 and 6 have suitable properties to replace diesel fuel [14,18,19]. Other applications of OME that have been discussed recently include the use as solvents in battery electrolytes, for hydrogen storage, as well as the direct use in fuel cells [14,20,21]. Formally, dimethyl ether (DME) and methylal (MAL) can be considered as OME with $n=0$ and $n=1$, respectively, but this is uncommon. Hence, the term OME is used here only for $n \geq 2$ and OME with individual chain lengths are designated with OME_n , while using OME for OME with any chain length $n \geq 2$.

A prerequisite for large-scale applications of OME as synthetic fuels is finding economic and sustainable routes for its production. Therefore, the development of production processes for OME has received much attention in recent research; for overviews see Baranowski et al.[22], Bhatelia et al.[23], Liu et al.[12], and Hackbarth et al.[14]. In all OME processes, two educts are used: one to provide the CH₂O-groups and another to provide the methyl end-groups. Two groups of OME processes that differ fundamentally can be distinguished: processes with and without water.

In aqueous OME synthesis, relatively inexpensive chemicals such as methanol and aqueous formaldehyde solutions can be used as reactants. When methanol is used to supply the methyl end-groups of the OME, water is formed in the synthesis. Additional water may come from using aqueous formaldehyde solutions as CH₂O feedstock. As already described, the water, however, forms oligomers with formaldehyde, which lead to a reduction of the concentration of the OME in the reaction product, and, as a consequence, to large recycle streams. Furthermore, the reaction product is an azeotropic multicomponent mixture, which is difficult to separate.

Nevertheless, Schmitz et al.[24,25] succeeded in designing an efficient distillation-based process that produces OME from aqueous formaldehyde solutions and methanol, which has been recently built on miniplant-scale [26]. Oestreich et al.[27] and Han et al.[28] describe alternative extraction-based processes. In all these processes, precipitation of solids may occur, which is unwanted. Therefore, mixtures containing formaldehyde, water, methanol, and OME were included in the studies described in Chapter 2.

In the anhydrous routes for OME production, the difficulties, resulting from the formation of the oligomers of formaldehyde and water, are circumvented; however, at the cost of more expensive starting materials. Instead of aqueous formaldehyde solutions, trioxane, paraformaldehyde, or monomeric formaldehyde have to be used. The methanol must be replaced by either MAL or DME. There are many studies on anhydrous routes for OME production [12,22,29–38], and an industrial production process of OME that has been described in the literature [12] belongs to this class.

MAL is produced on an industrial scale from formaldehyde and methanol in an acid-catalyzed reaction [22,39,40]. In recent work, catalysts have been developed for the direct oxidation of methanol to MAL, and even for the hydrogenation of carbon dioxide directly to MAL, but these developments are presently still in an exploratory stage [40,41].

DME is an interesting alternative to MAL for the OME production. It is a platform chemical which is produced directly from synthesis gas or by condensation from methanol and is, therefore, cheaper than MAL [22,37,42–44]. Chapter 4.2 describes the conceptual design of a production process of OME from DME and trioxane, which is economically attractive. However, the results obtained in the simulations on which this design is based depend strongly on the chemical

equilibrium of the formation of MAL from DME. As there was no information in the literature on this equilibrium constant, the studies in Chapter 3 were carried out, from which this equilibrium constant could be determined for the first time.

Several processes for the production of trioxane have been described in the literature [1,45]. All have in common that they are energy-intensive and costly. Therefore, Chapter 4.1 describes the conceptual design of a new crystallization-based production process for trioxane which is shown to be feasible and attractive.

In the last chapter of the thesis, the application of OME in blends with hydrogenated vegetable oil (HVO), is investigated and described. Both OME and HVO can be obtained from renewable resources. Mixtures of OME and HVO that were initially homogenous show a liquid-liquid phase split after some time in technical applications. This phenomenon, which was previously only poorly understood, was elucidated in the present work based in systematic experimental studies with model components. It results from the uptake of small amounts of water from the air by the blends.

2 Solid-liquid equilibria in formaldehyde-containing mixtures

2.1 Introduction

The formation of a formaldehyde-rich solid phase in mixtures of formaldehyde with water and alcohols causes problems in many chemical processes, including clogging of lines, blockage of valves, fouling of heat exchangers, etc., which are generally difficult to predict. The substantial efforts to circumvent them are usually based on operational experience with the equipment at hand. Only basic quantitative relations regarding the formation of solids in formaldehyde-containing mixtures are known, such as the increase of the formaldehyde solubility in the system (formaldehyde + water + methanol) with increasing temperature and methanol concentration [1,46]. A quantitative theory is lacking to an extent that it is difficult to say when equilibrium is reached. Given the extraordinary industrial importance of formaldehyde-containing mixtures, this lack of knowledge is striking, all the more so as efforts to understand the solid formation in formaldehyde-containing systems started over 100 years ago.

As early as 1908, Auerbach and Barschall[47] described the formation of formaldehyde-rich solids from aqueous formaldehyde-containing mixtures. Over the years, groups in both industry [48–51] and science [46,47,52–54] have repeatedly dealt with the problem, but their results are contradictory. Despite the practical importance of methanol as a stabilizer, there is also practically no quantitative information on the formation of solids in the system (formaldehyde + water + methanol), apart from three data points reported by Grützner and Hasse[53]. However, these points were measured at low methanol concentrations of less than 0.02 g g^{-1} . Furthermore, there are no quantitative data on the kinetics of the formation of solids in formaldehyde-containing systems in the literature.

These deficiencies are due to the high physico-chemical complexity of formaldehyde-containing systems [1]. As already mentioned, formaldehyde reacts with components containing hydroxyl groups, e.g., water or alcohols, in reversible reactions to form oligomers; formaldehyde solutions

are therefore complex reactive multicomponent mixtures whose individual components cannot be isolated. The solid formation in these systems cannot be understood without considering these chemical reactions in combination with the physical effects.

The present work closes some knowledge gaps described above by combining a new experimental approach to investigate the formation of solids in formaldehyde-containing systems with a physico-chemical model of the formation processes. This combination yields a clear picture of the underlying phenomena and the possibility of predicting the solid formation, including the kinetic effects, in the studied systems, which were shown to have extraordinarily large time constants. The modeling is based on extensive previous work of our group on the physico-chemical properties of formaldehyde-containing systems [4,7,55,56], including investigations of the reaction equilibria [2,57,58] and reaction kinetics [5,57,59] of these systems.

Furthermore, it is extended to mixtures that contain also OME to enable the prediction of the solid precipitation in mixtures of formaldehyde, water, methanol, and OME, as they occur in the production process of OME. Therefore, the new experimental methods were used to measure the solubility of formaldehyde in the systems (formaldehyde + water + OME) and (formaldehyde + water + methanol + OME). To investigate the influence of the chain length of the OME, the studies were carried out with OME₂ and OME₄. As mixtures of (formaldehyde + water + OME) show a liquid-liquid miscibility gap [60], also the solid-liquid-liquid equilibria (SLLE) were studied. Finally, also this data were modeled based on the physico-chemical model.

2.2 Literature data on the formation of solids in formaldehyde-containing mixtures

Quantitative data on the formation of solids in formaldehyde-containing mixtures are basically only available for the system (formaldehyde + water). The liquidus line in that system has two branches: at low formaldehyde concentrations, the solid is pure water, while at high formaldehyde concentrations, the solid is formaldehyde-rich. The nature of that solid is not precisely known, but it can be assumed (and is shown in the results) that it consists of long-chain formaldehyde polymers. The formaldehyde-rich solid that precipitates from the formaldehyde-containing solutions is always white, but depending on the conditions, different morphologies are observed, ranging from soft-cloudy to bone-hard. The two branches of the liquidus line meet in a eutectic point, the location of which can, however, not be determined from the existing literature data.

An overview of the literature data on the formation of solids in the system (formaldehyde + water) is given in Figure 1, where the temperature of the liquidus line is plotted as a function of the overall formaldehyde mass fraction. The branch where the solid is pure water has only been studied by Walker[46]. Data from different authors [46,47,52–54] are available for the branch where the solid

is formaldehyde-rich, which are, however, contradictory. The data of Walker[46], Grützner and Hasse[53], and Ma et al.[54] are in fair agreement and indicate a linear increase in formaldehyde solubility with increasing temperature. The same trend was found by Credali et al.[52]; however, the formaldehyde solubility reported by these authors is considerably lower than that reported by the others. Auerbach and Barschall[47] report an even lower solubility; their measurements indicate a decrease in formaldehyde solubility with increasing temperature, in contrast to all other data and the practical experience.

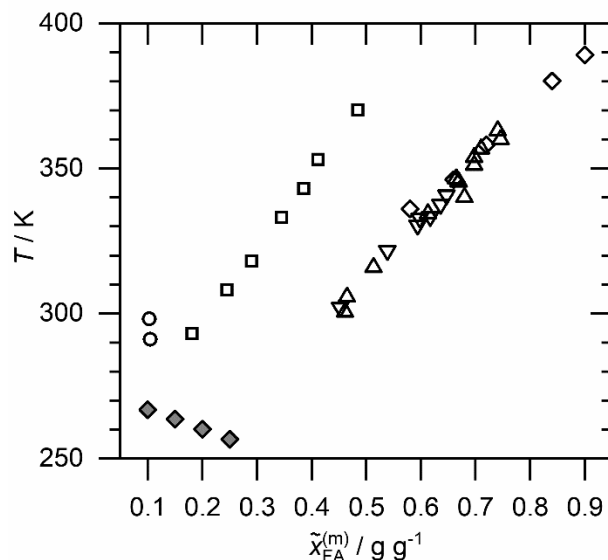


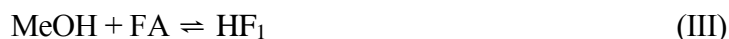
Figure 1: Experimental solubility data from the literature in the system (formaldehyde (FA) + water). Open symbols represent the solubility of formaldehyde. Filled symbols show the solubility of water. (○) Auerbach and Barschall[47], (□) Credali et al.[52], (△) Grützner and Hasse[53], (▽) Ma et al.[54], (◇/◆) Walker[46]. $\tilde{x}_{FA}^{(m)}$ is the overall mass fraction of formaldehyde.

The experimental methods used by the three groups, whose data are in good agreement with each other [46,53,54], were similar: homogeneous concentrated aqueous formaldehyde solutions were cooled, and the cloud point was observed. Credali et al.[52] and Auerbach and Barschall[47], on the other hand, dissolved short-chain paraformaldehyde in water at a constant temperature and measured the concentration of formaldehyde in the liquid phase after up to 2 months (Credali et al.[52]) or up to 5 months (Auerbach and Barschall[47]).

2.3 Chemical reactions in formaldehyde solutions

Pure monomeric formaldehyde is very reactive and tends to polymerize to unreactive paraformaldehyde, which is why monomeric formaldehyde is only very rarely used in the industry

[1,46]. In aqueous solutions, formaldehyde (FA) reversibly reacts with water (W) to form poly(oxymethylene) glycols (MG_n) according to Reactions (I) and (II) [7,46,61,62]. Together with methanol (MeOH), formaldehyde forms poly(oxymethylene) hemiformals (HF_n) according to Reactions (III) and (IV) [4,46,57]. Here, n indicates the number of formaldehyde units in the chain. In the following, n is also used to characterize the chain length and refer to it correspondingly.



These reactions always take place in aqueous and methanolic formaldehyde-containing mixtures; acids and bases can accelerate them, but no catalysts are needed to induce them [5,63]. The reaction rates have temperature-dependent minima in the range of $pH = 3$ to 4. The chemical equilibria and kinetics of these reactions have been studied extensively, and an overview of these measurements has recently been given by Kircher et al.[2].

Maurer[7] has developed a physico-chemical model of the vapor-liquid equilibrium in the system (formaldehyde + water + methanol). In that model, the equilibria of the chemical reactions according to Reaction (I) to (IV) are explicitly taken into account, and physical non-idealities are considered using a group contribution model based on UNIFAC.

The model of Maurer[7] was continuously updated in our group and extended to further systems [3,4,55,56]. The model version on which is built in the present chapter is that of Schmitz et al.[56]. It enables calculating the true species concentrations in the solutions from the overall composition and the temperature. Overall composition refers to the composition obtained if all reaction products were split up into formaldehyde, water, and methanol. Overall concentrations are labeled by a tilde over the symbol in the present work.

The distribution of the formaldehyde oligomers is similar to a Schulz-Flory distribution, i.e., the concentration of the oligomers decreases rapidly with increasing chain length. With higher overall formaldehyde concentrations, the distribution of the formaldehyde oligomers shifts to longer chains. The affinity of formaldehyde to methanol is stronger than its affinity to water, and, at the same overall formaldehyde mole fraction, the average chain length is shorter in methanol than in water [7,55]. Monomeric formaldehyde is only present in very low amounts (well below $0.001 \text{ mol mol}^{-1}$ for typical conditions in industrial applications).

As already mentioned, numerous authors have studied the reaction kinetics of the oligomerizations in aqueous and methanolic formaldehyde solutions [57,61–66]. In the present work, it is built on

the reaction kinetic model developed by Ott[65], which was coupled with the equilibrium model of Schmitz et al.[56].

Numerous further reactions can occur in formaldehyde-containing mixtures besides the oligomerization reactions. Depending on the conditions, they may lead to the formation of side components in formaldehyde solutions. Only the formation of formic acid is mentioned here, as it was the only side component, that was detected in the experiments, albeit in small amounts. In the Cannizzaro reaction, which can be accelerated both by acids and bases, formaldehyde reacts irreversibly with water to formic acid (FAc) and methanol according to Reaction (V) [1,46,67,68].



Besides formic acid, trioxane, methyl formate, and poly(oxymethylene) dimethyl ethers (OME) could in principle also be formed in the studied systems [1,45,46,58]. Beside the synthesis routes described in Chapter 3, OME can be formed from formaldehyde and methanol in the presence of strong acidic catalysts [58,59,69], which, however, was not the case in the experiments of the present work, so that the OME can be considered as inert components throughout the measurements of this chapter. Regarding the formation of trioxane, methyl formate, the samples were also analyzed for these components, but they were detected in no case. The formation pathways and the measurement methods are described in the Appendix A.2.

2.4 Experiments

2.4.1 Chemicals and sample preparation

Homogeneous formaldehyde solutions were prepared at elevated temperatures by dissolving paraformaldehyde (purity $\geq 0.95 \text{ g g}^{-1}$, Carl Roth) in water or methanol (purity $\geq 0.998 \text{ g g}^{-1}$, Sigma-Aldrich). The water came from a Milli-Q system from Merck Millipore (electrical resistance $> 15 \text{ M}\Omega \text{ cm}^{-1}$). The details of the procedure applied for dissolving the paraformaldehyde were the same as described by Schmitz et al.[58]. The solutions obtained in this way had a maximum overall formaldehyde concentration of 0.46 g g^{-1} in the case of water and 0.6 g g^{-1} for methanol. Due to water contained in the paraformaldehyde, the methanolic solution had a water fraction of about 0.01 g g^{-1} . Samples were prepared from the formaldehyde stock solutions by dilution with water and/or methanol. For measurements with OME additionally OME₂ or OME₄ was added. The different OME were provided by BASF SE with a purity of $>0.985 \text{ g g}^{-1}$.

Optionally, the pH was adjusted by adding sodium hydroxide solution (4 mol L^{-1}) for solutions that contained water and otherwise by adding sodium methylate solution (30% sodium methylate

in methanol, Merck). The maximum mass fraction of sodium hydroxide/sodium methylate was 0.002 g g^{-1} . The mass of the samples, which were kept in 50 mL centrifuge tubes, was about 40 g.

2.4.2 Studies of the formation of solids

Depending on the solid that was formed, two different types of measurements were carried out. At low formaldehyde concentrations, where the solid is pure water, samples were first cooled to a temperature below the expected liquidus temperature in a cryogenic refrigerator (Type B35-50, FRYKA). The pH value was not adjusted in these experiments. The temperature in the refrigerator was measured with a calibrated resistance thermometer with an accuracy of $\pm 0.1 \text{ K}$. After 2 days, most of the samples were still liquid. To initialize the precipitation of solid, a water-ice crystal was added to the sample, resulting in the onset of solid precipitation from the subcooled samples. After an additional five days at the same temperature, the mass fraction of formaldehyde in the liquid phase was measured. For taking a sample from the liquid phase, an isothermally conditioned syringe was used. It was ensured in prior tests, in which prolonged experiments were carried out, that this time is sufficient to establish the solid-liquid equilibrium if the solid is water. The uncertainty of this type of equilibrium measurements regarding the concentration was estimated to be below 0.005 g g^{-1} by repetition measurements.

A different technique was applied for measuring the solid-liquid equilibrium when the solid is formaldehyde-rich. Homogeneous, clear liquid samples were immersed in a thermostatted liquid bath. The studied temperatures were: 263.0, 273.2, 283.0, 293.3, and 303.4 K. The temperature was measured with a calibrated platinum resistance thermometer with an accuracy of $\pm 0.1 \text{ K}$. The formaldehyde concentration in the samples was chosen such that the concentration exceeded the expected solubility limit. Cloudiness of the samples was already observed in the first 24 h of the experiments, which were continued for up to 1000 days. At intervals from several days up to several weeks, the samples were temporarily removed from the bath, and the liquid phase was analyzed. For the analysis, the samples were placed in a centrifuge that was thermostatted to the same temperature as the bath and centrifuged for 15 min at 3500 rpm to separate the solid phase from the liquid phase. Subsequently, a part of the clear liquid phase (approx. 0.8 g) was taken with a syringe, which was equipped with a syringe attachment filter (PTFE-membrane, $0.2 \mu\text{m}$ pore diameter) as a precaution, and then analyzed. The samples were then put back into the thermostatted bath. In this way, the composition in the liquid phase was measured as a function of the time. If the composition, particularly the formaldehyde mass fraction, no longer changed, equilibrium was assumed between the liquid and solid phases. In particular, the variation of the formaldehyde mass fraction had to be below $2 \cdot 10^{-5} \text{ g g}^{-1} \text{ day}^{-1}$. In addition, there had to be at least 60 days between the two measurements where stationarity was detected. The uncertainty of the

equilibrium values regarding the concentration is $\pm 0.005 \text{ g g}^{-1}$ and was determined by repetition measurements.

The experiments were generally carried out without stirring. However, in a single experiment, the sample was stirred. For this experiment, the sample was kept in a 20 mL glass vial equipped with a magnetic stir bar. The closed vial was then placed in a thermostatted double-jacketed glass vessel on a stirring plate. The temperature was measured with a calibrated platinum resistance thermometer (accuracy $\pm 0.1 \text{ K}$). Otherwise, the experiment was carried out similarly as described above.

In some experiments with OME, a second liquid OME-rich phase was observed, like it is already known from Schmitz et al. [60]. That phase, was, however, so small that it could not be analyzed, so that the analytical results always only refer to the larger of the two liquid phases. The occurrence of a second liquid phase was, however, documented.

All measurements were done at 0.1 MPa.

2.4.3 Chemical analysis

The overall mass fraction of formaldehyde was measured using the sodium sulfite titration method [4,58,70]. An OMNIS titration robot (Metrohm) was used for this purpose. The analysis was generally repeated at least 2 times, and the average value is reported here. The maximum relative error of the formaldehyde concentration determined in this way is below 1%. This high accuracy was achieved by the complete automation and prior blank value measurements. Since it is impossible to produce reference samples of known composition with such an accuracy by gravimetric methods, at least dilution series experiments starting from concentrated stock solutions were carried out for verification.

The overall mass fraction of water was measured by Karl Fischer titration. For this purpose, 0.2 g of sample was mixed with 1 g of water-free methanol (Hydranal methanol dry, Honeywell Fluka) and left to stand for at least 24 hours. Subsequently, a volumetric Karl Fischer titration was carried out. The titration was carried out at least 2 times, and the sample's water content was calculated from the weights. The relative error of the measurement is a maximum of 2% and was checked with gravimetrically prepared samples that had similar compositions as the analyzed samples.

The mass fraction of formic acid was determined by ion chromatography, which is described in detail in the Appendix A.1.

For samples in the binary systems (formaldehyde + water) and (formaldehyde + methanol), the overall formaldehyde content was determined, and the water respectively methanol fraction was calculated from the summation equation. For samples in the system (formaldehyde + water +

methanol), the formaldehyde and water mass fractions were examined, and the mass fraction of methanol was calculated from the summation equation.

In samples with OME, the concentration of the OME was determined by gas chromatography as described by Schmitz et al. [58] with an uncertainty of 0.004 g g^{-1} .

In mixtures of (formaldehyde + water + OME) the overall mass fractions of formaldehyde and OME were measured, and the overall mass fraction of water was determined by difference to 1, as the mass fractions of formaldehyde and OME were known. In mixtures of (formaldehyde + water + methanol + OME), the overall mass fractions of formaldehyde, water, and OME were measured, and the overall mass fraction of methanol was again determined by difference to 1.

The concentration of formic acid was not always quantified. If it was, the mass fraction was always below 0.003 g g^{-1} , in most cases far below. Therefore, formic acid is neglected in the following.

2.5 Modeling

2.5.1 Physico-chemical model of the solid-liquid equilibrium

2.5.1.1 Overview

A physico-chemical model of the solid-liquid equilibrium in the system (formaldehyde + water + methanol + OME) was developed in the present work following the ideas of the modeling of the vapor-liquid equilibrium in formaldehyde-containing systems used in our group since the pioneering work of Maurer[7]. The description of the liquid phases was adopted here from Schmitz et al. [60]. The model is first explained for the system (formaldehyde + water) and then its extension to systems with methanol and OME is discussed.

A schematic representation of the model is shown in Figure 2. It refers only to the model for the case of a formaldehyde-rich solid. The model for the case when the solid is water is simpler and described below. Also, alternative models were considered. These alternatives are briefly discussed along with the presentation of the final model.

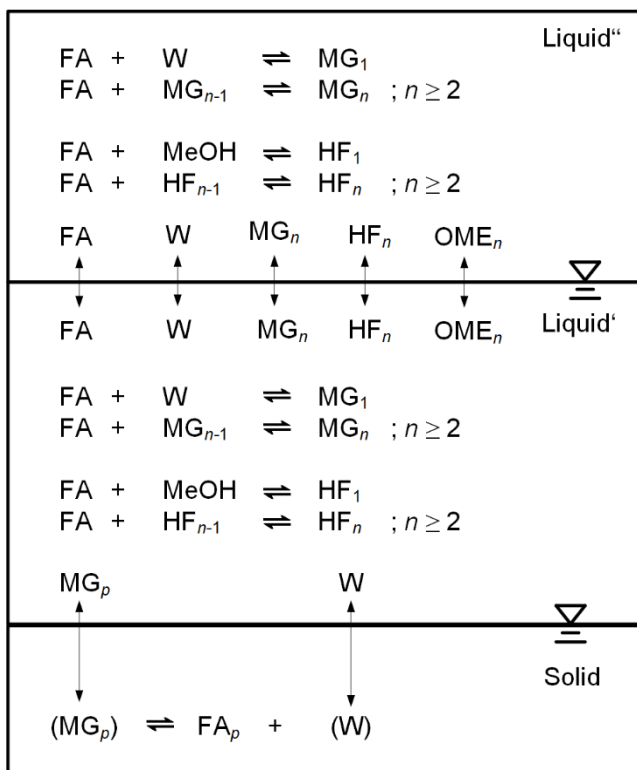


Figure 2: Scheme of the physico-chemical model of the solid-liquid-liquid equilibrium in the system (formaldehyde + water + methanol + OME_n). The symbols are explained in the text.

In the model, the liquid phase reactions of formaldehyde with water and methanol according to Reactions (I) to (IV) are explicitly considered, together with the physical nonideality of the liquid phases. The model is thermodynamically consistent.

As depicted in Figure 2, it is assumed that the solid-liquid equilibrium is established only for one particular poly(oxymethylene) glycol MG_p with the chain length *p*, while all other oligomers MG_{n≠p} remain dissolved. The idea behind this is the following: let us consider the solubility of the individual MG_n. Upon increasing the mole number of that MG_n and keeping all other mole numbers as well as the temperature and pressure constant, the solubility limit will be reached for a particular concentration of the considered MG_n, which is designated here as $x_{MG_n, sol}$. Kinetic effects are disregarded in the following discussion and it is assumed that the system is always in equilibrium. To ensure that the entire mixture is liquid, the concentrations of all MG_n must be below their solubility limit, i.e., $x_{MG_n} < x_{MG_n, sol}$ for all *n*. No numbers for the individual $x_{MG_n, sol}$ is available but it may be assumed that they decline with increasing *n*, i.e., that longer MG_n are less soluble than the shorter ones. On the other hand, the x_{MG_n} for a given overall composition and temperature can be calculated. Also, the x_{MG_n} decline with increasing *n*, as already described. Let us now consider an aqueous formaldehyde solution at a temperature and overall formaldehyde

concentration where it is liquid, i.e., $X_{MG_n} < X_{MG_n, \text{sol}}$ for all n . Now, when increasing the overall formaldehyde concentration (or decreasing the temperature), at a certain point, the liquidus line will be reached, and solids will start forming. It is reasonable to assume that the solubility limit, i.e., $X_{MG_n} = X_{MG_n, \text{sol}}$, is not reached for several or all MG_n simultaneously, but rather for a certain MG_p , while all other $MG_{n \neq p}$ remain dissolved: the smaller ones ($n < p$) as their solubility is high enough and the larger ones ($n > p$) as their concentration is low enough. As the physical solubility for each MG_n ($X_{MG_n, \text{sol}}$) and the species distribution are temperature-dependent, the number p , which characterizes the precipitating MG_p , may depend on the temperature too, but this will be neglected for now and it will be picked up again when discussing the results of the kinetic experiments.

In principle, the behaviour described above could lead to a simple solid-liquid equilibrium model where the solid is just pure MG_p . However, it is known that the solid contains basically only formaldehyde, whereas there is always a certain amount of water in MG_p (the overall molar water/formaldehyde ratio in the MG_p is $1/p$). To reconcile the simple model with the experimental findings on the solid, it might be assumed that p is very large (it would have to be well above 100); however, due to the decreasing concentration of every MG_n with increasing n , such long MG_n have exceedingly small concentrations; so building a model on this picture seems not attractive. The other option is to assume that p is in the range where oligomers are still present in appreciable amounts and to assume that the solid MG_p releases water into the liquid phase. This would be the case if it would polymerize and the solubility of water in that polymer would be low. These assumptions are reasonable, and they were therefore adopted for the model. This decision is supported by the fact that the resulting model describes the data better than the previously mentioned competing model variants. At this point, it is still open how to find out the number p ; this is discussed below. The polymerization of the solid phase is not explicitly accounted for here; It was simply assumed MG_p loses its capping water and forms FA_p . Physically, this can be interpreted as a formation of a paraformaldehyde-like oligomer. Considering the polymerization in more detail would not alter the results, as long as it is assumed that it is fast enough.

It is known that methanol is a good stabilizer for formaldehyde mixtures. This leads to the assumption that, also in mixtures of (formaldehyde + water + methanol), the oligomer for which the solubility limit is reached first is a methylene glycol MG_p , and not a hemiformal HF_q . This is adopted for the model. However, this excludes using the model for the system (formaldehyde + methanol), and leads to the expectation of its breaking down at high methanol/water ratios. (It will be shown below that the model assuming that the precipitating component is MG_p works up to unexpectedly high methanol/water ratios). The model could be extended to cover also these cases by considering a critical hemiformal HF_q . However, it was refrained from including this case in the present model, as the conditions where this would become relevant are outside of the technically relevant range.

So far, only solid-liquid equilibria for which the solid is formaldehyde-rich were discussed. At low formaldehyde concentrations, however, the solid is either pure water, pure methanol, or pure OME. Only the case where the solid is water will be discussed here; the cases with solid methanol or OME are analogous, and furthermore, solid methanol is expected to occur only at temperatures below 180 K and therefore far outside of any technical relevance [71]. It is mentioned here, only for completeness, that there is also a fourth solid phase in the system (water + methanol): the methanol monohydrate [71].

The model for the case where the solid is water is straightforward, as the solid-liquid equilibrium only has to be considered for water; the presence of the other components in the liquid phase leads to a freezing point depression compared to pure water, which can be calculated from the knowledge of the true composition of the liquid phase and the model used to describe its physical nonideality.

The second liquid phase only occurs in mixtures with OME and the liquid-liquid equilibrium is also described by the physico-chemical model.

2.5.1.2 Model equations and parameters

Wherever it was possible, information on the studied systems from previous works was adopted. The remaining model parameters were adjusted to the experimental data from the present work, as described below in more detail.

The chemical equilibria of the oligomerization reactions (according to Reaction (I) to (IV)) are described in the model by their activity-based chemical equilibrium constants K_a :

$$K_{a,j}(T) = \prod_{i=1}^{N_C} a_i^{v_{i,j}} = \prod_{i=1}^{N_C} (x_i \cdot \gamma_i)^{v_{i,j}} \quad (1)$$

Wherein a_i is the activity, x_i the true mole fraction, and γ_i the activity coefficient of component i . $v_{i,j}$ is the stoichiometric coefficient of component i in reaction j . N_C is the number of all components in the system. The activity coefficient is calculated with a UNIFAC-based activity coefficient model. The oligomers up to $n=15$ are considered for both MG_n and HF_n . The possibility of the formation of a second liquid phase in connection with OME is considered by taking into account the corresponding phase equilibrium conditions. For the calculation of the liquid-liquid equilibrium (LLE), the iso-activity criterion is applied for the true components. The temperature-dependent correlations for the equilibrium constants, the UNIFAC-based activity coefficient model and its parameters were adopted from Schmitz et al.[56] and are given in the Appendix A.3.

LLE in systems containing formaldehyde, water, methanol, and OME have been studied previously by Schmitz et al.[60]. The LLE model from the present work is identical with that of Schmitz et al.[60] and, therefore, describes the LLE generally well.

For the case of formaldehyde-rich solids, the solid-liquid equilibrium is described by



where L refers to the liquid phase and S to the solid phase. Equation (VI) accounts for the processes described above; see also Figure 2. It is assumed that the activity of the solid formaldehyde polymer is 1, which leads to the following equilibrium condition for the processes described by Equation (2):

$$K_p^{\text{SL}}(T) = \frac{a_{\text{W}}^{\text{L}}}{a_{\text{MG},p}^{\text{L}}} = \frac{x_{\text{W}}^{\text{L}} \cdot \gamma_{\text{W}}^{\text{L}}}{x_{\text{MG},p}^{\text{L}} \cdot \gamma_{\text{MG},p}^{\text{L}}} \quad (2)$$

Therein, K_p^{SL} is the equilibrium constant corresponding to Reaction (VI) and a_{W}^{L} and $a_{\text{MG},p}^{\text{L}}$ are the liquid phase activities of water and MG_p , respectively. The equilibrium constant K_p^{SL} , describing the solid-liquid equilibrium when the solid is formaldehyde-rich, cf. Equation (2), is described temperature-dependent by the integrated van't Hoff equation:

$$\ln(K_p^{\text{SL}}(T)) = A_p + \frac{B_p}{T/\text{K}} \quad (3)$$

In this work, $p = 9$ was chosen for reasons described below. The parameters A_p and B_p were determined from a fit to the experimental results on the solid-liquid equilibrium in the system (formaldehyde + water) from the present work: For the measured overall formaldehyde concentration and the temperature, the true composition was calculated with the reaction equilibrium model. Then, the value of K_p^{SL} was calculated such that the correct solubility limit was obtained. This procedure was repeated for all temperatures for which data on the solubility limit in the system (formaldehyde + water) had been measured. Then, A_p and B_p were determined by a least-squares fit of the experimental data for $\ln(K_p^{\text{SL}})$ and the correlation from Equation (3). In principle, any number of p can be chosen in this procedure. The resulting values of the equilibrium constants K_p^{SL} would differ, but the description of the equilibrium would be the same. If the number for K_p^{SL} is known for a certain p , the corresponding numbers for other p can be obtained from the chemical equilibrium constants of the oligomerization reactions, as shown in the Appendix A.5. The choice of p is, however, important for the description of the kinetics. No data for the ternary system (formaldehyde + water + methanol) were used for the fit. This resulted in

$$\ln(K_9^{\text{SL}}(T)) = -20.7952 + \frac{10278.78}{T/\text{K}} \quad (4)$$

The solid-liquid equilibrium for the case where the solid is water (W) is described by

$$\ln(x_{\text{W}} \cdot \gamma_{\text{W}}) = \frac{\Delta h_{\text{W}}^{\text{f}}}{RT_{\text{W}}^{\text{f}}} \left(1 - \frac{T_{\text{W}}^{\text{f}}}{T}\right) \quad (5)$$

where T_{W}^{f} and $\Delta h_{\text{W}}^{\text{f}}$ are the melting temperature and molar enthalpy of fusion of pure water, and R is the universal gas constant; x_{W} is the true mole fraction of water and γ_{W} is the corresponding activity coefficient. The pure component data were taken from the DIPPR database[72] and are $\Delta h_{\text{W}}^{\text{f}} = 6.00174 \text{ kJ mol}^{-1}$ and $T_{\text{W}}^{\text{f}} = 273.15 \text{ K}$.

2.5.2 Kinetic model of the solid formation

The kinetic model is based on the model of the solid-liquid equilibrium described above. It describes only the formation of a formaldehyde-rich solid, which is by far the most important in practice - and the one that causes the plethora of problems mentioned in the introduction.

The model is based on the experimental findings from the present work; the extraordinarily slow kinetic effects that were found are described well using the assumption that the kinetics of the solid formation are determined by the interaction of the liquid phase reaction kinetics with the precipitation of a single oligomer. Physical kinetic effects related to the formation of solids, such as nucleation, crystal growth, agglomeration, etc., occur in the present system on a much shorter time scale and are therefore neglected in the model; and, as a consequence, also supersaturation is disregarded.

The basic scheme for the kinetic model is the same as for the equilibrium model; see Figure 2. Furthermore, it is assumed that all processes described by Reaction (VI) are much faster than the liquid phase reaction kinetics. Hence, the equilibrium condition, Equation (2), is fulfilled at all times.

The reaction kinetic model was adopted from Ott[65]. It is based on activities and is consistent with the equilibrium model described above. The temporal change in the amount of substance of component i due to reactions (dn_i^{reac}/dt) is described according to Equation (6).

$$\frac{dn_i^{\text{reac}}}{dt} = n_{\text{tot}} \sum_{m=1}^{2N_{\text{R}}} \nu_{i,m} \cdot k_m \prod_{i=1}^{N_{\text{C}}} a_i^{|v_{i,m} \cdot z_{i,m}|} \quad (6)$$

$$\text{with } z_{i,m} = \begin{cases} 1, & \nu_{i,m} < 0 \\ 0, & \nu_{i,m} \geq 0 \end{cases}$$

Here, n_{tot} is the total amount of substance in the liquid phase. N_k is the number of equilibrium reactions so that the forward and reverse reactions must be considered separately from each other in the context of kinetics, resulting in a summation over $2 N_k$ reactions. The rate constants k_j of the forward (k_j^+) and reverse (k_j^-) reactions are interrelated by the equilibrium constant according to Equation (7).

$$K_{a,j} = \frac{k_j^+}{k_j^-} \quad (7)$$

Thus, only one rate constant for each equilibrium reaction has to be determined, since the other is determined by Equation (7). The information on the rate constants was taken from Ott[65]. The rate constants of the reactions in which monomeric formaldehyde is involved, i.e., k_1 and k_3 , depend only on temperature, the rate constants of the chain formation reactions, k_2 and k_4 , also depend on the pH value. The correlations and corresponding parameters are given in the Appendix A.6.

The amounts of MG_p and water in the liquid phase are influenced by the chemical reactions as well as by the formation (or dissolution) of the solid. For all other components, changes of the amounts can only result from chemical reactions, i.e.

$$\frac{dn_i}{dt} = \frac{dn_i^{\text{reac}}}{dt} \text{ for all } i \neq \text{MG}_p, \text{W} \quad (8)$$

For MG_p and water, the liquid phase component balance is

$$\frac{dn_{\text{MG}_p}}{dt} = \frac{dn_{\text{MG}_p}^{\text{reac}}}{dt} - \frac{dn_{\text{FA}_p}}{dt} \quad (9)$$

$$\frac{dn_{\text{W}}}{dt} = \frac{dn_{\text{W}}^{\text{reac}}}{dt} + \frac{dn_{\text{FA}_p}}{dt} \quad (10)$$

In applying Equations (9) and (10), different cases have to be distinguished. In the following, the onset of the formation of the solid is described. The case of the dissolution of the solid is analogue. In each time step, the solubility condition for MG_p , $X_{\text{MG}_p} < X_{\text{MG}_p, \text{sol}}$, is evaluated. The value of $X_{\text{MG}_p, \text{sol}}$ is found from the equilibrium condition according to Equation (2). If it is fulfilled, then dn_{FA_p}/dt is zero. When a violation of the solubility condition is detected, the concentration of MG_p is set to its equilibrium value and the excess of MG_p is assumed to be transformed to FA_p and W , according to Equation (VI). The amount of FA_p (i.e., the amount of the solid phase) that is formed is found from a mass balance and the corresponding terms in Equations (9) and (10) are non-zero. In this case, a differential-algebraic equation system (DAE) has to be solved. The equations were implemented in MATLAB and solved by the solver ode15s.

2.6 Results and discussion

2.6.1 Overview

In the following, the process of solid formation is discussed in general terms on the basis of measurements in the system (FA + W). Then the solid-liquid equilibria in the system (FA+W), system (FA+W+MeOH), and finally for the systems (FA + W + OME) and (FA + W + MeOH + OME) are presented, followed by the results on the kinetics.

Different types of experiments were performed in the present work. Experiments in which the solid was water were only carried out in the system (formaldehyde + water). In these experiments, only solid-liquid equilibria were measured, but not kinetics. There are eight such experiments; in six of which, metastable equilibria were studied.

In all other experiments, the solid was formaldehyde-rich. In all of these experiments, time-dependent kinetic data were taken. A stationary state was only reached when sodium hydroxide was added to increase the kinetics of the liquid phase reactions. In these experiments, along with the kinetic data, equilibrium data were also obtained. When no sodium hydroxide was added, the reactions were slow, and only kinetic data were obtained.

The samples labeled here as (formaldehyde + methanol) contained small amounts of water due to their preparation from paraformaldehyde, as described in the experimental section. The full set of experimental data are reported in the Appendix A.8.

2.6.2 Introductory examples

Three exemplary concentration profiles from experiments in which the solid was formaldehyde-rich are shown in Figure 3. They were carried out at different temperatures with mixtures of (formaldehyde + water). Even though sodium hydroxide was added to accelerate the kinetics, it took about 100 days until a stationary state was reached at the lowest temperature. The stationary state results show the increase of the formaldehyde solubility in water with increasing temperature.

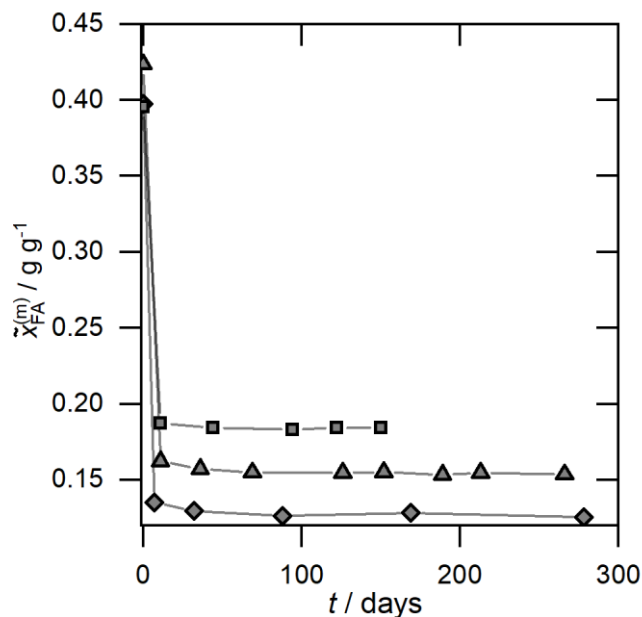


Figure 3: Overall formaldehyde concentration in the liquid phase during kinetic experiments in the system (formaldehyde + water) measured in three experiments at different temperatures. Sodium hydroxide was added to accelerate the liquid phase reaction kinetics. The pH value is about 9.5. The solid was formaldehyde-rich. Solid lines are linear splines of the data. (■) $T = 293.3$ (▲) $T = 283$ K (◆) $T = 273.2$ K.

The influence of the adjustment of the pH value is illustrated in Figure 4, where two experiments are compared in which the only difference was the addition of sodium hydroxide in one of them. With sodium hydroxide, the equilibrium was reached after about 100 days; without sodium hydroxide, it was still not reached after 1000 days.

Without adding acids or bases, formaldehyde solutions typically have a pH value of about 4. Hence, formaldehyde solutions to which neither acids nor bases are added tend to have pH values in the region where the reaction rates of the oligomerization reactions are minimal. In one set of experiments that were carried out in the present work, such mixtures were studied. In none of these was the solid-liquid equilibrium reached. In a second set of experiments, sodium hydroxide was added in an amount that resulted in a pH value of about 9.5 (or in case with OME to 11). Only these two sets were distinguished and not individual pH values were reported, as they slowly shifted with time. Details on the amount of sodium hydroxide that was added are reported in the Appendix A.8.

In principle, adding sodium hydroxide could influence the solid-liquid equilibrium by a salting-out effect. It was shown in prior experiments that this effect is negligible for the small concentrations of sodium hydroxide used in the present work. Furthermore, it was shown that the

formation of side products is not responsible for the stronger decrease of formaldehyde concentration when the sodium hydroxide is added. Only formic acid could be detected in measurable concentrations in all samples; these concentrations were, however, always negligible. Figure 4 also contains results for the equilibrium composition obtained from averaging the data of Walker[46], Grützner and Hasse[53], and Ma et al.[54]. It becomes clear that these authors have not considered long-term effects. This is in line with reports from Grützner and Hasse^[53], in which the authors had noticed that samples which, according to their measurements, should not form a solid phase showed turbidity after a few weeks. It will resume the discussion of these findings below.

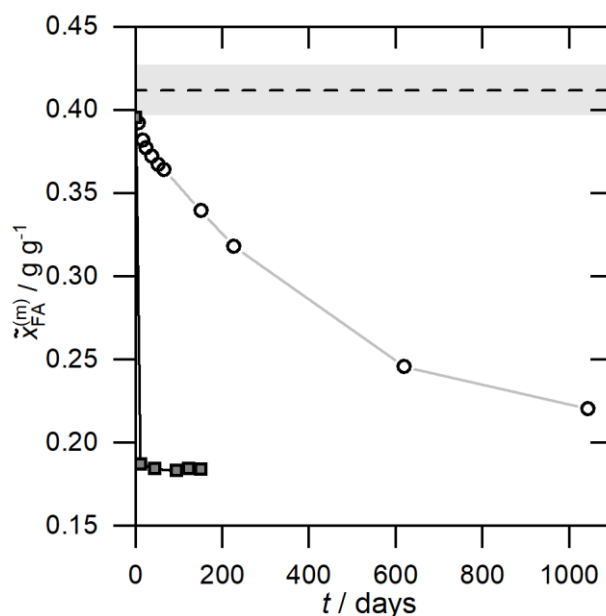


Figure 4: Overall formaldehyde concentration in the liquid phase measured in two kinetic experiments in the system (formaldehyde + water) at 293.3 K. The solid that was formed was formaldehyde-rich. (○) sample without sodium hydroxide (pH \approx 4), (■) sample with sodium hydroxide (pH \approx 9.5), (—) linear spline connecting the experimental data, (---) solubility from linear regression of the data of Grützner and Hasse[53], Ma et al.[54], and Walker[46]; the gray area indicates the standard deviation of the linear regression.

The results shown in Figure 4 demonstrate the influence of the reaction kinetics on the kinetics of the solid formation in the system (formaldehyde + water). Furthermore, the influence of the mass transfer was studied by conducting an experiment in which the solution was stirred. The results from that experiment are compared in Figure 5 to those from an experiment that was basically identical, except that the solution was not stirred. As expected, stirring accelerates the kinetic

processes, but the influence is small compared to that of adding sodium hydroxide. The experiment with the stirrer had to be stopped after 21 days, as the solid hindered the stirring.

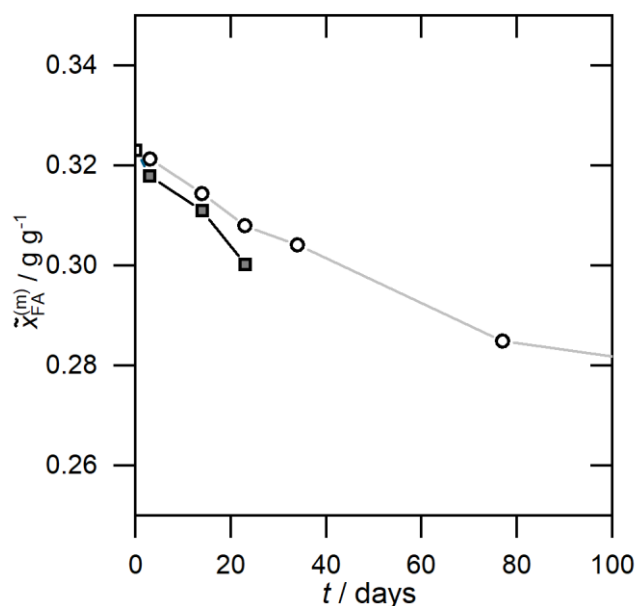


Figure 5: Overall formaldehyde concentration in the liquid phase measured in two kinetic experiments in the system (formaldehyde + water) at 273.2 K (no sodium hydroxide added). For better visualization, the profile of the unstirred sample is only shown for the first 100 days. The solid that was formed was formaldehyde-rich. (○) sample without stirring, (■) stirred sample. Solid lines are linear splines of the experimental data. The measurement of the stirred sample was stopped after 21 days as the stirrer was blocked by the solid.

2.6.3 Solid-liquid equilibria

2.6.3.1 System (formaldehyde + water)

The results of the solid-liquid equilibrium measurements in the system (formaldehyde + water) are shown in Figure 6. It contains data on both branches of the liquidus line: the branch where the solid is water, and the branch where the solid is formaldehyde-rich. They meet at a eutectic point. For the first branch, also metastable data points, at temperatures below the eutectic temperature, are reported. The data for the experiments in which the solid was water are shown in Table 1; those for the experiments in which the solid was formaldehyde-rich are shown in Table 2. The existence of the metastable solid-liquid equilibria with pure water as a solid phase at temperatures well below the eutectic temperature can probably be explained by different time scales of the

formation of the different solids. While solid water is readily formed, the formation of a formaldehyde-rich solid phase needs much more time. The kinetic hindrance is expected to be particularly important at low temperatures and is probably the reason why no formation of a second formaldehyde-rich solid phase was observed.

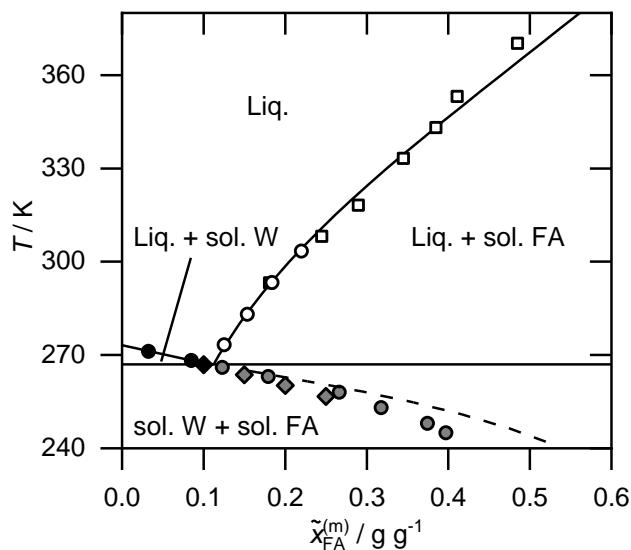


Figure 6: Solubility data for the system (formaldehyde + water). Data for two cases: (open) solid is formaldehyde-rich; (filled) solid is water; (\circ/\bullet) this work, (\square) Credali et al.[52], (\blacklozenge) Walker[46]. Lines are calculated by the models of the present work for both cases. The intersection of the lines is the eutectic point located at 266.96 K and $\tilde{x}_{FA}^{(m)} = 0.1123 \text{ g g}^{-1}$. The vertical solidus line through the eutectic point is also shown. The results for the case of solid water for temperatures below the eutectic point correspond to metastable equilibria. The metastable points are filled gray. Model results for metastable states are indicated by dashed lines.

Table 1: Solid-liquid equilibria in the system (formaldehyde + water) where the solid is water. Only equilibria marked with an asterisk are stable; all others are metastable.

T K	$\tilde{x}_{\text{FA}}^{(m)}$ g g^{-1}
271.1	0.0326*
268.2	0.0852*
266.0	0.1231
263.0	0.1795
258.0	0.2663
253.0	0.3179
248.0	0.3746
245.0	0.3973

Table 2: Solid-liquid equilibria in the system (formaldehyde + water) where the solid is formaldehyde-rich.

T K	$\tilde{x}_{\text{FA}}^{(m)}$ g g^{-1}
303.4	0.2200
293.3	0.1842
283.0	0.1537
273.2	0.1255

Figure 6 also contains literature data for both cases. Walker[46] has reported on data for the case where the solid is water. The agreement between our data and that of Walker[46] is good. For the case of a formaldehyde-rich solid, experimental data of Credali et al.[52] are included in Figure 6, which agree well with the new data from the present work. However, this is not the case for all other data sets from the literature, as can be seen from Figure 1. Most of the studies from the literature [46,53,54] report much higher solubilities of formaldehyde in water than those found in the present work as well as in the work of Credali et al.[52]. An explanation for these discrepancies is indicated by the findings shown in Figure 4: the time it takes to reach the equilibrium in the studied system is exceptionally long, much longer than the times the system was studied in the experiments of the literature carried out by Walker[46], Grützner and Hasse[53] and Ma et al.[54]. Unfortunately, Credali et al.[52] do not give many details on their experiments but state that they took up to two months, which can be sufficient to reach the equilibrium if the pH value is adjusted. Even though the data of Grützner and Hasse[53], Ma et al.[54], and Walker[46] do not describe the thermodynamic equilibrium, they remain practically relevant; they can be used when information on the short-term stability of aqueous formaldehyde solutions is needed. However,

this should be done cautiously, as in these publications [46,53,54] not equilibria but kinetic effects were measured, which depend on both the chosen initial and boundary conditions, which are, unfortunately, only partially reported. The fact that similar results were obtained by different authors [46,53,54] in different types of experiments gives some confidence regarding the application of the results, but basically, they should only be applied for predictions of situations that are not too far from those of the underlying experiments. The formation of solids can only be excluded with certainty based on the equilibrium data.

In Figure 6 results from the solid-liquid equilibrium models developed in the present work are also shown. Both branches of the liquidus line are described very well by the models. The model results for the branch where the solid is water are predictions obtained based on Equation (5) and literature data on the melting temperature and enthalpy of pure water[72]. The true composition of the liquid phase and the activity coefficients were calculated with the model of Schmitz et al.[56]. The freezing point depression is predicted very well even for most of the metastable states.

As already explained, the model for the branch of the liquidus line where the solid is formaldehyde-rich was obtained by fitting the temperature-dependent solubility constant of one of the MG_n to the present data. Hence, the good agreement between the model and the data from the present work is not astonishing. However, that model also predicts the data of Credali et al.[52] at higher temperatures well, which were not considered in the fitting. The results shown in Figure 6 were obtained assuming that the precipitating poly(oxymethylene) glycol is MG_9 . As the results for different numbers of p do not differ, it is impossible to rationally select the number for p based on the solid-liquid equilibrium data alone. However, this is possible if kinetic data are considered, as explained below. The selection $p = 9$ was therefore based on the kinetic results.

Up to now, no information regarding the eutectic point in the system (formaldehyde + water) has been reported in the literature. The coordinates of the eutectic point were determined here from the intersection of the models of the two liquidus lines and are:

$$T_{Eu} = 266.96 \pm 0.1 \text{ K and } \tilde{x}_{FA,Eu}^{(m)} = 0.1123 \pm 0.005 \text{ g g}^{-1}$$

The uncertainty is basically determined by the uncertainty of the experimental data for both lines.

2.6.3.2 Systems (formaldehyde + methanol) and (formaldehyde + water + methanol)

Figure 7 shows the measured liquid phase composition in equilibrium with a formaldehyde-rich solid in the ternary system (formaldehyde + water + methanol) as well as in the binary systems (formaldehyde + water) and (formaldehyde + methanol) as a triangular diagram. Three different solvent compositions were used in the ternary system, where, within each set, the water fraction in the solvent mixture of water and methanol ($\tilde{x}_{W,sol}^{(m)}$) was constant; i.e., the ratio of water/methanol in the feed was constant. Solid lines connect points measured at the same temperature. The

corresponding numerical data for the methanol-containing systems are given in Table 3 and Table 4.

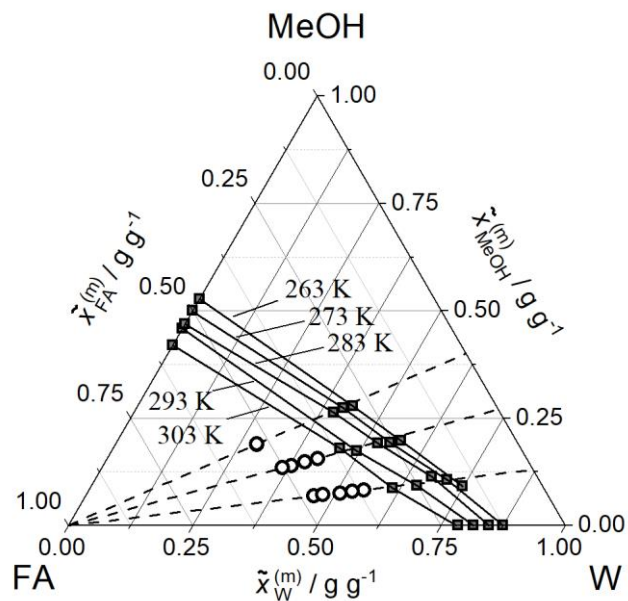


Figure 7: Experimental solubility data for the system (formaldehyde + water + methanol), including data for binary subsystems. Compositions of mixtures on the liquidus line are given as filled symbols for different temperatures. Solid lines connect results for the same temperature. Empty symbols are feed compositions for ternary mixtures. Dashed lines correspond to a constant ratio of water/methanol in the mixture. As all symbols agree with the mass balance lines, it is indicated that the solid is always basically oligomeric formaldehyde.

Table 3: Solid-liquid equilibria in the system (formaldehyde + water + methanol) where the solid is formaldehyde-rich.

T K	$\tilde{x}_{\text{FA}}^{(m)}$ g g^{-1}	$\tilde{x}_{\text{W}}^{(m)}$ g g^{-1}
303.4	0.3035	0.6097
	0.3632	0.4574
293.3	0.2513	0.6555
	0.3328	0.4943
283.0	0.2119	0.6741
	0.2807	0.5276
273.2	0.3345	0.4022
	0.1849	0.7093
	0.2562	0.5516
263.0	0.3101	0.4173
	0.1610	0.7473
	0.2321	0.5711
	0.2894	0.4363

Table 4: Solid-liquid equilibria in the system (formaldehyde + methanol) where the solid is formaldehyde-rich. The samples contained about 0.01 g g⁻¹ water from the preparation.

T K	$\tilde{x}_{\text{FA}}^{(m)}$ g g^{-1}
303.4	0.5802
293.3	0.5423
283.0	0.5300
273.2	0.5014
263.0	0.4722

The results presented in Figure 7 show that the solubility of formaldehyde increases with increasing methanol content. At 273 K, the solubility of formaldehyde in methanol is about 4 times higher than that in water when overall mass fractions are used for the specification (the corresponding number is 6 when overall mole fractions are used). At a given temperature, the solubility in the ternary system can basically be found from a linear interpolation between the data of the binary systems (formaldehyde + water) and (formaldehyde + methanol).

In addition to the equilibrium data for the ternary mixtures, the compositions of the feed solutions are also shown in Figure 7. Both the final equilibrium composition of the liquid phase and the feed composition lie on lines with constant mass fraction of water in the solvent (indicated as dashed

lines in Figure 7). This shows that the solid that is formed contains basically only CH_2O units, i.e., it must be long-chain oligomeric formaldehyde. This is also proven by the data of the system (FA + W + OME), cf. Chapter 2.6.3.3.

Figure 8 gives a different representation of these results: the data for the formaldehyde solubility at different temperatures are shown for different compositions of the solvent ranging from pure water to almost pure methanol. The symbols represent the experimental data from the present work, the dashed lines are linear splines connecting the data for a given solvent composition, and the solid lines are model results. The increase of the formaldehyde solubility with increasing temperature and methanol concentration in the solvent is clearly visible. The model was only fitted to data for the system (formaldehyde + water). Predicting the influence of methanol on the solubility of formaldehyde is, hence, a challenging test for the model, which it passes pretty well. Even the predictions for the solubility in almost pure methanol are reasonably good when keeping in mind that they are based only on information on the solubility of formaldehyde in pure water. These findings support the model assumption that the oligomer for which the solubility limit is reached first is a poly(oxymethylene) glycol. It is astonishing to see that this assumption seems to work even for mixtures containing only small quantities of water. Given these astonishingly good results, it was refrained from using data on methanol-containing systems for fitting model parameters or modifying the model for methanol-rich mixtures.

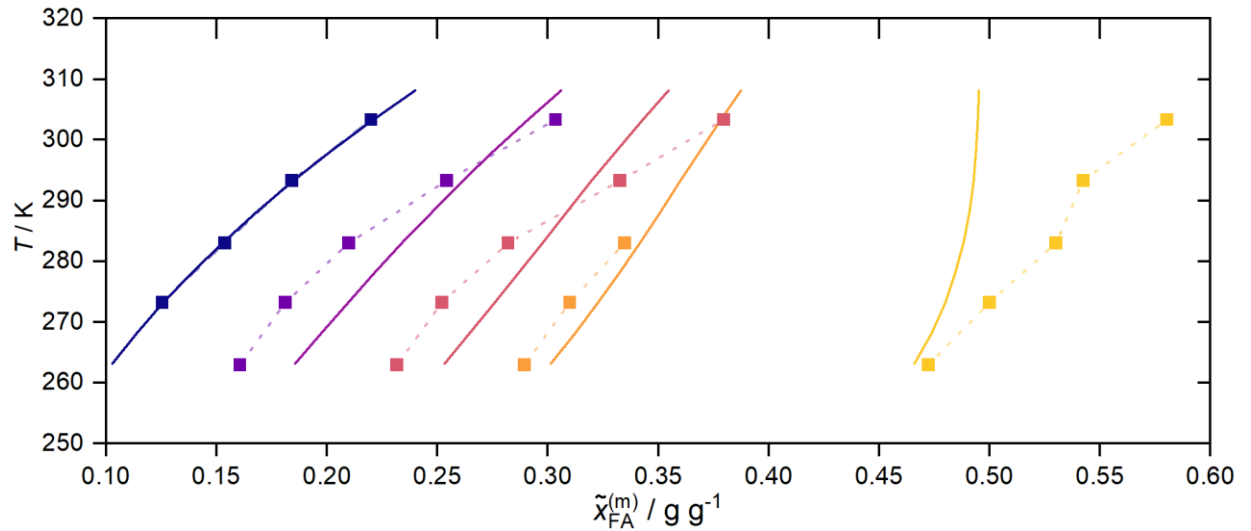


Figure 8: Formaldehyde solubility in (water + methanol) solvents. The color indicates the composition of the solvent, which is specified here by the mass fraction of water in the solvent ($\tilde{x}_{W,sol}^{(m)}$). (■) $\tilde{x}_{W,sol}^{(m)} = 1 \text{ g g}^{-1}$, (■) $\tilde{x}_{W,sol}^{(m)} = 0.87 \text{ g g}^{-1}$, (■) $\tilde{x}_{W,sol}^{(m)} = 0.73 \text{ g g}^{-1}$, (■) $\tilde{x}_{W,sol}^{(m)} = 0.6 \text{ g g}^{-1}$, and (■) $\tilde{x}_{W,sol}^{(m)} = 0.01 \text{ g g}^{-1}$. Squares indicate experimental data. Dashed lines are linear splines connecting the experimental data. Solid lines are calculated with the model. The model was fitted only to the data for the system (formaldehyde + water). The results for the methanol-containing mixtures are predictions.

2.6.3.3 System (formaldehyde + water + OME)

The feed compositions in the systems (FA + W + OME₂) and (FA + W + OME₄) were chosen as follows. Starting with an aqueous formaldehyde solution with $\tilde{x}_{FA}^{(m)} = 0.4 \text{ g g}^{-1}$ FA, three different amounts of OME were added. This resulted in three different overall fractions of OME in the solvent mixture ($\tilde{x}_{OME_n,sol}^{(m)}$), consisting of water and OME. This quantity will be also used in the tables to characterize the feed compositions of each experiment. The experiments were then carried out for the different temperatures until equilibrium was reached. In all measurements of this systems sodium hydroxide was added.

Both SLE and SLLE were observed. High amounts of OME in the feed mixture and low temperatures favor the formation of the second liquid phase.

The results for the SLE and SLLE are given in Table 5 for OME₂ and in Table 6 for OME₄. The results are also visualized in Figure 9 together with data for the liquid-liquid equilibrium in the studied systems from Schmitz et al. [60].

Table 5: Feed compositions and liquid phase compositions in solid-liquid equilibria in the system (formaldehyde + water + OME₂); the solid is basically pure oligomeric formaldehyde. Equilibria with a second liquid phase are marked with an asterisk. Note that in the specification of the feed composition, the number for OME₂ refers to the formaldehyde-free solvent. The feed compositions in simple mass fractions are given in the Appendix A.9.

Experiment	T K	feed composition		equilibrium composition	
		$\tilde{x}_{\text{FA}}^{(m)}$ g g ⁻¹	$\tilde{x}_{\text{OME2,sol}}^{(m)}$ g g ⁻¹	$\tilde{x}_{\text{FA}}^{(m)}$ g g ⁻¹	$\tilde{x}_{\text{OME2}}^{(m)}$ g g ⁻¹
OME-1	273.2	0.3571	0.1562	0.1064	0.1373
OME-2		0.3182	0.2935	0.0926	0.2618
OME-3		0.2783	0.4150	0.0912*	0.2942*
OME-4	283.0	0.3576	0.1569	0.1329	0.1291
OME-5		0.3179	0.2932	0.1186	0.2477
OME-6		293.3	0.3573	0.1569	0.1655
OME-7	0.3178		0.2939	0.1458	0.2416
OME-8	0.2782		0.4162	0.1373*	0.3052*
OME-9	303.4	0.3465	0.1528	0.2039	0.1124

Table 6: Feed compositions and liquid phase compositions in solid-liquid equilibria in the system (formaldehyde + water + OME₄); the solid is basically pure oligomeric formaldehyde. Equilibria with a second liquid phase are marked with an asterisk. Note that in the specification of the feed composition, the number for OME₂ refers to the formaldehyde-free solvent. The feed compositions in simple mass fractions are given in the Appendix A.9.

Experiment	T K	feed composition		equilibrium composition	
		$\tilde{x}_{\text{FA}}^{(m)}$ g g ⁻¹	$\tilde{x}_{\text{OME4,sol}}^{(m)}$ g g ⁻¹	$\tilde{x}_{\text{FA}}^{(m)}$ g g ⁻¹	$\tilde{x}_{\text{OME4}}^{(m)}$ g g ⁻¹
OME-10	273.2	0.3577	0.1561	0.1125	0.1363
OME-11		0.3179	0.2937	0.1020*	0.2465*
OME-12		0.2781	0.4164	0.1022*	0.2358*
OME-13	283.0	0.3578	0.1566	0.1330	0.1367
OME-14		0.3181	0.2930	0.1249*	0.2445*
OME-15		0.2778	0.4162	0.1220*	0.2286*
OME-16	293.3	0.3571	0.1584	0.1636	0.1334
OME-17		0.3177	0.2929	0.1478*	0.2404*
OME-18		0.2779	0.4167	0.1486*	0.2479*
OME-19	303.4	0.3573	0.1574	0.1989	0.1222

Table 6 continued

OME-20		0.3178	0.2939	0.1795	0.2350
OME-21		0.2777	0.4167	0.1670*	0.2624*

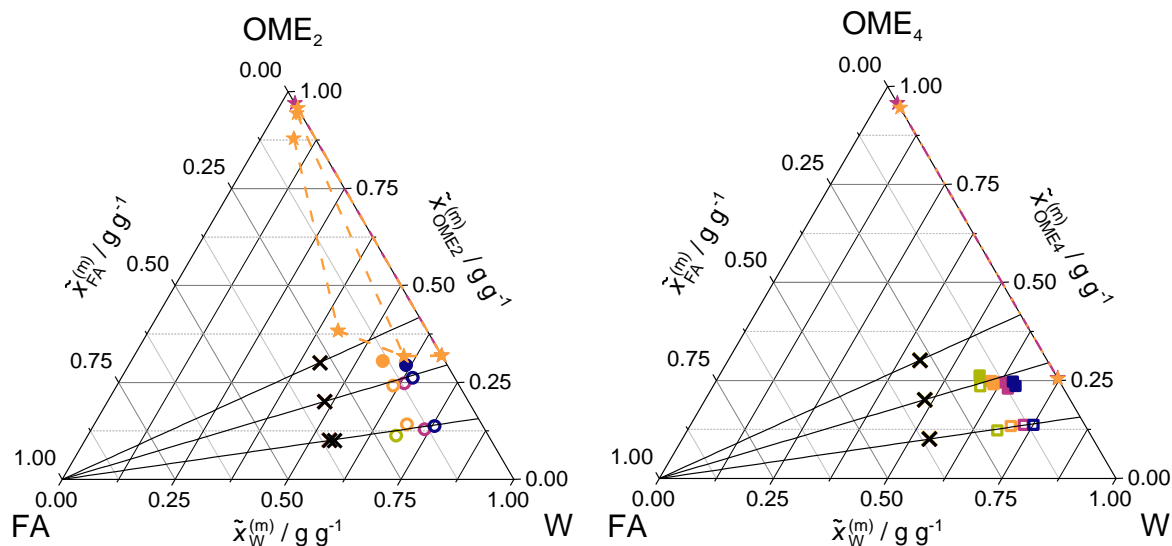


Figure 9: Results from experimental studies of the SLE and SLLE in the system (formaldehyde + water + OME₂, left) and (formaldehyde + water + OME₄, right). (×) feed compositions. Colored symbols: liquid phase compositions in SLE (empty) and SLLE (full, only data for the water-rich phase were measured). The solid lines are lines with a constant water/methanol ratio, namely that of the feed composition. The fact that also the compositions of the homogeneous liquid phases lie on these lines indicates that the solid contains in all cases basically only CH₂O. For the feed with the highest OME content, the liquid split in two phases, of which only one was analyzed. (---☆) results from Schmitz et al.[60] for tie lines of the LLE in the studied systems (for OME₄ only data for the formaldehyde-free binary system are available). The color refers to the temperature: (■) 393.4 K, (■) 293.3 K, (■) 283.0 K, (■) 273.2 K.

At low OME concentrations in the feed, SLE were observed, but upon increasing the OME concentration also SLLE occurred. In the formaldehyde-free binary systems as well as in the both ternary systems with OME, the formation of a second liquid phase occurs earlier for OME₄ than for OME₂. As expected, the solubility of formaldehyde increases with increasing temperature. The influence of OME on the formaldehyde solubility is difficult to discern from Figure 9 and is discussed below in more detail.

Also, for all SLE experiments in the ternary system with OME, the mass balance lines through the liquid phase and the feed meet (within the limits of the uncertainty of the data) in a single point, which is pure formaldehyde, indicating that the solid is oligomeric formaldehyde. For simplicity, in Figure 9, not the individual mass balance lines are shown, but a line at a constant water/OME ratio through the feed, which also goes through the homogenous liquid phases. This is in agreement with the findings from Chapter 2.6.3.2. In the SLLE, the data obtained for the system (formaldehyde + water + OME₂) for the liquid phase agree fairly well with the literature data for the LLE in that system from Schmitz et al.[60]. For OME₄ Schmitz et al.[60] only report data for the formaldehyde-free subsystem. As explained in the experimental section (cf. Chapter 2.4.2), only the water-rich liquid phase in the SLLE could be analyzed in the present work.

For a better assessment of the formaldehyde solubility in the studied mixtures, Figure 10 shows the liquidus temperature of the mixtures as a function of the overall formaldehyde mass fraction. The SLE data from the present work for mixtures containing OME₂ and OME₄ are presented together with data for the system (formaldehyde + water) from Chapter 2.6.3.1. The results clearly show that adding OME leads to a reduction of formaldehyde solubility. The differences between adding OME₂ and OME₄ are not large, and no systematic trend can be discerned from the available data. As expected, increasing the temperature has a strong effect on the formaldehyde solubility.

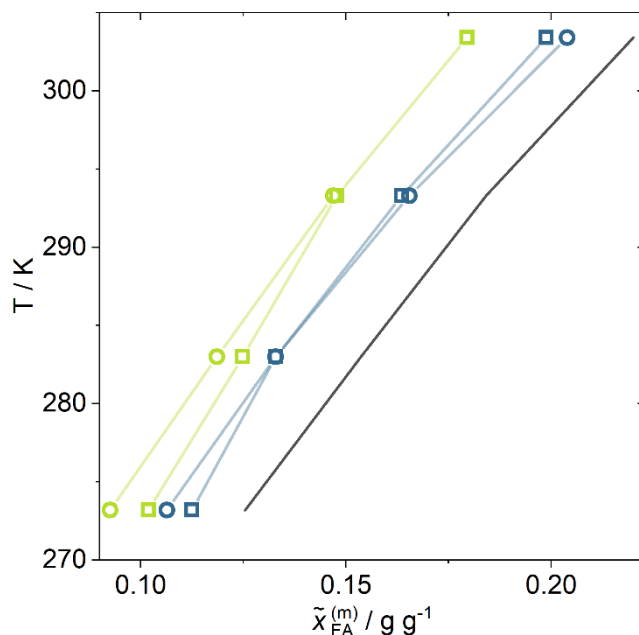


Figure 10: Experimental liquidus temperature as a function of the overall mass fraction of formaldehyde for the systems (formaldehyde + water + OME₂) (○) and (formaldehyde + water + OME₄) (□). The color indicates the OME mass fraction in the solvent mixture: (■) 0.156 g g⁻¹, (■) 0.293 g g⁻¹. (—) data for the system (formaldehyde + water) (cf. Chapter 2.6.3.1). All lines are linear splines.

The comparison of the results for the studied ternary systems with OME with those for the binary system (formaldehyde + water) shows that the curves are basically only shifted. This indicates that the reduction of the solubility could simply be caused by the replacement of the good solvent water with the poor solvent OME. This can be seen better in Figure 11 which gives a magnified view of the data from Figure 9 and additionally includes two sorts of lines. The solid lines were obtained from the model and are discussed below. The dashed lines indicate simply a constant formaldehyde/water mass ratio. Each of the lines starts at the solubility of formaldehyde in pure water at the studied temperature (cf. Table 2), shown as stars, and ends in pure OME. As basically all experimental data points fall approximately on these lines, it can be concluded that the solubility of formaldehyde in mixtures containing OME can be found from the solubility of formaldehyde in pure water, simply by a mapping using the formaldehyde/water mass ratio, cf. Figure 11.

Also, the results from the physico-chemical model are shown in Figure 11. Considering the fact that the model results are pure predictions and only data from the system (formaldehyde + water) were used for its training the agreement is very good. Even though slightly less accurate than the empirical construction described above, the basic facts regarding the formaldehyde solubility in the studied systems are predicted well.

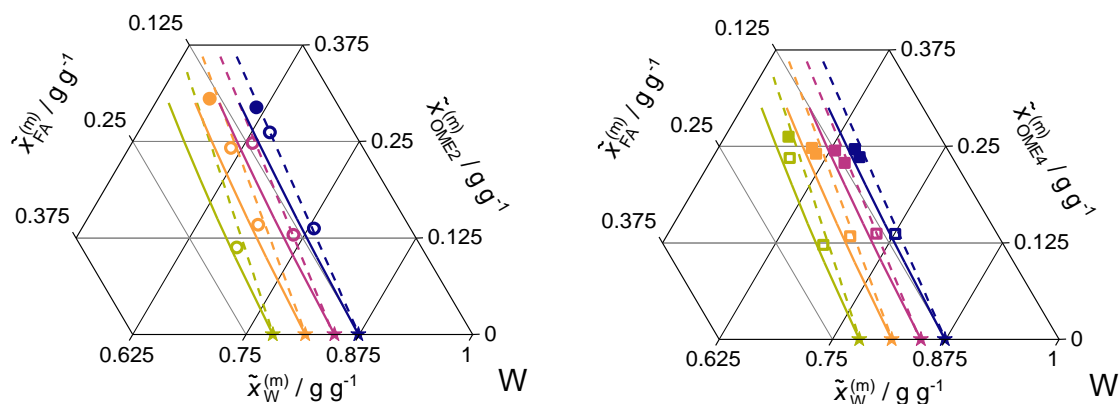


Figure 11: Magnified view of the experimental data shown in Figure 9. Additionally, two types of lines are shown. (—) solubility calculated by the model. (---) linear connections of the experimental solubility in the system (formaldehyde + water) with pure OME, i.e., they are lines of constant mass ratio of formaldehyde/water. Left: (formaldehyde + water + OME₂), Right: (formaldehyde + water + OME₄). Open symbols: SLE, filled symbols: SLLE. The color refers to the temperature: (■) 393.4 K, (■) 293.3 K, (■) 283.0 K, (■) 273.2 K.

All in all, the observations indicate a phase behavior of the studied systems as shown schematically in Figure 12. In that phase diagram, the SLE region for low water concentrations is speculative, as no corresponding data are available.

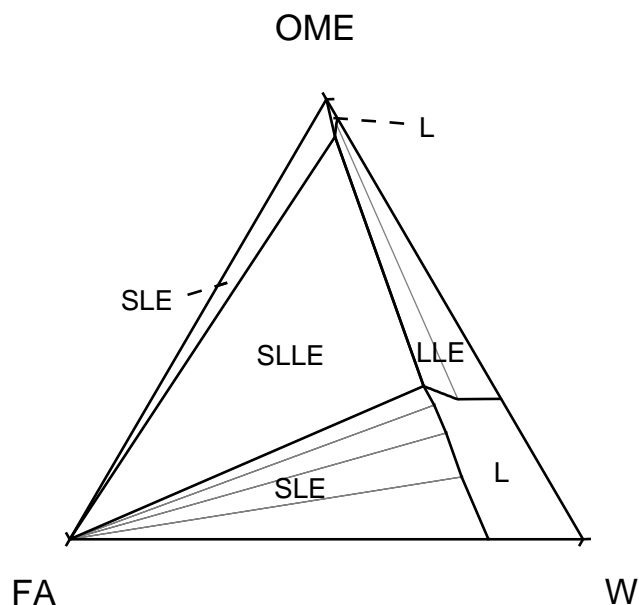


Figure 12: Qualitative phase diagram for mixtures of (formaldehyde + water + OME) for the conditions under which the measurements were carried out. Thin lines are tie lines and thick lines distinguish the different equilibrium areas. The feed of the equilibrium experiments of the present work was either in the SLE region at the (formaldehyde + water)-side of the diagram (homogenous liquid phase, SLE), or in the three phase region (two liquid phases, SLLE).

2.6.3.4 System (formaldehyde + water + methanol + OME)

In the quaternary systems, the feed compositions were chosen in a way that the water/methanol ratios were similar as in the system (formaldehyde + water + methanol) and the OME fractions in the solvent mixture were varied in the same range as in the ternary system (formaldehyde + water + OME). An overview of the samples and the corresponding equilibrium compositions of the liquid phase for the system (formaldehyde + water + methanol + OME) is given in Table 7.

Table 1: Feed compositions and liquid phase compositions in solid-liquid equilibria in the system (formaldehyde + water + methanol + OME). Note that in the specification of the feed composition, the number for OME_{*n*} refers to the formaldehyde-free solvent. The feed compositions in simple mass fractions are given in the Appendix A.9.

Experiment	OME _{<i>n</i>}	<i>T</i> K	feed composition			equilibrium composition		
			$\tilde{x}_{FA}^{(m)}$ g g ⁻¹	$\frac{\tilde{x}_{MeOH}^{(m)}}{\tilde{x}_W^{(m)}}$	$\tilde{x}_{OME,sol}^{(m)}$ g g ⁻¹	$\tilde{x}_{FA}^{(m)}$ g g ⁻¹	$\tilde{x}_W^{(m)}$ g g ⁻¹	$\tilde{x}_{OME_n}^{(m)}$ g g ⁻¹
OME-22	4	273.2	0.3783	0.1579	0.1685	0.1698	0.5956	0.1379
OME-23			0.3376	0.1580	0.3020	0.1516	0.5119	0.2541
OME-24			0.4118	0.3901	0.1701	0.2370	0.4506	0.1811
OME-25			0.3656	0.3924	0.3164	0.2069	0.3975	0.2461
OME-26	2	293.3	0.3803	0.1576	0.1613	0.2328	0.5572	0.1207
OME-27			0.3377	0.1588	0.3021	0.2057	0.4786	0.2379
OME-28			0.4117	0.3898	0.1705	0.2989	0.4219	0.1175
OME-29			0.3655	0.3896	0.3159	0.2534	0.3706	0.2335
OME-30	2	273.2	0.3801	0.1573	0.1615	0.1710	0.5977	0.1319
OME-31			0.3374	0.1576	0.3024	0.1521	0.5123	0.0833
OME-32			0.4118	0.3904	0.1705	0.2349	0.4558	0.1809

In principle, concentrations in a quaternary system can be represented in a tetrahedron. The use of projections of the points on sides of the tetrahedron were preferred for the representation. As shown schematically in Figure 13. Two projections are used, one onto the formaldehyde-free system (W + MeOH + OME) (blue in Figure 13) and a second onto the OME-free system (FA + W + MeOH) (red in Figure 13).

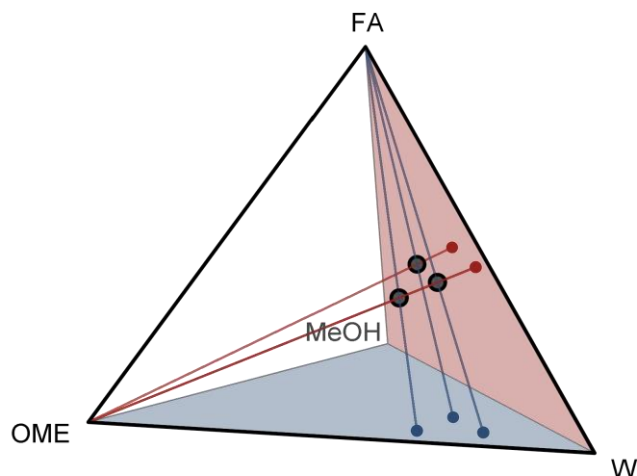


Figure 13: Sketch of the projections used to represent the results for concentrations in the quaternary system (formaldehyde + water + methanol + OME).

Figure 14 shows the results of the projection of feed compositions and equilibrium compositions obtained in the experiments with quaternary mixtures onto the formaldehyde-free ternary system. Results for OME₂ and OME₄ for 273 and 293 K are shown. As can be seen, the projections of the equilibrium compositions and the feed compositions agree perfectly well. This strongly supports the hypothesis that the formed solid is pure oligomeric formaldehyde.

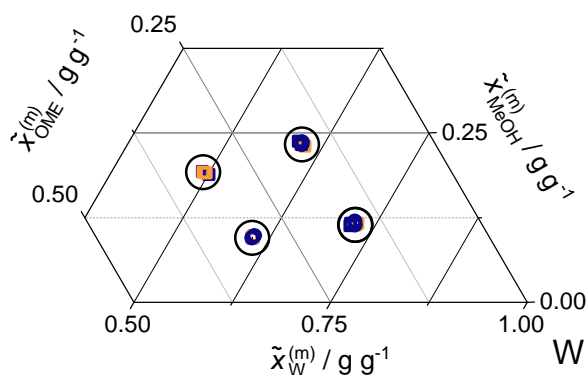


Figure 14: Projection of the feed composition (○) and the liquid phase composition in solid-liquid equilibrium in the quaternary system (formaldehyde + water + methanol + OME) onto the formaldehyde-free ternary system (blue triangle in Figure 13). Results for OME₂ (○) and OME₄ (□) for 273.2 (■) and 293.3 K (■) are shown. The radius of the symbol for the projection of the feed composition is 0.025 g g⁻¹ which corresponds to around twice the experimental uncertainty of the measurement.

Figure 15 shows the results of the projection of the equilibrium compositions obtained in the experiments with quaternary mixtures onto the OME-free ternary system. In addition to the results from the present work, also results for the system (formaldehyde + water + methanol), cf. Chapter 2.6.3.2, are shown (crosses and solid lines). In the projection, they coincide with the results for the quaternary system, indicating that, also here, the formaldehyde solubility can be inferred from the solubility in the OME-free systems, as for the studied ternary system (formaldehyde + water + OME).

Additionally, the solubilities calculated with the model are shown. The dotted line shows the calculated solubility for the ternary system (formaldehyde + water + methanol) and the dashed line the calculated solubility for the system (formaldehyde + water + methanol + OME₄) with an OME₄ fraction in the solvent mixture of 0.3 g g⁻¹. The results for OME₂ are almost identical to those for OME₄ and are therefore not included in Figure 15, where both sets could not be discerned. All in all, the model predicts the experimental results well. Again, it should be considered that no data from the measurements with OME used for training the model. The results for the SLE in the quaternary system were obtained using a model that was only trained with SLE data from the system (formaldehyde + water).

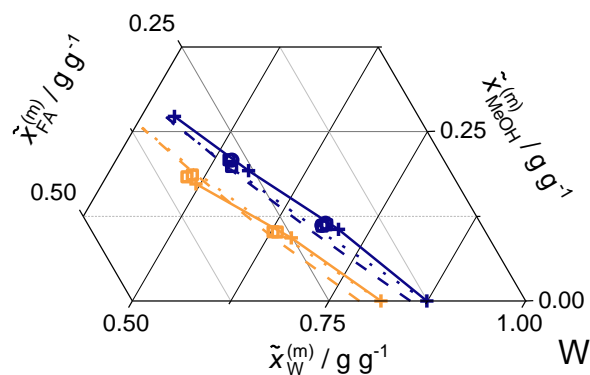


Figure 15: Projection of the liquid phase composition in solid-liquid equilibrium in the quaternary system (formaldehyde + water + methanol + OME) onto the OME-free ternary system (red triangle in Figure 13). Results for OME₂ (○) and OME₄ (□) are shown. (—) show results for the system (formaldehyde + water + methanol), cf. Chapter 2.6.3.2. The color corresponds to the temperature: (■) 273.2, (■) 293.3 K. (····) results from the physico-chemical model for the system (formaldehyde + water + methanol), and -- those for the system (formaldehyde + water + methanol + OME₄) with an OME₄ fraction in the solvent mixture of 0.3 g g⁻¹.

2.6.4 Kinetics of the formation of formaldehyde-rich solid

A survey of the kinetic experiments of the solid formation from formaldehyde-containing mixtures that were carried out in the present work has already been given in Chapter 2.6.2. The individual experiments differ mainly in the composition of the solvent (water, methanol, OME and mixtures thereof), the temperature, and the amount of sodium hydroxide that was added. A detailed description of the individual experiments, the profiles and the measured concentration of each experiment are given in the Appendix A.8.

As already shown, the kinetics of the solid formation from formaldehyde-containing mixtures show a strong dependence on the pH value (cf. Figure 4). The influence of other effects, such as nucleation and mass transfer, seems to be small compared to that of the reaction kinetics (cf. Figure 5). This is why the present model of the kinetics of the solid formation in formaldehyde-containing mixtures only accounts for the kinetics of the liquid phase reactions.

2.6.4.1 Modeling of the kinetic experiments

As described in the experimental section, cf. Chapter 2.4.2, the kinetic experiments were initiated by lowering the temperature, starting from a freshly prepared stock solution at high temperature.

For the kinetic simulation, a starting value for the true composition is needed, which has to be calculated from the experimental overall composition. As long as it has the correct overall composition, it is sufficient to estimate the true initial composition, as the chemical equilibration of the homogeneous mixtures at the temperatures of the preparation of the samples is fast compared to the duration of the kinetic experiments; the simple chemical equilibration (without precipitation) takes less than a day for the conditions studied in the present work. Therefore, for simplicity, for all simulations carried out in the present work, the initial composition was calculated from the overall composition assuming that the homogeneous mixture is equilibrated at 303 K (The temperature-dependence of the equilibrium composition is small, and therefore, the influence of the exact temperature for the starting value is negligible). The kinetic simulation was then carried out for the temperature of the individual experiment taking into account the solid precipitation. The formation of solid is observed early in the kinetic simulation, but the process of the solid formation is slow, as the MG_p , which precipitates to form FA_p , is only present in very small amounts (of the order $2 \cdot 10^{-7}$ mol mol⁻¹ for $p=9$) and the formaldehyde units in FA_p have to be supplied from small oligomers through a slow reaction kinetic network.

The prediction of the amount of solid formaldehyde that is formed depends only on the initial overall formaldehyde concentration and the solubility limit of formaldehyde predicted by the model. As the description of the solubility limit for the system (formaldehyde + water) is almost perfect, so is the prediction of the amount of solid formaldehyde that is formed in the experiments in that system. For the methanol-containing mixtures, some deviations occur, which are simply induced by the deviations in the predictions of the formaldehyde solubility of the model; see Figure 8. These deviations would lead to systematic shifts of the simulations results of the kinetic model and the experimental kinetic data, which, however, cannot be attributed to shortcomings of the kinetic model, as they are induced by the equilibrium model. This is a common problem, known, e.g., from fitting reaction kinetic data. It is solved usually by fitting the equilibrium constant of the model individually to the experimental kinetic data such as to get a good description of the data for large times. This procedure was adopted here for all experiments in the methanol-containing systems. For experiments where the equilibrium was not reached, the corresponding equilibrium value was adopted from a similar experiment, where the equilibrium was reached.

For the samples to which sodium hydroxide was added, the pH value was set to 9.5 (11 for samples with OME) for the kinetic simulations, otherwise the pH value was set to 4. The reaction kinetic model of Ott[65] was only fitted to kinetic data for pH values up to 7; hence using it for pH 9.5

(11 for experiments with OME) is an extrapolation. The behavior of the model of Ott[65] was checked and it was found that the extrapolations from the region in which it was fitted up to pH 9.5 are smooth and plausible. For the pH value of 11, as it was used for the samples with OME, the model is far out of the range for which it was parameterized. Nevertheless, it was applied – but the results should be interpreted cautiously. The only further model parameter that influences the kinetics is the choice of the chain length p of the precipitating methylene glycol MG_p .

2.6.4.2 Determination of the chain length p of the precipitating oligomer

As the reaction kinetic model was adopted from the literature, the only parameter left for modeling the kinetics of the solid formation in formaldehyde-containing systems is the choice of the parameter p , the number of CH_2O units in the precipitating poly(oxymethylene) glycol. In contrast to the equilibrium model, which is insensitive to the choice of p , that choice has a high impact on the kinetic model: the higher the number for p , the slower are the kinetics. Large amounts of solid formaldehyde may precipitate from the studied mixtures. This formaldehyde has to be supplied by small oligomers, which are present in sufficiently high concentrations. However, to find its way out of the liquid, the formaldehyde first has to be converted to MG_p , which is present only in very small amounts. Therefore, the formation of MG_p is a bottleneck for the solid precipitation: the lower the concentration of MG_p , the more complicated the passage. Furthermore, as the formaldehyde is supplied by the small oligomers, a high p means that it has to travel longer for reaching the narrow passage out. The findings are quantified in Figure 16. It shows two examples: a kinetic experiment in which sodium hydroxide was added ($pH \approx 9.5$), and one in which this was not done ($pH \approx 4$). For both experiments three model predictions are shown, which differ in the choice of p , which is either 8, 9, or 10. The influence of the choice of p is as expected: the larger p , the slower the kinetics. It can also be seen that the best agreement is observed in both cases for $p=9$. Figure 16 also contains information on the influence of the pH value on the predictions. The gray bands indicate the effect of a variation of the pH value by ± 0.5 on the model predictions. This is about the range of the uncertainty of the experimental pH value. An increase of the pH value accelerates the kinetics, i.e., leads to a downward trend in Figure 16. A variation of the temperature by ± 1 K shows a considerably smaller influence and is not shown here. It is astonishing how well the simple model describes the kinetics of the complex solid formation process.

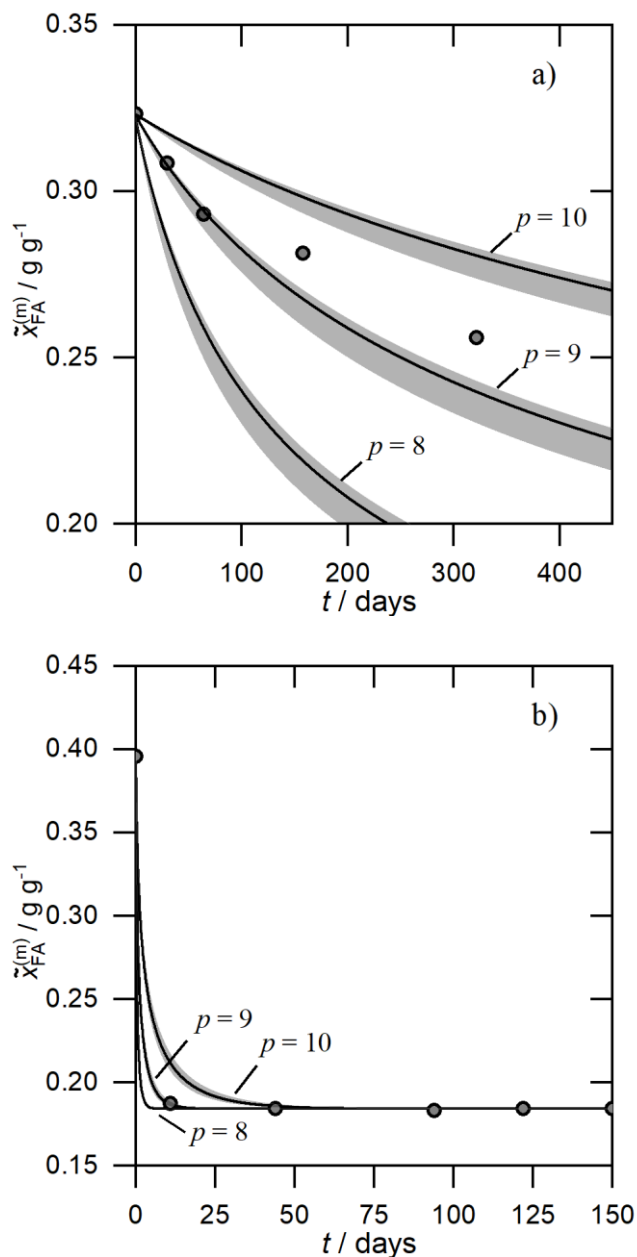


Figure 16: Overall formaldehyde concentration in the liquid phase for two kinetic experiments in the system (formaldehyde + water). a) at 273.2 K (no sodium hydroxide, pH ≈ 4), and b) at 293.2 K (with sodium hydroxide, pH ≈ 9.5). Symbols are experimental data. Solid lines are model predictions for different values of p , characterizing the precipitating MG_p . The gray area indicates the influence of variations of the pH value by ± 0.5 .

Figure 17 shows a comparisons between the measured and calculated concentration profiles for the Experiments with OME (OME-1, OME-13, and OME-27). The results for the experiments with

OME that are not shown in Figure 17 are presented in the Appendix A.9. Model results are presented for different choices of p , furthermore, also the pH value was varied, results are shown for the pH value 11 ± 1.5 .

A high pH value was chosen in the measurements with OME, in order to further accelerate the kinetics. Therefore, in many of the experiments, the equilibrium value was already almost reached in the first sample that was analysed, so that only little information on the kinetics was obtained.

For the experiments shown in the top-left and top-right panel of Figure 17 the variation of the concentration of the solution over time can be discerned, for the experiment in the bottom panel, the concentration remains basically constant, i.e., equilibrium was already reached at the time the first analysis was carried out, which was after about 60 days. The question can be raised, why the analysis was not carried out at shorter intervals. The reason is that with each analysis the mass of the sample reduces and a certain amount is needed for the handling.

In the two experiments shown in the upper two panels in Figure 17, the best agreement between the model predictions and the data is observed for $p = 7$ (top-left) and $p = 8$ (top-right), respectively, which is not far from the value $p = 9$ which is the best fitting value in Figure 16. From the experiment shown in the bottom panel of Figure 17, which was so fast that no change in concentration was monitored, only a statement on an upper limit for the choice of p can be made: it can be inferred from the results that p cannot be higher than 10, which is in line with the other findings.

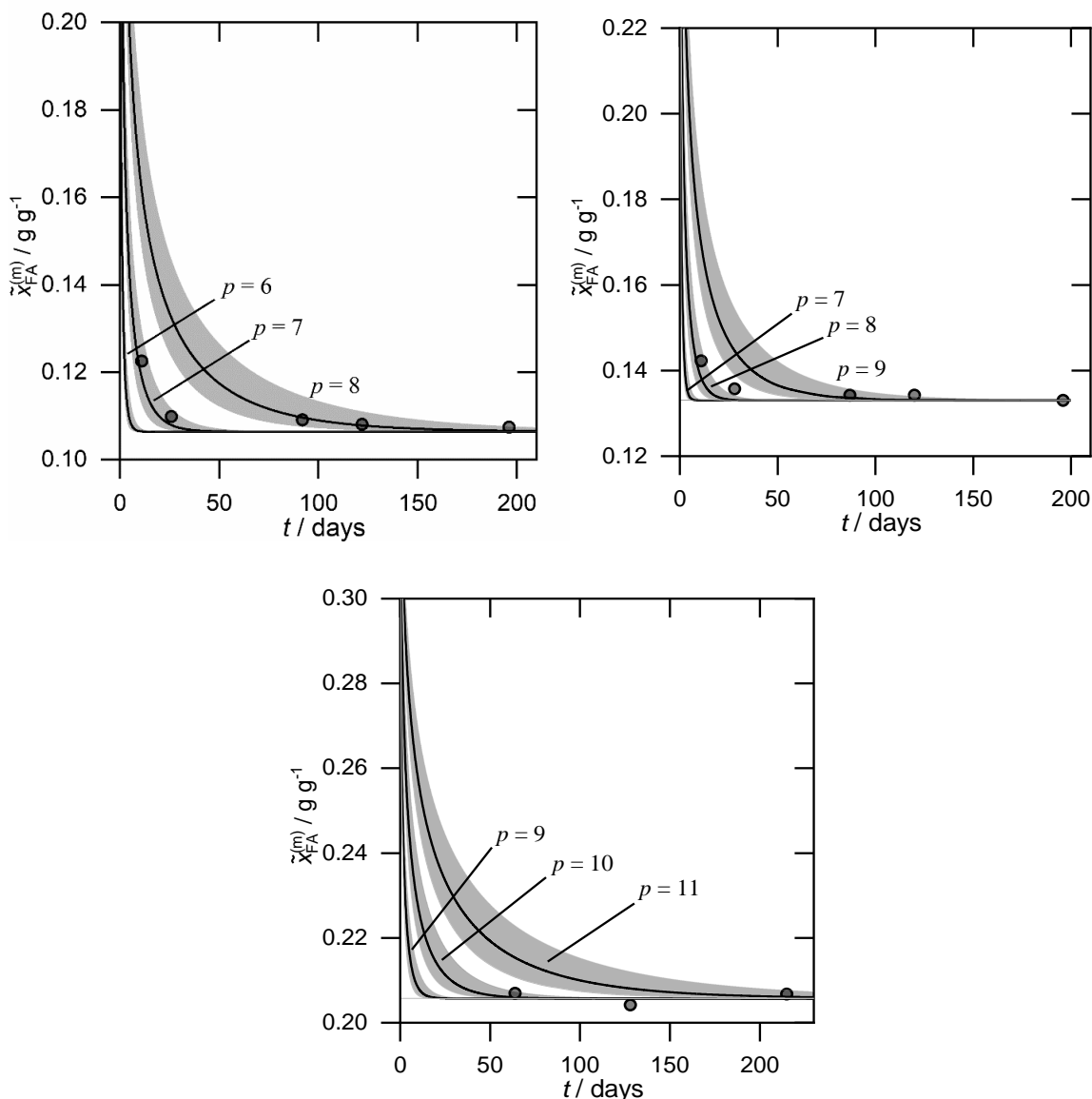


Figure 17: Overall formaldehyde concentration in the liquid phase for different experiments. Top-left: Experiment OME-1, top-right: Experiment OME-13, bottom: Experiment OME-27. Points are experimental data. Solid lines are calculated for different values of the chain length p of the precipitating MG_p . The grey area shows the influence of variations of the pH by ± 1.5 .

The question of the choice of p was addressed more comprehensively in simulations of all 46 kinetic experiments, in which p was varied and, for each experiment individually, the optimal number of p was determined. This also involved the determination of the solubility constant for each different MG_p . Figure 18 summarizes the results in two histograms. It can be seen that the distribution peaks at $p = 9$. The results for the system (formaldehyde + methanol) were not

included in the histogram, as these profiles show a significant dependence on the water fraction used in the model, which is not precisely known. The histogram in Figure 10 a) also contains information on the influence of the temperature on the choice of p . From the derivation of p , it is clear that the number for p may be temperature-dependent; in fact, the results shown in Figure 18 a) indicate that p increases with increasing temperature. Unfortunately, our database is not broad enough to quantify that trend. Figure 18 b) shows a histogram in which instead of the temperature, the pH value is indicated. No systematic trend can be discerned, which means that the model predicts the influence of the pH value reasonably well.

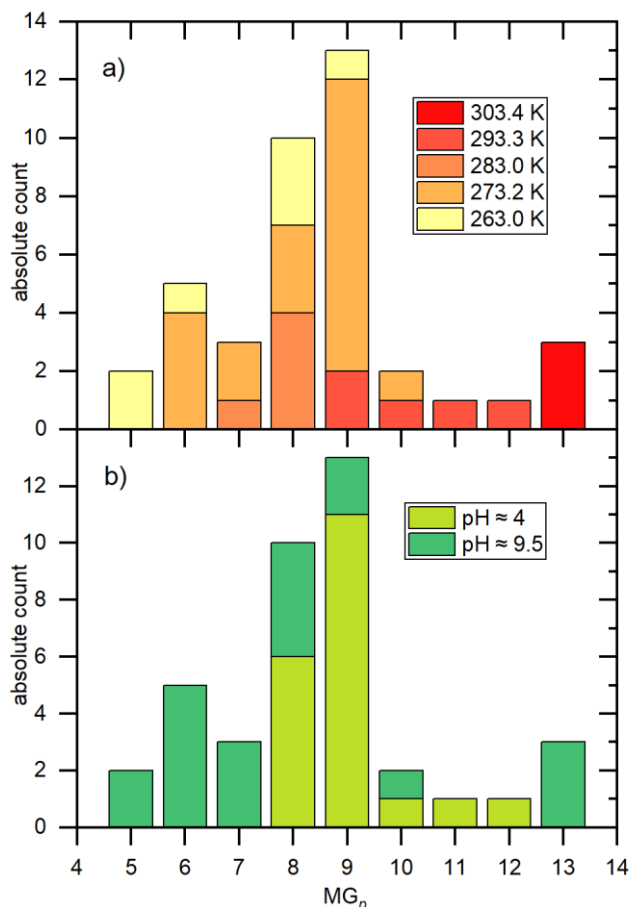


Figure 18: Histograms showing the results from the evaluation of the concentration profiles of the kinetic experiments in the systems (formaldehyde + water) and (formaldehyde + water + methanol) for the best-fitting precipitating poly(oxymethylene) glycol in the kinetic model for different a) sample temperature and b) pH values. The best agreement is achieved with $p = 9$. A temperature-dependence of p is recognizable, while no clear dependence on the pH value is noticeable.

Figure 19 shows the best fitting value for p for all experiments with OME, beside the experiments with the two liquid phases. The resulting values for p that were found show a dependency on the temperature.

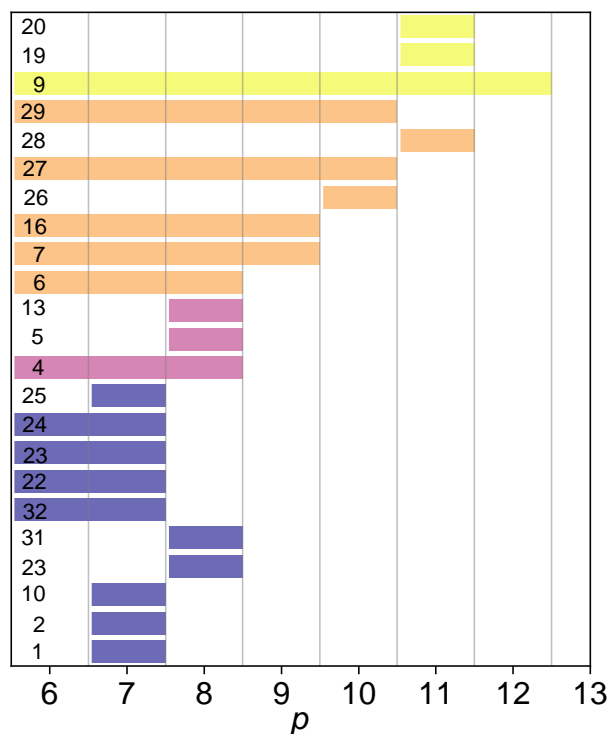


Figure 19: Optimal values for p obtained from the kinetic fits for the system (formaldehyde + water + OME) and (formaldehyde + water + methanol + OME). The line number indicates the number of the experiment. Bars indicate that only an upper limit of p could be determined. The color represents the temperature of the experiment: (■) 303.4 K, (■) 293.3 K, (■) 283.0 K, (■) 273.2 K.

It can be seen from Figure 19 that the values found for p depend on the temperature; the highest values for p are found for the highest temperature, the lowest for the lowest temperature. For a given temperature, the optimal value of p generally varies only between two neighboring values. The temperature trend is probably caused by deficiencies of the reaction kinetic model, which was used outside the range for which it was trained. Keeping this in mind, the results shown in Figure 17 and Figure 19 are quite satisfactory and indicating that the model reflects essential features of the formation of the solid.

2.7 Conclusions

In the present chapter an in-depth study on the formation of solids in the systems (formaldehyde + water), (formaldehyde + methanol), and (formaldehyde + water + methanol) is described and data on equilibria as well as on kinetics are supplied. Furthermore, solid-liquid equilibria and kinetics of the solid formation are described in mixtures containing (formaldehyde + water + OME) and (formaldehyde + water + methanol + OME) at temperatures between 273 to 303 K. The experiments were carried out with OME₂ and OME₄.

The main focus of the study was on the formaldehyde solubility, i.e., on the case where the solid phase is formaldehyde-rich, but for completeness, also the freezing point depression of water adding formaldehyde was measured, i.e., the case where the solid is pure water. This enabled the determination of the eutectic point in the system (formaldehyde + water), which was previously unknown and is located at ($T_{\text{Eu}} = 266.96$ K and $\tilde{x}_{\text{FA,Eu}}^{(m)} = 0.1123$ g g⁻¹).

To obtain a solid basis for the work, first a reliable experimental method to measure the equilibrium and kinetics of the formation of formaldehyde-rich solids in the studied systems had to be developed. It is based on monitoring the liquid phase composition of formaldehyde-containing mixtures during the process of the formation of the solids. It takes extremely long to reach the solid-liquid equilibrium in the studied systems, which is why many of the 78 experiments carried out in the present work took several hundred days. Even then, the solid-liquid equilibrium could only be reached if sodium hydroxide was added to the solution to increase the rates of the oligomerization reactions of formaldehyde in the mixtures. Even though a direct analysis of the solid that was formed was not possible, it can be concluded from overall mass balances that it contains practically only formaldehyde and no water, methanol or OME, i.e., that it must be long-chain paraformaldehyde.

The new solid-liquid equilibrium data can be compared to literature data only for the system (formaldehyde + water), where the data of the present work show a much lower solubility of formaldehyde in water than most of the literature data [46,53,54]; e.g., a solubility of about 0.2 g g⁻¹ at 298 K was found, whereas the majority of literature gives a value about 0.4 g g⁻¹. However, the data of the present agrees almost perfectly with the old data of Credali et al.[52] The reason for the discrepancies is the time scale of the observation, which was much shorter in the experiments that yielded high solubilities than in our experiments and those of Credali et al.[52].

It would be attractive to interpret the data of Walker[46], Grützner and Hasse[53], and Ma et al.[54] in terms of the kinetic model developed here. However, this would require detailed information on the initial conditions and boundary conditions of the experiments, which is, unfortunately, only partially available. Therefore, such an attempt in the present work was refrained. Using the kinetic model from the present work for developing practically useful

guidelines for handling metastable formaldehyde solutions without running into trouble with solid precipitation is highly attractive and should be addressed in future work.

Methanol is often added as a stabilizer to aqueous formaldehyde solutions. Data on the solubility of formaldehyde in the systems (formaldehyde + water + methanol) as well as in the system (formaldehyde + methanol) were provided for the first time. At 298 K, the formaldehyde solubility in methanol is almost three times higher than that in water (based on mass fractions).

In the ternary mixtures with OME, beside SLE, an SLLE was observed. The findings on the LLE are in line with those from previous work by Schmitz et al.[60].

Adding OME reduces the solubility of formaldehyde, and the reduction does not significantly depend on whether OME₂ or OME₄ is used. The interpretation of this empirical finding is that OME is a poor solvent for formaldehyde and basically only dilutes the good solvents water and methanol. It can be assumed that this finding holds not only for OME₂ and OME₄, but for all OME.

Since it takes so long to reach the solid-liquid equilibrium in the studied systems, information on the kinetics of the solid formation is extremely important. However, up to now, there has been neither a useful theory nor data on this. The experiments of this work clearly show that the extremely slow kinetics of the solid formation in the formaldehyde-containing systems result from chemical kinetics. This is why they can be accelerated by shifting the pH value.

A physico-chemical model for the formaldehyde solubility in aqueous mixtures, which may also contain methanol, was described. It is based on the knowledge of the true speciation of the mixtures and the assumption that the solubility limit is first reached for a certain poly(oxymethylene) glycol MG_p, with p CH₂O units. From solid MG_p, long-chain paraformaldehyde is formed, and water is released to the liquid phase.

After fitting the solubility constant of MG_p to data of the system (formaldehyde + water) the model was used to predict the influence of methanol on the formaldehyde solubility, which gave astonishingly good results, considering that no data on methanol-containing systems were used in the model development. It follows from the derivation of the model that p may depend on the temperature and also on the composition of the mixture. However, the quality of the description of the solid-liquid equilibrium is independent of the choice of p so that a constant value of $p = 9$ was used, which was selected based on the results from the kinetic modeling.

The physico-chemical model was extended to describe the kinetics of the solid formation. To keep it simple, it was assumed that the water release from the solid MG_p is instantaneous, i.e., the kinetics depend solely on the kinetics of the liquid phase reactions, which are well known from many previous studies. After fitting the number of p to the kinetic data, the model describes the kinetic data reasonably well, including the influence of the pH value. The present results indicate that it is about $p = 9$ in many cases. This model explains why the kinetics of the solid formation

in formaldehyde-containing systems are so exceptionally slow: it is a consequence of the interplay of the slow liquid phase reaction kinetics in the studied systems with the extremely low concentration of the precipitating MG_p ; the formaldehyde that precipitates can do this only by passing through a bottleneck.

With the present study light was brought into mostly unexplored territory, both on the experimental side as well as with the modeling. It is, hence, not astonishing that many open questions remain. The equilibrium studies of the present work were only carried out at low temperatures, partly to avoid side reactions in the very long experiments. It would be highly desirable to extend the data basis to higher temperatures. Furthermore, no studies in completely water-free methanolic formaldehyde-containing mixtures were carried out, which would be interesting to have. Furthermore, the kinetic studies were only done at two pH values. A more comprehensive study would be desirable.

With regard to the model, open questions according to the dependence of p on the external conditions remain. Furthermore, upon increasing the methanol concentration, at a certain point, the solubility limit will not be reached first for a poly(oxymethylene) glycol MG_p but for a poly(oxymethylene) hemiformal HF_q . In the present work the consequence of this was not explored.

Hence, despite the substantial insights that is gained and the new data that are provided, there remains plenty to do before it can be said that the formation of solids in formaldehyde-containing mixtures is fully understood.

3 Chemical reactions in the OME synthesis from dimethyl ether

3.1 Introduction

As described in Chapter 1, DME is an interesting alternative to MAL as starting material for anhydrous OME production, due to its lower price. Some publications consider the direct oxidation of DME to longer OME, but these works are also still in an exploratory stage [73,74].

In a feasibility study, Haltenort et al.[75] have shown that the conversion of DME with formaldehyde to MAL is feasible using acidic heterogeneous catalysis. In their anhydrous experiments, they used trioxane as a formaldehyde source. As expected, Haltenort et al.[75] also found that MAL reacts further with formaldehyde to OME oligomers. In a very recently published work, Drexler et al.[37] have extended these experiments and have performed a broader catalyst screening in a continuous reactor setup. For easier handling, they used dodecane as a solvent in their experiments. The differences they found between the results for the different catalysts are, however, probably mainly related to the different acidic strength, resulting in different reaction rates. A certain strength is required to achieve a significant conversion in typical technical set-ups, which exceeds the strength needed for catalyzing the formation of the OME in the subsequent oligomerization reactions.

In Chapter 4.2 a production process for OME₃₋₅ from DME and trioxane, which is based on a patent of Ströfer et al.[76], is discussed based results from process simulations that were obtained with a simple process model. The results confirm that the route is attractive. The key problem in modeling the process was to describe the relevant reactions. It was assumed, that using an acidic catalyst, the chemical equilibrium is achieved in the reactor. The work on the process simulation, described in Chapter 4.2, was done before the experimental work of the present chapter was done. Therefore, the equilibrium data for the cleavage of trioxane were calculated from data from literature [58,77]. The data on the oligomerization reactions leading from MAL to OME were taken from Schmitz et al [58]. No data were available in the literature for the formation of MAL

from DME and formaldehyde. Haltenort et al.[75] do not provide such data. Therefore, in the equilibrium constant of that reaction had to be estimated from the Gibbs enthalpy of formation obtained from standard state data of the pure components (for more information see Chapter 4.2.). As expected, a sensitivity analysis of the process model showed that the equilibrium constant of the reaction of DME with formaldehyde is a key parameter of the process, so reliable information on that equilibrium constant is highly important for the process development which emphasizes the need for a corresponding study. The results of this chapter close this gap with a study which combines both experiments on the one side with modeling and simulation on the other. The main goal was to obtain the missing equilibrium constant of the formation of MAL from DME and formaldehyde, but also valuable quantitative information on the reaction kinetics and side product formation was gathered. However, the corresponding experiments turned out to be highly demanding. There are several important challenges: 1) DME is highly volatile so that a high pressure has to be applied and the sampling is difficult; 2) Despite the catalysis, the reactions are slow so that the run takes days; 3) Unwanted polymerization of trioxane may occur; 4) There is an important side reaction, which cannot be suppressed: the formation of methyl formate; 5) the reaction mixture is complex, which requires applying advanced analytics. All these challenges were finally met, using an apparatus that was specially designed for these studies in connection with an analysis by nuclear magnetic resonance (NMR) spectroscopy. As a heterogeneous catalyst, a simple, commercially available, acidic ion-exchange resin was used, and the formaldehyde source was trioxane. It was refrained from using more complex catalysts, not having any indication that they would bring advantages, namely regarding the suppression of the side reaction. The experimental results were evaluated by a physico-chemical model to extract the relevant data on the reactions.

3.2 Chemical reactions

The present chapter focuses on the reversible formation of MAL from DME and formaldehyde. Due to the consecutive reactions of MAL to OME and the occurrence of side reactions, this reaction cannot be investigated alone; it is always embedded in a complex reaction network.

Furthermore, due to ongoing irreversible side reactions, the equilibrium state of the main reaction is never reached in this reaction network. Hence, the equilibrium constant of the main reaction has to be determined from a fit of parameters of a reaction kinetic model to the experimental data.

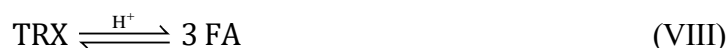
To obtain meaningful results from this procedure, it is essential to use an adequate reaction kinetic model. Unfortunately, for some of the reactions in the network, information on the mechanism is lacking and different routes are discussed in the literature. To keep the presentation concise, in the following, only the mechanism that were chosen in the present work for the evaluation of our experimental data are discussed. They are based on a broad range of publications [22,33–

37,58,59,68,78,79] and was found to be best suited for our purpose. It is not claimed that they are correct in all aspects. Alternatives are discussed in the Appendix B.1.

All reactions that are discussed in the following require the presence of strong acids. In the present work, a heterogeneous acidic catalyst was used. Dimethyl ether (DME, CH₃-O-CH₃) reacts reversibly with formaldehyde (FA, CH₂O) to methylal (MAL, CH₃-O-CH₂-O-CH₃), according to Reaction (VII).



In the present study, trioxane (TRX, [CH₂O]₃), the trimer of formaldehyde, was used as a formaldehyde source. The cleavage of TRX to formaldehyde is described by



In oligomerization reactions, MAL reacts with formaldehyde first to OME₂ (cf. Reaction (IX)) and then to OME_{*n*} (cf. Reaction (X)).

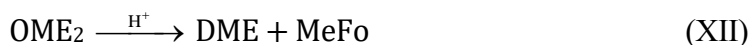


The experiments from the present work show that the oligomerization reactions leading from MAL to OME (cf. Reaction (IX) and (X)) and the cleavage of TRX (cf. Reaction (VIII)) are much faster than the formation of MAL. The difference is so large that Reactions (IX) and (X) are always in equilibrium, and, as a consequence, the exact mechanisms of the formation of OME, which are disputed in the literature, are not important for the modeling.

Unfortunately, there are several side reactions in the studied system, the most important of which is the formation of methyl formate (MeFo, HCOOCH₃). Several mechanisms for the formation of MeFo have been discussed in the literature; for anhydrous systems, most authors assume that it is formed by the Tishchenko reaction [22,37,46,68,77,80–82].



This reaction is described in the literature sometimes as reversible [22,80,81] and sometimes as irreversible [37,46,68,77,82]. Getting a good description of the present experimental data was not possible based on Reaction (XI). Therefore, a different mechanism for the formation of MeFo in the studied system was postulated, the cleavage of OME₂, as given by Reaction (XII). A comparison of both mechanisms, based on our experimental data, is presented in the Appendix B.8.



In addition to the components that were mentioned here so far (TRX, DME, MAL, OME_n, MeFo), also formic acid (FAc, COOH), and poly(oxymethylene) hemiformals (HF_n, HO(CH₂O)_nCH₃) were observed in low concentrations in the experiments of the present work. The presence of these components indicates that traces of water (W) were present so that from MeFo formic acid and methanol (MeOH) can be formed (cf. Reaction (XIII)); the latter reacts with formaldehyde to poly(oxymethylene) hemiformals as described in Chapter 2.3.



Poly(oxymethylene) glycols, which would result from analogous reactions of formaldehyde with water (cf. Chapter 2.3), were not observed. Further possible reactions of these minor components are briefly discussed in the Appendix B.1.

3.3 Experiments

3.3.1 Overview

In the present work, liquid phase reactions at temperatures up to 363 K were studied. Due to the high vapor pressure of DME (which has a normal boiling point of 248 K [72]) pressures of about 29 bar were applied. The experiments were carried out in a thermostatted high-pressure autoclave. The liquid phase composition was determined by quantitative NMR spectroscopy. For sampling, special high-pressure NMR tubes were used. Two different kinds of experiments (type A and B) were carried out.

In type A experiments, TRX and DME were used as starting materials. These experiments showed that the target reaction takes place, but they are not suited for the determination of the equilibrium constant of the MAL formation, as will be shown in the results section. In these experiments, the reactor was charged with solid TRX, then pressurized liquid DME was added. The catalyst could only be added after the reactor was heated up, and the liquid reaction mixture was homogenized. Otherwise, the catalyst would have caused a polymerization of the TRX yielding long-chain paraformaldehyde, which is only a poor formaldehyde source, as it is only weakly reactive. To realize the insertion of the catalyst into the filled and pressurized reactor, the catalyst was injected from a reservoir that was pressurized with nitrogen. Thereby, the starting point of the reaction can be precisely controlled, but it cannot be guaranteed that the entire amount of catalyst ends up in the liquid phase and does not partially stick to the head of the reactor.

In type B experiments, instead of TRX, the reactor was filled with a liquid mixture of OME of different chain lengths and the catalyst. Then the DME was added and the reactor was heated to

the desired temperature. This has the advantage that the amount of catalysts is precisely known, but the disadvantage is that the starting phase of the experiment is poorly defined. This is acceptable as the heating-up is short compared to the duration of the experiment. As will be shown in the results section, type B experiments are suited for determining the equilibrium constant of the MAL formation (cf. Reaction (VII)).

3.3.2 Apparatus

A schematic drawing of the reactor system that was used for the studies is shown in Figure 20. Details of the operating procedures for the type A and type B experiments are reported in the Appendix B.2.

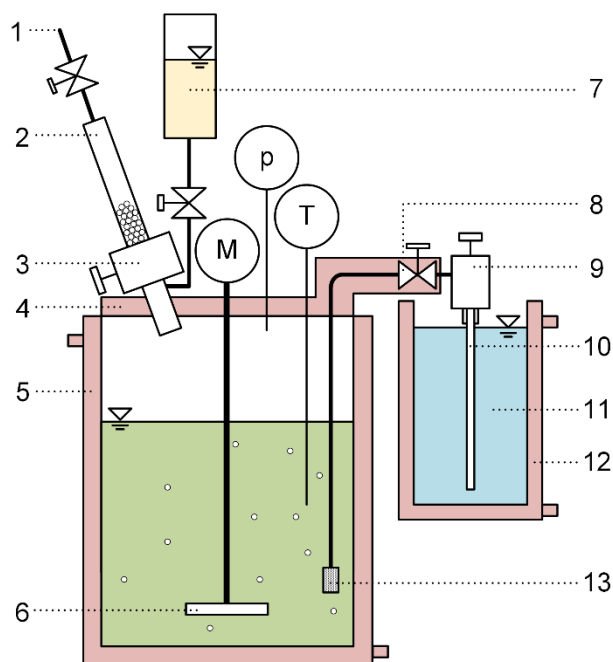


Figure 20: Schematic of the reactor system used for the experiments. 1: nitrogen feed, 2: catalyst reservoir, 3: catalyst valve, 4: electrical heating, 5: heating jacket, 6: stirrer, 7: DME reservoir, 8: sample pipe valve, 9: pressure NMR tube valve, 10: pressure NMR tube, 11: water bath, 12: water bath heating jacket, 13: frit, T: thermometer, p: pressure gauge, M: stirrer engine.

A stirred autoclave (BR-500 from Berghof Products + Instruments) with a volume of 0.67 L (± 0.005 L) was used. Depending on the type of experiment, the autoclave was filled either with solid TRX (type A) or with OME and catalyst (type B) before it was closed. In the type A experiments the catalyst was stored in the reservoir. After closing the autoclave, DME was introduced from a pressurized reservoir through the feed pipe. The reactor temperature was

controlled using a removable liquid heating jacket. Heat losses through the reactor head were minimized by a temperature-controlled electric heating. The temperature in the reactor was measured in the liquid phase with a calibrated PT-100 resistance thermometer with an accuracy of ± 0.05 K. The pressure inside of the reactor was measured with a calibrated membrane pressure gauge from WIKA International with an accuracy of ± 0.01 bar. The pressure was only measured for operational and safety reasons and not for a later evaluation. For the insertion of the catalyst, in the type A experiments, the catalyst reservoir was pressurized with nitrogen, and the valve separating the reservoir from the reactor was then opened. During the experiment, the liquid phase was stirred with a blade stirrer at 250 rpm. Samples from the liquid phase were taken through a sampling line starting near the reactor bottom, which was equipped with a frit to hold back the catalyst. To suppress the crystallization of TRX the sampling line was thermostatted electrically using the same equipment that was also used for thermostating the reactor head. The sampling line was connected to a high-pressure NMR sample tube made of sapphire glass. The tubes were purchased from Rototec-Spintec and equipped with a high-pressure valve made of non-magnetic brass alloy (ecobrass from MECUMetallhalbzeug) in the workshop of the TU Kaiserslautern. The NMR sample tube was immersed in a water bath that was thermostatted to the reactor temperature. Changing the sampling tube was facilitated by a second valve in the sampling line.

The mass of the educts in the reactor and the mass of the catalyst in experiments of type B was determined by weighing the corresponding reservoirs before and after the filling process (uncertainty of ± 0.1 g) and the starting composition was calculated from this. After the start of the experiment, samples were taken at regular intervals. Directly before sampling, the sample line was first flushed to remove residues from the previous sampling. For this purpose, small stainless steel vials ($V = 0.015$ L) were connected and filled in place of the NMR tube. The vials were preheated and also immersed into the water bath before they were filled. After this, the NMR tube was connected and filled with the liquid sample from the reactor. Finally, the mass of the sample (approx. 1 g) and liquid used for flushing (approx. 13 g) were determined by weighing (uncertainty of ± 0.05 g) to find the new mass of liquid in the reactor.

3.3.3 Chemicals and catalyst

Dimethyl ether (> 0.999 g g⁻¹) was purchased from Air Liquide. Methylal (> 0.999 g g⁻¹), trioxane (> 0.999 g g⁻¹), and methyl formate (> 0.99 g g⁻¹) were purchased from Sigma Aldrich. The TRX was dried in an exsiccator that was filled with dried molecular sieve for at least 48 hours. Amberlyst 36 and Amberlyst 46 in dry bead-form ($d \approx 550$ μm) were provided by Dow Chemical. They were dried in a vacuum oven at 383 K, at a pressure below 30 mbar for at least 24 hours. The molecular sieve (0.3 nm) was purchased from Carl Roth and dried in a vacuum oven at 423 K at a pressure of below 30 mbar for at least 24 hours.

3.3.4 Preparation of the OME mixture

For the type B experiments, an OME-mixture was prepared, using the same stirred batch reactor as Schmitz et al.[58]. First, the reactor was evacuated and flushed with nitrogen. 120 g of dried TRX was dissolved in 291 g of MAL and filled into the reactor. Then, 2 g of dried Amberlyst 46 and 5 g dried molecular sieve were added. The stirrer was started, and the reactor was heated to 50 °C. The reaction mixture was kept at these conditions for at least 24 h. After this, the mixture was filtered (pore size < 5 µm) and analyzed. As Amberlyst 46 is not acidic enough to catalyze Reaction (VII), no DME is formed. The resulting mixture is only in equilibrium regarding Reactions (VIII) to (X).

3.3.5 NMR analysis

All concentrations in the present work were measured by quantitative ¹³C-NMR spectroscopy using a Bruker instrument (Ascend 400 magnet, ADVANCE III HD 400 console, BBFO probe head). For the analysis of the OME-feed mixture, standard NMR tubes were used. Samples with DME were measured in the high-pressure NMR tubes (see 3.3.2).

For the measurement, a ¹³C {¹H} inverse gated pulse sequence was used. The parameters were: flip angle 30°, acquisition time 5.94 s, repetition time 120 s, 64 scans, and 256 k data points. The peak assignment was done in preliminary studies with pure components and mixtures; the results are given in the Appendix B.3, where also a typical NMR spectrum of a sample from the experiments is shown.

For the quantitative evaluation of the spectra, the model-based method of Matviyчук et al.[83] was used, which is based on Bayesian statistics and particularly suited for spectra with overlapping peaks with low signal-to-noise ratios, as they were obtained in the present work [84,85]. The corresponding software was provided by Yevgen Matviyчук and is written in python 3.5. It is based on the assumption that the proportionality constant relating the peak area to the amount of substance is the same for the signals that are used. The validity of this assumption was confirmed by measurements of gravimetrically prepared samples.

In all spectra, the assigned peaks represented over 99 percent of the total peak area. The assigned peaks stem from the following components: TRX, DME, MAL, OME₂₋₇, MeFo, formic acid, methanol, and HF₁₋₃. Due to its very low concentration, monomeric formaldehyde was not detected.

The mass fractions of the components in the OME-feed mixtures were measured with an uncertainty of ±0.003 g g⁻¹. This was confirmed by measuring gravimetrically prepared test samples.

Higher uncertainties occur in the analysis of the reaction mixtures. This is caused by the poorer signal quality when using the high-pressure sample tube, and the additional uncertainty introduced by the complex sampling process. To estimate this uncertainty, the high-pressure reactor was filled with a mixture of DME, MAL, and TRX with defined composition, and samples were repeatedly taken and analyzed. Furthermore, during some of the kinetic experiments samples were taken at short intervals ($\Delta t < 0.5$ h), to check the reproducibility. It was inferred from these results that the absolute uncertainty of the concentration measurement does not exceed ± 0.008 mol mol⁻¹.

3.4 Model

3.4.1 Overview

In the reaction kinetic model, the Reactions (VII) to (X), as well as the Reaction (XII), are considered. As the cleavage of TRX (Reaction (VIII)) and the oligomerization reactions (Reactions (IX) and (X)) are much faster than the formation of MAL (Reaction (VII)) and the formation of MeFo (Reaction (XII)), it is assumed that at any time the equilibrium condition for Reactions (VIII) to (X) is fulfilled, i.e., reaction kinetics are only taken into account for Reactions (VII) and (XII). OME_{*n*} were considered up to $n = 7$, as their concentrations drop off quickly with increasing n and are negligible here for $n > 7$. Reactions (XIII), (III), and (IV) were not considered.

As the amount of DME in the gas phase cannot be neglected, also the gas phase in the reactor is modeled. It is assumed that the gas phase is always in equilibrium with the liquid phase and that the temperature in the reactor is constant throughout the experiment. The reactions are modeled as pseudohomogeneous liquid-phase reactions as the solid catalyst is only present in the liquid phase. All 15 measured components are considered in the model; additionally, monomeric formaldehyde is considered, which cannot be measured due to its low concentration but is essential for the description of the reactions.

3.4.2 Model equations

The differential mass balance for each component i is given by Equation (11).

$$\frac{dn_i^L}{dt} - \frac{dn_{i,\text{reac}}^L}{dt} + \frac{dn_i^G}{dt} = 0 \quad (11)$$

Therein n_i is the amount of substance of component i , and the indices L and G refer to the liquid and gas phase, respectively. t is the time, and $dn_{i,\text{reac}}^L/dt$ is the change of n_i in the liquid phase caused by the chemical reactions and described by the reaction kinetics.

The vapor-liquid equilibrium is described by the extended version of Raoult's law according to Equation (12)

$$p_i^S \cdot \varphi_i^S \cdot \exp\left(\frac{1}{RT} \int_{p_i^S}^p v_{i,\text{pure}}^L dp\right) \cdot x_i \cdot \gamma_i = p \cdot y_i \cdot \varphi_i \quad (12)$$

where p_i^S is the vapor pressure of the pure component i at the temperature T , p is the pressure, x_i and y_i are the mole fractions in the liquid and the gas phase, respectively, φ_i^S is the fugacity coefficient of the pure component in the saturated gas phase at the temperature T , φ_i is the fugacity coefficient of the component i in the gas phase, γ_i is the activity coefficient of component i in the liquid phase, and $v_{i,\text{pure}}^L$ is the molar volume of the pure liquid component i . Correlations for the vapor pressures p_i^S and the molar volumes of the pure components were taken from literature or were fitted to data from literature and are given in the Appendix B.4.

The activity coefficients were calculated based on the UNIFAC-based model of Maurer[7]. A combined version of different sources was used and is described in more detail in the Appendix B.6.

The fugacity coefficients were calculated with the PSRK equation of state [86], using the UNIFAC-based model described above. For more details, see Appendix B.5.

The amount of substance in the gas phase was calculated from the total volume of the reactor V_{reactor}

$$V_{\text{reactor}} = \sum_{i=1}^{N_C} n_i^L \cdot v_i^L + \sum_{i=1}^{N_C} n_i^G \cdot v_i^G \quad (13)$$

where v_i^L and v_i^G are the partial molar volumes of component i in the liquid phase and gas phase, respectively, and N_C the number of components in the system. The partial molar volumes v_i^G were calculated from the PSRK equation of state; the excess volumes were neglected in the liquid phase so that v_i^L is equal to the molar volume of the pure component i .

To describe the reaction kinetics in the liquid phase, as in previous works on related systems, e.g. Schmitz et al.[59], Peláez et al.[33], and Voggenreiter and Burger[68], a pseudohomogeneous activity-based approach was used. Kinetic effects resulting from mass transfer or heat transfer cannot be ruled out strictly, but it is very unlikely that they may have had an important influence, given the fact that the experiments took between 100 and 200 hours and the solution was thoroughly stirred all the time. The general approach to describe the change in the amount of component i due to the reactions is given in Equation (14).

$$\frac{dn_i^{\text{reac}}}{dt} = n^L \sum_{r=1}^{N_R} m_{\text{cat}} \cdot \nu_{i,r} \cdot \left(k_r^+ \prod_{i=1}^{N_C} a_i^{-\nu_{i,r} \cdot z_{i,r}} - k_r^- \prod_{i=1}^{N_C} a_i^{\nu_{i,r} \cdot (1-z_{i,r})} \right) \quad (14)$$

$$\text{with } z_{i,r} = \begin{cases} 1, & \nu_{i,r} < 0 \\ 0, & \nu_{i,r} \geq 0 \end{cases}$$

Herein, n^L is the total amount of substance in the liquid phase, m_{cat} is the mass of the catalyst, and a_i is the activity of component i in the liquid phase, which is calculated from the mole fraction and the activity coefficient according to Equation (15).

$$a_i = x_i \cdot \gamma_i \quad (15)$$

$\nu_{i,r}$ is the stoichiometric coefficient of component i in reaction r . It is positive for products, negative for educts, and zero when component i is not involved in the reaction. k_r^+ and k_r^- are the forward and backward rate constants of reaction r . N_R is the number of reactions. The rate constants of the forward (k^+) and backward (k^-) reactions of each reversible reaction are coupled by the equilibrium constant (K) according to Equation (16).

$$K_r = \frac{k_r^+}{k_r^-} \quad (16)$$

In the present chapter, Equation (16) was used to calculate the rate constant of the backward reaction (k_r^-) from that of the forward reaction (k_r^+) and the equilibrium constant K_r . For simplicity, it will be referred in the discussion only to the reaction kinetic constant of the forward reaction and the index $+$ will be dropped, i.e. $k_r^+ = k_r$. Reaction (XII) is irreversible so that the rate constant of the backward reaction is set to zero. As only the Reactions (VII) and (XII) are kinetically controlled, only these two rate constants had to be considered and all other rate constants were set to sufficiently high values to guarantee equilibrium for their respective reactions.

The equilibrium constant is defined by Equation (17).

$$K_r = \prod_{i=1}^{N_C} a_i^{\nu_{i,r}} \quad (17)$$

Therein is a_i the activity of component i in equilibrium.

The equilibrium constants of the oligomerization Reactions (IX) and (X) were taken from Schmitz[87]. They are described by the integrated van't Hoff equation

$$\ln(K_r) = a_r + \frac{b_r}{(T/K)} \quad (18)$$

The parameters a_r and b_r are the same for Reaction (IX) and (X) and are -9.0546 and 4843.6, respectively.

For the MAL formation (Reaction (VII)), no experimental information on its equilibrium constant K_{MAL} and its reaction kinetic constant of the forward reaction was previously available. Therefore, they were determined from a fit to the data from the present work.

Also, the reaction kinetic constant of the irreversible formation of MeFo (k_{MeFo} , Reaction (XII)) was determined from the data of the present work.

Information on the equilibrium constant of the cleavage of TRX to formaldehyde (K_{TRX} , Reaction (VIII)) is not available in the literature. It can only be estimated with a higher uncertainty (cf. Chapter 4.2.3.2). Therefore, that equilibrium constant was also determined from the data of the experiments.

Hence, the reaction kinetic model presented here has four adjustable parameters: K_{MAL} , k_{MAL} , k_{MeFo} , K_{TRX} .

3.4.3 Implementation and parameterization

Equations (11) - (18) form a differential-algebraic system (DAE). The solution consists of the values of 33 variables (the amount of substance of 16 components in the liquid and the gas phase and the pressure in the reactor) as a function of time t . To obtain this solution, the temperature and the amounts of substances of the components in the reactor at $t=0$ have to be specified. To obtain consistent initial values for all variables, a V, T -flash calculation was carried out based on the initial amounts of substance determined gravimetrically in the experiment. The DAE was implemented in the software MATLAB and solved with the numerical solver ode15s. The calculated concentration profiles were compared to the experimental results. The results for the pressure were not included in the comparison, as the reactor contains inert gases that are not accounted for in the model. For a comprehensive evaluation of the results from a given experiment, the average absolute deviation between the liquid phase mole fractions from the model and the analytical results from experiments (AAD), as defined by Equation (19), was used.

$$AAD = \frac{1}{6 \cdot N_{\text{samp}}} \sum_{j=1}^{N_{\text{samp}}} \sum_{i=1}^6 |x_{i,j,\text{exp}}^L - x_{i,\text{mod}}^L(t = t_j)| \quad (19)$$

$$i = \text{TRX, DME, MAL, OME}_2, \text{ OME}_3, \text{ MeFo}$$

Therein j refers to the samples taken in the experiment, as characterized by the time t_j at which the given sample was taken, and N_{samp} is their total number. $x_{i,j,\text{exp}}^L$ and $x_{i,j,\text{mod}}^L$ are the liquid phase mole fractions of component i from the experiment and the model, respectively. The longer OME were not considered in the calculation of the AAD, as their concentration is so low that it is in the range of the experimental uncertainty.

In a first step, the adjustable model parameters k_{MAL} , k_{MeFo} , K_{TRX} , and K_{MAL} were determined separately for each experiment by minimizing AAD. A combination of a Nelder-Mead-based method and gradient-based method was used as optimization algorithm. To facilitate that a global optimum was reached, the starting values of the optimization were varied over a wide range. The results from the individual fits were then evaluated and combined as described in the next section.

3.5 Results and discussion

3.5.1 Overview

An overview of the experiments carried out in the present chapter is given in Table 8. An additional experiment of type A was made using a zeolite catalyst described by Haltenort et al.[75]. This catalyst showed no improvements regarding side reactions over the catalyst that was used here but is much more difficult to handle. The experiment was not included in the data base for the modeling and is described therefore only in the Appendix B.7.2.

Table 8: Overview of the reaction kinetic experiments carried out in the present work. The composition of the starting mixture is specified in the Appendix B.7.1. OME indicates a mixture containing different OME_{*n*}.

Experiment	Type	Feed mixture	Temperature
E1	A	DME + TRX	363 K
E2			
E3	B	DME + OME	363 K
E4			
E5			
E6			
E7			
E8	B	DME + OME + MeFo	363 K
E9	B	DME + OME	353 K
E10	B	DME + OME	373 K

Two of the experiments were of type A (E1, E2) and the remaining of type B. In all experiments, the catalyst was A36. To show that the MeFo formation is not limited by an equilibrium in the concentration range of interest, a feed mixture containing MeFo was used in experiment E8. Most experiments were carried out at 363 K. To investigate the influence of temperature, beside the experiments at 363 K one experiment was carried out at 353 K (E9) and one at 373 K (E10).

It is known that catalysts of the type that were used in the present study swell differently in different solvents and that this may have an influence on their activity[33,79]. Studying this effect was not in the scope of the present study. It is not to be expected that this effect to be of prime importance for the results and it was, therefore, neglected in the evaluation.

The numerical data for all experiments, including the specification of the feed and the composition profiles of all components, are reported in the Appendix B.7.1.

3.5.2 Experimental concentration profiles

Figure 21 shows concentration profiles from three experiments which were carried out at 363 K: one of type A (experiment E1), and two of type B (experiments E5 and E8). The most important difference between the latter two is that the feed mixture in experiment E8 contained the side product MeFo. The reactions were monitored for at least 158 h. Neither in these nor any other experiment carried out in the present chapter, a steady-state was reached. Only results for OME₂ and OME₃ are shown in Figure 21; the profiles for OME_{*n*} with $n > 3$ resemble those of OME₃, but on lower levels.

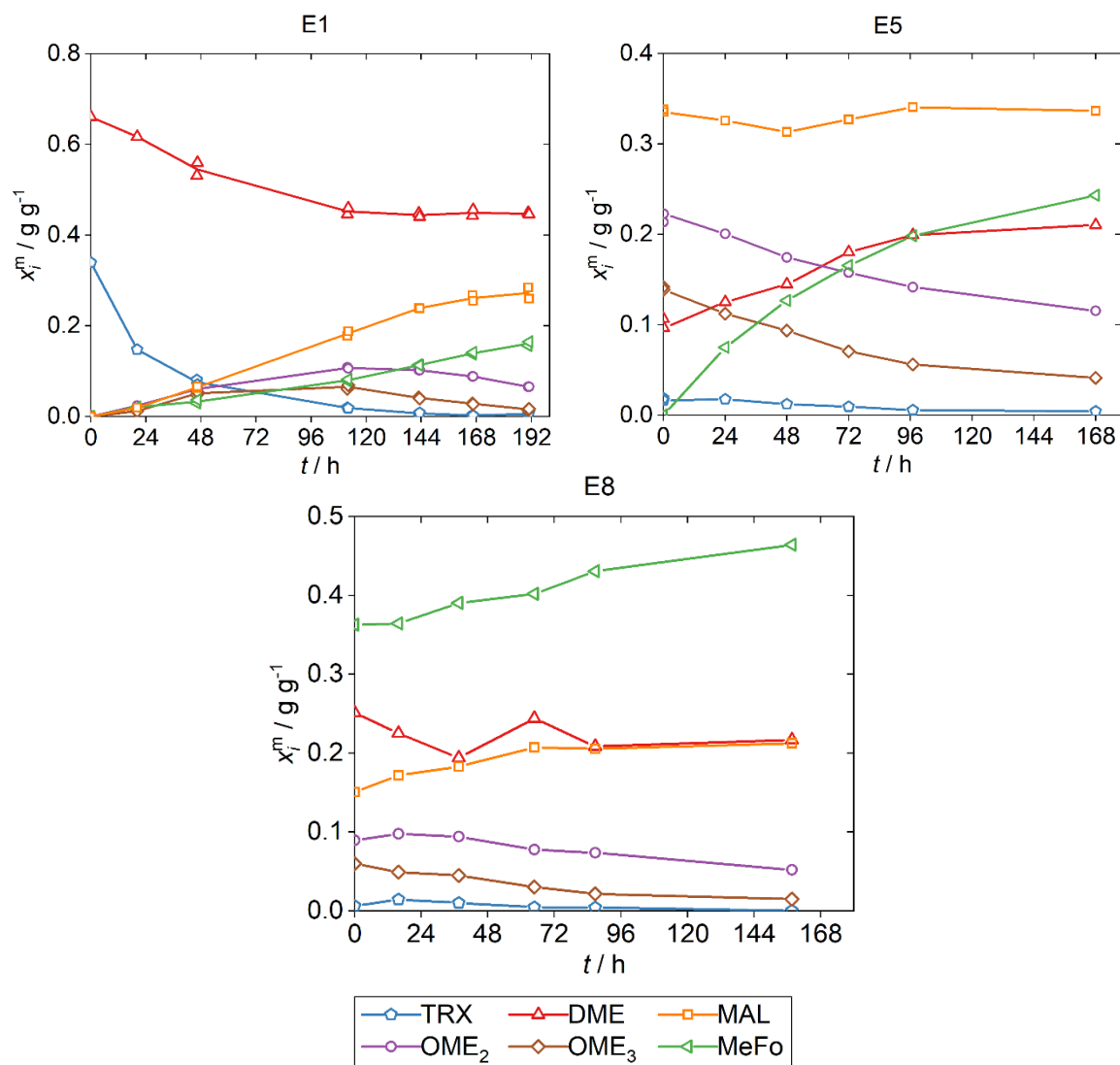


Figure 21: Experimental mass fraction profiles over time for the experiments E1, E5, and E8. Symbols are experimental data, lines are linear splines that are used here as guide for the eye. If samples were taken in short intervals, they were averaged for the spline. The initial mass ratios of catalyst to mass of reactants were 0.032 (E1), 0.025 (E5), and 0.016 (E8).

The results from experiment E1 show clearly that it is possible to form MAL and OME from DME and TRX: at the beginning of the experiment, the concentrations of DME and TRX decrease while the concentrations of MAL, OME₂, and OME₃ increase. However, also significant amounts of MeFo are formed. After about 110 h, the concentration of OME₂ passes through a maximum. The increase of the MAL concentration becomes weaker and the DME concentration changes hardly anymore. This can be attributed to the formation of MeFo from OME₂, which goes along with the formation of DME according to Reaction (XII).

In experiment E5, the starting material is a mixture of DME and OME. TRX is present in the first sample as it is quickly formed by the reverse Reaction (VIII), which shows that Reaction (VIII) is an equilibrium reaction. In experiment E5, the concentrations of all components containing CH₂O-groups (TRX, MAL, OME₂, OME₃) decrease or are roughly constant, while the DME concentration increases. This is only possible because the concentration of MeFo increases. The increase of the MeFo concentration is high first, but then falls and becomes almost constant, resulting in an almost linear MeFo concentration profile.

To check whether an equilibrium limitation could play a role in the MeFo formation (Reaction (XII)), an experiment was carried out in which a large amount of MeFo was added to the feed (experiment E8). If Reaction (XII) were an equilibrium reaction, one would expect the MeFo concentration in that experiment to decline or at least to increase only very weakly. The results from experiment E8 indicate that this is not the case: the MeFo concentration increases on a high level. This supports the assumption that Reaction (XII) is essentially irreversible; at least, an equilibrium limitation does not play a role up to high MeFo concentrations. Also, the other concentration profiles in experiment E8 are influenced by the MeFo formation from OME₂.

All profiles that are shown in Figure 21, as well as those from the other experiments, reveal the strong coupling between the concentrations of MAL, OME, and TRX. The equilibrium distribution of these components is found in all samples. This distribution is only influenced by the ratio of the CH₃-end groups, to the CH₂O groups. The CH₃-end groups of these components stem from the DME, while the number of CH₂O groups decreases as a result of the MeFo formation.

3.5.3 Modeling of the experimental results

The concentration profiles obtained in the experiments can be described well with the model developed in the present work after fitting the four model parameters. Two examples, one of type A (experiment E1) and one of type B (experiment E4) are shown in Figure 22. The results for the other experiments are presented in the Appendix B.7.1.

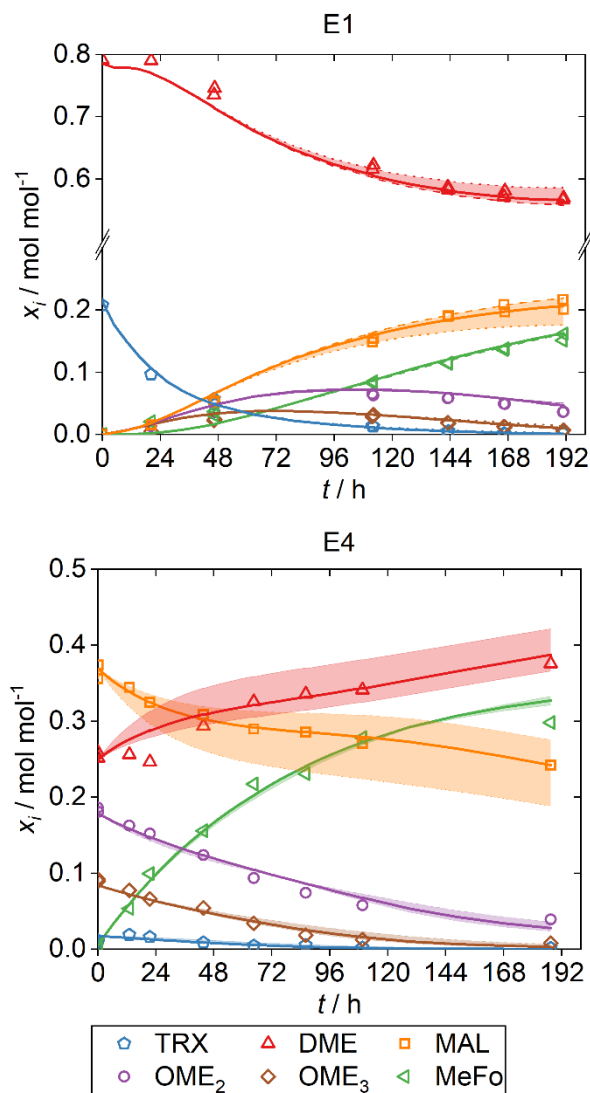


Figure 22: Experimental and calculated mole fraction profiles over time for the experiments E1 and E4. Symbols are the experimental data, lines are calculated with the model. (—) model parameters are fitted to the data, (---) resulting K_{MAL} multiplied by 1.5, (····) resulting K_{MAL} multiplied by 0.5.

The solid lines show the concentration profiles, that were obtained after adjusting the model parameters to the experimental data. The experimental concentration profiles are well reproduced by the model. Only the concentration of the DME shows some deviations, which may be due to the experimental uncertainty for this volatile component. The assumption that the formation of the longer OME and the TRX cleavage are in equilibrium at all times is confirmed: the concentrations of OME₂, OME₃, and TRX predicted by the model agree well with the experimental results. This

holds to the concentrations of OME_n with $n = 4$ to 7 too, but these are not shown for the sake of clarity.

In addition to the profiles of the respective fitted model, Figure 22 also shows results from a sensitivity analysis. For this analysis, all adjustable parameters were kept constant at the previously determined optimum, except for K_{MAL} , for which the value found in the optimization was increased or decreased by 50 percent. For experiment E1, which starts with a mixture of DME and TRX, the concentration profiles are only weakly sensitive to the choice of K_{MAL} . The experiment starts with a composition that is far from equilibrium, and therefore the influence of the forward Reaction (VII) dominates, while the reverse reaction takes place only to a small extent. The influence of the equilibrium constant K_{MAL} is accordingly low. The situation is different for experiment E4 starting from DME and the OME mixture. Here, the composition at the beginning was chosen so that it was close to the equilibrium composition that would be found if no MeFo were formed. As a consequence, the model is sensitive to the choice of K_{MAL} in this case.

3.5.4 Model parameters

Figure 23 shows the AAD that were obtained for each experiment after the model parameters were fitted individually to the respective experiment.

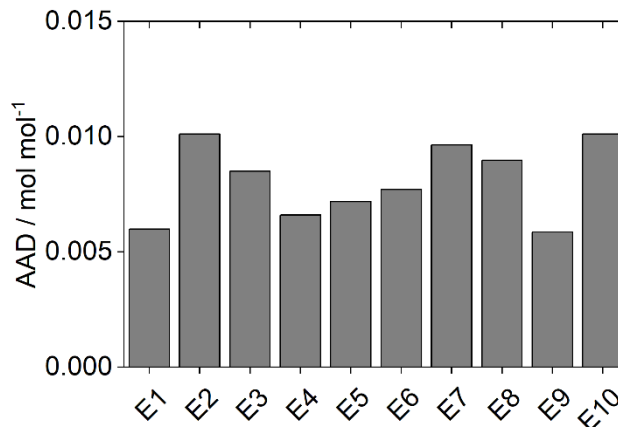


Figure 23: Average absolute deviation AAD in the mole fractions between model and experiment, obtained after fitting the model parameters individually to each experiment.

It can be seen from Figure 23 that the experimental results are represented well by the model; the AAD are of the same order of magnitude as the experimental uncertainty. This holds also when the results for the individual components are inspected (cf. Figure 22 and the corresponding

Figures for the other experiments in the Appendix B.7.1). The corresponding model parameters are shown in Figure 24 and the numerical data are reported in Table 9.

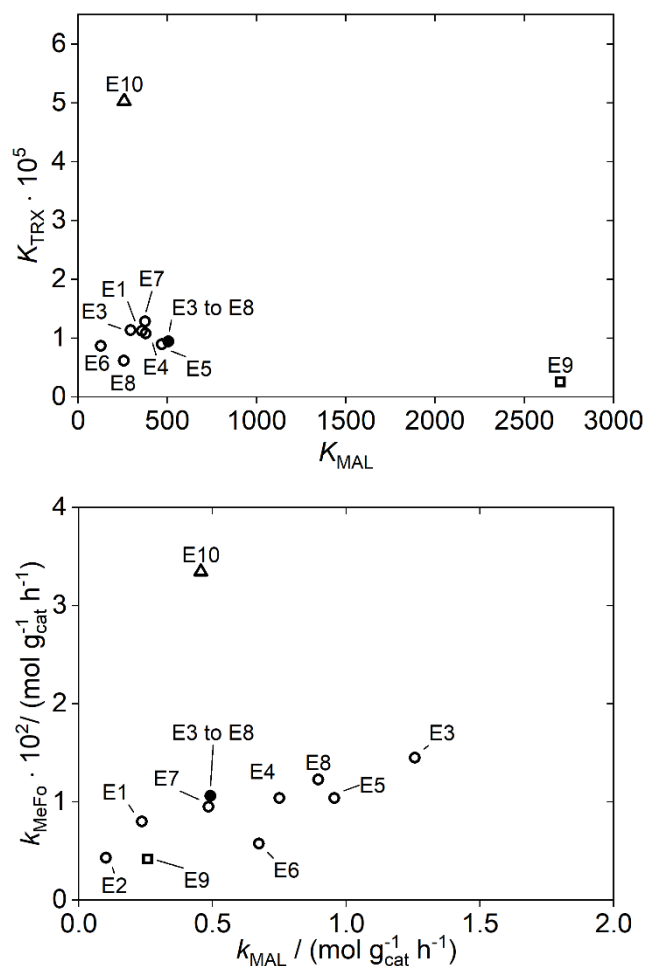


Figure 24: Results for the four model parameters obtained from individual fits to the experiments. Top: equilibrium constants of the MAL formation (K_{MAL} , Reaction (VII)) and the TRX cleavage (K_{TRX} , Reaction (VIII)), bottom: reaction kinetic constants of the MAL formation (k_{MAL} , Reaction (VII)) and the MeFo formation (k_{MeFo} , Reaction (XII)). The filled symbol indicates the result from a simultaneous fit to experiments E3 – E8. Symbols indicate the temperature: (\square) 353 K, (\circ): 363 K, (\triangle) 373 K.

Table 9: Numerical results for the four model parameters obtained from individual fits to the experiments. Equilibrium constants of the MAL formation (K_{MAL} , Reaction (VII)) and the TRX cleavage (K_{TRX} , Reaction (VIII)), the reaction kinetic constants of the MAL formation (k_{MAL} , Reaction (VII)), and the MeFo formation (k_{MeFo} , Reaction (XII)). The last line gives results from a simultaneous fit to experiments E3 – E8.

Fitted to	k_{MAL} ($\text{mol} \cdot \text{g}_{\text{cat}}^{-1} \cdot \text{h}^{-1}$)	K_{MAL}	$k_{\text{MeFo}} \cdot 10^2$ ($\text{mol} \cdot \text{g}_{\text{cat}}^{-1} \cdot \text{h}^{-1}$)	$K_{\text{TRX}} \cdot 10^5$
E1	0.24	357	0.80	1.13
E2	0.10	4902	0.43	1.11
E3	1.26	295	1.45	1.13
E4	0.75	378	1.04	1.08
E5	0.96	468	1.04	0.89
E6	0.67	126	0.58	0.87
E7	0.49	376	0.95	1.28
E8	0.90	256	1.23	0.62
E9	0.26	2701	0.42	0.26
E10	0.46	258	3.35	5.03
E3 to E8	0.49	506	1.06	0.94

First the results for 363 K (E1 – E8) will be discussed. As expected, the individual fits yield scattering results for the four parameters. For the equilibrium constants of the MAL formation K_{MAL} (Reaction (VII)) and the TRX cleavage K_{TRX} (Reaction (VIII)) the scattering is quite low. There is one outlier, the result for K_{MAL} from experiment E2, which is included in Table 9, but not shown in Figure 24. This outlier may be caused by the low sensitivity of that experiment regarding K_{MAL} . As the other results from experiment E2 show no unexpected behavior, they have been kept but their result will be ignored for K_{MAL} in the following.

The results for the rate constants of the MAL formation k_{MAL} (Reaction (VII)) scatter more than those for the MeFo formation k_{MeFo} (Reaction (XII)). However, it has to be considered that the experiments E1 and E2, which yield the lowest values for k_{MAL} , differ from the other experiments in several ways; they are of type A, whereas all others are of type B. Furthermore, in type A experiments, it cannot be guaranteed that in blowing-in the catalyst, all of it reaches the liquid phase.

Hence, these two experiments were disregarded in the averaging of the results at 363 K, and the averaging was only carried out for experiments E3 – E8. For the averaging, rather than taking a numerical average over the parameters obtained from the individual experiments, the fit of the model parameters was repeated but, this time, the complete data set from experiments E3 – E8 was used as data base to obtain numbers for the four parameters. The results from this

simultaneous fit are included in Figure 24 and Table 9. The AAD over the experiments E3 to E8 of this simultaneous fit is 0.012, which is only slightly worse than that of the individual fits. Within this group the maximum AAD is 0.014 (for E7). Using the parameters of this fit the AAD for the experiments of type A are 0.036 (E1) and 0.050 (E2).

3.5.4.1 Temperature dependence

The data base that is provided here regarding the temperature dependence of the studied reaction equilibria and kinetics, is very narrow, as only two experiments at other temperatures than 363 K were carried out (E9 at 353 K and E10 at 373 K). The results from the individual fits are shown in Figure 24 and Table 9. Nevertheless, the data are used to establish a preliminary correlation describing the temperature dependence of the model parameters.

The temperature dependence of equilibrium constants is described by Equation (18). Analogously, the Arrhenius equation according to Equation (20) is used for rate constants.

$$\ln\left(\frac{k_r}{\text{mol g}_{\text{cat}}^{-1} \text{h}^{-1}}\right) = A_r + \frac{B_r}{(T/\text{K})} \quad (20)$$

where A_r and B_r are parameters.

For correlating the temperature dependence, the results from the experiments E9 (353 K) and E10 (373K) were used together with those from the simultaneous fit of the model to the experiments at 363 K (E3 – E8). The results are shown in Figure 25. The resulting parameters are reported in Table 10.

Table 10: Parameters for the correlation of the equilibrium constants (cf. Equation (18)) and rate constants (cf. Equation (20)).

Reaction	a_r	b_r	A_r	B_r
(VII)	-36.180	15507.326	9.583	-3821.088
(VIII)	42.467	-19560.728	-	-
(XII)	-	-	33.192	-13665.278

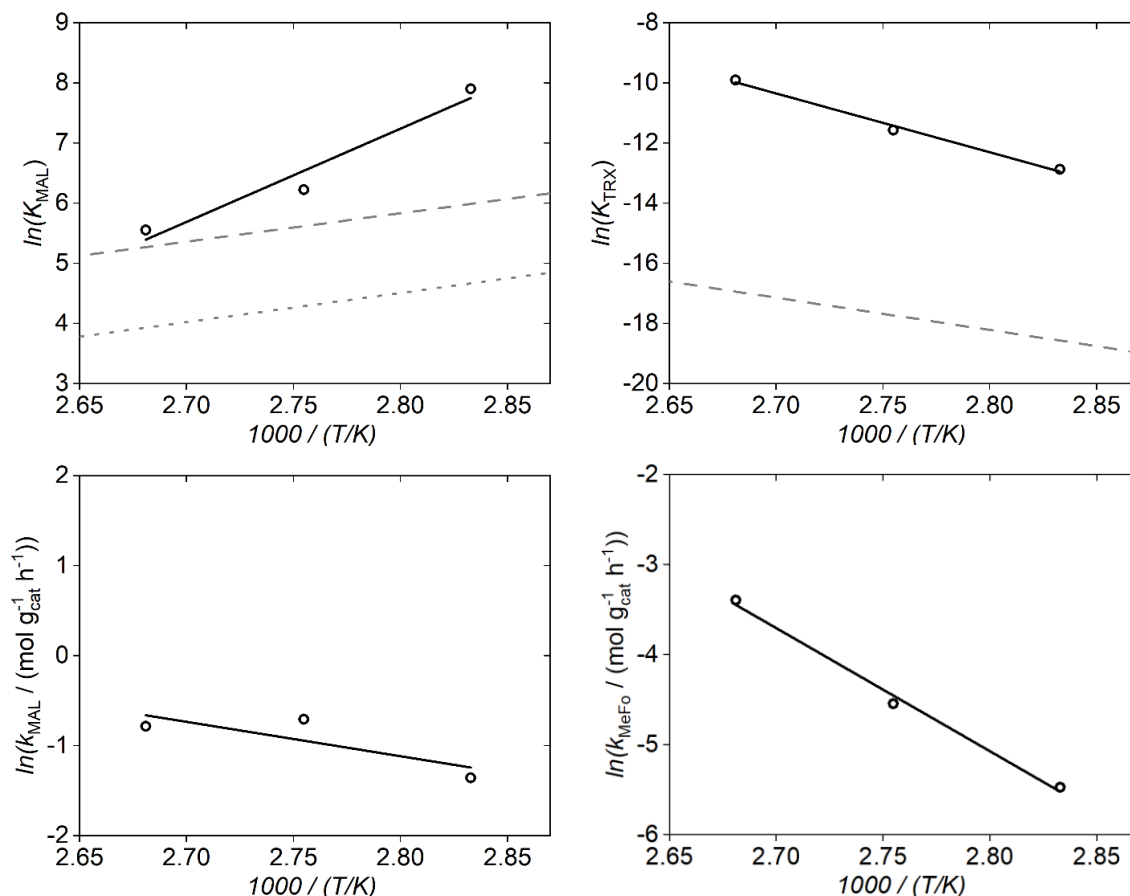


Figure 25: Results for the temperature dependence of the equilibrium constants of Reaction (VII) (K_{MAL}) and Reaction (VIII) (K_{TRX}) and the reaction kinetic constants of Reaction (VII) (k_{MAL}) and Reaction (XII) (k_{MeFo}). (○) Results obtained from experimental data from the present work, (—) correlations (see text). For comparison also results for K_{MAL} obtained from standard state data (---), results for the equilibrium constant of OME_D from Schmitz[87] (⋯⋯), and results for K_{TRX} from calculations with literature data (—) are shown. The calculations from standard state data and literature data are described in Chapter 4.2.3.2. The correction of this data to a activity based constant is described in Appendix B.9.

It can be seen from Figure 25 that the correlations represent the temperature dependence of the data from the present work quite well. From the correlation of the equilibrium constants the molar reaction enthalpies ($\Delta h_{\text{reac},r}$), of Reaction (VII) and (VIII), can be calculated from $\Delta h_{\text{reac},r} = -R \cdot b_r$, where R is the universal gas constant. They are -128 kJ mol^{-1} for Reaction (VII) and 162 kJ mol^{-1} for Reaction (VIII). The activation energy of the reaction ($E_{a,r}$) can be calculated from $E_{a,r} = -R \cdot B_r$. It is 31 kJ mol^{-1} for Reaction (VII) and 113 kJ mol^{-1} for Reaction (XII).

In Figure 25, the data from the present work for the equilibrium of the MAL formation (K_{MAL}) are compared with results from Chapter 4.2.3.2, that were obtained from standard state enthalpies and entropies. Also for K_{TRX} the data from the present chapter are compared to results from Chapter 4.2.3.2 that were estimated from data on the equilibrium constant of the OME formation. Neither this estimate nor that obtained in the present chapter is based on experimental results for the concentration of monomeric formaldehyde. The data from Chapter 4.2.3.2 are shown as dashed lines. The mole-fraction based data were converted to activity-based data, as described in the Appendix B.9, to enable a direct comparison with the results from the present chapter. In principle, DME can be considered as an OME with $n = 0$. Therefore, for a comparison also the equilibrium constant of the formation of OME from Schmitz[87] is shown as a dotted line in Figure 25.

Regarding K_{MAL} , it can be seen that the data of the present work and the data from Chapter 4.2.3.2 show a good agreement for the highest temperature, at lower temperatures, deviations occur. Such discrepancies are not unexpected, given the uncertainties in the calculation of thermodynamic equilibrium from standard state data and the uncertainties in their experimental determination. The equilibrium constant of the OME oligomerization is significantly smaller than that for the MAL formation K_{MAL} for all temperatures.

The comparison of the data for the equilibrium constant of the cleavage of TRX K_{TRX} obtained in the present work and the corresponding data from Chapter 4.2.3.2 reveals significant differences for all temperatures. To resolve these differences experiments would be needed that yield information on the true concentration of monomeric formaldehyde.

In case of the rate constants k_{MAL} and k_{MeFo} , no data for comparison are available in the literature, as the numerical value depend on the nature of the catalyst.

3.6 Conclusions

The present chapter closes some of the biggest gaps in the field of the reaction of DME and TRX to OME. OME synthesis from DME and formaldehyde proceeds in a complex reaction network, in which first MAL and then OME is formed in oligomerization reactions. All these reactions require strong acidic catalysis. Previous studies with different acidic catalysts reveal an influence of their strength on the reaction rate, but other differences have not been clearly shown so far. It is also known that under the required strongly acidic conditions besides the desired products MAL and OME also substantial amounts of MeFo are formed in a side reaction [31,37,75].

This complex synthesis was studied in the present chapter in a fully thermostatted high-pressure batch reactor using a commercial heterogeneous acidic catalyst. TRX was used as formaldehyde source. Both the experiments and their evaluation are challenging. The analysis was carried out by quantitative NMR spectroscopy, using special high-pressure sampling tubes. Despite very long

reactions times of up to about 200 h, in none of the experiments, a steady-state was reached. This is caused by the irreversible MeFo formation in the side-reaction. The long reaction times were required as the rate-determining step, the formation of MAL, is slow at the studied temperatures, which were between 353 K and 373 K. The formation of the side product MeFo takes place with a rate that is similar to that of the MAL formation, while the oligomerization reactions leading to OME are much faster and can be considered to be in equilibrium at any given time of the experiment.

A physico-chemical model was used for the evaluation of the experimental results. It accounts for all reactions mentioned above as well as for the physical non-ideality of the liquid and the gas phase in the reactor. The model builds preliminary work, from which many of its parameters could be taken. Only four parameters had to be fitted to the data from the present work: the chemical equilibrium constants of the MAL formation K_{MAL} and the cleavage of TRX K_{TRX} , and the reaction kinetic constants of the MAL formation k_{MAL} and the MeFo formation k_{MeFo} . Temperature-dependent correlations are presented for these physico-chemical quantities. The resulting model describes the experimental data well.

This new information is essential for the conceptual design of OME processes starting from DME and formaldehyde. The equilibrium constant of the MAL formation, which is the essential first step in the reaction network leading to the OME, is larger than predicted from standard state properties (cf. Chapter 4.2), which is favorable for the process. However, two major obstacles remain: the MAL formation is very slow, despite the catalysis; the residence time needed to achieve acceptable conversion is of the order of 10 - 100 hours at the temperatures and reactand-to-catalyst ratios studied in the present work. An even bigger challenge is the formation of the side-product MeFo, which is formed in very substantial amounts. In the conceptual design presented in Chapter 4.2, the formation of MeFo was neglected. Hence, the design needs to be revised in future work to enable the separation of MeFo, which can probably be achieved by distillation. Furthermore, a strategy for using the MeFo would be needed. MeFo is used on a large scale, e.g., for the production of formic acid, but it has recently also been discussed as synthetic fuel [88,89].

The present chapter provides the basis for a more realistic assessment of the route leading from formaldehyde and DME to OME.

4 Production processes for OME and trioxane

In the following two conceptual designs of formaldehyde-based processes are presented. Chapter 4.1 deals with a crystallization-based process of the anhydrous formaldehyde-source trioxane. Chapter 4.2 shows the conceptual design of a OME production process based on DME and trioxane.

4.1 Trioxane production process

4.1.1 Introduction

Current production processes for trioxane are complex and energy-intensive so that there is a strong incentive for developing enhanced alternatives [90]. All industrial trioxane production processes described in the literature [1,91] use aqueous formaldehyde solutions as precursor. In most trioxane production processes, the solution is first concentrated by distillation or evaporation to reduce the amount of water that has to be handled in the process. This concentration step has to be done on site, as concentrated formaldehyde solutions are difficult to transport due to the risk of the formation of a formaldehyde-rich solid phase, like it is already described in Chapter 2. The concentrated formaldehyde solution is fed to a reactor, where formaldehyde is partly converted to trioxane in the presence of an acid catalyst. Low conversion, caused by an unfavorable chemical equilibrium, and the formation of various low-boiling side products in small amounts, such as formic acid, methylal, or methyl formate, have stimulated research in catalyst optimization and reactor design [92–99]. The reactor product is fed to a separation train, which has to accomplish the following: a) separate the rather small amounts of trioxane from the reactor product; b) remove the water; and c) recycle the rest. In basically all established processes, the first step is a distillation, in which the top product is an azeotrope that is rich in trioxane, whereas the bottom product is rich in formaldehyde and recycled back to the reactor. The following steps for the purification of the trioxane-rich top product vary from process to process. The most common process relies on the extraction of trioxane with methylene dichloride or other solvents, such as benzene, 1,2-dichloroethane, or nitrobenzene [1]. This route requires solvent recycling and is known to have both high capital and operation expenditures. Another possibility is to use pressure swing

distillation to obtain pure trioxane. Such a process has been developed by Grützner et al.[45,91,100]. The pressure swing process is more favorable than extraction processes and therefore used as a reference in the present chapter. However, this process also has drawbacks: it has large recycle streams and is energy-intensive. Another option is to use crystallization to obtain pure trioxane from the trioxane-rich top product of the preceding distillation step. In the scientific literature, only Synowiec et al.[101] report on the technical feasibility of the crystallization of trioxane in the presence of water and formaldehyde. In several patents, crystallization is mentioned in connection with trioxane production processes [102–105]. To the best of our knowledge, no conceptual design of a crystallization-based process for the production of trioxane has been described in the literature up to now. As the above-mentioned pressure swing distillation process, a crystallization-based process requires no auxiliary materials, but it has the advantage of avoiding the recycling of large amounts of material, as it is required in the pressure swing distillation process [91]. Potential drawbacks of crystallization processes are low temperatures that may be required to obtain sufficient amounts of solid, the complex handling of the slurry, and the washing and drying of the crystals. Trioxane is at present almost exclusively produced for polymer production, which requires ultra-pure reactants [1]. This is not the case for trioxane that is used as feedstock for biotechnological processes, where residues of water pose no problem. This opens up new options for the trioxane production process. In particular, it strongly facilitates the application of crystallization-based processes, as expensive washing and drying steps can be omitted.

In the present chapter, a crystallization-based trioxane production process consisting of a reactor, two distillation columns, and a crystallizer is described. The level of detail of the discussion is that of a conceptual process design, i.e. information on the main streams, energies, temperatures, etc. are given but do not consider the design of individual apparatuses. The process design strategy, that was applied here, is heuristic: it was started from the knowledge of existing processes and adopt those parts, for which no promising alternatives are known, and which are, therefore, used in all established trioxane processes. This is namely the reaction stage, consisting of a liquid phase reactor and a first concentration step, in which the reaction product is distilled and a trioxane-rich top product is obtained, while the bottom product is recycled to the reactor. Our focus is on the following separation train, for which presently either a pressure-swing distillation is used or an extraction process with solvent recovery. The task was to find out, how the separation train would look like, if crystallization is used. This was studied applying a combination of process simulations, based on equilibrium stage models of the units, and simple crystallization experiments. Those process simulations are far from being trivial, as the studied system is highly reactive and multiple reactions have to be considered in all parts of the process. We rely here on extensive previous work of our group on formaldehyde-containing systems, e.g. [6], and use the

physico-chemical model of the system (formaldehyde + water + trioxane) described in detail by Grützner[91] for our simulations.

This model, however, does not describe the solid-liquid equilibria in the system (formaldehyde + water + trioxane), which is a prerequisite for the simulation of the crystallization step. As no data on the solid-liquid equilibria of this ternary system have been reported in the literature up to now, experiments were carried out. The solid-liquid phase behavior of the ternary system (formaldehyde + water + trioxane) is complex and very difficult to investigate, due to the chemical reactions. This is discussed in more detail in the following section.

Based on the new experimental data, the crystallization step of the proposed process was simulated as an equilibrium stage yielding pure trioxane; no kinetic effects such as nucleation or nucleus growth were taken into account, and the crystallization temperature is identical with the solid-liquid equilibrium temperature in this work. Two versions of the crystallization-based process were studied: one with a crystallization temperature of 288 K, which is considered to be achieved using chilled water in an industrial application, and one with a higher crystallization temperature of 303 K, which could even be achieved using inexpensive cooling water. The new crystallization-based trioxane production process is compared to the state-of-the-art pressure swing distillation process of Grützner[91] in a consistent manner on the basis of streams and energies.

4.1.2 Processes

4.1.2.1 New crystallization-based process

The process flow diagram of the new crystallization-based (CR) trioxane production process is shown in Figure 26.

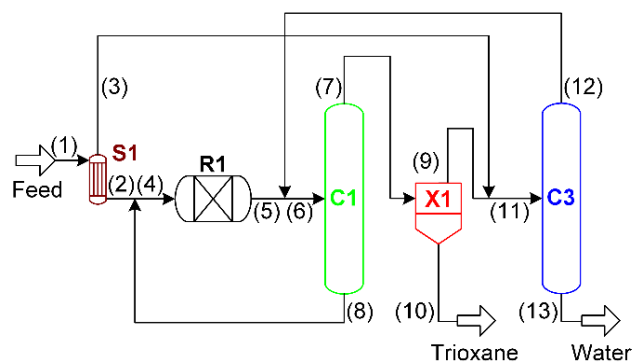


Figure 26: Process flow diagram of the new crystallization-based trioxane process. The process consists of an evaporator S1, a reactor R1, a crystallizer X1, and two distillation columns C1 and C3. Compositions for a design operating point are indicated in Figure 29 and the corresponding streams are given in Table 13.

The aqueous formaldehyde solution (1) is at first partially evaporated in the evaporator S1. The formaldehyde-rich solution (2) from the bottom of the evaporator S1 is mixed with the bottom product of the first column C1 (8), which mainly consists of formaldehyde, water, and traces of trioxane. The resulting mixture (4) is then fed to reactor R1, where trioxane is formed by heterogeneous catalysis. The product stream (5) leaving the reactor is mixed with the top product of column C3 (12) and fed to column C1 (6), in which a trioxane-rich top product (7) is obtained. The bottom product (8) is recycled. The maximum achievable concentration of trioxane in the top product (7) is limited by a ternary light-boiling azeotropic point in the system (formaldehyde + water + trioxane). The azeotropic point depends on pressure; a low pressure is preferred in column C1 to achieve a high trioxane concentration. All major side products in the process are light-boiling and can be removed from the process at the top of column C1 (7) by partial condensation; due to the small amounts, this is not explicitly taken into account in our process model. Formaldehyde, water, and trioxane are condensed to liquid state and fed to the crystallizer X1. From the crystallization, pure solid trioxane is obtained (10). Potential subsequent washing and drying of the solid is not considered here. The liquid supernatant of the crystallization (9) is mixed with the condensed vapor phase from the evaporator S1 (3) and fed to column C3 (11), in which pure water is obtained as bottom product (13); the trioxane-rich top product (12) is recycled. In column C3, a high pressure is favorable, as this enables higher formaldehyde concentrations in the top product.

4.1.2.2 Pressure swing process

The structure of the pressure swing (PS) process of Grützner[91] is similar to that of the CR process introduced in this work. Instead of a crystallizer, an additional distillation column C2 is used. The process flow diagram is shown in Figure 27.

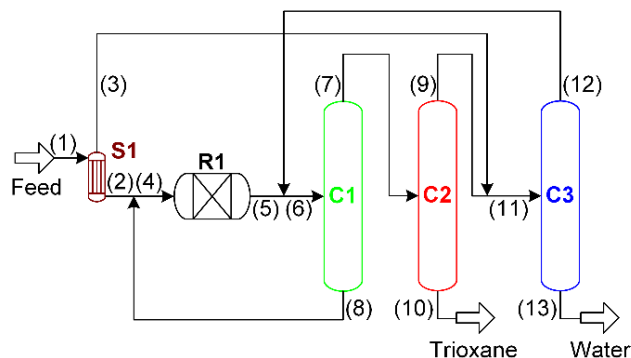


Figure 27: Process flow diagram of the pressure swing trioxane process [91]. The process consists of an evaporator S1, a reactor R1, and three distillation columns C1, C2, and C3. Compositions for a design operating point are indicated in Figure 30 and the corresponding streams are given in Table 13.

The column C2 is operated at a higher pressure than column C1 to enable the pressure swing, i.e., both columns are operated in different distillation regions. The top product of column C1 (7) serves as feed of column C2, at the bottom of which pure trioxane is obtained (10). The top product of column C2 (9), consisting of formaldehyde, water, and trioxane, is fed to column C3, in which water is removed. The role of column C3 and its integration in the PS process are the same as in the CR process.

4.1.3 Solid-liquid equilibrium measurements

4.1.3.1 Overview

To model the crystallization in the new trioxane process, information on the solid-liquid equilibria in the system (formaldehyde + water + trioxane) at the temperatures and compositions relevant to the crystallization step is needed. However, only very little is known on the solid-liquid phase behavior of the system (formaldehyde + water + trioxane). The melting points of pure water and trioxane (334.75 K [101]) are available, and so is data on the non-reactive system (trioxane + water) [53,106–109], which has an eutectic point at about 271 K and 0.1 g g⁻¹ trioxane. In principle, in the system (formaldehyde + water + trioxane) also the formation of a formaldehyde-rich phase as it is described in Chapter 2 is to be expected. However, as also stated in Chapter 2, the time

constant of the formation of this formaldehyde-rich solid exceeds the time constants of the solid formation in technical crystallizers as they would be used here by several orders of magnitude. Therefore, in the framework of this conceptual design the possible precipitation of formaldehyde-rich solid is neglected, which is also supported by the experimental results, which are described later on.

What is to be known about the solid-liquid equilibria in the system (formaldehyde + water + trioxane) for solving the present design task? First, it is need to know if there is a region in the phase diagram, where the solid is pure trioxane. The information on the sub-system (water + trioxane) [53,106–109], as well as observations of Synowiec[101] and the patent literature [102–105], indicate that such a region exists this was also confirmed by the experiments of the present work. It would, furthermore, be desirable to know the limits of that region. Unfortunately, for the reasons mentioned above, their elucidation would be extremely tedious and is clearly out of the scope of the present work. Therefore, adopted a different strategy was adopted: It have been simply carried out crystallization experiments for a feed condition that was of particular interest. That composition was determined in preliminary process simulations, which were carried out assuming pure trioxane can be obtained as solid. As that assumption was confirmed experimentally, the argument is solid. This could have been repeated for different feed compositions, which, however, was not necessary as the initial guess was good. Furthermore, to a certain extent, information on the single feed point can be extrapolated, as it is known the behavior of the formaldehyde-free subsystem (water + trioxane) and it can be assumed that upon increasing the trioxane concentration in the feed, still pure trioxane will be obtained as crystallisate.

The feed composition for the crystallization experiment was determined as follows: in the process flow diagram of the process (cf. Figure 26), the feed of the crystallization is stream (7). This stream comes from the reaction step of the process, which consists of the pre-concentration S1, the reactor R1, and the concentration column C1. The bottom product of the column C1 (8) is recycled to the reactor and contains basically no trioxane. In the PS process, the top stream (7) is close to the ternary azeotrope in the system (formaldehyde + water + trioxane). In the crystallization process, that requirement can be relaxed, such that one degree of freedom is gained in column C1. By varying a corresponding parameter different compositions of stream (7) are obtained. That variation was carried out in preliminary simulations of the process assuming that for all choices, pure trioxane is obtained as product of the crystallization. The final choice was made so as to achieve a minimal energy demand of the process for a given crystallization temperature. The choice of that temperature has only a minor influence on the composition of stream (7) resulting from the optimization.

4.1.3.2 Chemicals and measurement method

Trioxane ($\geq 0.99 \text{ g g}^{-1}$) and paraformaldehyde ($\geq 0.95 \text{ g g}^{-1}$) were purchased from Sigma-Aldrich. An aqueous formaldehyde solution was prepared by dissolving paraformaldehyde in deionized water (electrical resistivity of 10-15 M Ω cm), which was prepared using a Milli-Q system from Merck. A detailed description of the preparation procedure is given in preliminary work by Schmitz et al.[58]. For the experiments, a clear single phase stock solution of (formaldehyde + water + trioxane) was prepared by mixing the aqueous formaldehyde solution with trioxane at 313 K; the composition of the stock mixture (cf. Table 11) was chosen based on preliminary process simulations. Samples of the stock mixture were filled in 100 or 200 ml glass flasks and thermostatted at temperatures ranging from 253 to 291 K for three days. It was checked in preliminary experiments that, after three days, no further change in the composition of the liquid phase was observable. The temperature inside the flasks was measured with a platinum resistance thermometer with an uncertainty of $\pm 0.1 \text{ K}$. The variations of the temperature during thermostatization was within this threshold. The conditions were such that, during the equilibration time, crystals were formed in all studied solutions (at all investigated temperatures). After the equilibration time, a small amount of liquid phase was isothermally taken from each sample using a 2 ml syringe and was filtered using a 0.45 μm syringe filter to separate any drawn crystals. The overall mass fraction of formaldehyde in the drawn liquid was analyzed with the Na_2SO_3 titration method as described by Schmitz et al.[58]. The overall mass fraction of trioxane was determined by gas chromatography using the same equipment and method as already described by Schmitz et al.[58]. The relative uncertainty of the measured trioxane and formaldehyde mass fractions was determined to be below 2 %. Each analysis was repeated at least three times and the arithmetic mean of the results is reported here. The composition of the crystals was not measured, but was inferred from the mass balance.

4.1.3.3 Results

The results of the solid-liquid equilibria experiments are given in Table 11 and are also depicted in Figure 28.

Table 11: Experimental results of this work for the liquid phase composition of solid-liquid equilibria in the system (formaldehyde (FA) + water (WA) + trioxane (TRX)). The solid was pure trioxane in the experiments, except for the one marked with an asterisk, for which the solid composition is unknown. The feed solution was the same in all experiments ($\tilde{x}_{\text{FA}}^{(m)} = 0.170 \text{ g g}^{-1}$, $\tilde{x}_{\text{W}}^{(m)} = 0.590 \text{ g g}^{-1}$, $\tilde{x}_{\text{TRX}}^{(m)} = 0.240 \text{ g g}^{-1}$).

T K	$\tilde{x}_{\text{FA}}^{(m)}$ g g^{-1}	$\tilde{x}_{\text{TRX}}^{(m)}$ g g^{-1}
291.05	0.194	0.147
283.35	0.197	0.117
273.35	0.205	0.085
263.36	0.205	0.063
258.36	0.219	0.053
253.35	0.284	0.044*

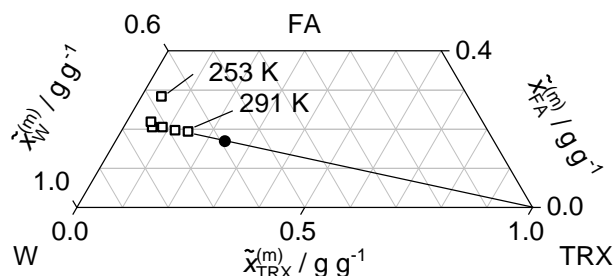


Figure 28: Liquid phase composition (Squares) of the solid-liquid equilibria experiments of this work in the system (formaldehyde (FA) + water (W) + trioxane (TRX)) at temperatures ranging from 253 to 291 K. The temperature is indicated for the experiments with the lowest and the highest temperature. The composition of the stock solution of the experiments (○) is close to the feed composition of the crystallization in the trioxane process described in this work. The mass balance line (—) indicates that the solid is pure trioxane, except for the experiment at 253 K.

The extension of the mass balance line that connects the composition of the liquid phase in equilibrium with that of the feed in Figure 28 indicates that in all experiments, except for the one at 253 K (i.e., at the lowest temperature) pure trioxane crystals were formed, which is in agreement with the patent literature [102]. The position of the point for 253 K in Figure 28, suggests for that temperature, the crystallisate contains also water, besides trioxane, i.e. a co-crystallization occurs. In no case the precipitation of solid formaldehyde oligomers was observed. Solid formaldehyde-rich phases are white and can be distinguished well from solids containing trioxane and water. Therefore, it can be assumed to neglect the formation of a formaldehyde-rich phase on the time

scale of this process. Although in a more detailed investigation of this process this should be reviewed in detail.

4.1.4 Modeling and simulation

4.1.4.1 Process model

Except for the description of the crystallizer, the process model used in this work is the same as the one employed by Grützner[91]. The process model comprises three different apparatus models, which are described in the following. For brevity, only a short outline of the three models is given here. A detailed description of the models, including all model equations and parameters for the calculation of chemical equilibria, phase equilibria, and enthalpies is given in the Appendix C.1.1. The process model was implemented in the process simulator *Chemasim*, which was used for all simulations in this chapter.

Evaporator S1 and distillation columns C1, C2, and C3

An equilibrium stage model was used to describe the evaporator S1 and the distillation columns C1, C2, and C3. In the present chapter the chemical and phase equilibria in the system (formaldehyde + water + trioxane) were calculated with the well-established models of Kuhnert[110], which provided information on the system (formaldehyde + water), and Albert[111], which extended the model of Kuhnert[110] to include trioxane. In the resulting model, the chemical equilibria and the vapor-liquid equilibria are calculated consistently using activities. The vapor-liquid equilibria are described by the extended Raoult's law and activity coefficients are calculated using a modified version of the UNIFAC model [112]. In the liquid phase, the oligomerization reactions of formaldehyde and water are explicitly taken into account as they are described in Section 2.3. In the vapor phase, only Reaction (I) takes place. Oligomers with $n \geq 2$ were considered nonvolatile so that they only appear in the liquid phase. Trioxane was considered non-reactive in the separation units of the process, as no catalyst is present in these apparatuses.

Reactor R1

The reactor R1 was modeled as an equilibrium stage with a single feed and a single outlet, in which the equilibrium is reached. This formally corresponds to a large stirred tank reactor. For simplicity and following Grützner[91], the outlet stream was specified as a boiling liquid at

$p = 1$ bar with a vapor fraction of $X = 0$. To achieve that, heat transfer to the reactor was allowed in the simulation.

In the liquid phase, in addition to the formaldehyde oligomerization Reactions (I) and (II), also the formation of trioxane was considered, i.e., it was considered that a heterogeneous catalyst was present. Following Grützner[91] in the present chapter, trioxane ((CH₂O)₃, TRX) is formed from MG₃ by ring formation in Reaction (XIV), in which water is released:



The equilibria of the formaldehyde oligomerization Reactions (I) and (II) were calculated using activities with the well-established models of Kuhnert[110] and Albert[111], as already mentioned above. The chemical equilibrium of the trioxane formation (Reaction (XIV)) was modeled using a mole fraction-based approach. This inconsistency was accepted here for practical reasons. Developing a consistent chemical equilibrium model would have had no practical advantages, as only liquid phase reactions are considered and the feed composition does not vary strongly. It is emphasized that this approach would not have been acceptable for modeling reactive vapor-liquid equilibria, where thermodynamically consistent models must be used [113]. As trioxane is inert in the separation trains discussed in the present work, this does not pose a problem.

Crystallizer

The crystallizer was modeled as a combination of a heat exchanger and a stream splitter, in which, first, the feed stream was cooled down to the crystallization temperature and second, pure trioxane was separated from the feed stream. The amount of trioxane that was separated from the stream was calculated from an empirical solid-liquid equilibrium model that was established using the new experimental data from the present chapter; kinetic effects, which can play an important role in crystallizers, were not considered. The model correlates the mole fraction of trioxane in the supernatant and the crystallization temperature and is described in more detail in the Appendix C.1.1. It is assumed that the crystals are pure trioxane. The option to develop a physico-chemical model of the solid-liquid equilibrium was considered but discarded, as the amount of available experimental data was found to be too low (only a single data point per temperature was available).

4.1.4.2 Process specifications and optimization

In the following, the process specifications and the optimization strategy that was applied for optimizing the two processes discussed in this chapter, namely the CR and the PS trioxane process, are described. An overview of the process specifications of both processes is given in Table 12.

Only the process specifications for a crystallization temperature of 288 K are tabulated. The process specifications for a crystallization temperature of 303 K are given in the Appendix C.1.3.

Table 12: Overview of the process specifications of the crystallization-based (CR) and the pressure swing (PS) trioxane process. The reflux ratios and feed stages of the distillation columns C1, C2, and C3 were adjusted during the optimization as described in the text.

apparatus	specification	
	CR	PS
S1	$\tilde{x}_{FA,1}^{(m)} = 0.49 \text{ g g}^{-1}$ $p = 0.1 \text{ bar}$ $\dot{m}_3 / \dot{m}_2 = 1$	$\tilde{x}_{FA,1}^{(m)} = 0.49 \text{ g g}^{-1}$ $p = 0.1 \text{ bar}$ $\dot{m}_3 / \dot{m}_2 = 1$
R1	$p = 1.0 \text{ bar}$ boiling state $N = 15$	$p = 1.0 \text{ bar}$ boiling state $N = 15$
C1	feed stage = 8 $p = 1.0 \text{ bar}$ $R = 3.000$	feed stage = 10 $p = 0.8 \text{ bar}$ $R = 2.053$
X1	$\tilde{x}_{FA,8}^{(m)} = 0.70 \text{ g g}^{-1}$ $T = 288.15 \text{ K}$ $p = 1.0 \text{ bar}$ $\tilde{x}_{TRX,10}^{(m)} = 1 \text{ g g}^{-1}$	$\tilde{x}_{FA,8}^{(m)} = 0.70 \text{ g g}^{-1}$
C2		$N = 17$ feed stage = 12 $p = 4.0 \text{ bar}$ $R = 0.172$ $\tilde{x}_{TRX,10}^{(m)} = 0.999999 \text{ g g}^{-1}$ $N = 18$
C3	feed stage = 10 $p = 2.5 \text{ bar}$ $R = 1.230$ $\tilde{x}_{W,13}^{(m)} = 0.99 \text{ g g}^{-1}$	feed stage = 12 $p = 2.5 \text{ bar}$ $R = 0.905$ $\tilde{x}_{W,13}^{(m)} = 0.99 \text{ g g}^{-1}$

The comparison of the two processes was carried out based on their energy demand. It was therefore essential to treat the processes in a consistent way, i.e., to have equal specifications of the input and output streams and an equal number of stages of the columns C1 and C3, which occur in both processes. Wherever it was possible, the process specifications were simply adopted

from Grützner[91], with one exception: Grützner[91] chose a rather low pressure of $p = 0.8$ bar in column C1 of the PS process to enhance the effect of the pressure swing. This was not necessary for the CR process so that the pressure was set to $p = 1$ bar. This difference in the pressure has only a minor influence on the separation in column C1.

The feed stages and the reflux ratios of the columns of both processes were considered as adjustable parameters, which were chosen such that the sum of all column reboiler duties was minimized. Other heat duties that appear in the processes, such as the heat duties of the evaporator S1 and the reactor R1, were not considered for the optimization, as they were small compared to the column reboiler duties and similar for both processes.

The optimization was carried out as follows: first, the reflux ratios of the columns were successively adjusted in the order C1, C2, and C3 and second, the feed stages of all columns were adjusted simultaneously. This procedure was repeated at least two times, until the change in the sum of all column reboiler duties was less than 0.1 % of the final value. It may be astonishing that the final reflux ratios obtained for the CR process are slightly higher than those of the PS process for both columns C1 and C3. This is a result of the much smaller recycle streams in the CR process.

4.1.5 Results and discussion

In this section, first the results for the new CR process are presented and compared to the PS process, then alternatives to the CR process are briefly discussed. Only the results for the CR process with a crystallization temperature of 288 K are discussed here, if not explicitly stated otherwise; the results for 303 K are presented in the Appendix C.1.3. The results of the two versions of the CR process do not differ strongly so that the general findings discussed here are valid for both cases. Here, the focus is on the results for the crystallization temperature 288 K, as they are within the range which was studied experimentally. The results for 303 K are extrapolation.

4.1.5.1 New crystallization-based process and comparison to the pressure swing process

The streams of the CR and the PS trioxane process are reported in Table 13.

Table 2: Stream tables of the crystallization-based (CR) and the pressure swing (PS) process for the trioxane production. The stream numbers are the same as in the Figure 26 and Figure 27.

Stream	1		2		3		4		5		6		7	
	CR	PS	CR	PS	CR	PS	CR	PS	CR	PS	CR	PS	CR	PS
$\dot{m}^{(j)} / \dot{m}^{(10)}$	2.06	2.06	1.03	1.03	1.03	1.03	44.7	34.94	44.70	34.94	47.09	42.59	3.42	8.38
$\tilde{x}_{FA}^{(m)} / g g^{-1}$	0.4900	0.4900	0.6609	0.6609	0.3191	0.3191	0.6991	0.6989	0.6767	0.6702	0.6611	0.5705	0.1636	0.0647
$\tilde{x}_W^{(m)} / g g^{-1}$	0.5100	0.5100	0.3391	0.3391	0.6809	0.6809	0.2900	0.2966	0.2900	0.2966	0.3003	0.2870	0.4480	0.2543
$\tilde{x}_{TRX}^{(m)} / g g^{-1}$	0.0000	0.0000	0.0000	0.0000	0.0000	0.0000	0.0109	0.0045	0.0333	0.0332	0.0386	0.1425	0.3884	0.6810
Stream	8		9		10		11		12		13			
	CR	PS	CR	PS	CR	PS	CR	PS	CR	PS	CR	PS		
$\dot{m}^{(j)} / \dot{m}^{(10)}$	43.67	33.91	2.42	7.68	1.00	1.00	3.45	8.72	2.38	7.65	1.06	1.06		
$\tilde{x}_{FA}^{(m)} / g g^{-1}$	0.7000	0.7000	0.2313	0.0731	0.0000	0.0000	0.2876	0.1022	0.3680	0.1151	0.0100	0.0100		
$\tilde{x}_W^{(m)} / g g^{-1}$	0.2888	0.2953	0.6336	0.2874	0.0000	0.0000	0.6477	0.3340	0.4952	0.2428	0.9900	0.9900		
$\tilde{x}_{TRX}^{(m)} / g g^{-1}$	0.0112	0.0047	0.1351	0.6395	1.0000	1.0000	0.0947	0.5638	0.1368	0.6421	0.0000	0.0000		

The composition of the streams of the CR process are visualized in Figure 29, those of the PS process are in Figure 30. These figures also show the chemical equilibrium line for the formation of trioxane and the distillation boundaries for the different pressure levels that were considered here. They are calculated with the same models for the chemical and phase equilibria as used in the process model. The shaded area in the Figure 29 and Figure 30 indicates that there is a region with high formaldehyde-to-water ratios, where the physico-chemical model should not be used. Furthermore, high formaldehyde-to-water ratios favor the formation of formaldehyde-rich solids. This area is only qualitatively known and was adopted from Grützner[91]. The colors of the points and their connecting lines in the Figure 29 and Figure 30 correspond to the colors of the apparatuses as depicted in the Figure 26 and Figure 27.

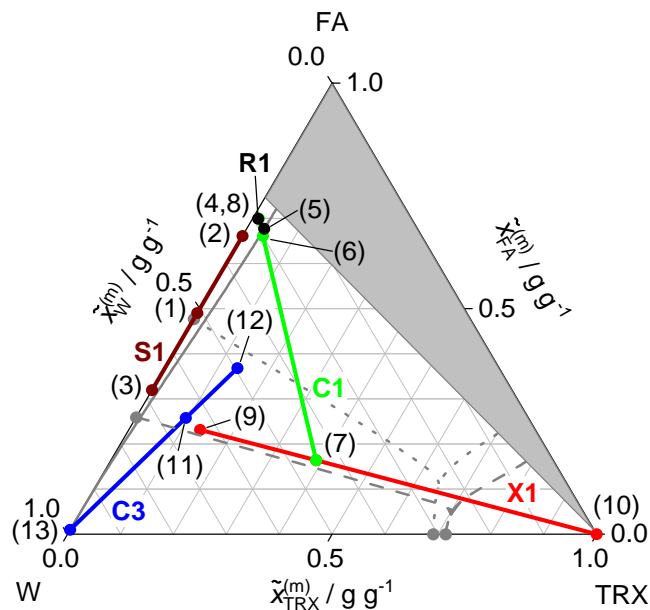


Figure 29: Overview of the compositions of the streams in the new crystallization-based trioxane process depicted in Figure 26. Gray lines represent distillation boundaries at 1 bar (---) and 2.5 bar (.....), and the chemical equilibrium line of the trioxane formation (—) in the reactor R1. The black line represents the change in composition in the reactor R1 (—). Colored lines represent separation cuts of the evaporator S1 (—), the crystallizer X1 (—), and the distillation columns C1 (—) and C3 (—). The stream numbers and colors are the same as in Figure 26. The gray shaded area indicates that the model should not be used at very high formaldehyde-to-water ratios and is only qualitative.

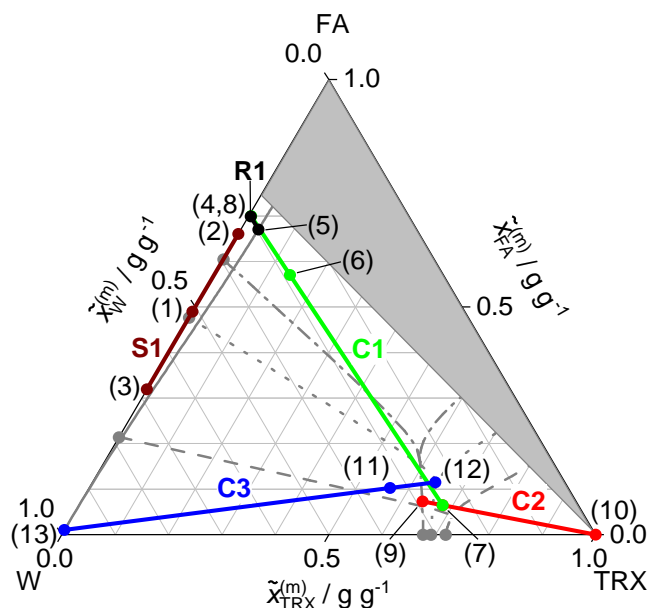


Figure 30: Overview of the compositions of the streams in the pressure swing trioxane process depicted in Figure 27. Gray lines represent distillation boundaries at 0.8 bar (---), 2.5 bar (.....), and 4 bar (-.-.-), and the chemical equilibrium line of the trioxane formation (—) in the reactor R1. The black line represents the change in composition in the reactor R1 (—). Colored lines represent separation cuts of the evaporator S1 (—) and the distillation columns C1 (—), C2 (—), and C3 (—). The stream numbers and colors are the same as in Figure 27. The gray shaded area indicates that the model should not be used at very high formaldehyde-to-water ratios and is only qualitative.

While the compositions in the evaporator and reactor differ only slightly between the CR and PS process, there are significant differences in the subsequent separation train. In both processes, the composition of the bottom product of column C1 (8) is restricted by the risk of solid precipitation (cf. shaded area in Figure 29 and Figure 30). Furthermore, in both processes the purities of the trioxane that is produced (10) and the water that is purged (13) are the same. However, the separation cuts are different, leading to a different length and orientation of the lines representing these cuts in the Figure 29 and Figure 30. The fact that the streams (7) and (9) lie in close vicinity in the PS process (cf. Figure 30) leads to a very high overhead recycle stream (12) in that process, resulting in a high energy demand. In that respect, the situation is completely different for the CR process (cf. Figure 29).

This difference in the size of the recycle streams results in high reboiler duties for the PS process compared to those in the CR process. The corresponding numbers for the heat and cooling duties of the columns in both processes are summarized in Table 14, which also includes information on

the cooling duty of the crystallizer in the CR process. As other heat duties are comparatively small and similar for both processes, they are not considered here; taking into account these heat duties do not significantly change the results.

The total specific reboiler duty is 29.27 MJ kg⁻¹ for the CR process and 50.08 MJ kg⁻¹ for the PS process. The specific reboiler duty is defined as the heat duty per mass of produced trioxane. The total reboiler duty of the PS process is about 70% higher than that of the CR process. The cooling duty of the crystallizer -0.82 MJ kg⁻¹ is small compared to the reboiler duties. Moreover, the cooling duty is required at a moderate temperature of 288 K. The column C2 in the PS process has a heating duty of 10.08 MJ kg⁻¹ and a cooling duty of -9.06 MJ kg⁻¹. The temperature at which heat has to be supplied to column C2 in the process is the highest of all temperatures in both processes (438 K). At the same time, the high temperature at which the cooling duty of column C2 is provided opens up opportunities for heat integration.

Table 14: Specific reboiler and condenser duties of the distillation columns of the crystallization-based (CR) and the pressure swing (PS) trioxane process at the respective temperatures. The specific cooling duty of the crystallizer X1 is $q = -0.82$ MJ kg⁻¹ at the crystallization temperature of 288 K. Specific heat duties are defined as $q = \dot{Q}/\dot{m}^{(10)}$, i.e., as heat duty per mass of the product trioxane.

		reboiler		condenser	
		q MJ kg ⁻¹	T K	q MJ kg ⁻¹	T K
C1	CR	19.82 (10.39 ^a)	373.9	20.00	365.0
	PS	25.46 (1.84 ^a)	368.8	26.24	358.2
C2	PS	10.08	438.4	9.06 (0,0 ^a)	406.3
C3	CR	9.45	400.3	9.43 (0,0 ^a)	394.0
	PS	14.54	400.3	14.56 (0,0 ^a)	390.7
total	CR	29.27 (19.84 ^a)	-	29.43 (20.00 ^a)	-
	PS	50.08 (26.46 ^a)	-	49.86 (26.24 ^a)	-

^arequired external specific heat duty with heat integration

Heat integration is possible in both processes. In the PS process, more than 90 % of the reboiler duty of column C1 can be covered by the condenser duties of the columns C2 and C3. In the CR process, the condenser of column C3 can cover about 50 % of the reboiler duty of column C1. The temperature difference that is available for the heat transfer is larger than 20 K in all cases. With these heat integration measures, the overall specific energy demand of the CR process can be reduced to 19.84 MJ kg⁻¹ and that of the PS process to 26.46 MJ kg⁻¹. Figure 31 summarizes the findings regarding the heat duties. The results for the total heat duties of the PS and the CR process for the cases with and without heat integration are shown. For the CR process, also the cooling

duty is reported. The substantial reduction of the reboiler duty in the CR process compared to the PS process is clearly illustrated, as well as the fact that the crystallizer cooling duty is only small.

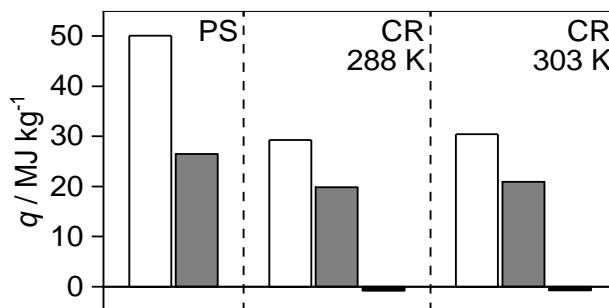


Figure 31: Influence of heat integration and crystallization temperature on the specific energy demand of the crystallization-based (CR) and the pressure swing (PS) trioxane process. Results for crystallization temperatures of 288 K and 303~K are shown. Bars are labeled as follows: sum of specific reboiler duties of all columns without heat integration (□) and with heat integration (■), and specific cooling duty of the crystallizer (■). Specific heat duties are defined as $q = \dot{Q}/\dot{m}^{(10)}$.

In Figure 31, additionally the energy demand of the CR process with a crystallization temperature of 303 K is shown. At this temperature, the cooling can be accomplished simply by using river water in temperate climate zones. This leads to a slightly lower yield of solid trioxane in the crystallizer, cf. Figure 28, and therefore to slightly larger recycle streams (9), (11), and (12). This, in turn, leads to an increase of the heat duties of columns C1 and C3 of only 4 % without heat integration and 5 % with heat integration. This operation point could be attractive, as the slightly higher heat duties might be compensated by the thereby not required refrigerator system for supplying chilled water. However, as already mentioned for these cases the correlation of the solid-liquid equilibria has to be extrapolated.

It will not be discussed the realization of the consequences of the conceptual design for the apparatus design. It has only to be mentioned that the large recycle streams lead to high costs of the corresponding equipment, e.g., large column diameters. The difference in the energy demand can be diminished by the heat integration measures, but they produce additional effort regarding equipment. All this is disadvantageous for the PS process and may lead to favoring the CR process, which basically only has the drawback of the complex equipment needed for the crystallization step. However, a discussion of costs is beyond the scope of this work.

4.1.5.2 Discussion of process alternatives

In the following, some alternative designs of crystallization-based trioxane production processes are discussed. The stream numbers and apparatus labels used in the discussion refer to Figure 26.

The first option that is discussed here is to replace the concentration step carried out in the distillation column C1 by a crystallization. The trioxane concentration in the reactor product (5) is very low, and the formaldehyde concentration is still high. Under these conditions, a crystallization does not yield pure trioxane but formaldehyde solid. In principle, the solid could be separated and recycled to the reactor, while the liquor could be sent to the separation train. But this seems hardly attractive considering the kinetic problems connected to obtaining solid formaldehyde oligomers and their difficult handling, especially as the recycle stream is large compared to the trioxane-rich stream. In contrast, the well-established distillation in column C1 poses no special problems, the large recycle stream is the bottom product and only the small trioxane-rich top product has to be evaporated.

In principle, one could also try to replace the column C3, in which the water is removed, by a crystallization. However, this would require a water-rich feed, from which pure water would crystallize. It is not trivial to obtain such a feed in the process, and even if this would succeed without prohibitively large recycle streams, the temperature required for that crystallization would be well below 273 K, which makes this option hardly attractive.

Last not least, one could consider obtaining additional trioxane from a crystallization of the top product of the water removal column C3 (12). This could be possible but would require a second crystallizer, which would have to be operated at a much lower temperature than the first one and would yield only small amounts of trioxane, which makes also this alternative unattractive.

4.1.6 Conclusions

A conceptual design of a new process for the production of trioxane is described. The new process uses a combination of distillation and crystallization to obtain pure trioxane after the reaction step. In contrast to established processes, the new process does not rely on auxiliary chemicals or energy-intensive pressure swing distillation. A comparison of the simulation results revealed that the energy demand of the new process is significantly lower than for the state-of-the-art pressure swing process. The simulations of the present study were carried out with a focus on enabling a fair comparison of the new crystallization-based process with the pressure swing process. This leaves ample room for a further optimization of the new promising process. For the full exploitability of the optimization potential, a consistent physico-chemical modeling of the formation of trioxane and the solid-liquid equilibria in the system (formaldehyde + water +

trioxane) would be of interest. As a basis for this, a comprehensive investigation of the solid-liquid equilibria in the mentioned system should be carried out.

4.2 OME production process

4.2.1 Introduction

As already described in Chapter 1 and 3, using DME instead of MAL as feedstock is a promising alternative for OME production by the anhydrous route. Haltenort et al.[75] demonstrated the feasibility of the acid-catalyzed reaction of dimethyl ether and trioxane into OME. In the patent literature, however, Ströfer et al.[76] describe a process for the production of OME from dimethyl ether and trioxane. In the present work, the process of Ströfer et al.[76] is evaluated in detail to provide a basis for the assessment of this production pathway in contrast to the routes mentioned in the introduction. A simulation-based design and optimization of the process was carried out using two process models of different model depth. To the start of the work on this conceptual design process no data was available on the equilibrium of the reaction, as the first data were collected in the course of subsequent work. Therefore, a assessment of this production route was done based on estimations before the extensive study on the equilibrium was started (cf. Chapter 3)

4.2.2 Process concept

A flowsheet of the OME production process from dimethyl ether and trioxane, as described by Ströfer et al.[31], is shown in Figure 32.

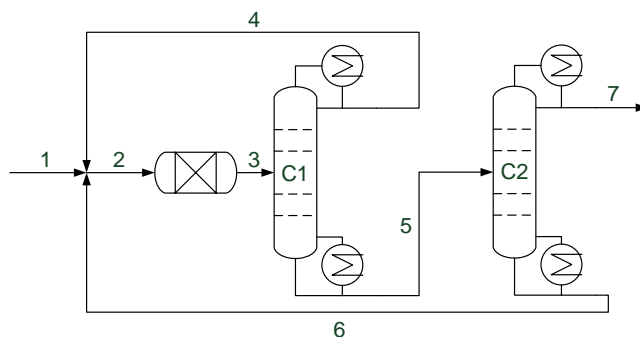


Figure 32: Flowsheet of the OME production process from dimethyl ether and trioxane [76].

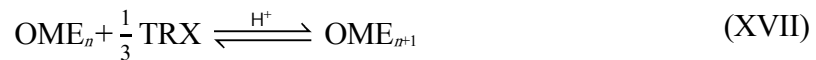
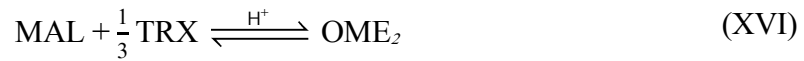
A stream of dimethyl ether and trioxane (stream 1) is mixed with two recycle streams 4 and 6. This mixed stream 2 enters the reactor containing a heterogeneous acidic catalyst. The reactor

outlet (stream 3) enters the distillation column C1. This column separates dimethyl ether, methylal, OME₂, formaldehyde, and trioxane as overhead product (stream 4), from the OME of chain length $n \geq 3$. In the distillation column C2 stream 5 is separated into the product fraction of OME with $n = 3 - 5$ (stream 7) and the heavy-boiling fraction of OME with $n \geq 6$ (stream 6). Stream 4 and stream 6 are recycled back to the reactor. This is possible, because all reactions in the present system are reversible, see Chapter 3.2

4.2.3 Chemical model

4.2.3.1 Chemical reactions

As described in Chapter 3.2 OME is formed from DME and Trioxane according to Reactions (VII) to (X). Reactions (XV) to (XVII) describe an alternative mechanism of the chain growth by direct reaction of OME with trioxane. Since in this chapter, only the chemical equilibrium and not the kinetics are considered, it is irrelevant for the calculations which of the two mechanisms are assumed. All reactions are catalyzed by acids and are reversible equilibrium reactions.



4.2.3.2 Chemical equilibrium constants

The equilibrium is modeled with equilibrium constants K_j based on mole fractions (x), cf. Equations (21) to (27). Therein, the subscript j denotes the reaction number.

$$K_{(\text{VIII})} = \frac{x_{\text{FA}}^3}{x_{\text{TRX}}} \quad (21)$$

$$K_{(\text{VII})} = \frac{x_{\text{MAL}}}{x_{\text{DME}} \cdot x_{\text{FA}}} \quad (22)$$

$$K_{(\text{IX})} = \frac{x_{\text{OME}_2}}{x_{\text{MAL}} \cdot x_{\text{FA}}} \quad (23)$$

$$K_{(\text{X})} = \frac{x_{\text{OME}_{n+1}}}{x_{\text{OME}_n} \cdot x_{\text{FA}}} \quad (24)$$

$$K_{(XV)} = \frac{x_{MAL}}{x_{DME} \cdot x_{TRX}^{\frac{1}{3}}} \quad (25)$$

$$K_{(XVI)} = \frac{x_{OME_2}}{x_{MAL} \cdot x_{TRX}^{\frac{1}{3}}} \quad (26)$$

$$K_{(XVII)} = \frac{x_{OME_{n+1}}}{x_{OME_n} \cdot x_{TRX}^{\frac{1}{3}}} \quad (27)$$

The equilibrium constants for Reactions (IX) and (X), respectively Reactions (XVI) and (XVII) are simplified in literature to one constant [58,77]. The temperature dependency of the chemical equilibrium constant is described by Equation (28).

$$\ln(K_j) = a_j + \frac{b_j}{(T/K)} \quad (28)$$

The Reactions (XV) to (XVII) are linear dependent on the Reactions (VII) to (X). In this work for the description of the chemical equilibrium in the reactor, Reactions (VII) to (X) are used. The equilibrium constant $K_{(VIII)}$ is reported by Burger et al.[77]. Therein, the constant $K_{(VIII)}$ is only given with high uncertainty because of the difficult measurement of monomeric formaldehyde concentration. Therefore, the literature value of $K_{(VIII)}$ is not used in the present work. The constant $K_{(VII)}$ is not reported in the literature. The constants $K_{(IX)}$ and $K_{(X)}$ are reported by Schmitz et al.[58] and adopted in the present work. The constants $K_{(VIII)}$ and $K_{(VII)}$ are calculated from three other constants via Equations (29) and (30).

$$K_{(VIII)} = \left(\frac{K_{(XVII)}}{K_{(X)}} \right)^3 \quad (29)$$

$$K_{(VII)} = \frac{K_{(XV)}}{K_{(VIII)}^{\frac{1}{3}}} \quad (30)$$

Equation (29) is obtained by dividing Equation (27) by Equation (24) to the power of three and comparing with Equation (21). Equation (30) is obtained by dividing Equation (25) by Equation (21) to the power of one third and comparing with Equation (22). The constants $K_{(XVI)}$ and $K_{(XVII)}$ are reported by Burger et al.[77] and adopted in the present work. The missing constant $K_{(XV)}$ is estimated from the Gibbs energy of formation of dimethyl ether, trioxane and methylal using the data for the standard state presented in Table 15 and the data for heat capacities in

Table 16. The pressure dependency of the enthalpy and entropy is neglected as a liquid phase reaction is studied. Constant $K_{(XV)}$ is calculated for various temperatures in the range 298.15 - 353.15 K. The results are regressed with Equation (28). The calculation is described in detail in the Appendix C.2.1. A comparison of the estimated constant $K_{(VII)}$ with the constant for the OME formation $K_{(IX)}$ is shown in Figure 33. The reaction enthalpy for the formation of methylal

from dimethyl ether and formaldehyde is $18.25 \text{ kJ mol}^{-1}$. This is slightly less than the reaction enthalpy of Reaction (IX) respectively (X).

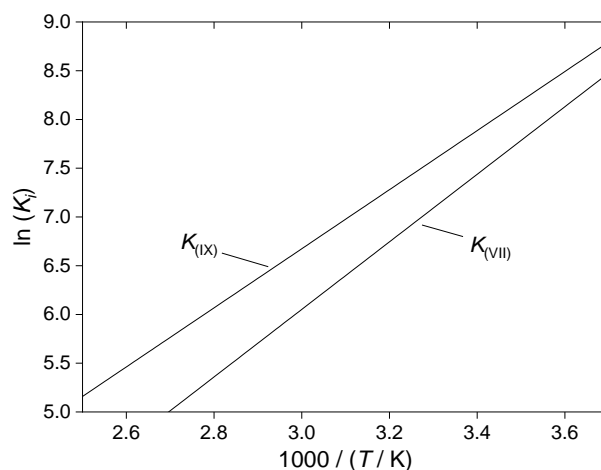


Figure 33: Molar equilibrium constants of the formation of methylal from formaldehyde and dimethyl ether ($K_{(VII)}$) and the constant for the formation of OME₂ from methylal and formaldehyde ($K_{(IX)}$) in a logarithmic plot over the inverse temperature.

Table 15: Standard enthalpy and entropy of formation, enthalpy and entropy of vaporization, enthalpy and entropy of fusion at 298.15 K and 1 bar used in the estimation of the present work [72].

Component i	DME	TRX	MAL
standard state	gas	solid	liquid
$h_i^\theta / \text{kJ mol}^{-1}$	-184.0	-522.5	-378.2
$\Delta h_{\text{vap},i}^\theta / \text{kJ mol}^{-1}$	18.63	-	-
$\Delta h_{\text{fus},i}^\theta / \text{kJ mol}^{-1}$	-	14.62 ^a	-
$s_i^\theta / \text{J mol}^{-1}\text{K}^{-1}$	266	129.1	244
$\Delta s_{\text{vap},i}^\theta / \text{J mol}^{-1}\text{K}^{-1}$	62.48	-	-
$\Delta s_{\text{fus},i}^\theta / \text{J mol}^{-1}\text{K}^{-1}$	-	49.04	-

^(a) value adopted from melting point

Table 16: Parameters of the correlation of the liquid molar heat capacity $c_{p,i}^{\text{liq}}$ ($c_{p,i}^{\text{liq}}(T) / (\text{kJ mol}^{-1} \text{K}^{-1}) = A_i + B_i \cdot (T/\text{K}) + C_i \cdot (T/\text{K})^2$)[72].

Component i	A_i	B_i	C_i
DME	110100	-157.47	0.51853
TRX	94990	-60.319	0.68234
MAL	156280	-189.65	0.69486

The parameters a_j and b_j for the calculation of the chemical equilibrium constants for all reactions are given in Table 17.

Table 17: Parameters for the correlation of the equilibrium constants K_j for the reactions according to Equation (28).

Reaction	a_j	b_j	ref.
(VIII)	6.436	-8197.8	this work
(VII)	-4.341	3464.3	this work
(IX)	-2.415	3029.6	[58]
(X)	-2.415	3029.6	[58]
(XV)	-6.587	2195.1	this work
(XVI)	-0.2699	297	[77]
(XVII)	-0.2699	297	[77]

4.2.4 Physical property model

4.2.4.1 Pure component properties

The pure component properties required for the simulation are the vapor pressure, the enthalpy of vaporization, the ideal gas heat capacity at constant pressure, and the liquid molar density. The correlations for the pure component properties, except for dimethyl ether, are taken from Burger et al. [29]. The correlations for dimethyl ether are taken from DIPPR [72].

4.2.4.2 Vapor-liquid equilibrium

The vapor-liquid equilibrium in the system (formaldehyde + trioxane + dimethyl ether + OME_n) is calculated with the extended Raoult's law. For the description of the non-ideality in the liquid phase a UNIFAC-based model is used as described by Schmitz et al.[60]. These authors did, however, not consider dimethyl ether and trioxane. Albert et al.[114] modeled trioxane as one

structural group in the UNIFAC model. The volume- and surface-parameters of that group and its interaction parameters with the group formaldehyde are adopted from Albert et al.[114]. The interaction-parameters with the groups describing methylal and OME_n are set to zero. Further, dimethyl ether is also modeled as one structural group in the present work. The volume- and surface-parameters are adopted from Sundberg et al.[115]. The interaction parameters of the dimethyl ether group are set equal to those of methylal. The interaction-parameters between methylal and dimethyl ether are set to zero. All values are given in Appendix C.2.2.

4.2.5 Process design

4.2.5.1 Implementation

The physical-property model was implemented into the equation-oriented flowsheet simulation tool Chemasim, an in-house tool of BASF. The distillation columns are simulated using the equilibrium-stage model. The process design is carried out using process simulation and optimization with two models of varying model depth. This hierarchical design method is adopted from the work of Burger et al.[116]. The two different process models are described in the following.

4.2.5.2 ∞/∞ model of the process

For the reactor it is assumed, that chemical equilibrium is reached. The two columns C1 and C2 are assumed to have an infinite number of stages (N) and an infinite reflux ratio (R). This enables sharp separations only constrained by distillation boundaries and mass balances [117]. In the system of the present chapter, there are no distillation boundaries and the top and bottom products can be gained in arbitrary purity as long as the boiling sequence is considered.

4.2.5.3 Design with an ∞/∞ model

Due to the simplifying assumptions of the ∞/∞ model, only five design parameters need to be specified. The reactor temperature is set to 353.15 K. It is expected that at this temperature the formation of side products, such as methyl formate, is suppressed [77]. Further, the influence of the temperature on the compositions in chemical equilibrium is small [58,77]. Because all results scale linearly with the mass flow of the feed stream, it is set arbitrarily to 10 kg s^{-1} . The distillate-to-feed ratios of the columns C1 and C2 are specified with the sharp separation described above in the process concept.

The only degree of freedom left is the mass fraction of dimethyl ether $x_{\text{DME}}^{(m)}$ in the feed stream. The ∞/∞ model gives no information on the energy demand and the size of the equipment of the OME process. Therefore, here the mass flows of the recycle streams 4 and 6 are defined as objectives to be minimized. These two flows are conflicting objectives. By varying the mass fraction of dimethyl ether in the feed stream, the Pareto front representing the set of best compromises, is calculated. On the Pareto front, a decrease in one recycle mass flow can only be achieved by an increase of the other recycle mass flow. More details on Pareto optimization and its application to process engineering are given in the work of Bortz et al.[118]. The Pareto front is shown in Figure 34.

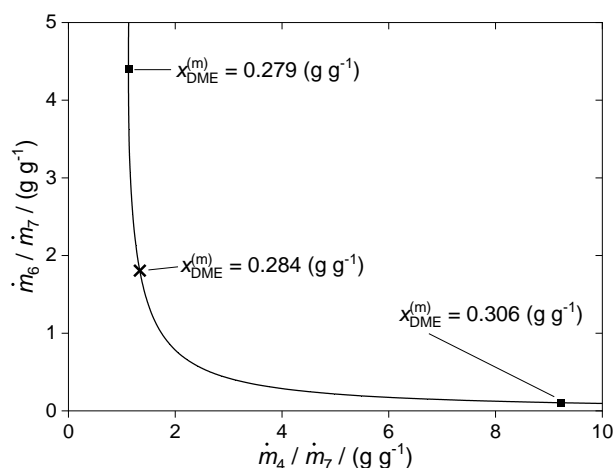


Figure 34: Pareto front for the objectives mass flow of recycle stream 6 and mass flow of recycle stream 4, normalized with the mass flow of stream 7 (product). The operating point (\times) is assumed to be a good compromise between the two objectives.

Figure 34 contains also an operating point. It is assumed to be a good compromise between the two goals in which the objective of minimizing the overhead recycle stream is prioritized. The corresponding mass fraction of dimethyl ether in the feed stream is 0.283 g g^{-1} and was fixed for the subsequent optimization of the OME process using a more detailed process model.

4.2.5.4 Detailed process model

The reduced model gives no information on properties such as the heat duties (\dot{Q}), reflux ratios or stage numbers. To obtain this information, the process is modeled in more detail. As no information on the kinetics of the chemical reactions in the present system is available, the reactor outlet is still assumed to be in the chemical equilibrium. The temperature of the feed stream is set to 335.15 K, the melting temperature of trioxane, to have a liquid stream. In the detailed process

model, the distillation columns have finite number of stages and reflux ratios. For each distillation column the following design parameters have to be specified in the simulations: columns pressure, number of stages in rectifying and stripping section, and two further specifications (e.g. purities or reflux ratio). The design procedure to set these specifications is described in the following.

The pressure of column C1 is specified such that the condenser temperature is 313 K. At this temperature cooling water can be used throughout the year. The pressure of column C2 is set to 50 mbar to minimize thermal OME decomposition in the bottom. Lower pressures were not used to avoid a further increase of the volumetric flow rate of the gas in the column. One specification per column is given by the product specifications, which were adopted from the work of Burger et al.[23]: In the product stream 7, the sum of the mass fractions of OME with $n \leq 2$ and trioxane is set to 0.0005 g g^{-1} and the sum of the mass fractions of OME with chain length $n \geq 6$ is set to 0.0095 g g^{-1} . Furthermore, the recycle ratios of OME₃ and that of OME₅ are used as design parameters. The recycle ratio of OME₃ is defined as the ratio between the component mass flow of OME₃ in stream 4 and the component mass flow of OME₃ in the feed of column C1 (stream 3) ($\dot{m}_{\text{OME}_3,4} / \dot{m}_{\text{OME}_3,3}$). The recycle ratio of OME₅ is defined as the component mass flow of OME₅ in stream 6 divided by the component mass flow of OME₅ in stream 5 ($\dot{m}_{\text{OME}_5,6} / \dot{m}_{\text{OME}_5,5}$). Both ratios as well as the stage numbers of the columns are used as optimization parameters. These four optimization parameters are varied to minimize the sum of heat duties in the reboilers of the columns. For the optimization the following strategy was selected:

1. The process was simulated with $N=30$ for both columns and the feed stages were set on stage 15 (counting from the bottom).
2. The recycle ratios of OME₃ and OME₅ were simultaneously optimized to minimize the sum of the reboiler duties of both columns.
3. A N, \dot{Q} -study as described by Zeck[119] was performed for columns C1 and C2. The resulting N, \dot{Q} -curves are presented in Figure 35. The number of stages corresponding to 1.2 times the minimum reboiler duty, with two additional stages as safety margin, was selected as design for the columns. The optimal feed stages were taken from the N, \dot{Q} -study.

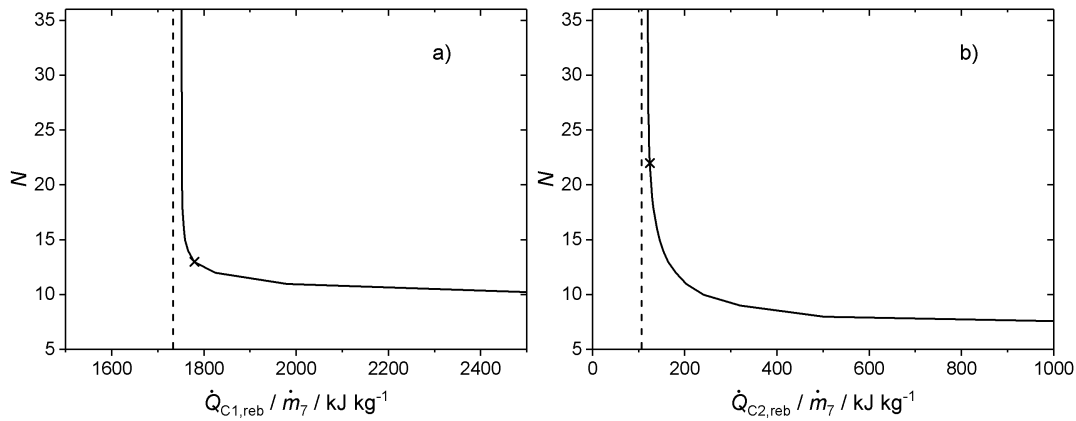


Figure 35: N, Q -curves showing the Trade-off between number of stages and reboiler duty for a) C1 and b) C2. \times : design point. $--$: minimum reboiler duty.

4. Step 2 was repeated.

Further iterations showed no significant changes of the results. The specifications of the process are given in Table 18. The resulting parameters of the columns C1 and C2 are presented in

Table 19. A stream table of the whole process is presented in Table 20.

Table 18: Specifications for the process given in Figure 32. The reactor temperature is always 353.15 K and the mass flow of the feed stream 10 kg s⁻¹.

Model	Process specification	Value
∞/∞ model	$x_{1,DME}^{(m)}$	varied / g g ⁻¹
Detailed model	$x_{1,DME}^{(m)}$	0.284 g g ⁻¹
	T_1	353.15 K
	$x_{7,OME2}^{(m)} + x_{7,TRX}^{(m)}$	0.0005 g g ⁻¹
	$x_{7,OMEn>5}^{(m)}$	0.0095 g g ⁻¹
	$T_{C1,cond}$	313.15 K
	p_{c2}	50 mbar
	$\dot{m}_{OME3,4} / \dot{m}_{OME3,3}$	varied / g g ⁻¹
$\dot{m}_{OME5,6} / \dot{m}_{OME5,5}$	varied / g g ⁻¹	

Table 19: Operating parameters for the columns C1 and C2 using the detailed process model. Heat flows are normalized by dividing by the mass flow of the product stream \dot{m}_7 .

Column	C1	C2
N	13	22
N_{feed}	12	15
$\dot{m}_{\text{OME}_{3,4}} / \dot{m}_{\text{OME}_{3,3}}$	0.1141 g g ⁻¹	-
$\dot{m}_{\text{OME}_{5,6}} / \dot{m}_{\text{OME}_{5,5}}$	-	0.003 g g ⁻¹
R	0.015	1.367
$\dot{Q}_{\text{cond}} / \dot{m}_7$	846 kJ kg ⁻¹	879 kJ kg ⁻¹
$\dot{Q}_{\text{reb}} / \dot{m}_7$	1749 kJ kg ⁻¹	121 kJ kg ⁻¹
p	4.86 bar	0.05 bar

Table 20: Stream table of the process given in Figure 32, simulated with the detailed process model. Mass flows are normalized with the mass flow of the product stream 7.

Stream	1	2	3	4	5	6	7
T / K	335.15	363.73	353.15	313.15	572.48	476.43	360.60
\dot{m} / \dot{m}_7	1.000	4.043	4.043	1.660	2.383	1.383	1.000
	mass fraction / g g ⁻¹						
FA	0.0000	0.0004	0.0004	0.0010	0.0000	0.0000	0.0000
DME	0.2840	0.2175	0.1472	0.3586	0.0000	0.0000	0.0000
TRX	0.7160	0.2386	0.0615	0.1498	0.0000	0.0000	0.0000
MAL	0.0000	0.0918	0.0918	0.2236	0.0000	0.0000	0.0000
OME ₂	0.0000	0.0967	0.0968	0.2355	0.0002	0.0000	0.0005
OME ₃	0.0000	0.0107	0.0939	0.0261	0.1412	0.0000	0.3364
OME ₄	0.0000	0.0018	0.0867	0.0045	0.1440	0.0000	0.3430
OME ₅	0.0000	0.0006	0.0774	0.0008	0.1307	0.0007	0.3106
OME ₆	0.0000	0.0651	0.0675	0.0001	0.1144	0.1902	0.0095
OME ₇	0.0000	0.0578	0.0578	0.0000	0.0980	0.1689	0.0000
OME ₈	0.0000	0.0488	0.0488	0.0000	0.0828	0.1427	0.0000
OME ₉	0.0000	0.0408	0.0408	0.0000	0.0692	0.1192	0.0000
OME ₁₀	0.0000	0.0338	0.0338	0.0000	0.0573	0.0987	0.0000
OME ₁₁	0.0000	0.0277	0.0277	0.0000	0.0471	0.0811	0.0000
OME ₁₂	0.0000	0.0226	0.0226	0.0000	0.0384	0.0662	0.0000
OME ₁₃	0.0000	0.0184	0.0184	0.0000	0.0312	0.0538	0.0000
OME ₁₄	0.0000	0.0149	0.0149	0.0000	0.0252	0.0435	0.0000
OME _{≥15}	0.0000	0.0120	0.0120	0.0000	0.0203	0.0350	0.0000

4.2.6 Discussion

The results obtained with the detailed process model show that the reboiler duty of column C1 is about 15 times that of column C2, although the heat duty of the condenser is nearly the same. This is caused by the large pressure difference between the two columns. The feed stream of column C2 is overheated and only little additional energy is needed. The total heat requirement per kg product is 1870 kJ kg^{-1} , which is 40 % higher than the number reported by Burger et al.[29] for Route B with the same product specifications. This is mainly caused by the large amount of dimethyl ether that has to be recycled in the present process. The number of stages of the columns is similar in both processes. The higher energy costs of the present process may be compensated as dimethyl ether is cheaper than methylal.

The above results should be used with caution. They are based on an estimation of the chemical equilibrium of the methylal formation from dimethyl ether. The simulation results are quite sensitive to the value of that equilibrium constant: e.g. an increase of the equilibrium constant $K_{(VII)}$ by 12.7 % decreases the size of both recycle streams by 15.2 %. With the results from Chapter 3, the missing data on the equilibrium constant of the MAL formation from DME $K_{(VII)}$ is now available. It is around 6.7 times higher than the estimated value at 353 K. We have refrained from repeating the conceptual design with the new value, as the experiments from Chapter 3 have also shown that an important formation of side products MAL must be expected, which has to be considered in the design. It was out of the scope of the thesis, to carry out this new design.

4.2.7 Conclusion

This chapter presents a closed material and energy balance of the OME production process from trioxane and dimethyl ether. Based on thermodynamic estimations of unknown chemical equilibrium constants, the OME production process described by Ströfer et al.[76] was simulated and optimized. The results show that this synthesis route can be an interesting alternative to the OME production from methylal and trioxane, which is conceptually similar to the process simulated in the present work. The energy demand for this process is higher than for the methylal process, but the reactant dimethyl ether is cheaper than methylal. The chemical equilibrium constant of the formation of methylal from dimethyl ether and trioxane was estimated here from the free energies of the pure components in the standard state. As the process performance depends strongly on this equilibrium constant, the experimental studies described in Chapter 3 were carried out. The simulation of the process was not repeated based on the new experimental data, as the experiments show also a strong formation of methyl formate. Therefore, the whole process has to be redesigned considering the separation of methyl formate, which was behind the scope of this thesis.

5 Application of OME as fuel

5.1 Introduction

As already mentioned, the use of synthetic fuels produced from renewable resources can make a significant contribution to moving away from fossil fuels and, thus, to reduce greenhouse gas emissions [15,120–122]. Two particularly interesting synthetic fuels are OME and hydrogenated vegetable oils (HVO).

Hydrogenated vegetable oils, HVO, are produced from triglyceride acids obtained from plants such as oilseed rape, and are often designated simply as “oils”. HVO contain mainly n-alkanes, but also some branched alkanes, with C-numbers typically between 15 and 20, but basically no sulfur, nitrogen, or aromatics [15,123–126]. HVO have similar physical properties as fossil diesel, but higher cetane numbers and lower toxic emissions [127,128]. It can be used directly as a diesel substitute without any modification of the engine. Only at low temperatures, the high viscosity can cause problems in some cases [128].

HVO are already produced on a large scale, whereas there are only a few facilities for OME production. The use of blends of (OME + HVO) is of great interest for a market launch of OME [12,14,15].

One problem with the application of blends of (OME + HVO) is the miscibility [23,122,129–131]. HVO are non-polar, while OME are moderately polar, due to the oxygen in the backbone. This can induce a miscibility gap in mixtures of (OME + HVO), which, however, is typically not large and can be avoided by a suitable choice of the composition. This is mandatory for the application as fuels, where homogeneity of the fluid is required. However, it is known that initially homogenous mixtures of (OME + HVO) show a liquid-liquid phase split after some time in many technical applications. Typically, not only a small amount of the second phase is formed, but the amounts of both phases can be of the same order of magnitude, with one phase being OME-rich and the other HVO-rich. Only qualitative information on this phenomenon is available in the literature [23,122,129–131] and its reasons are not fully understood. A hypothesis is that the initially homogenous (OME + HVO) mixture takes up small amounts of water from the air, which induces the phase split – however not by forming a (small) second water-rich phase, but by leading to a separation of OME and HVO.

This phenomenon was studied in the present work by phase equilibrium experiments, in which liquid-liquid equilibria (LLE), as well as liquid-liquid-liquid equilibria (LLLE), were measured,

and by accompanying modeling and simulation. A challenge in designing such study is that both HVO and technical OME are mixtures. The composition of HVO depend on the raw material and production process, and also the composition of technical OME varies. Therefore, it was decided to carry out experiments with model components. Two OME were used: OME₄ because it is in the middle of the typical range of OME_n components in OME-fuels (OME₃ – OME₅). Additionally, OME₂ was also included in the study, to get information on the influence of the chain length of the OME_n on the results. Longer OME_n were not used, as they were not available in sufficient amounts as pure components. As model component for HVO, n-hexadecane was used. Also here, the influence of the chain length on the results was investigated by including n-dodecane in the study. Longer n-alkanes were not studied to avoid experimental problems with solid-precipitation at room temperature. Hence, LLE and LLLE in well-defined binary and ternary mixtures of the type (OME_n + n-alkane + water) were studied.

Additionally, also an OME-mixture, as it is used in fuels, was included in the study. Furthermore, also mixtures containing toluene were investigated, to see whether problems with de-mixing could also occur in mixtures of OME with fossil diesel fuel, which contains considerable amounts of aromatic hydrocarbons, in contrast to HVO.

There are only few studies in the literature on LLE in the systems that are of interest here, Table 21 gives an overview.

Table 21: Overview of experimental studies of LLE in systems that are related to the ones studied in the present work.

system	source
OME _n + water	Schmitz et al.[60]
n-alkanes + water	Mokbel et al.[132]
n-alkanes + water	Sutton et al.[133]
OME _n + n-hexane + water	Zhuang et al.[134]
OME ₃ + (n-heptane, p-xylene, toluene) + water	Shi et al.[135,136]
OME ₁ + (cyclohexane, n-heptane) + water	Shi et al.[136]
OME _n + o-xylene + water	Li et al.[137]
OME _n + toluene + water	Li et al.[138]

Modeling LLE in mixtures containing small, highly polar components, such as water, and large unpolar or weakly polar components (as the n-alkanes and OME studied here) is challenging. Two options were tried: modeling with molecular equations of state (EOS), namely PC-SAFT [139,140], and modeling with UNIFAC [141], a group-contribution model of the Gibbs excess energy. The latter is distinctly simpler and, as preliminary tests with PC-SAFT indicated no advantages, it was continued only with UNIFAC, and it is reported here on the results, which were

obtained with this method. The UNIFAC model enables predictions of the complex phase behavior of the studied ternary systems, some of which show not only LLE but also liquid-liquid-liquid equilibria (LLE).

There are only two modeling and simulation studies of related systems in the literature, in which, however, other models were used. Recently, Yang et al.[142] carried out a simulation study on the miscibility of OME_n with model components of diesel fuel using the COSMO-RS method [143]. Yu et al.[144] investigated the miscibility of OME with diesel fuel components using molecular dynamics simulations.

5.2 Experimental apparatus and procedure

5.2.1 Chemicals

OME₂ and OME₄ were provided by BASF SE with a purity of 0.985 g g⁻¹. The OME-mixture was provided by ASG Analytik-Service. The OME-mixture comprised OME₃ (0.58 g g⁻¹), OME₄ (0.27 g g⁻¹), OME₅ (0.11 g g⁻¹), and OME₆ (0.04 g g⁻¹). n-dodecane (C12), purity > 0.99 g g⁻¹, was purchased from ThermoFisher. n-hexadecane (C16), purity > 0.99 g g⁻¹, and toluene (Tol), purity > 0.998 g g⁻¹, were purchased from Merck. The purified water (specific resistance > 15 MΩ cm⁻¹) was prepared with a Milli-Q system from Merck Millipore.

5.2.2 Phase equilibrium measurements

For the measurement of LLE, feed mixtures of different compositions were prepared from the pure components, except for the feed mixtures with low water fraction, for which not pure water but OME was used that was saturated with water at 293 K. Where appropriate, OME was dried with molecular sieve (3A) before use. For the preparation of the feed mixtures, an analytical balance (AG 204, Mettler Toledo) was used and the composition was calculated based on the masses of the pure substances.

For the measurements at 293 K, 20 g of the feed mixture was filled into a glass vial which contained a magnetic stir bar, and was closed with a septum cap. The closed vial was stored in an air-thermostatted cabinet on a magnetic stir plate. The mixture was stirred for at least 24 hours. Then, the stirrer was turned off and the phases were allowed to settle for at least 48 hours. Subsequently, samples of the different phases were taken with syringes through the septum. Before use, the syringes were dried in an exsiccator that was filled with dried molecular sieve for at least 48 hours. The temperature was measured in the cabinet with a calibrated platinum resistance thermometer. In preliminary experiments, in which the temperature was also measured in a vial, the maximal

temperature difference between the air and the vial was measured. The overall uncertainty of the reported temperature in the vial is estimated to be 0.1 K.

For the measurements at 278 and 265 K, 40 g of the feed mixture was filled into a glass vial with a cooling jacket, which, in turn, was isolated from the surroundings by a vacuum jacket. The vial was equipped with a magnetic stir bar. The cooling medium was a mixture of water and mono ethylene glycol and was thermostatted with a cryostat. The temperature inside the vial was measured with a platinum resistance thermometer (uncertainty of 0.1 K). The times for mixing and settling were the same as in the measurements at 293 K. After the settling period samples from the different phases were taken through septa which are located at different heights of the vial. For the sampling dried syringes were used.

All experiments were carried out at ambient pressure ($1 \text{ bar} \pm 0,05 \text{ bar}$); as only equilibria with liquid phases were studied variations of the pressure have no significant influence on the results. This could, however, be different for the pressures used in injection systems in diesel engines, which can be more than 1000 bar.

5.2.3 Chemical analysis

Only the samples from the coexisting phases were analyzed. The composition of the feed was known from the gravimetric preparation. The uncertainty of the feed composition is better than 0.001 g g^{-1} .

All samples were first analyzed with quantitative ^1H -nuclear magnetic resonance (NMR) spectroscopy to determine the concentrations of OME, water, and the hydrocarbons. The equipment was the same as described in Chapter 3.3.5. The acquisition parameters were the following: flip angle: 90° , acquisition time: 4 s, repetition time: 20 s, 8 scans, and 65 k data points. The peak assignment was done in preliminary studies based on experiments with pure components and mixtures. For the evaluation of the spectra, the software MestReNova 14.2 was used and it was assumed that the proportionality constant relating the peak area to the amount of substance is the same for all peaks. Sample spectra and the peak assignment are reported in the Appendix D.1. Results from test measurements with samples that were prepared gravimetrically showed that the uncertainty for the results for the concentrations of the different components do not exceed $0.01 \text{ mol mol}^{-1}$. For the measurements with the OME-mixture, additionally ^{13}C NMR spectroscopy was used to avoid problems with peak overlaps. The procedure is the same as in Chapter 3.3.5. For samples with water-contents below 0.1 g g^{-1} , additionally, Karl-Fischer titration was used to determine the water concentration (for mass fractions in the range of 0.1 to 0.005 g g^{-1} volumetric Karl-Fischer titration and below 0.005 g g^{-1} coulometric Karl-Fischer titration). Each titration was carried out at least three times and the mean value was used as the result. The uncertainty of the

Karl-Fischer titration results for the water concentration is estimated to be 80 ppm for the coulometric titration and 0.001 g g⁻¹ for volumetric titration, based on experiments with gravimetrically prepared samples. Further information on the Karl-Fischer titration is given in the Appendix D.2. When Karl-Fischer titration results were available, they were used and the results were discarded.

5.3 Modeling

The phase equilibria were calculated using the isoactivity criterion in Equation (31) which is given here for LLLE.

$$x_i' \cdot \gamma_i' = x_i'' \cdot \gamma_i'' = x_i''' \cdot \gamma_i''', i = 1 \dots N \quad (31)$$

Therein is x_i the mole fraction of component i and γ_i the corresponding activity coefficient; N is the number of components in the mixture and the primes refer to the phases. The activity coefficient was calculated with the group contribution model UNIFAC with parameters from Schmitz et al.[56], or, where this was not possible, from the original UNIFAC model [112]. Furthermore, group interaction parameters representing interactions between groups in OME and in hydrocarbons were fitted to experimental results from the present work. Details on the parameterization are reported in the Appendix D.3. The split of the considered components into UNIFAC groups is reported in Table 22, the group parameters and the interaction parameters in Table 23. Table 22 and Table 23 also contain detailed information on the source of all parameters. As the activity coefficients calculated with UNIFAC depend only on a temperature and composition, the model does not account for the pressure.

Table 22: Group assignment and size and surface parameters of the groups for the UNIFAC-based activity coefficient model.

Comp. i	group	count	R_i	Q_i	Ref.
OME _n	MAL	1	2.9644	2.7160	[56]
	FA _{OME}	($n-1$)	0.9183	0.7800	[56]
C12	CH ₃	2	0.9011	0.8480	[145]
	CH _{2,alk}	10	0.6744	0.5400	[56]
C16	CH ₃	2			
	CH _{2,alk}	14			
Tol	ACH	5	0.5313	0.4000	[145]
	ACCH ₃	1	1.2663	0.9680	[145]
W	H ₂ O	1	0.9200	1.4000	[56]

Table 23: Group interaction parameters for the UNIFAC activity coefficient model.

group j → group i ↓	MAL	FA _{OME}	CH ₃ / CH ₂	ACH	ACCH ₃	H ₂ O
MAL	-	26.0 ^a	-45.522 ^c	-103.618 ^c	-45.522 ^c	1031.0-1.749 • T/K ^a
FA _{OME}	141.5 ^a	-	265.483 ^c	52.13 ^b	265.48 ^c	670.7 ^a
CH ₃ / CH ₂	51.251 ^c	148.309 ^c	-	61.13 ^b	76.5 ^b	1318 ^b
ACH	6400.299 ^c	32.14 ^b	-11.12 ^b	-	167.0 ^b	903.8 ^b
ACCH ₃	51.251 ^c	148.309 ^c	-69.7 ^b	-146.8 ^b	-	5695.0 ^b
H ₂ O	-225.5+0.7205•T/K ^a	168.9-0.8776•T/K ^a	300 ^b	362.3 ^b	377.6 ^b	-

^(a)Schmitz et al.[56] ^(b)Gmehling et at.[145] ^(c)this work

Isothermal flash calculations were used to determine the two-phase and the three-phase equilibria studied in the present chapter. The feed composition for the flash-calculation was calculated from the experimental phase compositions assuming an equimolar phase split and the initial guess for the algorithm was calculated with the method of Ohanamah and Thompson[146]. The flash model was implemented in the software MATLAB. Details on the calculation can be found in the Appendix D.4.

5.4 Results and discussion

5.4.1 Overview

Before the experimental and model results are presented, the topologies of the corresponding phase diagrams are discussed. Both the experimental results and the model show that there are three types of phase diagrams in the systems studied here (in the temperature range that was investigated). The three topologies, labeled here as type A, B, and C, respectively, are depicted in Figure 36.

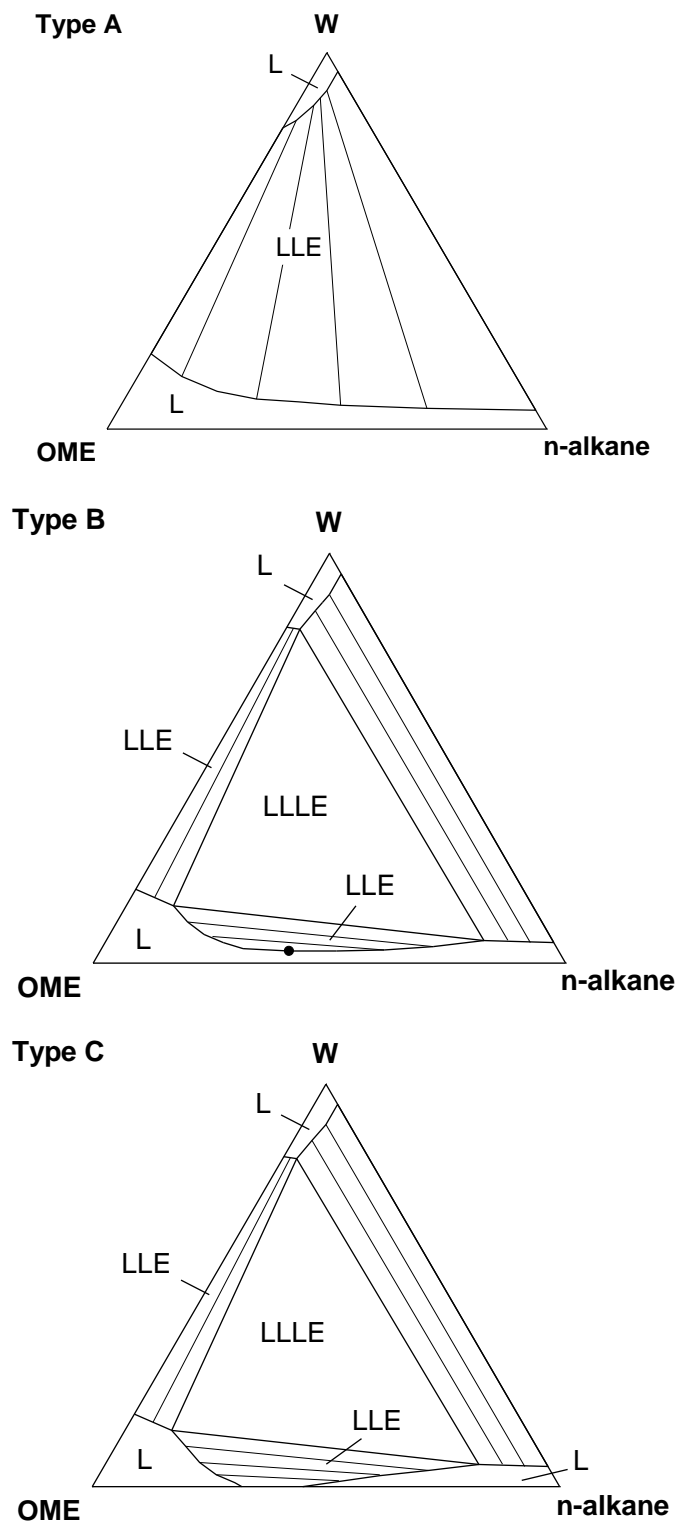


Figure 36: Schematic representation of the three topologies of the phase behavior of the systems studied in this work. The straight lines represent LLE conodes. The point mark in type B diagram is a critical point.

Type A was observed in all experiments with OME₂: OME₂ and the n-alkanes are completely miscible, while there are miscibility gaps in the binary systems with (OME₂ + water) and (n-alkane + water). A ternary LLE region connects these two binary LLE.

In the type C phase diagram, there is also a miscibility gap in the binary system (OME + n-alkane). This is the case for (OME₄ + C16) for all temperatures and (OME₂ + C16) for the two lower studied temperatures (278 and 265 K). In the ternary system, there are three (two-phase) LLE regions that stretch out from the binary sides of the phase diagram and meet in a (three-phase) LLLE in the center of the diagram.

Type B phase diagram has features from the other two types, which are, however, combined differently. As in the type C phase diagram, there is a (three-phase) LLLE. On the three sides of this LLLE-region, there are two phase LLE regions. However, only two of them are connected to binary sides of the phase diagram, whereas the third one, that on the side with low water concentrations, ends in a critical point, as there is no miscibility gap on the (OME + n-alkane) side of the phase diagram. This phase behavior was observed in the system (OME₄ + C12) at the highest studied temperature 293 K.

For some of the studied systems and temperatures, it is not possible to decide whether the phase behavior is of type B or C. An overview of the assignments of systems and temperatures to the phase behavior is given in Table 24.

The phenomenon of the unexpected phase split in technical mixtures of OME and HVO is very likely related to the occurrence of phase behavior of type B, cf. Figure 36. In the absence of water, OME and HVO are completely miscible. However, upon taking up water, the closed LLE region is reached and the mixture splits up in a OME-rich phase and a HVO-rich phase. If larger amounts of water are added (more than is usually taken up from the air), the three-phase region is reached and an additional third, water-rich phase forms.

Table 24: Overview of the systems studied in this work. The third or fourth component was always water.

OME	Hydrocarbon	Temperature K	Number of feed mixtures	Topology type
OME ₂	C12	293	6	A
		278	4	A
OME ₄	C16	293	6	A
	C12		5	B
		278	5	C
		265	4	C
	C16	293	5	C
OME _{mix}	C16 + Tol		3	B or C ^a
	C12		1	B or C ^a
	C16		1	B or C ^a

^(a) not clarified

5.4.2 Experiments in the system (OME + n-alkane + water)

The numerical results are presented in Table 25 to Table 28. The data for each system are grouped in isothermal subsets. In some of these sets, the temperature was only constant to about 1 K, which was due to problems with the setting of the temperature. The uncertainty of the reported individual values is as specified above.

Table 25: Experimental LLE data for the system (OME₂ + C12 + water). The composition of the feed is reported in the Appendix D.5.

<i>T</i> / K	water-rich phase		organic phase	
	$x_W^{(m)}$ g g ⁻¹	$x_{\text{OME}_2}^{(m)}$ g g ⁻¹	$x_W^{(m)}$ g g ⁻¹	$x_{\text{OME}_2}^{(m)}$ g g ⁻¹
264.37	solid ^a		0.00082	0.32896
278.28	0.81298	0.18702	0.00020	0.13227
278.50	0.72190	0.27810	0.00236	0.44964
278.71	0.70824	0.29176	0.00580	0.64208
293.15	0.70542	0.29458	0.01533	0.80287
	0.71217	0.28783	0.0113	0.73489
	0.75418	0.24582	0.00184	0.36483
	0.79698	0.20302	0.00118	0.22086
	0.73127	0.26873	0.00464	0.54201
	0.83542	0.16458	0.00030	0.12311

^(a) not analyzed

Table 26: Experimental LLE data for the system (OME₂ + C16 + water). The composition of the feed is reported in the Appendix D.5.

<i>T</i> /K	water-rich phase		organic phase	
	$x_{\text{W}}^{(m)}$	$x_{\text{OME2}}^{(m)}$	$x_{\text{W}}^{(m)}$	$x_{\text{OME2}}^{(m)}$
	g g ⁻¹	g g ⁻¹	g g ⁻¹	g g ⁻¹
293.15	0.71318	0.28682	0.01053	0.69712
	0.70225	0.29775	0.01159	0.71517
	0.70206	0.29794	0.00672	0.59913
	0.72288	0.27712	0.00319	0.43885
	0.75770	0.24230	0.00098	0.25675
	0.84827	0.15173	0.00030	0.11452

Table 27: Experimental LLE and LLLE data for the system (OME₄ + C12 + water). The composition of the feed is reported in the Appendix D.5.

<i>T</i> /K	water-rich phase		alkane-rich phase		OME-rich phase	
	$x_{\text{W}}^{(m)}$	$x_{\text{OME4}}^{(m)}$	$x_{\text{W}}^{(m)}$	$x_{\text{OME4}}^{(m)}$	$x_{\text{W}}^{(m)}$	$x_{\text{OME4}}^{(m)}$
	g g ⁻¹	g g ⁻¹	g g ⁻¹	g g ⁻¹	g g ⁻¹	g g ⁻¹
264.27	solid ^a		0.00014	0.14184	0.01312	0.93722
265.63	solid ^a		0.00013	0.15365	0.00937	0.93394
266.71	solid ^a		0.00011	0.16427	0.00395	0.92538
266.78	solid ^a		0.00075	0.17159	0.00206	0.92198
267.19	solid ^a		0.00015	0.15918	0.00755	0.92815
278.63	0.75422	0.2457	0.00040	0.19534	0.01783	0.91661
278.41	solid ^a		0.00039	0.22168	0.00917	0.90416
278.43	solid ^a		0.00033	0.24130	0.00538	0.89221
278.84	solid ^a		0.00041	0.20566	0.01436	0.91330
278.86	solid ^a		0.00023	0.25988	0.00267	0.87831
293.15	0.76914	0.23086	0.00106	0.27533	0.02135	0.89178
293.15	solid ^a		0.00111	0.39496	0.00505	0.80965
293.15	solid ^a		0.00111	0.33457	0.00870	0.85102
293.15	solid ^a		0.00103	0.27956	0.01221	0.87208

^(a) not analyzed

Table 28: Experimental LLE and LLLE data for the system (OME₄ + C16 + water). The composition of the feed is reported in the Appendix D.5.

T / K	water-rich phase		alkane-rich phase		OME-rich phase	
	$x_{\text{W}}^{(m)}$ g g^{-1}	$x_{\text{OME4}}^{(m)}$ g g^{-1}	$x_{\text{W}}^{(m)}$ g g^{-1}	$x_{\text{OME4}}^{(m)}$ g g^{-1}	$x_{\text{W}}^{(m)}$ g g^{-1}	$x_{\text{OME4}}^{(m)}$ g g^{-1}
293.15	0.74974	0.25026	0.00046	0.16656	0.02794	0.93775
			0.00046	0.18150	0.01820	0.95525
			0.00041	0.19751	0.01096	0.94194
			0.00024	0.22350	0.00351	0.91804
			0.00017	0.23519	0.00041	0.87702

In Figure 37, the LLE in the systems (OME₂ + C12 + water) and (OME₂ + C16 + water) are shown. The different temperatures are indicated by different colors and the symbol type indicates the n-alkane that was used. The feed compositions for the different tie lines are shown as crosses.

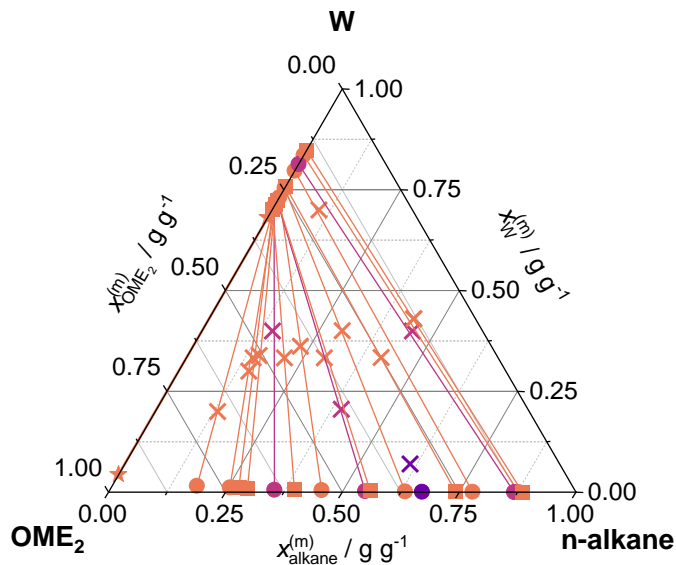


Figure 37: Experimental results for the LLE in the system (OME₂ + C12 + water, ○) and the system (OME₂ + C16 + water, □). The color indicates the temperature: (■) 293 K, (■) 278 K, (■) 265 K. (☆) Data from Schmitz et al.[60] for the binary system (OME₂ + water). (×) feed compositions. Lines are tie lines. For the measurement at 278 K, only one liquid phase could be measured due to ice formation.

It can be seen that the feed compositions lie perfectly on the tie lines, indicating a good quality of the experimental results. In all experiments, a split into a water-rich phase and an organic phase was observed. In the water-rich phase, no n-alkane was found. The concentration is so small that it is below the detection limit of the NMR measurement. This is consistent with reports from the literature [132,133] for the solubility of C12 and C16 in pure water, which does not exceed 0.1 ppm.

The OME fraction in the water-rich phase increases with increasing ratio of OME₂/n-alkane in the feed and approaches the value for the system (OME₂ + water) from Schmitz et al.[60], which is also indicated in Figure 37. There is no data for the composition of the water-rich phase at 265 K, for which only the organic liquid phase could be analyzed, due to ice formation. The resolution of the presentation of the data in Figure 37 is too low to discern an influence of the temperature or the type of n-alkane.

Therefore, the results for the composition of the organic phase, which is of special interest for fuel applications, are shown separately in Figure 38. Additionally, also the experimental data from Zhuang et al.[134] for the system (OME₂ + n-hexane + water) are shown.

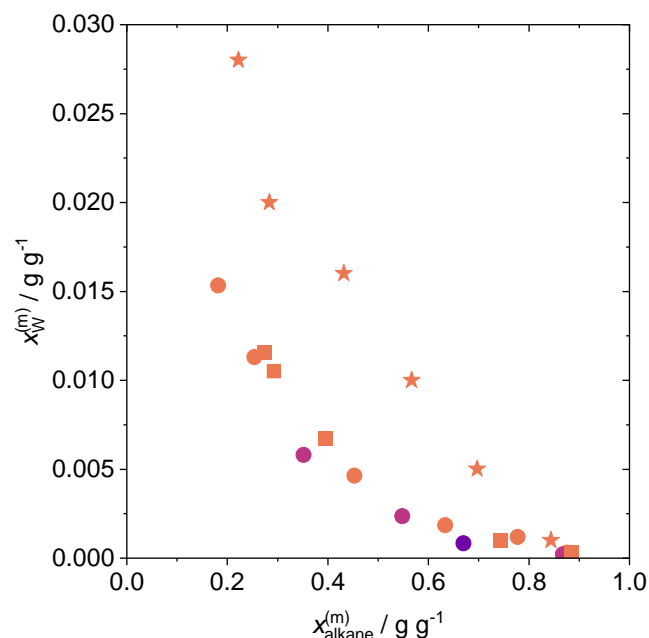


Figure 38: Experimental results for the composition of the organic phase in LLE in the system (OME₂ + C12 + water, ○) and the system (OME₂ + C16 + water, □). The color represents the temperature: (■) 293 K, (■) 278 K, (■) 265 K. (☆) Data from Zhuang et al.[134] for the system (OME₂ + n-hexane + water).

As expected, the concentration of water increases with increasing amount of OME₂ (decreasing amount of the n-alkane). The differences between the different data sets from the present work are not large (as could be expected from Figure 37) but indicate a tendency for an increasing water amount with increasing temperature, which is also not unexpected, due to the weaker influence of H-bonds at higher temperatures. The differences between the results for C12 and C16 are basically within the scattering of the data. The results of Zhuang et al.[134] for the system (OME₂ + n-hexane + water) at 292 K show significantly higher water solubilities in the organic phase than the results from the present work that were, however, obtained with longer n-alkanes.

The LLE measured in the systems (OME₄ + C12 + water) and (OME₄ + C16 + water) are shown in Figure 39. For (OME₄ + C12 + water), results for different temperatures are presented.

The variation of the temperature and alkane hardly affects the water-rich phase (that contains practically no alkane) and has only a moderate influence on the OME₄-rich phase. A stronger influence is observed for the alkane-rich phase.

This is discussed in more detail using Figure 40, which shows results for the two organic phases of the LLE together with results for the LLE in the region with low water concentrations (cf. Figure 36).

All results shown in Figure 40 belong to the type C phase behavior, except those for the system (OME₄ + C12 + water) at 293 K, which has type B phase behavior.

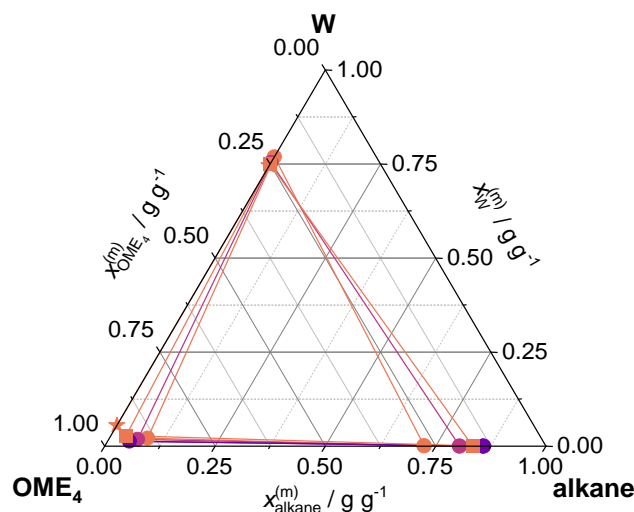


Figure 39: Experimental results for the LLE in the system (OME₄ + C12 + water, ○) and the system (OME₄ + C16 + water, □). The color represents the temperature: (■) 293 K, (■) 278 K, (■) 265 K. (☆) Data from Schmitz et al.[60] for the binary system (OME₄ + water). Lines are tie lines.

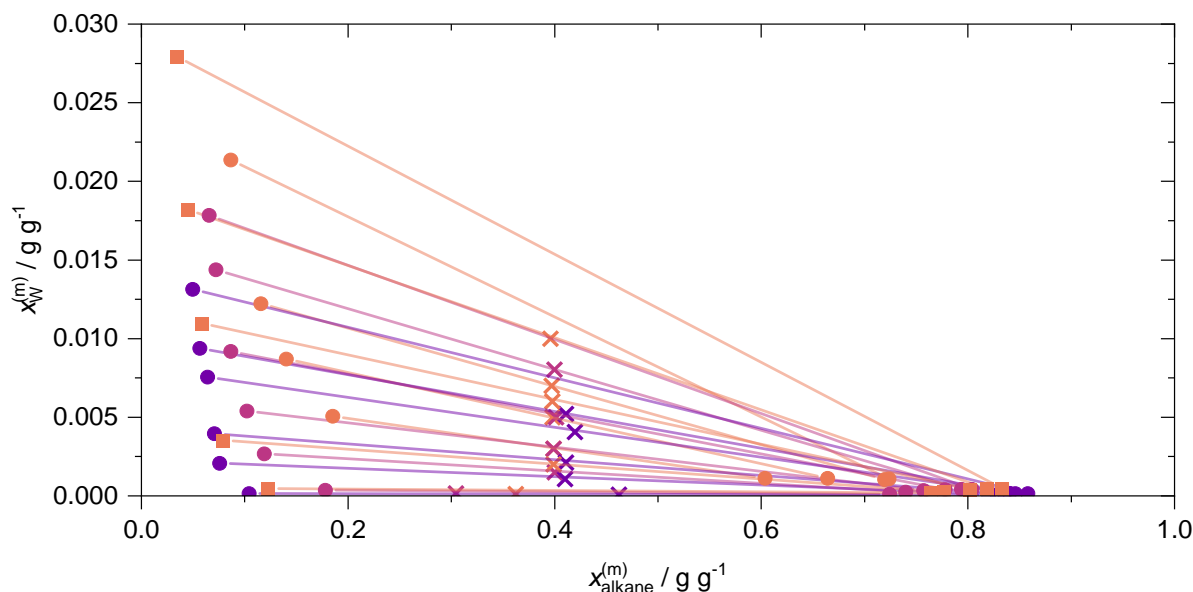


Figure 40: Experimental results for the LLE in the system (OME₄ + C12 + water, ○) and the system (OME₄ + C16 + water, □) at low water fractions. The color represents the temperature: (■) 293 K, (■) 278 K, (■) 265 K. (×) represent the feed compositions. Lines are tie lines. The top results for each temperature and alkane represent the phases with low water fractions of the LLE.

Figure 40 shows that decreasing the temperature leads to a widening of the LLE region, i.e. to an increasing mole fraction of OME₄ in the OME₄-rich phase as well as an increasing mole fraction of C12 in the C12-rich phase. The water-content in the alkane-rich phase is always very low; it increases with increasing OME-content of that phase (not discernable in Figure 40). Water from the feed is basically only found in the OME₄-rich phase. Also the increase in the chain-length of the n-alkane from C12 to C16 increases the width of the miscibility gap. Again, the feed concentrations lie on the LLE tie-lines.

In the present chapter, the type A phase behavior was only observed for OME₂. Zhuang et al.[134] mixed OME₄ with the smaller alkane n-hexane and also observed type A phase behavior. Type B phase behavior can be considered as an intermediate between types A and C, the difference is mainly caused by the differences in the solubility of the binary system (OME + n-alkane).

5.4.3 Modeling of the system (OME + n-alkane + water)

In the following, modeling results are compared to experimental results in figures that are similar to Figure 37 to Figure 40. However, for the comparison, mole fractions are used, which enables a better resolution of differences than the mass fractions used in Figure 37 to Figure 40, which were

preferred in these figures, as they are more convenient for applications. It was refrained from presenting the modeling results already in Figure 37 to Figure 40, to avoid an overloading with information.

In Figure 41, the experimental results for the LLE in the studied systems of the type (OME₂ + n-alkane + water) are compared to the results from the model and Figure 42 shows the corresponding results for the LLLE in the system of the type (OME₄ + n-alkane + water). The modeling results for these two systems in plots that are similar to the ones shown in Figure 38 and Figure 40 are shown in the Appendix D.6.

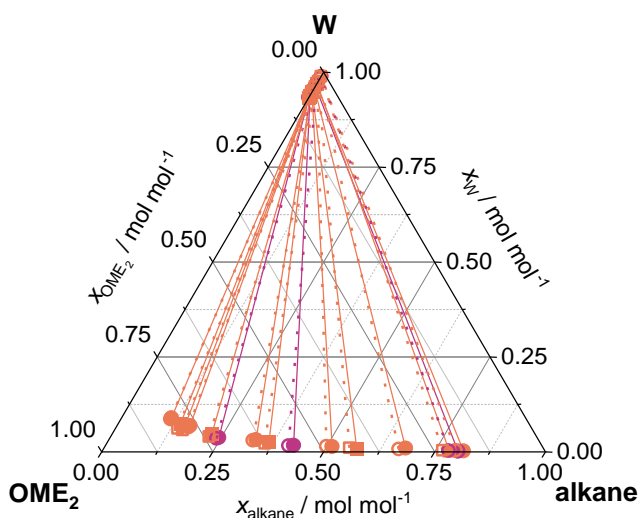


Figure 41: Experimental results (filled symbols and full line) and model results (open symbols and dashed line) for the LLE in the system (OME₂ + C12 + water, ○) and the system (OME₂ + C16 + water, □). The color represents the temperature: (■) 293 K, (■) 278 K. Lines are tie lines.

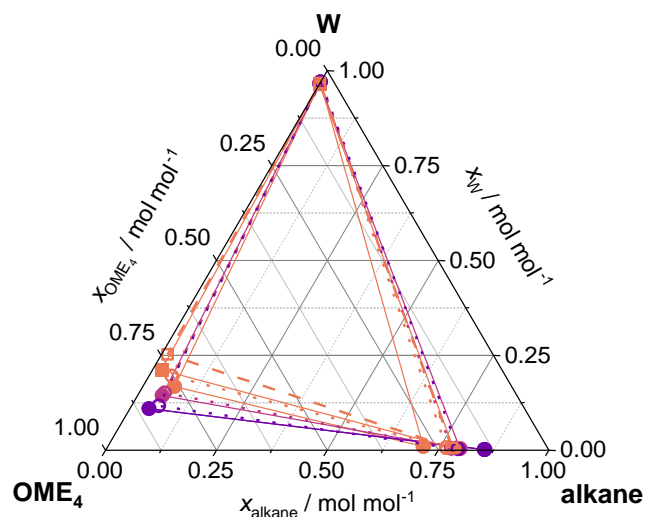


Figure 42: Experimental results (filled symbols and full line) and model results (open symbols and dashed line) for the LLE in the system (OME₄ + C12 + water, ○) and the system (OME₄ + C16 + water, □). The color represents the temperature: (■) 293 K, (■) 278 K, (■) 265 K.

The model confirms the topologies A to C discussed above. The water-rich phase is described well in all cases. The water mole-fraction in the OME-rich phase is overestimated and the width of the miscibility gap between the OME-rich and the alkane-rich phase is underestimated, but the trends regarding the influence of the temperature and alkane chain length are described correctly.

5.4.4 Experiments with systems with more than three components

5.4.4.1 System (OME₄ + n-hexadecane + toluene + water)

LLLE in mixtures of (OME₄ + C16 + Tol + water) were studied at 293 K. In the experiments, the ratio OME₄/(C16 + Tol)/water was held constant, and only the ratio C16/Tol was varied. The feed composition was chosen so that the resulting mixture split into three phases. The numerical results are presented in Table 29. The results are discussed here using ternary phase diagrams, in which Tol and C16 were lumped into a single component.

Figure 43 shows the experimental results together with those for the Tol-free system. Besides the experimental data also the results from the model are depicted.

Table 29: LLE data of the system (OME₄ + C16 + Tol + water) at 293.15 K. The composition of the feed is reported in the Appendix D.5.

water-rich phase			(C16 + Tol)-rich			OME-rich phase		
$x_W^{(m)}$ g g ⁻¹	$x_{\text{OME4}}^{(m)}$ g g ⁻¹	$x_{\text{Tol}}^{(m)}$ g g ⁻¹	$x_W^{(m)}$ g g ⁻¹	$x_{\text{OME4}}^{(m)}$ g g ⁻¹	$x_{\text{Tol}}^{(m)}$ g g ⁻¹	$x_W^{(m)}$ g g ⁻¹	$x_{\text{OME4}}^{(m)}$ g g ⁻¹	$x_{\text{Tol}}^{(m)}$ g g ⁻¹
0.75725	0.24275	0.00000	0.00049	0.17216	0.01251	0.02615	0.92808	0.00907
0.75923	0.24077	0.00000	0.00057	0.18501	0.02802	0.02388	0.91189	0.02183
0.88856	0.11144	0.00000	0.00163	0.22853	0.33292	0.01400	0.76441	0.12984

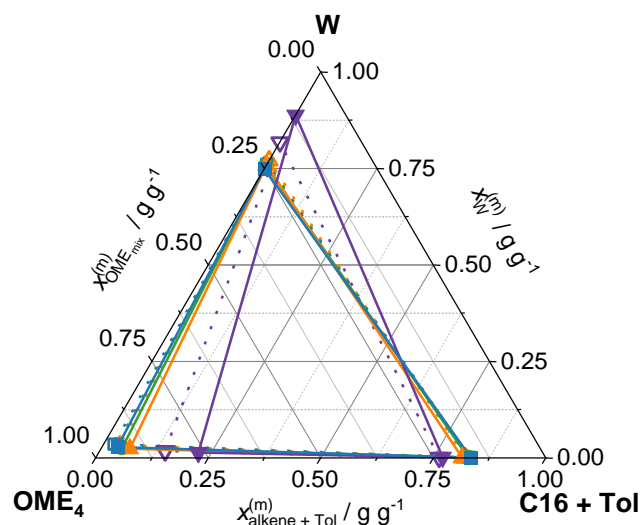


Figure 43: Experimental results (filled symbols and straight line) and model results (open symbols and dashed line) for the LLE in the system (OME₄ + C16 + Tol + water) at 293.15 K. Tol and C16 are lumped in the representation. Results from experiments with varying ratios of Tol/C16 are shown. The mass fractions of Tol in the (C16 + Tol) feed mixture ($x_{\text{Tol,mix}}^{(m)}$) were: (■) $x_{\text{Tol,mix}}^{(m)} = 0.0 \text{ g g}^{-1}$, (■) $x_{\text{Tol,mix}}^{(m)} = 0.02 \text{ g g}^{-1}$, (▲) $x_{\text{Tol,mix}}^{(m)} = 0.05 \text{ g g}^{-1}$, (▼) $x_{\text{Tol,mix}}^{(m)} = 0.2 \text{ g g}^{-1}$.

In the Tol-containing systems, the basic findings regarding the three phases are the same as for the Tol-free system. Upon increasing the amount of Tol, the amount of water in the water-rich phase increases and the miscibility gap between the hydrocarbon-rich phase and the OME-rich phase gets smaller, i.e., Tol acts as a solubilizer. This can be attributed to a mediating influence of the pi-electron systems of Tol. The model predicts these trends right but underestimates the magnitude of the influence of Tol. A detailed analysis of the numerical results presented in Table 29 reveals that the ratio of C16/Tol in the different phases is similar, i.e., they do not separate.

5.4.4.2 Systems of the type (OME-mixture + n-alkane + water)

Measurements in systems containing a mixture of OME₃, OME₄, OME₅, and OME₆ of a fixed composition (OME_{mix}), water, and either C12 or C16 were carried out at 293.15 K. The feed was again chosen so that it was inside the three phase region. The numerical results for the LLE are reported in Table 30 and are illustrated in Figure 44, which shows a ternary diagram, in which OME₃, OME₄, OME₅, and OME₆ are lumped into one pseudo-component OME_{mix}. Additionally, Figure 45 depicts the analytical results for the individual components in the three phases.

Table 30: Experimental LLE data of systems of the type (OME_{mix} + alkane + water) at 293.15 K. OME_{mix} is a mixture of OME₃ to OME₆. The composition of the feed is reported in the Appendix D.5.

alkane	phase	$x_W^{(m)}$ g g ⁻¹	$x_{\text{alkane}}^{(m)}$ g g ⁻¹	$x_{\text{OME3}}^{(m)}$ g g ⁻¹	$x_{\text{OME4}}^{(m)}$ g g ⁻¹	$x_{\text{OME5}}^{(m)}$ g g ⁻¹	$x_{\text{OME6}}^{(m)}$ g g ⁻¹
C16	OME-rich	0.02561	0.09234	0.35272	0.28715	0.17995	0.06224
	water-rich	0.70621	0	0.16640	0.11312	0.01017	0.00410
	alkane-rich	4.04E-4	0.78126	0.11119	0.06731	0.0292	0.01063
C12	OME-rich	0.02734	0.09217	0.35209	0.28664	0.17963	0.06213
	water-rich	0.71700	0	0.13711	0.08413	0.04696	0.01330
	alkane-rich	0.00127	0.71756	0.14174	0.08388	0.04344	0.01211

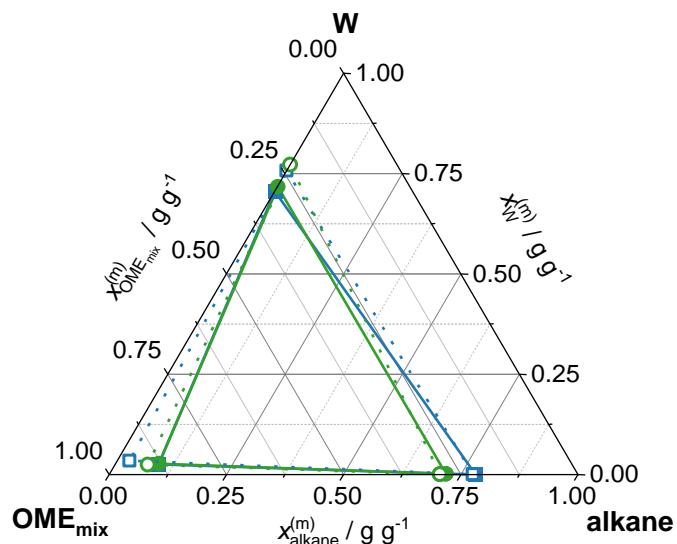


Figure 44: Experimental results (filled symbols and straight line) and model results (open symbols and dashed line) for the LLE in systems of the type (OME_{mix} + alkane + water) at 293 K. The symbols represent the alkane: (O) C12, (□) C16.

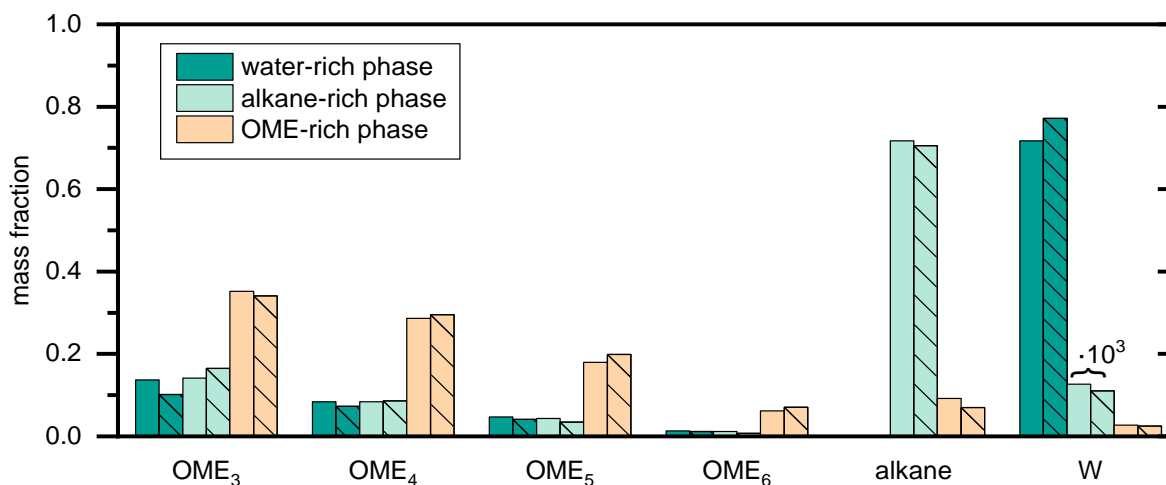


Figure 45: Results for LLE in systems of the type (OME_{mix} + C12 + water) at 293 K. Experimental mass fractions (unhatched bars) are compared to mass fractions from the model (hatched bars) for all three phases. The water fraction in the C12-rich phase was multiplied by 1000 for a better visualization.

The experimental results are similar to those of the measurements with pure OME₄ (cf. Figure 39). The ratios OME₃ / OME₄ / OME₅ / OME₆ do not differ significantly in the different phases and are

therefore also basically the same as in the feed mixture. All in all, the model shows a good agreement with the experimental data. The alkane-rich phase is described very well (cf. Figure 45). The distribution of the individual OME is also reproduced well by the model. The water fraction in the water-rich phase is somewhat underestimated.

5.5 Conclusions

Mixtures of poly(oxymethylene) dimethyl ethers (OME) and hydrogenated vegetable oil (HVO) are interesting synthetic fuels. However, in technical applications of these fuels, a liquid-liquid phase split was observed, which is unwanted. Up to now only qualitative information on this phenomenon was available and its causes were unclear. In the present chapter, the hypothesis that the phase separation is a consequence of the uptake of water from the air by the (OME + HVO) mixtures is confirmed. This leads to a separation into an OME-rich phase, which contains basically all the water, and a HVO-rich phase, which is almost water-free. This can be deduced from the results of the experimental studies on liquid-liquid equilibria (LLE) and liquid-liquid-liquid equilibria (LLLE) in model systems of the type (OME + alkane + water) that were carried out in the present work.

Depending on the system and temperature, three different topologies of the phase behavior were observed. The phenomenon observed in the technical processes is related to a topology, in which there is a two-phase LLE-region in the ternary system (OME + alkane + water), which is very close to the binary system (OME + alkane), which is still fully miscible. I.e., in the ternary system, there is an LLE critical point at very low water concentrations.

The liquid-liquid phase split is induced by a latent incompatibility of the OME with the alkane, which becomes only manifest, when water is added. In the experimental studies mentioned above, pure OME₂ and OME₄ were used. OME₂ is less polar than OME₄, leading to a better compatibility of OME₂ with the alkane. As a consequence, the phase split was not observed for OME₂, but only for OME₄. Upon the phase split, all water goes to the more polar OME₄-rich phase, while the alkane-rich phase can basically take up no water, as expected. Experiments with a mixture of (OME₃ + OME₄ + OME₅ + OME₆), as it is used as fuel, showed results that were similar to those found for OME₄.

Furthermore, experiments with mixtures that contained not only alkanes but also toluene were carried out. The presence of the aromatic compound makes the alkane-rich phase more hydrophilic, and, hence, more compatible with OME. This reduces the risk for the phase split.

The experimental findings were also confirmed by simulations, in which UNIFAC, a model of the Gibbs excess energy, was used for describing the liquid phases. Most of the model parameters

were taken from the literature, but a few parameters had to be fitted to selected experimental results from the present work. This comparatively simple modeling approach gave good results.

Now that the causes of the phase split are clear, measures to circumvent it can be found: a straightforward approach is to reduce the humidity in the fuel storage tank, e.g., by common drying agents, such as molecular sieves. Another approach is to add further fuel components that act as solubilizers. Ranked on a polarity scale, they should lie between OME₄ and the alkanes. The model developed in the present chapter can be used for a screening of such solubilizers.

6 Conclusions

In this thesis, fundamental findings on the formation of solids in mixtures of formaldehyde with water and methanol were obtained. Up to now, only data on the system (formaldehyde + water) were known and these were contradictory. These contradictions could be clarified within this thesis and a consistent physico-chemical model of the precipitation process was developed. For this purpose, not only the equilibrium was studied, but also the precipitation kinetics. Furthermore, the formation of solids in the systems (formaldehyde + water + methanol), (formaldehyde + water + OME) and (formaldehyde + water + methanol + OME) was studied. With the physico-chemical model from the present work also predictive calculations of solubilities in mixtures with different alcohols are possible. It would be of great interest to validate these predictions with further measurements of other systems. Furthermore, the measurements of the solubility at higher temperatures would be of interest to validate the extrapolation of the model.

Beside the work on the solid formation, also an attractive OME production process starting from dimethyl ether and trioxane was developed in this work and the relevant reaction equilibria were investigated experimentally. The experiments show a strong formation of methyl formate as a side product. The aim of future work should be the development of improved catalysts with lower methyl formate formation. Furthermore, the developed process has to be extended by a methyl formate separation.

Furthermore, also a new production process for trioxane starting from aqueous formaldehyde solutions was developed. Existing trioxane production processes are energy-intensive, as either extraction or pressure-swing distillation is used to obtain pure trioxane. The new process is based on crystallization and shows a lower energy demand per ton of product. In the present work, only a simple model was used to describe the crystallization step. More detailed knowledge of the solid-liquid equilibria in the system (formaldehyde + water + trioxane) would be necessary for a detailed process design.

Finally, blends of OME and hydrogenated vegetable oil (HVO) were investigated. In technical applications, blends of OME and HVO that are initially homogenous tend to show a liquid-liquid phase split after some time. The reasons for the phenomenon were unclear. Therefore,

measurements of the liquid-liquid and liquid-liquid-liquid equilibria of mixtures of individual components of the blends were carried out and modeled. The results show that the uptake of small amounts of water from the air is the reason for this effect. Based on the findings from the present work phase stabilization additives can be identified to avoid the phase separation.

Literature

- [1] A.W. Franz, H. Kronemayer, D. Pfeiffer, R.D. Pilz, G. Reuss, W. Disteldorf, A.O. Gamer, A. Hilt: Formaldehyde, Ullmann's Encyclopedia of Industrial Chemistry, Vol. 19, Wiley-VCH Verlag GmbH & Co. KGaA, Weinheim, Germany, 2016, pp. 1–34.
- [2] R. Kircher, N. Schmitz, J. Berje, K. Münnemann, W.R. Thiel, J. Burger, H. Hasse: Generalized Chemical Equilibrium Constant of Formaldehyde Oligomerization, *Ind. Eng. Chem. Res.* 59 (2020) 11431–11440.
- [3] M. Dyga, A. Keller, H. Hasse: Vapor–Liquid Equilibria and Chemical Equilibria in the System (Formaldehyde + Water + Isoprenol), *Ind. Eng. Chem. Res.* 60 (2021) 4471–4483.
- [4] C. Kuhnert, M. Albert, S. Breyer, I. Hahnenstein, H. Hasse, G. Maurer: Phase Equilibrium in Formaldehyde Containing Multicomponent Mixtures: Experimental Results for Fluid Phase Equilibria of (Formaldehyde + (Water or Methanol) + Methylal) and (Formaldehyde + Water + Methanol + Methylal) and Comparison with Predictions, *Ind. Eng. Chem. Res.* 45 (2006) 5155–5164.
- [5] M. Ott, H.H. Fischer, M. Maiwald, K. Albert, H. Hasse: Kinetics of oligomerization reactions in formaldehyde solutions: NMR experiments up to 373K and thermodynamically consistent model, *Chemical Engineering and Processing: Process Intensification* 44 (2005) 653–660.
- [6] H. Hasse, I. Hahnenstein, G. Maurer: Revised vapor-liquid equilibrium model for multicomponent formaldehyde mixtures, *AIChE J.* 36 (1990) 1807–1814.
- [7] G. Maurer: Vapor-liquid equilibrium of formaldehyde-and water-containing multicomponent mixtures, *AIChE J.* 32 (1986) 932–948.
- [8] M. Härtl, P. Seidenspinner, E. Jacob, G. Wachtmeister: Oxygenate screening on a heavy-duty diesel engine and emission characteristics of highly oxygenated oxymethylene ether fuel OME1, *Fuel* 153 (2015) 328–335.
- [9] S.E. Iannuzzi, C. Barro, K. Boulouchos, J. Burger: Combustion behavior and soot formation/oxidation of oxygenated fuels in a cylindrical constant volume chamber, *Fuel* 167 (2016) 49–59.
- [10] J. Liu, H. Wang, Y. Li, Z. Zheng, Z. Xue, H. Shang, M. Yao: Effects of diesel/PODE (polyoxymethylene dimethyl ethers) blends on combustion and emission characteristics in a heavy duty diesel engine, *Fuel* 177 (2016) 206–216.

- [11] J.V. Pastor, A. García, C. Micó, F. Lewiski: Soot reduction for cleaner Compression Ignition Engines through innovative bowl templates, *International Journal of Engine Research* (2020) 2477-2491.
- [12] H. Liu, Z. Wang, Y. Li, Y. Zheng, T. He, J. Wang: Recent progress in the application in compression ignition engines and the synthesis technologies of polyoxymethylene dimethyl ethers, *Applied Energy* 233-234 (2019) 599–611.
- [13] S. Schemme, R.C. Samsun, R. Peters, D. Stolten: Power-to-fuel as a key to sustainable transport systems – An analysis of diesel fuels produced from CO₂ and renewable electricity, *Fuel* 205 (2017) 198–221.
- [14] K. Hackbarth, P. Haltenort, U. Arnold, J. Sauer: Recent Progress in the Production, Application and Evaluation of Oxymethylene Ethers, *Chemie Ingenieur Technik* 90 (2018) 1520–1528.
- [15] A. Holzer, M. Guenther: Investigation of the Emission Reduction Potential of HVO-OME Fuel Blends in a Single-Cylinder Diesel Engine, SAE Technical Paper Series, SAE International, Warrendale, 2021.
- [16] P. Dworschak, V. Berger, M. Härtl, G. Wachtmeister: Neat Oxymethylene Ethers: Combustion Performance and Emissions of OME 2 , OME 3 , OME 4 and OME 5 in a Single-Cylinder Diesel Engine, SAE Technical Paper Series, SAE International, Warrendale, 2020.
- [17] B. Lumpp, D. Rothe, C. Pastötter, R. Lämmermann, E. Jacob: Oxymethylene ethers as diesel fuel additives of the future, *MTZ Worldw* 72 (2011) 34–38.
- [18] M. Münz, A. Mokros, D. Töpfer, C. Beidl: OME - Partikelbewertung unter Realfahrbedingungen, *MTZ Motortech Z* 79 (2018) 16–21.
- [19] L. Pellegrini, M. Marchionna, R. Patrini, C. Beatrice, N. Del Giacomo, C. Guido: Combustion Behaviour and Emission Performance of Neat and Blended Polyoxymethylene Dimethyl Ethers in a Light-Duty Diesel Engine, SAE Technical Paper Series, SAE International, Warrendale, 2012.
- [20] K. Kakinuma, N. Hirayama, A. Iiyama, M. Watanabe, M. Uchida: Electrochemical Oxidation of Hydrolyzed Poly-Oxymethylene-Dimethylether by Pt and PtRu Catalysts on Ta-Doped SnO₂ Supports for Direct Oxidation Fuel Cells, *J. Electrochem. Soc.* 164 (2017) F1226-F1233.
- [21] Q. Sun, A. Auroux, J. Shen: Surface acidity of niobium phosphate and steam reforming of dimethoxymethane over CuZnO/Al₂O₃-NbP complex catalysts, *Journal of Catalysis* 244 (2006) 1–9.
- [22] C.J. Baranowski, A.M. Bahmanpour, O. Kröcher: Catalytic synthesis of polyoxymethylene dimethyl ethers (OME), *Applied Catalysis B: Environmental* 217 (2017) 407–420.

- [23] T. Bhatelia, W.J. Lee, C. Samanta, J. Patel, A. Bordoloi: Processes for the production of oxymethylene ethers: promising synthetic diesel additives, *Asia-Pac. J. Chem. Eng.* 12 (2017) 827–837.
- [24] N. Schmitz, C.F. Breitzkreuz, E. Ströfer, J. Burger, H. Hasse: Separation of water from mixtures containing formaldehyde, water, methanol, methylal, and poly(oxymethylene) dimethyl ethers by pervaporation, *Journal of Membrane Science* 564 (2018) 806–812.
- [25] N. Schmitz, E. Ströfer, J. Burger, H. Hasse: Conceptual Design of a Novel Process for the Production of Poly(oxymethylene) Dimethyl Ethers from Formaldehyde and Methanol, *Ind. Eng. Chem. Res.* 56 (2017) 11519–11530.
- [26] A. Ferre, J. Voggenreiter, Y. Tönges, J. Burger: Demonstration Plant for the Synthesis of OME Fuels, *MTZ Worldw* 82 (2021) 26–31.
- [27] D. Oestreich, L. Lautenschütz, U. Arnold, J. Sauer: Production of oxymethylene dimethyl ether (OME)-hydrocarbon fuel blends in a one-step synthesis/extraction procedure, *Fuel* 214 (2018) 39–44.
- [28] Z. Han, Y. Ren, H. Li, X. Li, X. Gao: Simultaneous Extractive and Azeotropic Distillation Separation Process for Production of PODeN from Formaldehyde and Methylal, *Ind. Eng. Chem. Res.* (2019) 5252–5260.
- [29] J. Burger, E. Ströfer, H. Hasse: Production process for diesel fuel components poly(oxymethylene) dimethyl ethers from methane-based products by hierarchical optimization with varying model depth, *Chemical Engineering Research and Design* 91 (2013) 2648–2662.
- [30] L. Lautenschütz, D. Oestreich, P. Haltenort, U. Arnold, E. Dinjus, J. Sauer: Efficient synthesis of oxymethylene dimethyl ethers (OME) from dimethoxymethane and trioxane over zeolites, *Fuel Processing Technology* 165 (2017) 27–33.
- [31] P. Haltenort, L. Lautenschütz, U. Arnold, J. Sauer: (Trans)acetalization Reactions for the Synthesis of Oligomeric Oxymethylene Dialkyl Ethers Catalyzed by Zeolite BEA25, *Top Catal* 62 (2019) 551–559.
- [32] T.J. Goncalves, U. Arnold, P.N. Plessow, F. Studt: Theoretical Investigation of the Acid Catalyzed Formation of Oxymethylene Dimethyl Ethers from Trioxane and Dimethoxymethane, *ACS Catal.* 7 (2017) 3615–3621.
- [33] R. Peláez, P. Marín, S. Ordóñez: Synthesis of poly(oxymethylene) dimethyl ethers from methylal and trioxane over acidic ion exchange resins: A kinetic study, *Chemical Engineering Journal* 396 (2020) 125305.
- [34] Y. Zheng, Q. Tang, T. Wang, Y. Liao, J. Wang: Synthesis of a Green Fuel Additive Over Cation Resins, *Chem. Eng. Technol.* 36 (2013) 1951–1956.
- [35] Q. Wu, M. Wang, Y. Hao, H. Li, Y. Zhao, Q. Jiao: Synthesis of Polyoxymethylene Dimethyl Ethers Catalyzed by Brønsted Acid Ionic Liquids with Alkanesulfonic Acid Groups, *Ind. Eng. Chem. Res.* 53 (2014) 16254–16260.

- [36] D. Wang, F. Zhao, G. Zhu, C. Xia: Production of eco-friendly poly(oxymethylene) dimethyl ethers catalyzed by acidic ionic liquid: A kinetic investigation, *Chemical Engineering Journal* 334 (2017) 2616–2624.
- [37] M. Drexler, P. Haltenort, U. Arnold, J. Sauer: Continuous Synthesis of Oxymethylene Ether Fuels from Dimethyl Ether in a Heterogeneously Catalyzed Liquid Phase Process, *Chemie Ingenieur Technik* 94 (2022) 256–266.
- [38] Y. Meng, H. Li, C. Dai, B. Chen, Z. Lei, X. Li, X. Gao: Innovative reactive distillation process for the eco-friendly Poly(oxymethylene) dimethyl ethers synthesis from methylal and trioxane, *Separation and Purification Technology* 278 (2021) 119538.
- [39] J.-O. Weidert, J. Burger, M. Renner, S. Blagov, H. Hasse: Development of an Integrated Reaction–Distillation Process for the Production of Methylal, *Ind. Eng. Chem. Res.* 56 (2017) 575–582.
- [40] C.H. Gierlich, K. Beydoun, J. Klankermayer, R. Palkovits: Challenges and Opportunities in the Production of Oxymethylene Dimethylether, *Chemie Ingenieur Technik* 92 (2020) 116–124.
- [41] K. Thavornprasert, M. Capron, L. Jalowiecki-Duhamel, F. Dumeignil: One-pot 1,1-dimethoxymethane synthesis from methanol: a promising pathway over bifunctional catalysts, *Catal. Sci. Technol.* 6 (2016) 958–970.
- [42] U. Arnold, P. Haltenort, K. Herrera Delgado, B. Niethammer, J. Sauer: Die Rolle von Dimethylether (DME) als Schlüsselbaustein synthetischer Kraftstoffe aus erneuerbaren Rohstoffen, in: W. Maus (Ed.), *Zukünftige Kraftstoffe*, Springer, Heidelberg, 2019, pp. 532–561.
- [43] M. Oles, W. Lücke, R. Kleinschmidt, K. Büker, H.-J. Weddige, P. Schmöle, R. Achatz: Carbon2Chem® - Ein cross-industrieller Ansatz zur Reduzierung der Treibhausgasemissionen, *Chemie Ingenieur Technik* 90 (2018) 169–178.
- [44] C. Arcoumanis, C. Bae, R. Crookes, E. Kinoshita: The potential of di-methyl ether (DME) as an alternative fuel for compression-ignition engines, *Fuel* 87 (2008) 1014–1030.
- [45] T. Grützner, H. Hasse, N. Lang, M. Siegert, E. Ströfer: Development of a new industrial process for trioxane production, *Chemical Engineering Science* 62 (2007) 5613–5620.
- [46] J.F. Walker: *Formaldehyde*, Reinhold Publishing Corporation, New York, 1964.
- [47] F. Auerbach, H. Barschall: Studien über Formaldehyd: Die festen Polymeren des Formaldehyds, *Arbeiten aus dem Kaiserlichen Gesundheitsamte* 27 (1908) 183–230.
- [48] J.L. Biesecker: Stabilized powdered formaldehyde (US35759603) 2003.
- [49] H. Diem, H. Libowitzky, G. Matthias, C. Dudeck, G. Lehmann: Stabilisierte, wässrige Formaldehydlösungen und Verfahren zu ihrer Herstellung (DE2358856A1) 1975.
- [50] H. Junkermann, G. Pohl: Stabilisierung wässriger Formaldehydlösungen (DE2138309A) 1977.
- [51] P. Werle, H. Focke, K. Popp, W. Merk: Neue Bismelamine (DE3143920A1) 1983.

- [52] L. Credali, L. Mortillaro, G. Galiazzi, M. Russo, C. de Checchi: Pressione di vapore sul sistema acqua-formaldeide liquido e solido, *Chim. Ind.* 47 (1965) 732–736.
- [53] T. Grützner, H. Hasse: Solubility of Formaldehyde and Trioxane in Aqueous Solutions, *J. Chem. Eng. Data* 49 (2004) 642–646.
- [54] W. Ma, Y. Hu, H. Wang, Di Zhao: The effects of typical salts, acids and ionic liquids on the solubility of formaldehyde in aqueous solutions, *Fluid Phase Equilibria* 460 (2018) 51–56.
- [55] M. Albert, I. Hahnenstein, H. Hasse, G. Maurer: Vapor–liquid equilibrium of formaldehyde mixtures: New data and model revision, *AIChE J.* 42 (1996) 1741–1752.
- [56] N. Schmitz, C.F. Breitzkreuz, E. Ströfer, J. Burger, H. Hasse: Vapor-liquid equilibrium and distillation of mixtures containing formaldehyde and poly(oxymethylene) dimethyl ethers, *Chemical Engineering and Processing: Process Intensification* 131 (2018) 116–124.
- [57] I. Hahnenstein, M. Albert, H. Hasse, C.G. Kreiter, G. Maurer: NMR Spectroscopic and Densimetric Study of Reaction Kinetics of Formaldehyde Polymer Formation in Water, Deuterium Oxide, and Methanol, *Ind. Eng. Chem. Res.* 34 (1995) 440–450.
- [58] N. Schmitz, F. Homberg, J. Berje, J. Burger, H. Hasse: Chemical Equilibrium of the Synthesis of Poly(oxymethylene) Dimethyl Ethers from Formaldehyde and Methanol in Aqueous Solutions, *Ind. Eng. Chem. Res.* 54 (2015) 6409–6417.
- [59] N. Schmitz, J. Burger, H. Hasse: Reaction Kinetics of the Formation of Poly(oxymethylene) Dimethyl Ethers from Formaldehyde and Methanol in Aqueous Solutions, *Ind. Eng. Chem. Res.* 54 (2015) 12553–12560.
- [60] N. Schmitz, A. Friebel, E. von Harbou, J. Burger, H. Hasse: Liquid-liquid equilibrium in binary and ternary mixtures containing formaldehyde, water, methanol, methylal, and poly(oxymethylene) dimethyl ethers, *Fluid Phase Equilibria* 425 (2016) 127–135.
- [61] J.G. Winkelmann, M. Ottens, A.A.C.M. Beenackers: The kinetics of the dehydration of methylene glycol, *Chemical Engineering Science* 55 (2000) 2065–2071.
- [62] H.-G. Schecker, G. Schulz: Untersuchungen zur Hydratationskinetik von Formaldehyd in wäßriger Lösung, *Zeitschrift für Physikalische Chemie* 65 (1969) 221–224.
- [63] H. Hasse, G. Maurer: Kinetics of the poly(oxymethylene) glycol formation in aqueous formaldehyde solutions, *Ind. Eng. Chem. Res.* 30 (1991) 2195–2200.
- [64] E. Koberstein, K.-P. Müller, G. Nonnenmacher: Molekulargewichtsverteilung von Formaldehyd in wäßrigen Lösungen, *Berichte der Bunsengesellschaft für physikalische Chemie* 75 (1971) 549–553.
- [65] M. Ott: Reaktionskinetik und Destillation formaldehydhaltiger Mischungen, PhD Dissertation, Shaker Verlag, Aachen, 2004.
- [66] M. Rivlin, U. Eliav, G. Navon: NMR studies of the equilibria and reaction rates in aqueous solutions of formaldehyde, *The journal of physical chemistry. B* 119 (2015) 4479–4487.
- [67] Y. Tsujino, C. Wakai, N. Matubayashi, M. Nakahara: Noncatalytic Cannizzaro-type Reaction of Formaldehyde in Hot Water, *Chem. Lett.* 28 (1999) 287–288.

- [68] J. Voggenreiter, J. Burger: Side Products in the Water-Tolerant Synthesis of Poly(oxymethylene) Dimethyl Ethers: Formation Kinetics and Implications for Process Design, *Ind. Eng. Chem. Res.* 60 (2021) 2418–2429.
- [69] D. Oestreich, L. Lautenschütz, U. Arnold, J. Sauer: Reaction kinetics and equilibrium parameters for the production of oxymethylene dimethyl ethers (OME) from methanol and formaldehyde, *Chemical Engineering Science* 163 (2017) 92–104.
- [70] F. Auerbach, H. Barschall: Studien über Formaldehyd: Formaldehyd in wässriger Lösung, *Arbeiten aus dem Kaiserlichen Gesundheitsamte* 22 (1905) 584–629.
- [71] J. Bevan Ott, J. Rex Goates, B.A. Waite: (Solid + liquid) phase equilibria and solid-hydrate formation in water + methyl, + ethyl, + isopropyl, and + tertiary butyl alcohols, *The Journal of Chemical Thermodynamics* 11 (1979) 739–746.
- [72] R.L. Rowley, W.V. Wilding, J.L. Oscarson, Y. Yang, N.A. Zundel, T.E. Daubert, P. Danner: The DIPPR Information and Data Evaluation Manager for the Design Institute for Physical Properties, *AIChE*, 2018, version 12.2.0.
- [73] Q. Zhang, W. Wang, Z. Zhang, Y. Han, Y. Tan: Low-Temperature Oxidation of Dimethyl Ether to Polyoxymethylene Dimethyl Ethers over CNT-Supported Rhenium Catalyst, *Catalysts* 6 (2016) 43.
- [74] W. Wang, X. Gao, Q. Yang, X. Wang, F. Song, Q. Zhang, Y. Han, Y. Tan: Vanadium oxide modified H-beta zeolite for the synthesis of polyoxymethylene dimethyl ethers from dimethyl ether direct oxidation, *Fuel* 238 (2019) 289–297.
- [75] P. Haltenort, K. Hackbarth, D. Oestreich, L. Lautenschütz, U. Arnold, J. Sauer: Heterogeneously catalyzed synthesis of oxymethylene dimethyl ethers(OME) from dimethyl ether and trioxane, *Catalysis Communications* 109 (2018) 80–84.
- [76] E. Ströfer, H. Schelling, H. Hasse, S. Blagov: Method for the production of polyoxymethylene dialkyl ethers from trioxane and dialkylethers (US7999140 B2) 2011.
- [77] J. Burger, E. Ströfer, H. Hasse: Chemical Equilibrium and Reaction Kinetics of the Heterogeneously Catalyzed Formation of Poly(oxymethylene) Dimethyl Ethers from Methylal and Trioxane, *Ind. Eng. Chem. Res.* 51 (2012) 12751–12761.
- [78] M. Shi, X. Yu, L. Wang, F. Dai, G. He, Q. Li: Reaction Equilibrium and Kinetics of Synthesis of Polyoxymethylene Dimethyl Ethers from Formaldehyde and Methanol, *Kinet Catal* 59 (2018) 255–261.
- [79] R. Peláez, P. Marín, S. Ordóñez: Effect of formaldehyde precursor and water inhibition in dimethoxymethane synthesis from methanol over acidic ion exchange resins: mechanism and kinetics, *Biofuels, Bioprod. Bioref.* 15 (2021) 1696–1708.
- [80] R. Wang, Z. Wu, Z. Qin, C. Chen, H. Zhu, J. Wu, G. Chen, W. Fan, J. Wang: Graphene oxide, *Catal. Sci. Technol.* 6 (2016) 993–997.

- [81] J. Zhang, D. Liu: Preparation of a hydrophobic-hydrophilic adjustable catalyst surface for the controlled synthesis of polyoxymethylene dimethyl ethers: A potential replacement of diesel fuel, *Int J Energy Res* 42 (2018) 1237–1246.
- [82] V. Gnanadesikan, Y. Horiuchi, T. Ohshima, M. Shibasaki: Direct catalytic asymmetric aldol-Tishchenko reaction, *Journal of the American Chemical Society* 126 (2004) 7782–7783.
- [83] Y. Matviychuk, E. von Harbou, D.J. Holland: An experimental validation of a Bayesian model for quantification in NMR spectroscopy, *Journal of magnetic resonance* 285 (2017) 86–100.
- [84] Y. Matviychuk, E. Steimers, E. von Harbou, D.J. Holland: Bayesian approach for automated quantitative analysis of benchtop NMR data, *Journal of magnetic resonance* 319 (2020) 106814.
- [85] E. Steimers, Y. Matviychuk, A. Friebel, K. Münnemann, E. von Harbou, D.J. Holland: A comparison of non-uniform sampling and model-based analysis of NMR spectra for reaction monitoring, *Magnetic resonance in chemistry* 59 (2021) 221–236.
- [86] S. Horstmann, A. Jabłoniec, J. Krafczyk, K. Fischer, J. Gmehling: PSRK group contribution equation of state: comprehensive revision and extension IV, including critical constants and α -function parameters for 1000 components, *Fluid Phase Equilibria* 227 (2005) 157–164.
- [87] N. Schmitz: Production of poly(oxymethylene) dimethyl ethers from formaldehyde and methanol, PhD Dissertation, Laboratory of Engineering Thermodynamics (LTD), Kaiserslautern, 2018.
- [88] T. Maier, M. Härtl, E. Jacob, G. Wachtmeister: Dimethyl carbonate (DMC) and Methyl Formate (MeFo): Emission characteristics of novel, clean and potentially CO₂-neutral fuels including PMP and sub-23 nm nanoparticle-emission characteristics on a spark-ignition DI-engine, *Fuel* 256 (2019) 115925.
- [89] S. Blochum, B. Gadowski, M. Retzlaff, F. Thamm, C. Kraus, M. Härtl, R. Gelhausen, S. Hoppe, G. Wachtmeister: Potential Analysis of a DMC/MeFo Mixture in a DISI Single and Multi-Cylinder Light Vehicle Gasoline Engine, SAE Technical Paper Series, SAE International, Warrendale, 2021.
- [90] A. Stammer, T. Heitz, M. Kramp, J.-M. Kim, I.-G. Cho, J.-S. Choi, S.-Y. Lee: Energy recovery in a method for preparing 1,3,5-trioxane (US20200261823) 2020.
- [91] T. Grützner: Entwicklung eines destillationsbasierten Verfahrens zur Herstellung von Trioxan, PhD Dissertation, Logos Verlag, Berlin, 2007.
- [92] X. Zhang, Y. Hu, W. Ma, J. Qi, S. Mo: Vapor-liquid and chemical equilibria model for formaldehyde + 1,3,5-trioxane + methanol + salt + water system, *Fluid Phase Equilib* 507 (2020) 112434.
- [93] W. Ma, Y. Hu, J. Qi, L. Wei, X. Zhang, Z. Yang, S. Jiang: Acid-Catalyzed Synthesis of Trioxane in Aprotic Media, *Ind. Eng. Chem. Res.* 56 (2017) 6910–6915.

- [94] S. Jiang, X. Zhang, Y. Hu, L. Yin, J. Qi, C. Ren, S. Mo: Vapor-liquid and chemical equilibria model for formaldehyde-trioxane-sulfuric acid-water mixtures, *J. Chem. Technol. Biotechnol.* 95 (2019) 719–729.
- [95] J. Masamoto, K. Hamanaka, K. Yoshida, H. Nagahara, K. Kagawa, T. Iwaisako, H. Komaki: Synthesis of Trioxane Using Heteropolyacids as Catalyst, *Angew. Chem. Int. Ed.* 39 (2000) 2102–2104.
- [96] Q. Jianguang, H. Yufeng, M. Weiting, W. Haiyan, J. Siqu, Y. Liuyi, Z. Xianming, Y. Zhenyu, W. Yichuan: The reactions that determine the yield and selectivity of 1,3,5-trioxane, *Chem. Eng. J.* 331 (2018) 311–316.
- [97] Liu-Yi Yin, Yu-Feng Hu, Hai-Yan Wang: The remarkable effect of organic salts on 1,3,5-trioxane synthesis, *Petroleum Science* 13 (2016) 770–775.
- [98] Z. Yamei, H. Yufeng, Q. Jianguang, M. Weiting: Brønsted-acidic ionic liquids as catalysts for synthesizing trioxane, *Chinese Journal of Chemical Engineering* 24 (2016) 1392–1398.
- [99] X. Zhang, Y. Hu, W. Ma: A model for the reaction kinetics of main and side reactions during the industrial production of trioxane, and its applications, *J. Chem. Technol. Biotechnol.* 93 (2018) 2111–2117.
- [100] N. Lang, E. Ströfer, A. Stammer, T. Friese, M. Siegert, H. Hasse, T. Grützner, S. Blagov: Integriertes Verfahren zur Herstellung von Trioxan aus Formaldehyd (DE102005036544) 2005.
- [101] P.M. Synowiec, B. Bunikowska, A. Respondek, P. Tyński: New technology of vacuum trioxane crystallization from water solutions, *Chemical Engineering Research and Design* 88 (2010) 1284–1289.
- [102] H. Sokol: Production of Trioxane (US2465489) 1949.
- [103] S. Rittner, K. Burg, H. Schlaf: Verfahren zur Herstellung von reinem Trioxan (DE3508668) 1985.
- [104] H. Kniep, C. Meister, E. Schweers, I. Nicolaou, D. Scheid: Separating of trioxane from gaseous mixtures with formaldehyde (US6121467) 2000.
- [105] K. Friese, M. Rauls, R. Freyhof, T. Friese, H. Armbruster, H. Zeiner, G. Egbers, E. Ströfer, L. Heck: Method for producing pure trioxane (WO2003097630) 2003.
- [106] B.Y. Okamoto, R.H. Wood, J.E. Desnoyers, G. Perron, L. Delorme: Freezing points and enthalpies of dilute aqueous solutions of tetrahydropyran, 1,3-dioxane, 1,4-dioxane, and 1,3,5-trioxane. Free energies and enthalpies of solute-solute interactions, *Journal of Solution Chemistry* 10 (1981) 139–152.
- [107] M.L. Sagu, J. Swarup, K.M. Sharan, K.K. Bhattacharyya: Solubility of trioxane in some common solvents, *J. Chem. Eng. Data* 28 (1983) 81–83.
- [108] S. Brandani, V. Brandani, D. Flammini: Solubility of trioxane in water, *J. Chem. Eng. Data* 39 (1994) 201–202.

- [109] H. Freund, R. Steiner: Determination of Binary Melt Freezing Curves under Gas Pressure, *Chem. Eng. Technol.* 21 (1998) 719–723.
- [110] C. Kuhnert: Dampf-Flüssigkeits-Gleichgewichte in mehrkomponentigen formaldehydhaltigen Systemen, PhD Dissertation, Shaker Verlag, Aachen, 2004.
- [111] M. Albert: Thermodynamische Eigenschaften formaldehydhaltiger Mischungen, PhD Dissertation, Shaker Verlag, Aachen, 1999.
- [112] R. Wittig, J. Lohmann, J. Gmehling: Vapor–Liquid Equilibria by UNIFAC Group Contribution. 6. Revision and Extension, *Ind. Eng. Chem. Res.* 42 (2003) 183–188.
- [113] H. Hasse: Thermodynamics of reactive separations, in: K. Sundmacher, A. Kienle (Eds.), *Reactive distillation: status and future directions*, Wiley-VCH Verlag GmbH & Co. KGaA, Weinheim, 2003, pp. 65–96.
- [114] M. Albert, H. Hasse, C. Kuhnert, G. Maurer: New Experimental Results for the Vapor–Liquid Equilibrium of the Binary System (Trioxane + Water) and the Ternary System (Formaldehyde + Trioxane + Water), *J. Chem. Eng. Data* 50 (2005) 1218–1223.
- [115] A.T. Sundberg, P. Uusi-Kyyny, M. Pakkanen, V. Alopaeus: Vapor–Liquid Equilibrium for Methoxymethane + Methyl Formate, Methoxymethane + Hexane, and Methyl Formate + Methanol, *J. Chem. Eng. Data* 56 (2011) 2634–2640.
- [116] J. Burger, E. Ströfer, H. Hasse: Process Design in World 3.0 - Challenges and Strategies to Master the Raw Material Change, *Chem. Eng. Technol.* 39 (2016) 219–224.
- [117] O. Ryll, S. Blagov, H. Hasse: ∞/∞ -Analysis of homogeneous distillation processes, *Chemical Engineering Science* 84 (2012) 315–332.
- [118] M. Bortz, J. Burger, N. Asprion, S. Blagov, R. Böttcher, U. Nowak, A. Scheithauer, R. Welke, K.-H. Küfer, H. Hasse: Multi-criteria optimization in chemical process design and decision support by navigation on Pareto sets, *Computers & Chemical Engineering* 60 (2014) 354–363.
- [119] S. Zeck: Einfluß von thermophysikalischen Stoffdaten auf die Auslegung und den Betrieb von Destillationskolonnen, *Chemie Ingenieur Technik* 62 (1990) 707–717.
- [120] M. Münz, A. Mokros, C. Beidl: Analysis of two engine configurations using OME as a potential CO₂-neutral and low emission diesel substitute, in: J. Liebl, C. Beidl, W. Maus (Eds.), *Internationaler Motorenkongress 2019*, Springer Fachmedien Wiesbaden, Wiesbaden, 2019, pp. 369–384.
- [121] M. Härtl, K. Gaukel, D. Pélerin, G. Wachtmeister: Oxymethylenether als potenziell CO₂-neutraler Kraftstoff für saubere Dieselmotoren Teil 1, *MTZ Motortech Z* 78 (2017) 52–59.
- [122] M. Unglert, D. Bockey, C. Bofinger, B. Buchholz, G. Fisch, R. Luther, M. Müller, K. Schaper, J. Schmitt, O. Schröder, U. Schümann, H. Tschöke, E. Remmele, R. Wicht, M. Winkler, J. Krahl: Action areas and the need for research in biofuels, *Fuel* 268 (2020) 117227.

- [123] A. Sonthalia, N. Kumar: Hydroprocessed vegetable oil as a fuel for transportation sector: A review, *Journal of the Energy Institute* 92 (2019) 1–17.
- [124] P. Simacek, I. Soucek, M. Pospisil, D. Vrtiska, H. Kittel: Impact of hydrotreated vegetable oil and biodiesel on properties in blends with mineral diesel fuel, *Therm sci* 23 (2019) 1769–1777.
- [125] A. Vonortas, N. Papayannakos: Comparative analysis of biodiesel versus green diesel, *WIREs Energy Environ* 3 (2014) 3–23.
- [126] M. Al-Sabawi, J. Chen: Hydroprocessing of Biomass-Derived Oils and Their Blends with Petroleum Feedstocks: A Review, *Energy Fuels* 26 (2012) 5373–5399.
- [127] J.V. Pastor, J.M. García-Oliver, C. Micó, A.A. García-Carrero, A. Gómez: Experimental Study of the Effect of Hydrotreated Vegetable Oil and Oxymethylene Ethers on Main Spray and Combustion Characteristics under Engine Combustion Network Spray A Conditions, *Applied Sciences* 10 (2020) 5460.
- [128] S.-Y. No: Application of hydrotreated vegetable oil from triglyceride based biomass to CI engines – A review, *Fuel* 115 (2014) 88–96.
- [129] J. Preuß, K. Munch, I. Denbratt: Performance and emissions of renewable blends with OME3-5 and HVO in heavy duty and light duty compression ignition engines, *Fuel* 303 (2021) 121275.
- [130] A. Omari, B. Heuser, S. Pischinger, C. Rüdinger: Potential of long-chain oxymethylene ether and oxymethylene ether-diesel blends for ultra-low emission engines, *Applied Energy* 239 (2019) 1242–1249.
- [131] E. Jacob, I. Bogatykh, T. Goral, P. Seidenspinner, T. Wilharm, A. Peter, H. Scherer, I. Krossing: Synthetische Kraftstoffe gegen Klimawandel und für die Reinhaltung der Umwelt /Synthetic Fuels against Climate Change and Environmental Pollution, 41. Internationales Wiener Motorensymposium, II-114-II-148.
- [132] I. Mokbel, C. Lindemann, P. Duchet-Suchaux, J. Jose: Liquid–liquid equilibria of binary and ternary systems involving monoethyleneglycol, water, n-alkanes at three temperatures: 283.15, 303.15 and 333.15 K, *Fuel* 163 (2016) 17–24.
- [133] C. Sutton, J.A. Calder: Solubility of higher-molecular-weight normal-paraffins in distilled water and sea water, *Environ. Sci. Technol.* 8 (1974) 654–657.
- [134] Z. Zhuang, J. Zhang, D. Liu: Liquid-liquid equilibria for ternary systems polyoxymethylene dimethyl ethers + water + n-hexane, *CIESC Journal* 67 (2016) 3545–3551.
- [135] M. Shi, X. Yu, G. He, Q. Li: Liquid-liquid equilibrium for the ternary systems water + DMM 3 + (p -xylene, toluene, and n -heptane) at different temperatures, *Can. J. Chem. Eng.* 96 (2018) 968–977.

- [136] M. Shi, G. He, F. Gan, X. Yu, Q. Li: Extraction of Low Concentration Aqueous Solution of Methylal: Liquid–Liquid Equilibrium in Water + Methylal + (Cyclohexane and n - Heptane) Ternary Systems, *J. Chem. Eng. Data* 62 (2017) 2183–2190.
- [137] X. Li, H. Tian, D. Liu: Liquid–Liquid Equilibrium for Ternary Systems of Polyoxymethylene Dimethyl Ethers + o -Xylene + Water at 293.15 K, *J. Chem. Eng. Data* (2019).
- [138] X. Li, J. Cao, M.A. Nawaz, Y. Hu, D. Liu: Experimental and Correlated Liquid–Liquid Equilibrium Data for Ternary Systems (Water + Poly(oxymethylene) Dimethyl Ethers + Toluene) at T = 293.15 and 303.15 K and p = 101.3 kPa, *J. Chem. Eng. Data* 64 (2019) 5548–5557.
- [139] J. Gross, G. Sadowski: Application of the Perturbed-Chain SAFT Equation of State to Associating Systems, *Ind. Eng. Chem. Res.* 41 (2002) 5510–5515.
- [140] J. Gross, J. Vrabec: An equation-of-state contribution for polar components: Dipolar molecules, *AIChE J.* 52 (2006) 1194–1204.
- [141] S. Skjold-Jorgensen, B. Kolbe, J. Gmehling, P. Rasmussen: Vapor-Liquid Equilibria by UNIFAC Group Contribution. Revision and Extension, *Ind. Eng. Chem. Proc. Des. Dev.* 18 (1979) 714–722.
- [142] Z. Yang, C. Ren, S. Jiang, Y. Xin, Y. Hu, Z. Liu: Theoretical predictions of compatibility of polyoxymethylene dimethyl ethers with diesel fuels and diesel additives, *Fuel* 307 (2022) 121797.
- [143] A. Klamt: Conductor-like Screening Model for Real Solvents: A New Approach to the Quantitative Calculation of Solvation Phenomena, *J. Phys. Chem.* 99 (1995) 2224–2235.
- [144] M. Yu, C. Chen, X. Jiang: Understanding the miscibility of polyoxymethylene dimethyl ethers (OMEn) and diesel blend using molecular dynamics simulation, *Fuel* 323 (2022) 124348.
- [145] J. Gmehling, P. Rasmussen, A. Fredenslund: Vapor-liquid equilibria by UNIFAC group contribution. Revision and extension. 2, *Ind. Eng. Chem. Proc. Des. Dev.* 21 (1982) 118–127.
- [146] M.O. Ohanamah, D.W. Thompson: Computation of multicomponent phase equilibria— Part II. Liquid-liquid and solid-liquid equilibria, *Computers & Chemical Engineering* 8 (1984) 157–162.
- [147] M. Kang, H. Song, F. Jin, J. Chen: Synthesis and physicochemical characterization of polyoxymethylene dimethyl ethers, *Journal of Fuel Chemistry and Technology* 45 (2017) 837–845.
- [148] M. Dyga, A. Keller, H. Hasse: Density of solutions of formaldehyde in water and alcohols, *AIChE J.* (2022).
- [149] J. Marrero, R. Gani: Group-contribution based estimation of pure component properties, *Fluid Phase Equilibria* 183-184 (2001) 183–208.

-
- [150] R. Reid: The properties of gases and liquids, McGraw-Hill, New York, 1987.
- [151] G. H. Thomson: The DIPPR databases, *Int. J. Thermophys.* 17 (1996) 223–232.
- [152] Michael Kleiber: The trouble with c_p^{liq} , *Ind. Eng. Chem. Res.* 42 (2003) 2007–2014.
- [153] Milan Zábanský, Vlastimil Růžička: Estimation of the heat capacities of organic liquids as a function of temperature using group additivity: an amendment, *J. Phys. Chem. Ref. Data* 33 (2004) 1071–1081.
- [154] National Institute of Advanced Industrial Science and Technology: SDBSWeb. <https://sdfs.db.aist.go.jp>. Accessed 17 October 2022.

Appendix

In the following, supporting information for each chapter is given. UNIFAC-based activity coefficient models were used in different chapters. They are similar, but differ in details, i.e., some groups and some interaction parameters may differ. For clarity, for each chapter the whole parameterization is given.

A Supporting information for Chapter 2

A.1 Ion chromatography

To measure the concentration of formic acid in the liquid phase, ion chromatography was used. For sample preparation, 0.1 g of the liquid phase was diluted with about 11.9 g water. The diluted sample was measured in a Compact 930 IC Flex from Metrohm. Every sample was measured at least 3 times. First, the peak areas of the individual measurements were averaged and then the concentration was calculated using a quadratic calibration curve, which was done with every series. The apparatus was equipped with an anion exchange column from Metrohm (Metrosep A Supp 5 – 250/ 4.0) and a conductivity detector. An aqueous solution of 3.2 mM sodium carbonate and 1 mM sodium hydrogen carbonate was used as eluent. The uncertainty was estimated with gravimetrically prepared samples to be below 2%.

A.2 Formation of further side components and their measurement

In the presence of acids, formaldehyde can form trioxane (TRX) according to Reaction (VIII). As in the present work, time periods up to 1000 days were studied, these products could, in principle, have been formed even though no acids were added [33,59]. Furthermore, the condensation of formic acid and methanol to methyl formate is possible. Therefore, in this work, the samples were also tested for trioxane, and methyl formate. This was done by gas chromatography using the same equipment as for the analysis for OME. Therefore, the formation of OME in samples without OME would have been recognized. None of the side products mentioned in the present section were found in the samples from Chapter 2.

A.3 UNIFAC-based model for the calculation of the activity coefficient

The non-ideality in the liquid phase is described in this work by the UNIFAC-based model developed by Maurer[7]. In this work, the most recent version is used from Schmitz et al.[56]. The equations can be found at Wittig et al.[112]. The group assignment is given in Table 31. The size and surface parameters are shown in Table 32 and the interaction parameters in Table 33.

Table 31: Group assignment for the UNIFAC-based model adopted from Schmitz et al.[56].

Component	Structural groups
FA	1 CH ₂ O
W	1 H ₂ O
MeOH	1 CH ₃ OH
MG ₁	1 HO-CH ₂ O-H
HF ₁	1 CH ₃ O, 1 CH ₂ OH
MG _{<i>n</i>} (<i>n</i> ≥ 2)	(<i>n</i> -1) CH ₂ O, 2 OH, 1CH ₂
HF _{<i>n</i>} (<i>n</i> ≥ 2)	(<i>n</i> -1) CH ₂ O, 1 CH ₃ O, 1 CH ₂ OH

Table 32: Size (R) and surface (Q) parameters of the groups used in the UNIFAC-based model. Parameters are adopted from Schmitz et al.[56].

Structural group	Number	R	Q
CH ₂ O	1	0.9183	0.780
H ₂ O	2	0.9200	1.400
CH ₃ OH	3	1.4311	1.432
HO-CH ₂ O-H	4	2.6744	2.940
CH ₂ OH	5	1.2044	1.124
CH ₃ O	6	1.1459	1.088
OH	7	1.000	1.200
CH ₂	8	0.6744	0.540

Table 33: Interaction parameters $a_{k,m}/K$ for the UNIFAC based model. All parameters are adopted from Schmitz et al.[56]. Numeration of the groups is shown in Table 32.

k/m	1	2	3	4	5	6	7	8
1	-	867.8	238.4	189.2	238.4	0	237.7	83.36
2	-254.5	-	289.6	189.5	$a_{2,8}(T)$	-219.3	-229.1	300
3	-128.6	-181.0	-	-181	0	-128.6	249.1	16.5
4	59.2	-191.8	289.6	-	289.6	-142.4	-229.1	300
5	-128.6	$a_{8,2}(T)$	0	-181	-	-128.6	249.1	16.5
6	0	423.8	238.4	774.8	238.4	-	1164.8	273
7	28.06	353.5	-137.1	353.5	-137.1	-137.1	-	156.4
8	251.5	1318	697.2	1318	697.2	447.8	986.5	-

$$a_{2,8}(T): 451.64-114100/(T \text{ K}^{-1}); a_{8,2}(T): -1018.57 + 329900 / (T \text{ K}^{-1})$$

A.4 Chemical equilibrium model

According to Reaction (I) to (IV), the equilibrium constants of the reactions are described as temperature-dependent by an extended Van't Hoff approach, as shown in Equation (32). The values for the parameters are adopted from Schmitz et al.[56] and are given in Table 34.

$$\ln(K_{a,j}(T)) = A_j + B_j/T/K + C_j \cdot \ln(T/K) + D_j \cdot (T/K) \quad (32)$$

Table 34: Parameters for the correlation of the reaction equilibrium constants (cf. Equation (32)) from Schmitz et al.[56].

reaction	<i>A</i>	<i>B</i>	<i>C</i>	<i>D</i>
1	-30.946	4.819•10 ³	3.741	-4.534•10 ⁻³
2 with <i>n</i> = 2	-30.941	5.653•10 ³	3.741	-4.534•10 ⁻³
2 with <i>n</i> > 2	-30.933	5.361•10 ³	3.741	-4.534•10 ⁻³
3	1.1297•10 ³	-2.510•10 ⁴	-1.984•10 ²	0.316
4 with <i>n</i> = 2	1.129•10 ³	-2.551•10 ⁴	-1.984•10 ²	0.316
4 with <i>n</i> > 2	1.129•10 ³	-2.563•10 ⁴	-1.984•10 ²	0.316

A.5 Coupling of the solubility constants for different values of *p*

As described in the main body, the solubility constant K_p^{SL} is calculated from the liquid phase composition in equilibrium by Equation (2) for one specific number of *p*. In this equation, the activity of the precipitating MG_p is used. The activity of this MG_p is coupled to the activities of other MG_{p-1} by the chemical equilibrium condition:

$$K_{a,2} = \frac{a_{MG,p}}{a_{MG,p-1} \cdot a_{FA}} \quad (33)$$

Therefore the solubility constant for MG_p can be calculated from the solubility constant of MG_{p-1} by Equation (34).

$$K_p^{SL} = K_{p-1}^{SL} \cdot \frac{1}{a_{FA} \cdot K_{a,2}} \quad (34)$$

Equation (34) shows that all solubility constants in an equilibrated mixture are related. Still, upon changing the external conditions, such as the temperature or the overall formaldehyde concentration, it is one specific MG_p for which the solubility limit is reached first.

A.6 Reaction kinetic model

The equations and parameters are adopted from Ott[65], except for the parameters for describing the degradation of MG_2 . These had to be readjusted to the experimental data of Ott since the original adjustment resulted in a physically impossible change of sign at temperatures of about 273 K and pH values close to 3. The problem is described in the following. For the correlation of k_j of the reactions according to Reaction (I) and (III) of the main manuscript Equation (35) and Equation (36), for the Reaction (II), Equation (37), and for the Reaction (IV), Equation (34) are used. The corresponding parameters for Equations (37) and (38) are given in Table 35.

$$k_1^+ = 0.785 \cdot 10^5 \cdot \exp\left(-\frac{2936}{T/K}\right) \quad (35)$$

$$k_3^+ = \exp\left(10.987 - \frac{4939}{T/K}\right) \quad (36)$$

$$k_2^- = \exp\left(A - \frac{B}{T/K}\right) \left[\exp\left(C - \frac{D}{T/K}\right) \cdot pH^2 - \exp\left(E - \frac{F}{T/K}\right) \cdot pH + G \right] \quad (37)$$

$$k_4^- = \exp\left(A - \frac{B}{T/K + C}\right) \cdot pH^2 - \exp\left(D - \frac{E}{T/K + F}\right) \cdot pH \quad (38)$$

$$+ \exp\left(G - \frac{H}{T/K + I}\right)$$

Table 35: Parameters for the correlation of the rate constants k_j . For the different reactions j the corresponding parameters are dependent on the oligomer chain length n , which is formed in the corresponding reaction.

j	n	A	B	C	D	E	F	G	H	I
2	2	4.53	4220.32	-6.65	-2040.33	-3.47	-1661.38	-28.54		
2	> 2	13.89	7865.23	4.78	-223.07	7.24	-78.93	3525.97		
4	2	3.61	2758.14	-91.29	9.98	4935.07	-17.42	24.05	15833.14	214.55
4	> 2	5.86	2926.03	-111.2	10.78	4309.9	-64.69	25.15	14325.41	148.93

A.7 New fit of the rate constant of the degradation of MG₂

Ott[65] used the correlation according to Equation (37) to describe the rate constant for the back reaction of MG₂ to formaldehyde and MG₁ (cf. Reaction (XVIII)).



Ott adjusted the correlation to the experimental values given in Table 36. The parameters obtained are given in Table 35.

Table 36: Experimental values for the reaction rate constant of the degradation of MG_2 in dependence of temperature and pH value from Ott[65].

T / K	pH	$k_{\text{MG}_2}^- / \text{s}^{-1} \cdot 10^4$
293.60	2.99	4.500
292.90	3.97	5.163
293.35	5.38	12.470
293.00	6.89	17.410
313.50	2.76	25.600
313.45	3.46	25.800
313.00	4.01	21.000
313.70	4.75	32.300
313.00	5.89	34.640
323.00	1.93	43.870
323.00	3.17	36.210
323.00	4.17	35.760
323.00	4.97	50.990
323.00	5.99	38.820
323.00	6.93	52.440

Figure 46 shows the model and the experimental data plotted over temperature and pH value. The already mentioned negative values for temperatures below 273 K and pH values close to 3 can be seen as white areas. Unfortunately, these values are not physically possible and mean that the kinetic model cannot be used in the context of this work without any modification.

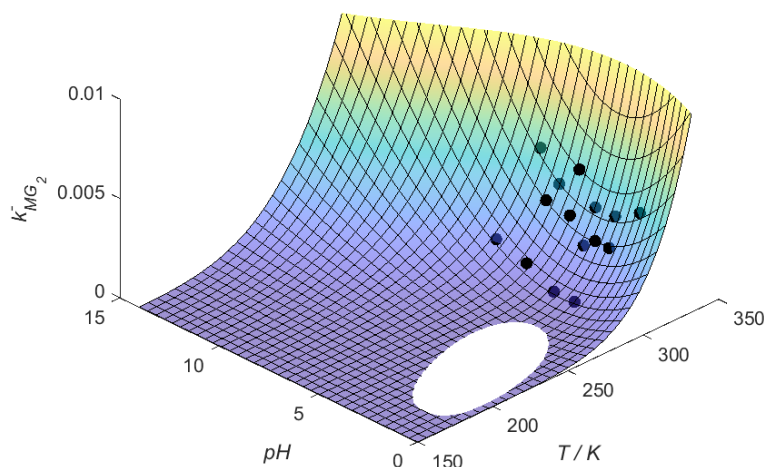


Figure 46: Rate constant for the degradation of MG_2 in dependence of temperature and pH value. The surface is calculated with Equation (37) and the parameters of Ott[65]. Symbols show the experimental values from Ott (cf. Table 36). The white area shows the cut with $k_{\text{MG}_2}^- = 0$.

To preserve the structure of the original model, but at the same time to obtain physically meaningful values for the temperatures up to 263 K that are relevant in this work, the model parameters were changed slightly. As a result, the relative deviation between model and experimental data has slightly increased from 0.1373 to 0.1662. The newly obtained parameters are given in Table 37. Experimental data and the model data calculated with the new parameters are shown in Figure 47. The negative values are now only obtained at lower temperatures.

Table 37: Parameters of this work for correlating the rate constant of MG_2 degradation according to Equation (37).

A	B	C	D	E	F	G
4.53	4220.32	-6.65	-2040.32	-3.47	-1661.38	-28.54

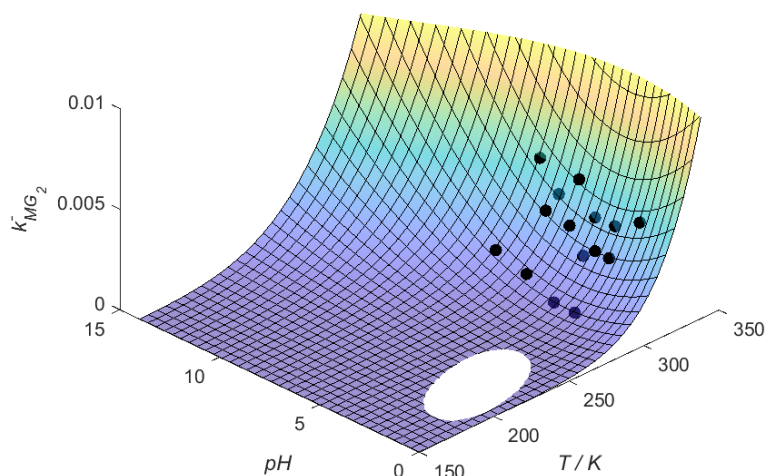


Figure 47: Rate constant for the degradation of MG_2 in dependence of temperature and pH value. The surface is calculated with Equation (37) and the parameters of this work (cf. Table 37). Symbols show the experimental values from Ott[65] (cf. Table 36). The white area shows the cut with $k_{\text{MG}_2}^- = 0$.

Since the formation of MG_2 from MG_1 is secondary in the modelling within the scope of this work, because it is more about the formation and degradation of the longer chains, it is assumed that this slight deterioration of the description of the experimental data does not have a major impact. Nevertheless, the choice of a fully physically meaningful correlation approach and an extension of the experimental data to lower temperatures would be of great benefit. However, this was not the scope of this work.

A.8 Experimental data for the systems (formaldehyde + water) and (formaldehyde + water + methanol)

Table 38 first gives an overview of all measurements carried out in this work concerning the precipitation of solid formaldehyde. In the following, the measured overall formaldehyde concentration profiles over time for all experiments are shown. Furthermore, all measured concentrations, also of formic acid (FAc) and water, are given in the corresponding tables. The figures also show the kinetic model profiles calculated for precipitating MG_9 and, if it differs, for the most matching MG_p . The grey area shows the variance that is achieved for the profiles by varying the pH by 0.5. For samples 18 to 22, the water content in the solvent mixture $\tilde{x}_{\text{W,sol}}^{(m)}$ is also varied by 0.01 g g^{-1} . Disturbances in the test procedure are noted in the tables for the respective sample.

Table 38: Overview of all samples measured in this work regarding the precipitation of solid formaldehyde.

Sample	T	$\tilde{x}_{\text{NaOH}}^{(m)}$ in feed $\text{g g}^{-1} \cdot 10^{-3}$	$\tilde{x}_{\text{W,sol}}^{(m)}$ in feed g g^{-1}	Equilibrium	Shown in Figure	Best fitting p
1	303.4	1.080	1	yes	Figure 3, Figure 4, Figure 16 b)	13
				yes		9
2	293.3	0.902	1			
3	283.0	0.390	1	yes	Figure 3	8
4	273.2	0.784	1	yes	Figure 3	7
5	303.4	1.060	0.869	yes		13
6	293.3	0.772	0.870	yes		10
7	283.0	0.382	0.870	yes		8
8	273.2	0.389	0.870	yes		6
9	263.0	0.389	0.870	yes		5
10	303.4	1.030	0.729	yes		13
11	293.3	0.786	0.732	yes		10
12	283.0	0.774	0.731	yes		8
13	273.2	0.588	0.731	yes		6
14	263.0	0.819	0.732	yes		5
15	283.0	1.030	0.601	yes		7
16	273.2	1.050	0.600	yes		6
17	263.0	1.060	0.598	yes		6
18	303.4	1.130 ^a	≤ 0.02	yes		
19	293.3	1.770 ^a	0.02	yes		
20	283.0	1.956 ^a	≤ 0.02	yes		
21	273.2	1.916 ^a	≤ 0.02	yes		
22	263.0	0.736 ^a	≤ 0.02	yes		
23	293.3	0	1	no	6	12
24	293.3	0	1	no		11
25	283.0	1.333	1	no		8
26	273.2	0.836	1	no		7
27	273.2	0.773	1	no		6
28	273.2	0	1	no		8
29	273.2	0	1	no		9
30	273.2	0	1	no		9
31	273.2	0	1	no	Figure 16 a)	9
32	273.2	0	1	no		9
33	273.2	0	1	no	Figure 5	9
34	273.2	0	0.87	no		8

Table 38 continued

35	273.2	0	087	no		9
36	273.2	0	0.84	no		9
37	273.2	0	0.752	no		10
38	273.2	0	0.72	no		8
39	273.2	0	0.641	no		9
40	273.2	0	0.631	no		9
41	273.2	0	0.728	no		9
42	263.0	0	0.872	no		8
43	263.0	0	0,861	no		8
44	263.0	0	0.729	no		9
45	263.0	0	0.727	no		8
46	273.2	0	1	no	Figure 5	

^(a) Instead of sodium hydroxide the fraction of sodium methylate is given

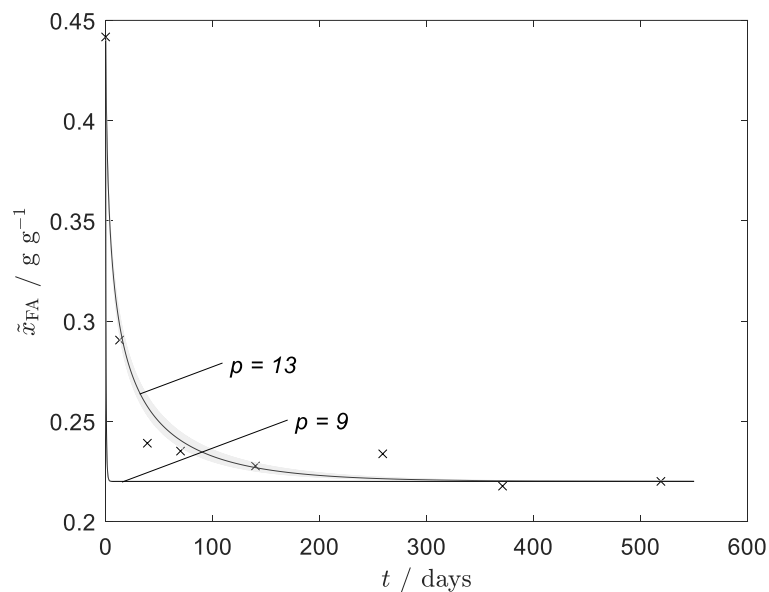


Figure 48: Experimental and calculated overall formaldehyde concentration profile over time for sample No. 1. Grey area shows a variation of the pH in the model by 0.5. (×) Measurement, (—) model.

Table 39: Measured concentrations of the liquid phase over time for sample No. 1.

t / days	$\tilde{x}_{\text{FA}}^{(m)} / \text{g g}^{-1}$	$\tilde{x}_{\text{FAc}}^{(m)} / \text{g g}^{-1} \cdot 10^{-3}$
0	0.4417	n.a.
13	0.2905	1.389
39	0.2390	n.a.
70	0.2351	n.a.
140	0.2277	1.778
259	0.2338	1.680
371	0.2176	1.629
519	0.2200	n.a.

n.a. : not available

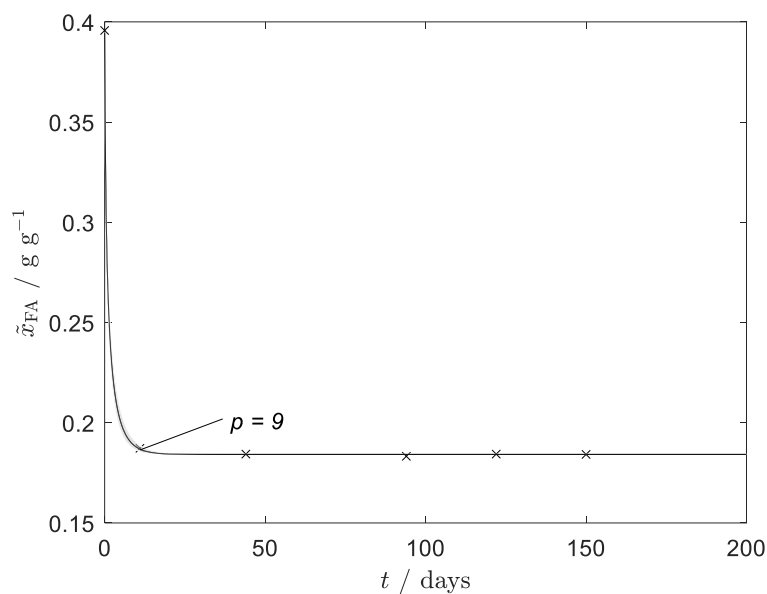


Figure 49: Experimental and calculated overall formaldehyde concentration profile over time for sample No. 2. Grey shaded area shows a variation of the pH in the model by 0.5. (×) Measurement, (—) model.

Table 40: Measured concentration of the liquid phase over time for sample No. 2.

t / days	$\tilde{x}_{\text{FA}}^{(m)} / \text{g g}^{-1}$	$\tilde{x}_{\text{FAc}}^{(m)} / \text{g g}^{-1} \cdot 10^{-3}$
0	0.3957	n.a.
11	0.1873	1.153
44	0.1844	1.453
94	0.1833	1.440
122	0.1844	1.460
150	0.1842	n.a.

n.a. : not available

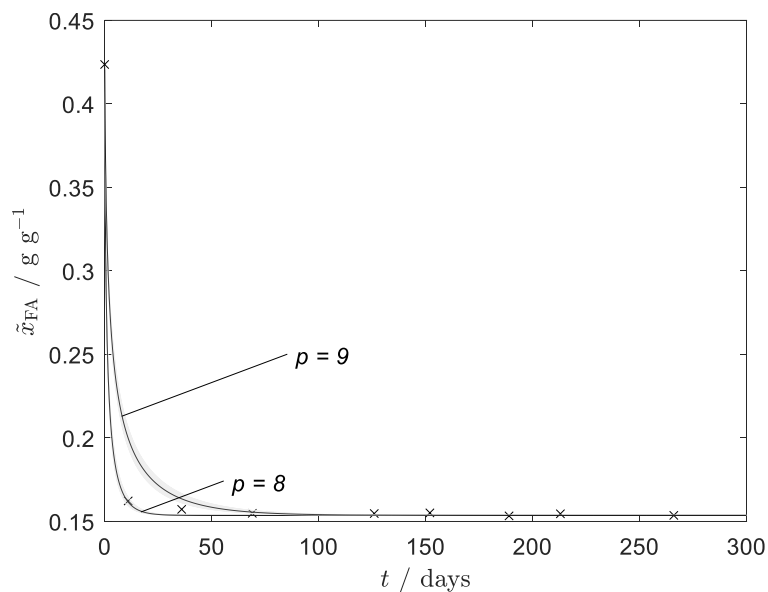


Figure 50: Experimental and calculated overall formaldehyde concentration profile over time for sample No. 3. Grey shaded area shows a variation of the pH in the model by 0.5. (×) Measurement, (—) model.

Table 41: Measured concentration of the liquid phase over time for sample No. 3.

t / days	$\tilde{x}_{\text{FA}}^{(m)} / \text{g g}^{-1}$	$\tilde{x}_{\text{FAc}}^{(m)} / \text{g g}^{-1} \cdot 10^{-3}$
0	0.4236	n.a.
11	0.1623	n.a.
36	0.1573	n.a.
69	0.1549	n.a.
126	0.1548	n.a.
152	0.1552	0.552
189	0.1534	0.540
213	0.1546	n.a.
266	0.1538	n.a.

n.a. : not available

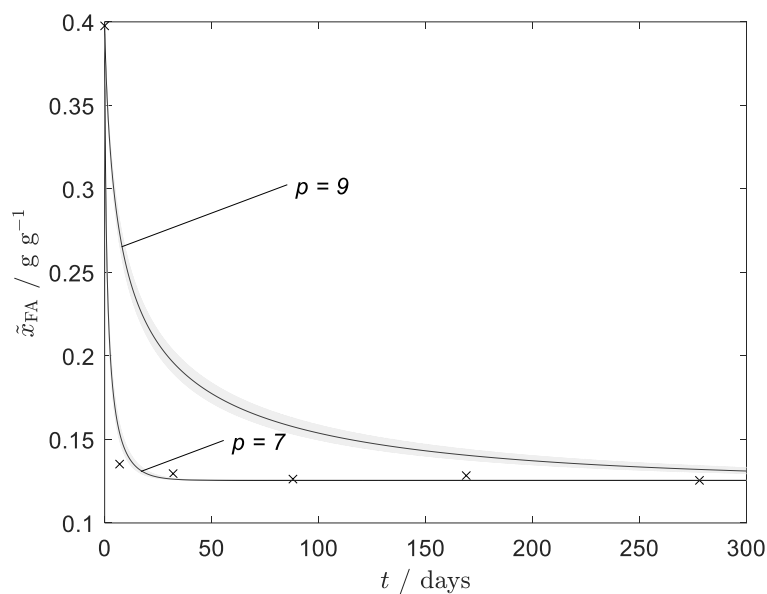


Figure 51: Experimental and calculated overall formaldehyde concentration profile over time for sample No. 4. Grey shaded area shows a variation of the pH in the model by 0.5. (×) Measurement, (—) model.

Table 42: Measured concentration of the liquid phase over time for sample No. 4.

t / days	$\tilde{x}_{\text{FA}}^{(m)} / \text{g g}^{-1}$	$\tilde{x}_{\text{FAc}}^{(m)} / \text{g g}^{-1} \cdot 10^{-3}$
0	0.3976	n.a.
7	0.1352	n.a.
32	0.1295	0.735
88	0.1263	n.a.
169	0.1284	n.a.
278	0.1255	1.190

n.a. : not available

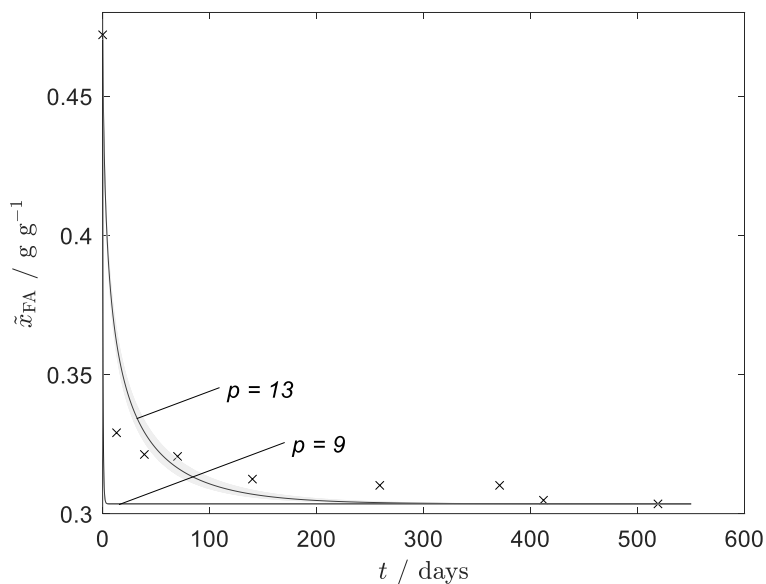


Figure 52: Experimental and calculated overall formaldehyde concentration profile over time for sample No. 5. Grey shaded area shows a variation of the pH in the model by 0.5. (×) Measurement, (—) model.

Table 43: Measured concentration of the liquid phase over time for sample No. 6.

t / days	$\tilde{x}_{\text{FA}}^{(m)} / \text{g g}^{-1}$	$\tilde{x}_{\text{W}}^{(m)} / \text{g g}^{-1}$	$\tilde{x}_{\text{FAC}}^{(m)} / \text{g g}^{-1} \cdot 10^{-3}$
0	0.472	0.4586	n.a.
13	0.3291	0.586	1.392
39	0.3213	0.5886	n.a.
70	0.3206	0.5883	n.a.
140	0.3124	0.5959	1.721
259	0.3102	0.534	1.650
371	0.3102	0.6038	1.621
412	0.3048	0.6072	1.974
519	0.3035	0.6097	n.a.

n.a. : not available

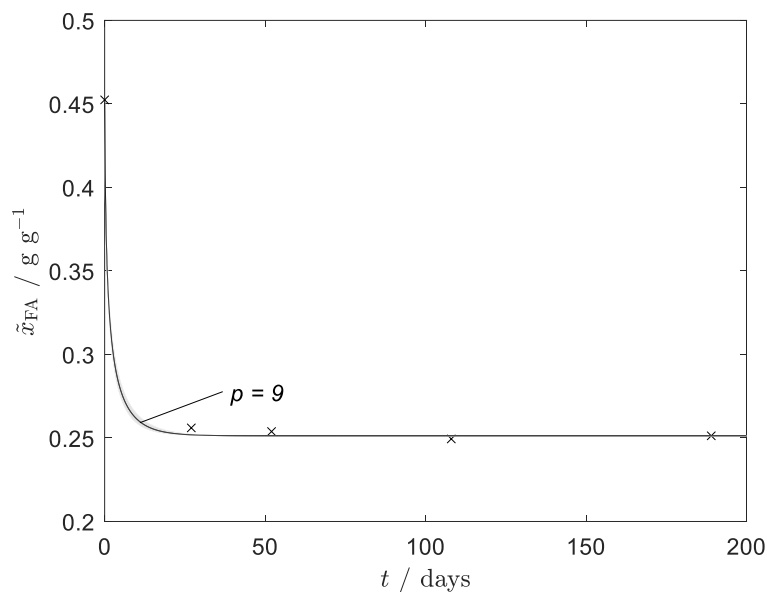


Figure 53: Experimental and calculated overall formaldehyde concentration profile over time for sample No. 6. Grey shaded area shows variation of the pH in the model by 0.5. (×) Measurement, (—) model.

Table 44: Measured concentration of the liquid phase over time for sample No. 6.

t / days	$\tilde{x}_{\text{FA}}^{(m)} / \text{g g}^{-1}$	$\tilde{x}_{\text{W}}^{(m)} / \text{g g}^{-1}$	$\tilde{x}_{\text{FAC}}^{(m)} / \text{g g}^{-1} \cdot 10^{-3}$
0	0.4524	0.4764	n.a.
27	0.256	0.6398	n.a.
52	0.2539	0.6466	1.071
108	0.2494	0.6527	1.140
189	0.2513	0.6555	1.260

n.a. : not available

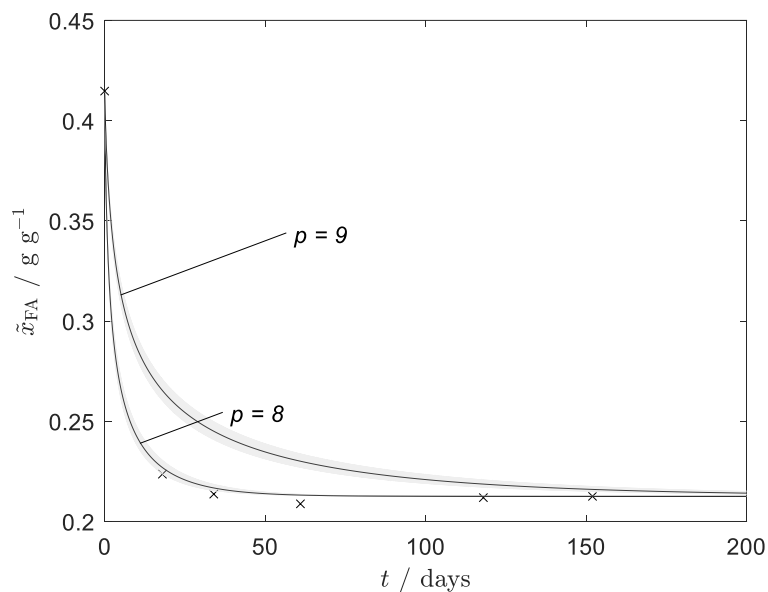


Figure 54: Experimental and calculated overall formaldehyde concentration profile over time for sample No. 7. Grey shaded area shows a variation of the pH in the model by 0.5. (×) Measurement, (—) model.

Table 45: Measured concentration of the liquid phase over time for sample No. 7.

t / days	$\tilde{x}_{\text{FA}}^{(m)} / \text{g g}^{-1}$	$\tilde{x}_{\text{W}}^{(m)} / \text{g g}^{-1}$	$\tilde{x}_{\text{FAC}}^{(m)} / \text{g g}^{-1} \cdot 10^{-3}$
0	0.4147	0.5093	n.a.
18	0.2236	0.7059	0.344
34	0.2137	0.6894	0.470
61	0.2088	0.677	n.a.
118	0.2119	0.6741	0.502
152	0.2126	0.7031	0.522

n.a. : not available

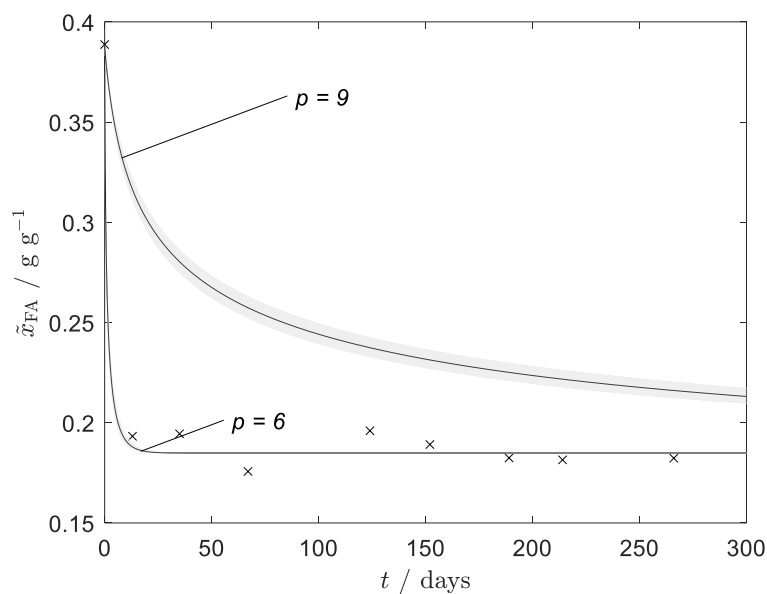


Figure 55: Experimental and calculated overall formaldehyde concentration profile over time for sample No. 8. Grey shaded area shows a variation of the pH in the model by 0.5. (×) Measurement, (—) model.

Table 46: Measured concentration of the liquid phase over time for sample No. 8.

t / days	$\tilde{x}_{\text{FA}}^{(m)} / \text{g g}^{-1}$	$\tilde{x}_{\text{W}}^{(m)} / \text{g g}^{-1}$	$\tilde{x}_{\text{FAC}}^{(m)} / \text{g g}^{-1} \cdot 10^{-3}$
0	0.3887	0.5321	n.a.
13	0.1933	0.7284	n.a.
35	0.1945	0.7164	n.a.
67	0.1757	0.7104	n.a.
114		Temperature control failure	
124	0.1960	0.7151	0.332
152	0.1892	0.7287	0.394
189	0.1825	0.7247	0.402
214	0.1815	0.7546	0.5
266	0.1823	0.5279	n.a.

n.a. : not available

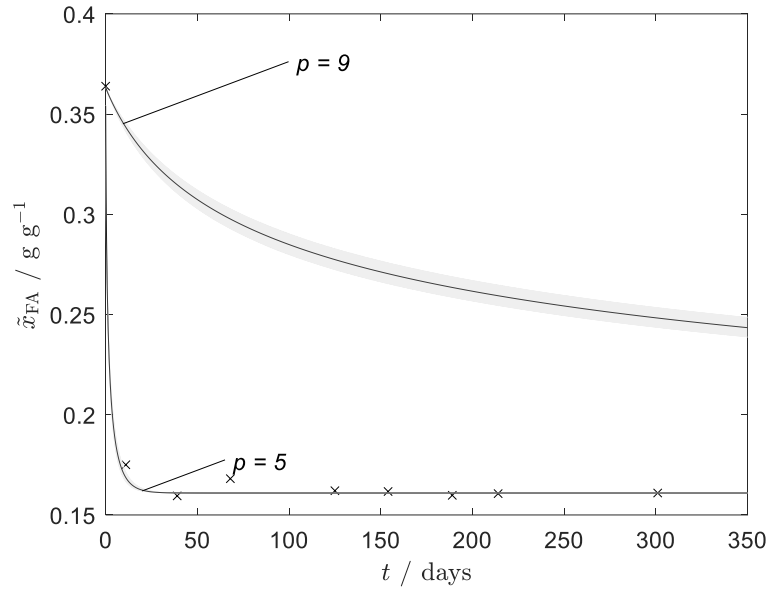


Figure 56: Experimental and calculated overall formaldehyde concentration profile over time for sample No. 9. Grey shaded area shows a variation of the pH in the model by 0.5. (×) Measurement, (—) model.

Table 47: Measured concentration of the liquid phase over time for sample No. 9.

t / days	$\tilde{x}_{\text{FA}}^{(m)} / \text{g g}^{-1}$	$\tilde{x}_{\text{W}}^{(m)} / \text{g g}^{-1}$	$\tilde{x}_{\text{FAC}}^{(m)} / \text{g g}^{-1} \cdot 10^{-3}$
0	0.3639	0.5536	n.a.
11	0.1751	0.745	0.208
39	0.1595	0.7514	0.194
68	0.1681	0.7066	n.a.
125	0.1621	0.7318	0.215
154	0.1617	0.745	0.207
189	0.1598	0.7364	0.234
214	0.1607	0.7642	0.249
301	0.1610	0.7473	0.270

n.a. : not available

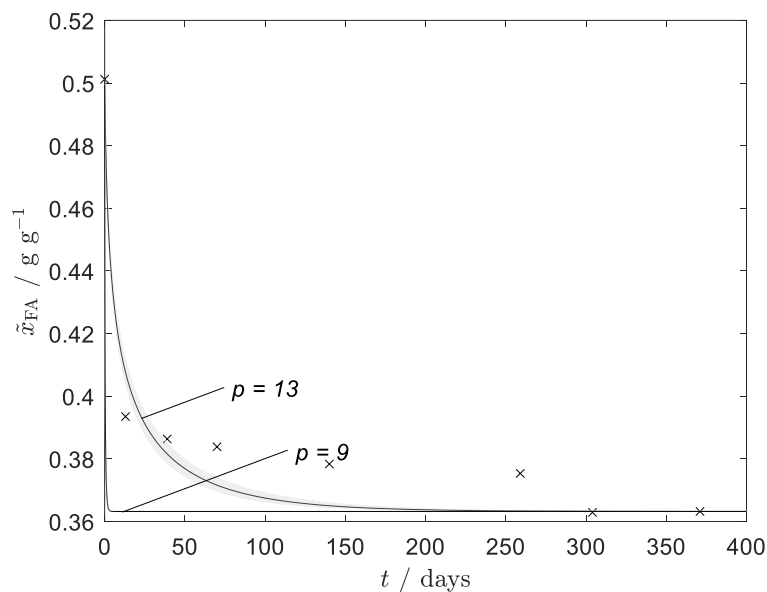


Figure 57: Experimental and calculated overall formaldehyde concentration profile over time for sample No. 10. Grey shaded area shows a variation of the pH in the model by 0.5. (×) Measurement, (—) model.

Table 48: Measured concentration of the liquid phase over time for sample No. 10.

t / days	$\tilde{x}_{\text{FA}}^{(m)} / \text{g g}^{-1}$	$\tilde{x}_{\text{W}}^{(m)} / \text{g g}^{-1}$	$\tilde{x}_{\text{FAC}}^{(m)} / \text{g g}^{-1} \cdot 10^{-3}$
0	0.5012	0.3636	n.a.
13	0.3935	0.4446	1.285
39	0.3864	0.4437	n.a.
70	0.3839	0.4473	n.a.
140	0.3784	0.4569	1.754
259	0.3754	0.4671	1.550
304	0.3629	0.4735	n.a.
371	0.3632	0.4574	1.526

n.a. : not available

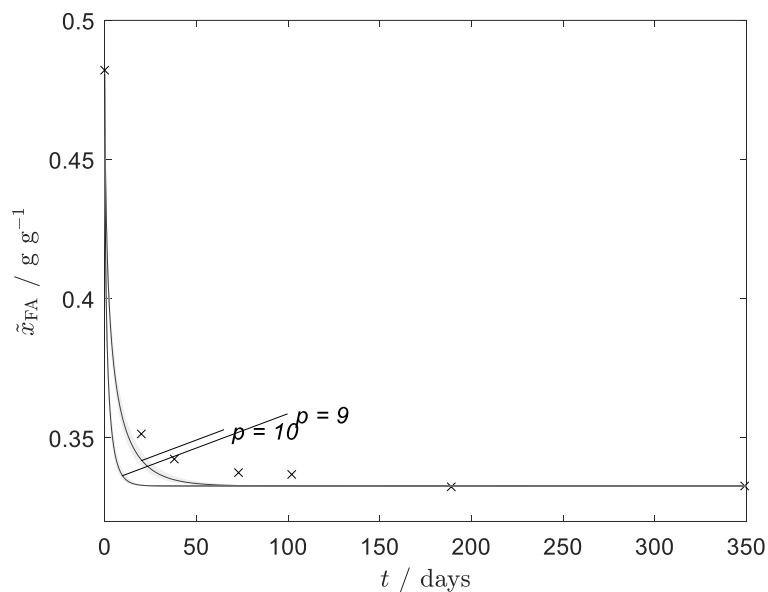


Figure 58: Experimental and calculated overall formaldehyde concentration profile over time for sample No. 11. Grey shaded area shows a variation of the pH in the model by 0.5. (×) Measurement, (—) model.

Table 49: Measured concentration of the liquid phase over time for sample No. 11.

t / days	$\tilde{x}_{\text{FA}}^{(m)} / \text{g g}^{-1}$	$\tilde{x}_{\text{W}}^{(m)} / \text{g g}^{-1}$	$\tilde{x}_{\text{FAC}}^{(m)} / \text{g g}^{-1} \cdot 10^{-3}$
0	0.4821	0.379	n.a.
20	0.3515	0.4831	0.982
38	0.3424	nm	n.a.
73	0.3376	0.4797	1.034
102	0.3369	0.491	1.153
189	0.3325	0.5017	1.220
349	0.3328	0.4943	n.a.

n.a. : not available

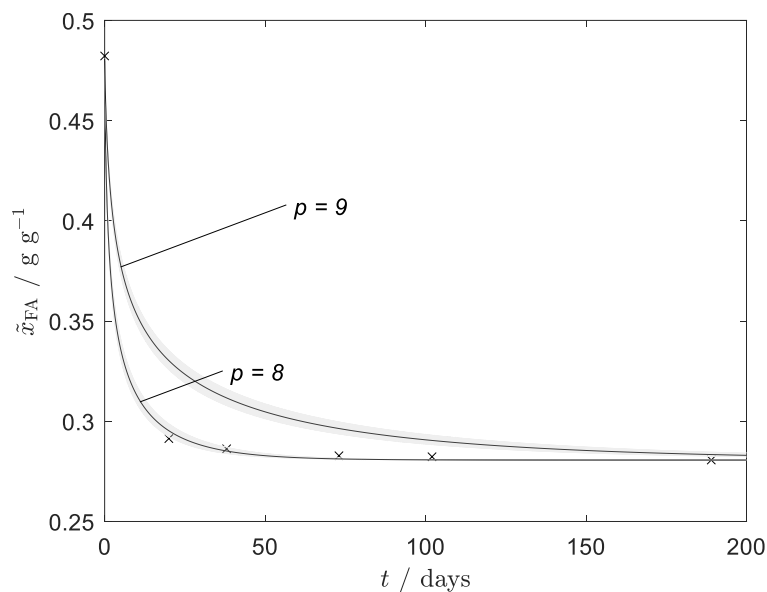


Figure 59: Experimental and calculated overall formaldehyde concentration profile over time for sample No. 12. Grey shaded area shows a variation of the pH in the model by 0.5. (×) Measurement, (—) model.

Table 50: Measured concentration of the liquid phase over time for sample No. 12.

t / days	$\tilde{x}_{\text{FA}}^{(m)} / \text{g g}^{-1}$	$\tilde{x}_{\text{W}}^{(m)} / \text{g g}^{-1}$	$\tilde{x}_{\text{FAC}}^{(m)} / \text{g g}^{-1} \cdot 10^{-3}$
0	0.4822	0.3786	n.a.
20	0.2914	0.5282	0.720
38	0.2863	nm	n.a.
73	0.2828	0.512	1.378
102	0.2823	0.5253	1.183
189	0.2807	0.5276	1.270

n.a. : not available

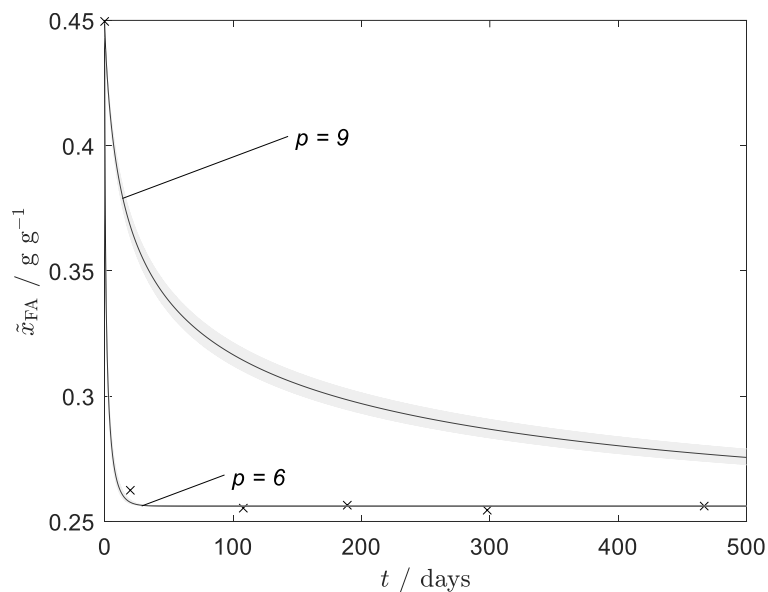


Figure 60: Experimental and calculated overall formaldehyde concentration profile over time for sample No. 13. Grey shaded area shows a variation of the pH in the model by 0.5. (×) Measurement, (—) model.

Table 51: Measured concentration of the liquid phase over time for sample No. 13.

t / days	$\tilde{x}_{\text{FA}}^{(m)} / \text{g g}^{-1}$	$\tilde{x}_{\text{W}}^{(m)} / \text{g g}^{-1}$	$\tilde{x}_{\text{FAC}}^{(m)} / \text{g g}^{-1} \cdot 10^{-3}$
0	0.4496	0.4023	n.a.
20	0.2625	0.5498	0.476
108	0.2553	0.5484	0.690
189	0.2565	0.5484	n.a.
298	0.2545	0.5147	0.819
467	0.2562	0.5516	0.948

n.a. : not available

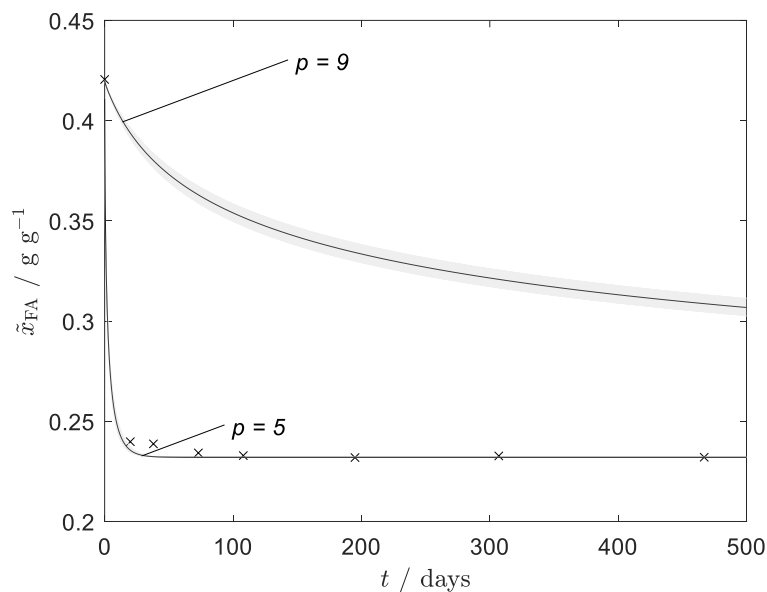


Figure 61: Experimental and calculated overall formaldehyde concentration profile over time for sample No. 14. Grey shaded area shows a variation of the pH in the model by 0.5. (×) Measurement, (—) model.

Table 52: Measured concentration of the liquid phase over time for sample No. 14.

t / days	$\tilde{x}_{\text{FA}}^{(m)} / \text{g g}^{-1}$	$\tilde{x}_{\text{W}}^{(m)} / \text{g g}^{-1}$	$\tilde{x}_{\text{FAC}}^{(m)} / \text{g g}^{-1} \cdot 10^{-3}$
0	0.4205	0.4241	n.a.
20	0.2398	0.5665	0.455
38	0.2387	nm	n.a.
73	0.2342	0.5553	0.366
108	0.2329	0.5667	0.424
195	0.2319	0.5711	0.244
307	0.2327	0.5683	0.590
467	0.2321	0.5711	0.679

n.a. : not available

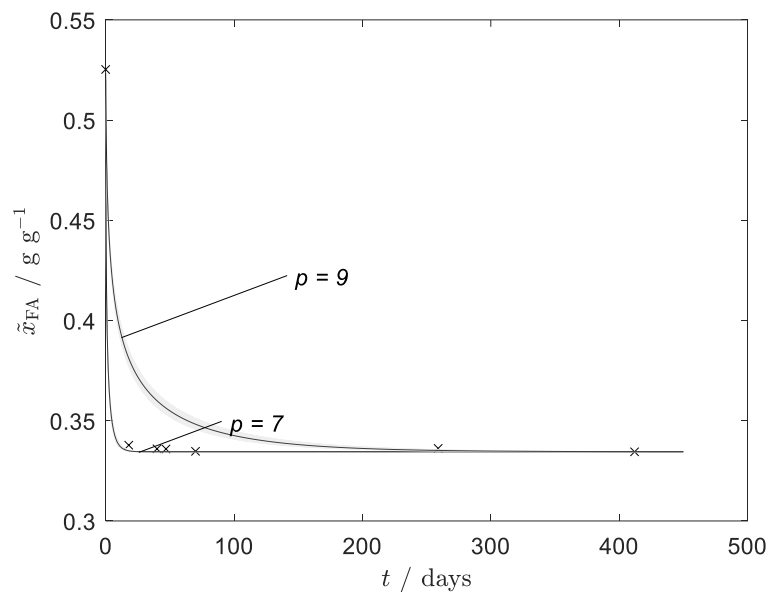


Figure 62: Experimental and calculated overall formaldehyde concentration profile over time for sample No. 15. Grey shaded area shows a variation of the pH in the model by 0.5. (×) Measurement, (—) model.

Table 53: Measured concentration of the liquid phase over time for sample No. 15.

t / days	$\tilde{x}_{\text{FA}}^{(m)} / \text{g g}^{-1}$	$\tilde{x}_{\text{W}}^{(m)} / \text{g g}^{-1}$	$\tilde{x}_{\text{FAC}}^{(m)} / \text{g g}^{-1} \cdot 10^{-3}$
0	0.5253	0.2851	n.a.
18	0.3378	0.3918	n.a.
40	0.3360	0.4028	n.a.
47	0.3359	0.4023	1.166
70	0.3348	0.4023	n.a.
259	0.3362	0.4062	1.650
412	0.3345	0.4022	1.834

n.a. : not available

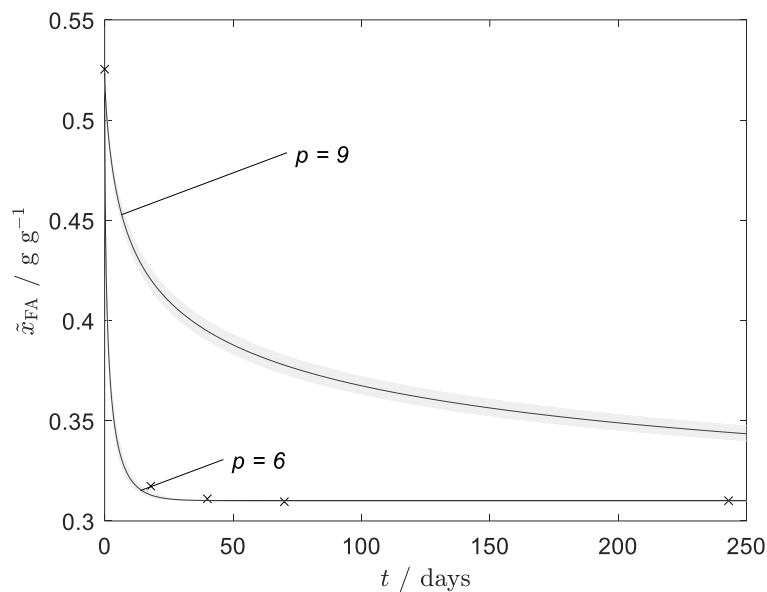


Figure 63: Experimental and calculated overall formaldehyde concentration profile over time for sample No. 16. Grey shaded area shows a variation of the pH in the model by 0.5. (×) Measurement, (—) model.

Table 54: Measured concentration of the liquid phase over time for sample No. 16.

t / days	$\tilde{x}_{\text{FA}}^{(m)} / \text{g g}^{-1}$	$\tilde{x}_{\text{W}}^{(m)} / \text{g g}^{-1}$	$\tilde{x}_{\text{FAC}}^{(m)} / \text{g g}^{-1} \cdot 10^{-3}$
0	0.5254	0.2846	n.a.
18	0.3174	0.4071	n.a.
40	0.3111	0.4169	n.a.
70	0.3096	0.4173	n.a.
243	0.3101	0.4173	1.160

n.a. : not available

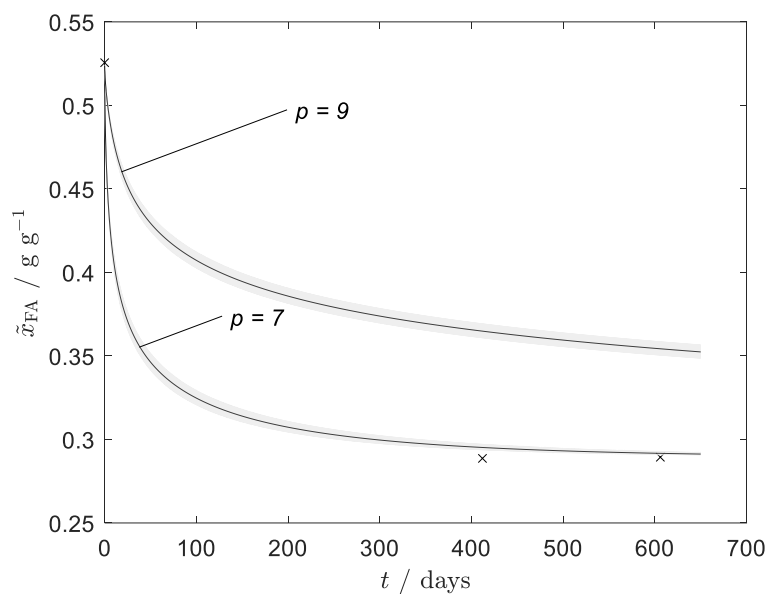


Figure 64: Experimental and calculated overall formaldehyde concentration profile over time for sample No. 17. Grey shaded area shows a variation of the pH in the model by 0.5. (×) Measurement, (—) model.

Table 55: Measured concentration of the liquid phase over time for sample No. 17.

t / days	$\tilde{x}_{\text{FA}}^{(m)} / \text{g g}^{-1}$	$\tilde{x}_{\text{W}}^{(m)} / \text{g g}^{-1}$	$\tilde{x}_{\text{FAC}}^{(m)} / \text{g g}^{-1} \cdot 10^{-3}$
0	0.5256	0.2839	n.a.
412	0.2887	0.4363	0.817
606	0.2894	0.4315	n.a.

n.a. : not available

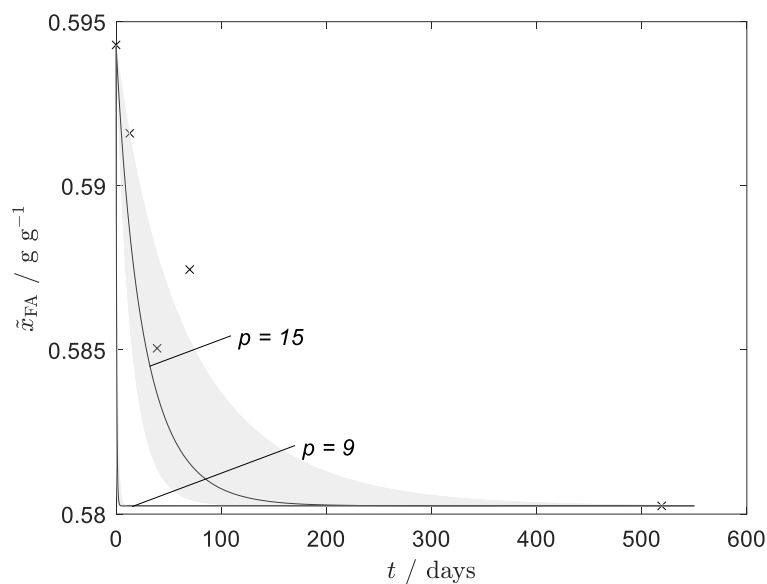


Figure 65: Experimental and calculated overall formaldehyde concentration profile over time for sample No. 18. Grey shaded area shows a variation of the pH by 0.5 and $\tilde{x}_{W,LM}^{(m)}$ by 0.01 g g^{-1} in the model by 0.5. (×) Measurement, (—) model.

Table 56: Measured concentration of the liquid phase over time for sample No. 18.

t / days	$\tilde{x}_{FA}^{(m)} / \text{g g}^{-1}$	$\tilde{x}_W^{(m)} / \text{g g}^{-1}$	$\tilde{x}_{FAC}^{(m)} / \text{g g}^{-1} \cdot 10^{-3}$
0	0.5943	n.a.	n.a.
13	0.5916	n.a.	1.155
39	0.5851	n.a.	n.a.
70	0.5875	n.a.	n.a.
519	0.5803	n.a.	n.a.

n.a. : not available

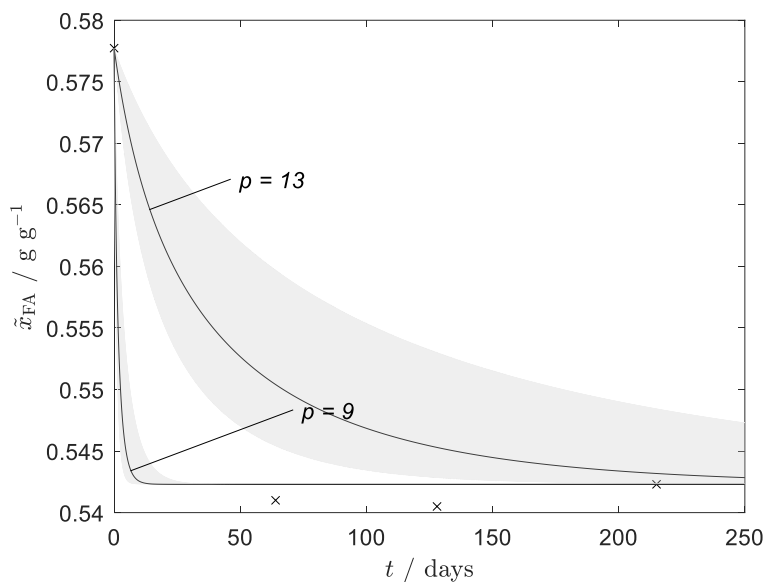


Figure 66: Experimental and calculated overall formaldehyde concentration profile over time for sample No. 19. Grey shaded area shows a variation of the pH by 0.5 and $\tilde{x}_{W,LM}^{(m)}$ by 0.01 g g⁻¹ in the model by 0.5. (×) Measurement, (—) model.

Table 57: Measured concentration of the liquid phase over time for sample No. 19.

t / days	$\tilde{x}_{FA}^{(m)} / \text{g g}^{-1}$	$\tilde{x}_W^{(m)} / \text{g g}^{-1}$	$\tilde{x}_{FAC}^{(m)} / \text{g g}^{-1} \cdot 10^{-3}$
0	0.5777	0.0197	n.a.
64	0.541	n.a.	1.596
128	0.5405	n.a.	n.a.
215	0.5423	0.0247	n.a.

n.a. : not available

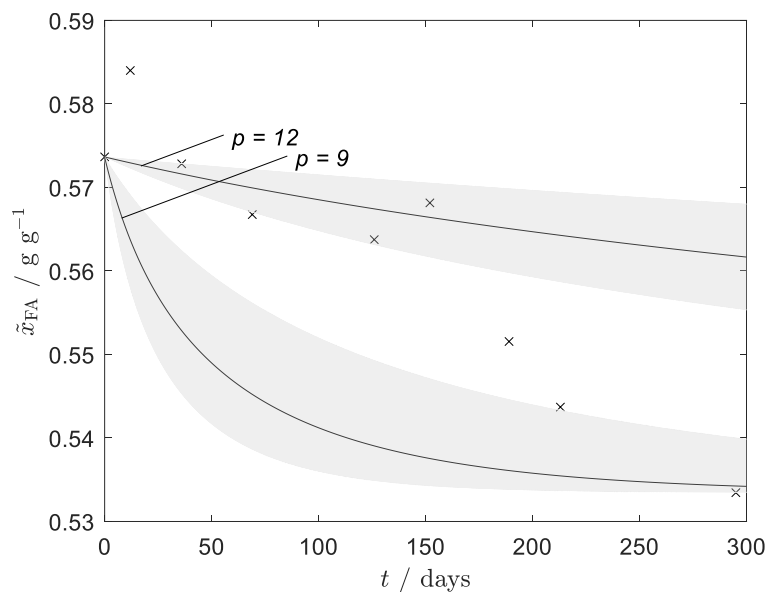


Figure 67: Experimental and calculated overall formaldehyde concentration profile over time for sample No. 20. Grey shaded area shows a variation of the pH by 0.5 and $\tilde{x}_{\text{W,LM}}^{(m)}$ by 0.01 g g⁻¹ in the model by 0.5. (×) Measurement, (—) model.

Table 58: Measured concentration of the liquid phase over time for sample No. 20.

t / days	$\tilde{x}_{\text{FA}}^{(m)} / \text{g g}^{-1}$	$\tilde{x}_{\text{W}}^{(m)} / \text{g g}^{-1}$	$\tilde{x}_{\text{FAC}}^{(m)} / \text{g g}^{-1} \cdot 10^{-3}$
0	0.5737	n.a.	n.a.
12	0.584	n.a.	n.a.
36	0.5728	n.a.	n.a.
69	0.5668	n.a.	n.a.
126	0.5638	n.a.	n.a.
152	0.5682	n.a.	0.440
189	0.5516	n.a.	0.435
213	0.5437	n.a.	n.a.
295	0.5335	n.a.	0.539

n.a. : not available

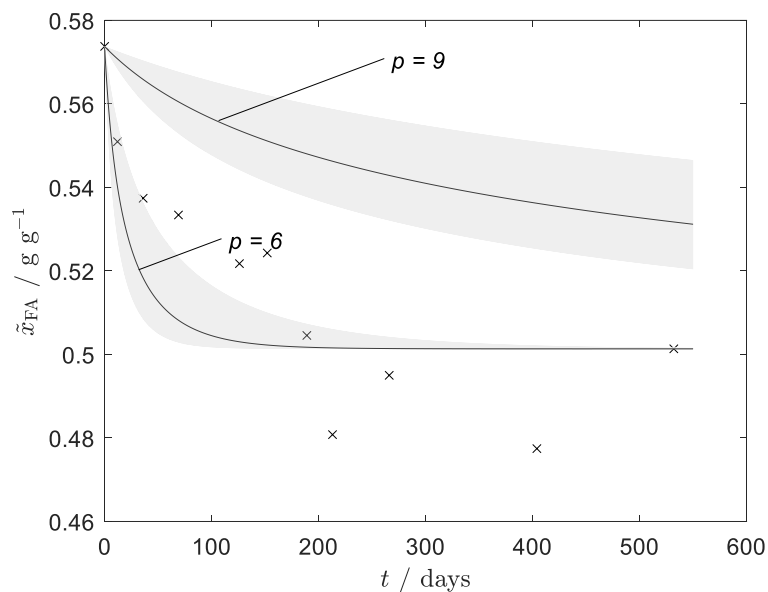


Figure 68: Experimental and calculated overall formaldehyde concentration profile over time for sample No. 21. Grey shaded area shows a variation of the pH by 0.5 and $\tilde{x}_{W,LM}^{(m)}$ by 0.01 g g⁻¹ in the model by 0.5. (×) Measurement, (—) model.

Table 59: Measured concentration of the liquid phase over time for sample No. 21.

t / days	$\tilde{x}_{FA}^{(m)} / \text{g g}^{-1}$	$\tilde{x}_W^{(m)} / \text{g g}^{-1}$	$\tilde{x}_{FAC}^{(m)} / \text{g g}^{-1} \cdot 10^{-3}$
0	0.5738	n.a.	n.a.
12	0.551	n.a.	n.a.
36	0.5374	n.a.	n.a.
69	0.5334	n.a.	n.a.
126	0.5218	n.a.	n.a.
152	0.5243	n.a.	0.286
189	0.5046	n.a.	0.271
213	0.4808	n.a.	n.a.
266	0.495	n.a.	n.a.
404	0.4775	n.a.	0.306
532	0.5014	n.a.	0.404

n.a. : not available

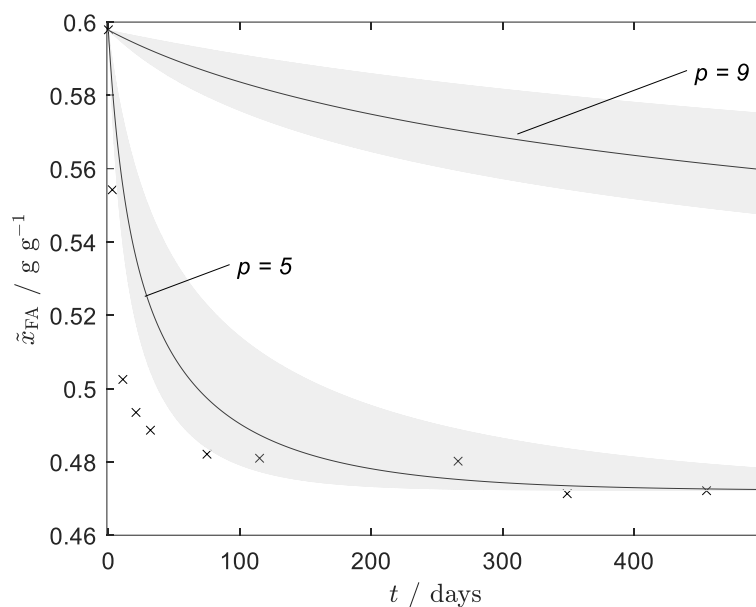


Figure 69: Experimental and calculated overall formaldehyde concentration profile over time for sample No. 22. Grey shaded area shows a variation of the pH by 0.5 and $\tilde{x}_{W,LM}^{(m)}$ by 0.01 g g^{-1} in the model by 0.5. (×) Measurement, (–) model.

Table 60: Measured concentration of the liquid phase over time for sample No. 22.

t / days	$\tilde{x}_{FA}^{(m)} / \text{g g}^{-1}$	$\tilde{x}_W^{(m)} / \text{g g}^{-1}$	$\tilde{x}_{FAC}^{(m)} / \text{g g}^{-1} \cdot 10^{-3}$
0	0.5738	n.a.	n.a.
12	0.551	n.a.	n.a.
36	0.5374	n.a.	n.a.
69	0.5334	n.a.	n.a.
126	0.5218	n.a.	n.a.
152	0.5243	n.a.	0.286
189	0.5046	n.a.	0.271
213	0.4808	n.a.	n.a.
266	0.495	n.a.	n.a.
404	0.4775	n.a.	0.306
532	0.5014	n.a.	0.404

n.a. : not available

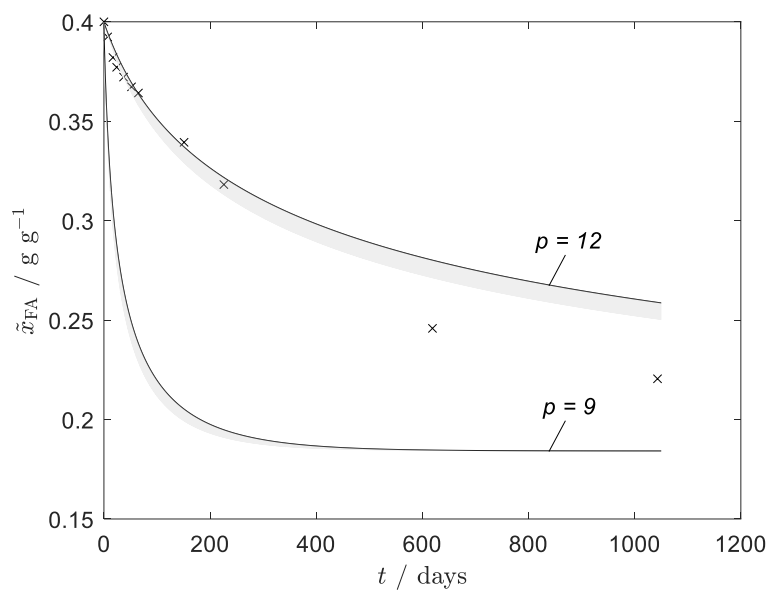


Figure 70: Experimental and calculated overall formaldehyde concentration profile over time for sample No. 23. Grey shaded area shows a variation of the pH in the model by 0.5. (×) Measurement, (—) model.

Table 61: Measured concentration of the liquid phase over time for sample No. 23.

t / days	$\tilde{x}_{FA}^{(m)} / \text{g g}^{-1}$	$\tilde{x}_{FAC}^{(m)} / \text{g g}^{-1} \cdot 10^{-3}$
0	0.4000	n.a.
7	0.3924	n.a.
17	0.3820	n.a.
24	0.3771	n.a.
37	0.3722	n.a.
52	0.3673	n.a.
65	0.3642	n.a.
151	0.3394	0.307
226	0.3182	0.260
619	0.2459	n.a.
1043	0.2205	0.488

n.a. : not available

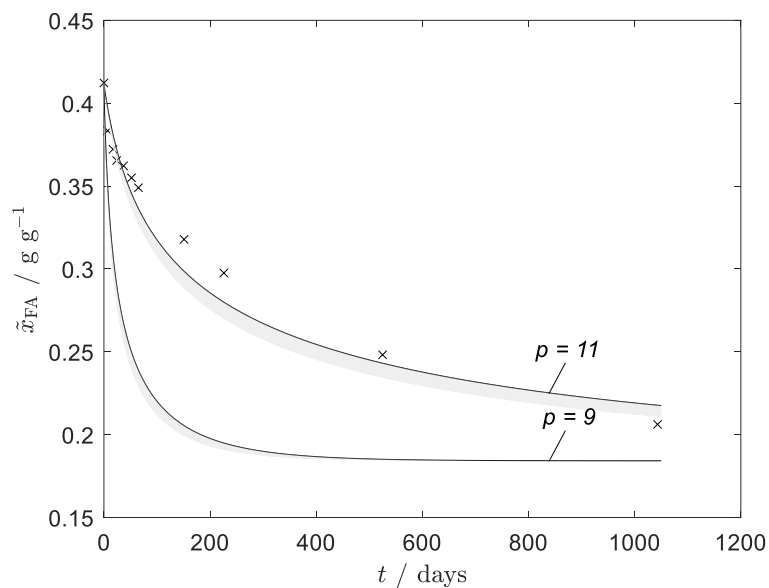


Figure 71: Experimental and calculated overall formaldehyde concentration profile over time for sample No. 24. Grey shaded area shows a variation of the pH in the model by 0.5. (×) Measurement, (–) model.

Table 62: Measured concentration of the liquid phase over time for sample No. 24.

t / days	$\tilde{x}_{\text{FA}}^{(m)} / \text{g g}^{-1}$	$\tilde{x}_{\text{FAC}}^{(m)} / \text{g g}^{-1} \cdot 10^{-3}$
0	0.4122	n.a.
7	0.3834	n.a.
17	0.3722	n.a.
24	0.3654	n.a.
37	0.3622	n.a.
52	0.355	n.a.
65	0.349	n.a.
151	0.3178	0.289
226	0.2976	0.286
525	0.2482	0.525
1043	0.2062	n.a.

n.a. : not available

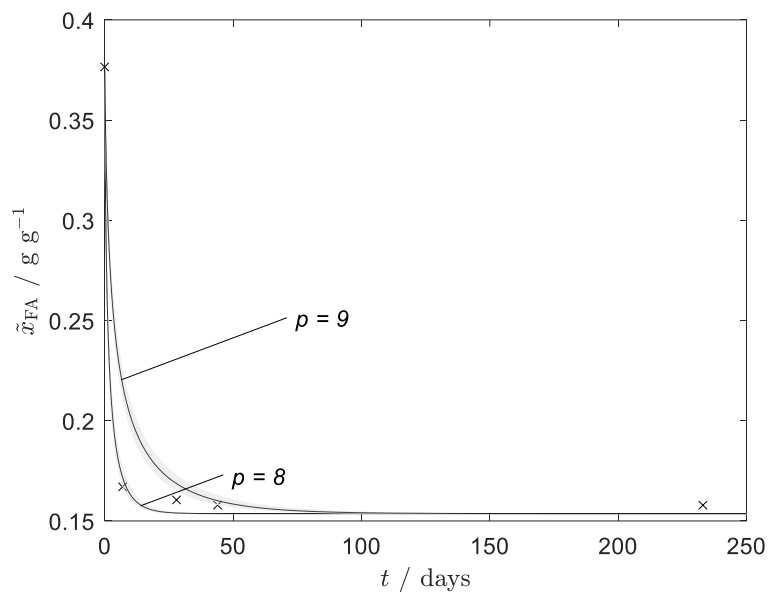


Figure 72: Experimental and calculated overall formaldehyde concentration profile over time for sample No. 25. Grey shaded area shows a variation of the pH in the model by 0.5. (×) Measurement, (—) model.

Table 63: Measured concentration of the liquid phase over time for sample No. 25.

t / days	$\tilde{x}_{\text{FA}}^{(m)} / \text{g g}^{-1}$	$\tilde{x}_{\text{FAC}}^{(m)} / \text{g g}^{-1} \cdot 10^{-3}$
0	0.3765	n.a.
7	0.167	n.a.
28	0.1605	n.a.
44	0.1579	0.507
233	0.1579	0.561

n.a. : not available

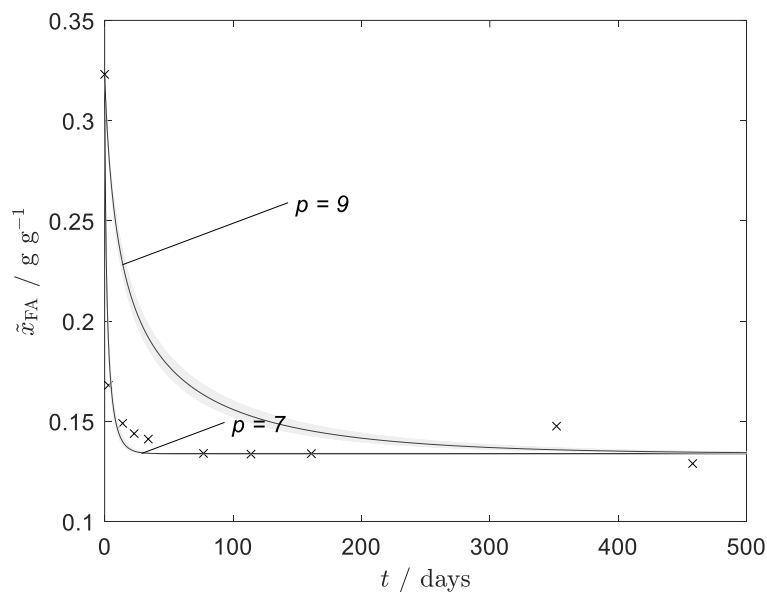


Figure 73: Experimental and calculated overall formaldehyde concentration profile over time for sample No. 26. Grey shaded area shows a variation of the pH in the model by 0.5. (×) Measurement, (—) model.

Table 64: Measured concentration of the liquid phase over time for sample No. 26.

t / days	$\tilde{x}_{\text{FA}}^{(m)} / \text{g g}^{-1}$	$\tilde{x}_{\text{FAc}}^{(m)} / \text{g g}^{-1} \cdot 10^{-3}$
0	0.3231	n.a.
3	0.168	n.a.
14	0.149	n.a.
23	0.1439	n.a.
34	0.1411	n.a.
77	0.134	n.a.
114	0.1336	0.688
161	0.1339	0.624
326	Temperature control failure	
352	0.1476	n.a.
458	0.1289	0.823

n.a. : not available

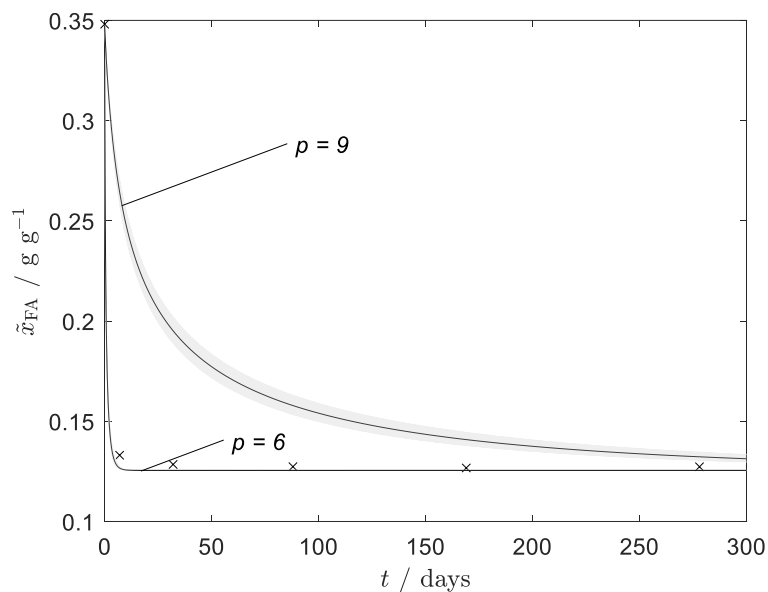


Figure 74: Experimental and calculated overall formaldehyde concentration profile over time for sample No. 27. Grey shaded area shows a variation of the pH in the model by 0.5. (×) Measurement, (—) model.

Table 65: Measured concentration of the liquid phase over time for sample No. 27.

t / days	$\tilde{x}_{\text{FA}}^{(m)} / \text{g g}^{-1}$	$\tilde{x}_{\text{FAC}}^{(m)} / \text{g g}^{-1} \cdot 10^{-3}$
0	0.3481	n.a.
7	0.1331	n.a.
32	0.1285	n.a.
88	0.1274	n.a.
169	0.1267	n.a.
278	0.1273	1.03

n.a. : not available

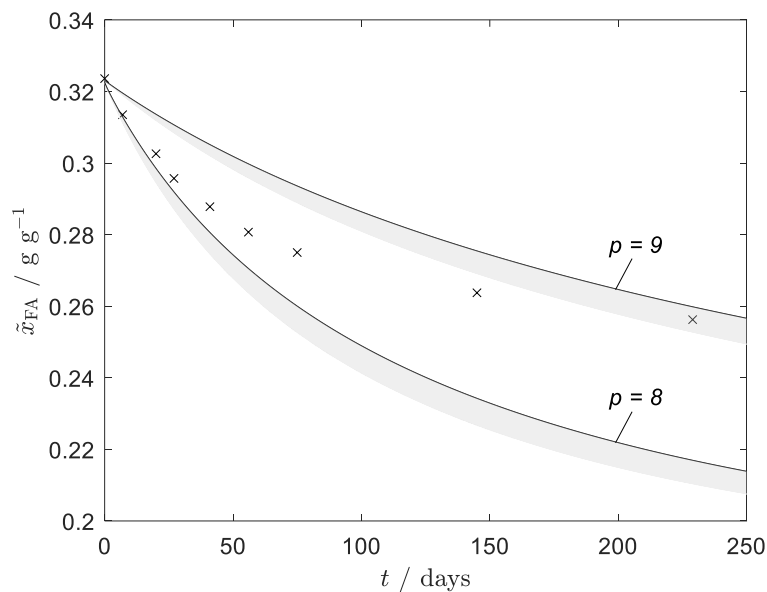


Figure 75: Experimental and calculated overall formaldehyde concentration profile over time for sample No. 28. Grey shaded area shows a variation of the pH in the model by 0.5. (×) Measurement, (—) model.

Table 66: Measured concentration of the liquid phase over time for sample No. 28.

t / days	$\tilde{x}_{\text{FA}}^{(m)} / \text{g g}^{-1}$	$\tilde{x}_{\text{FAC}}^{(m)} / \text{g g}^{-1} \cdot 10^{-3}$
0	0.3236	n.a.
7	0.3135	n.a.
20	0.3026	n.a.
27	0.2957	n.a.
41	0.2878	n.a.
56	0.2807	n.a.
75	0.275	n.a.
145	0.2638	0.458
229	0.2563	0.421

n.a. : not available

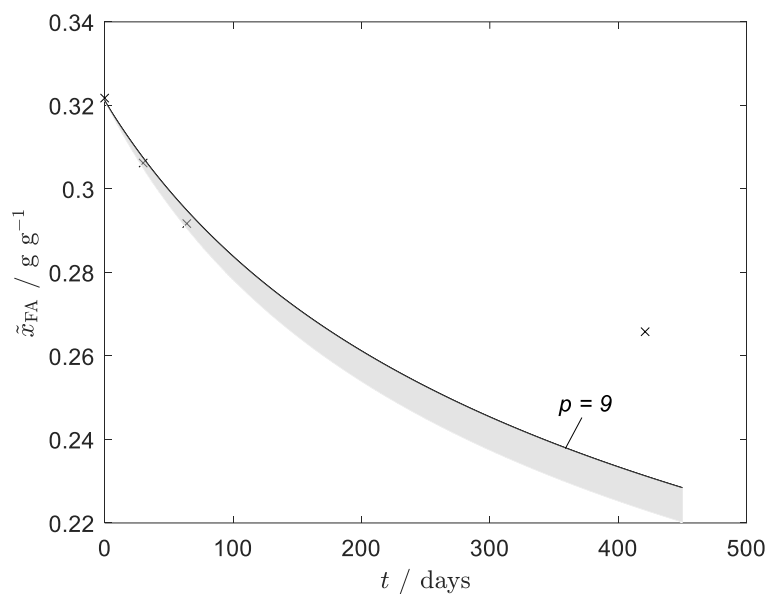


Figure 76: Experimental and calculated overall formaldehyde concentration profile over time for sample No. 29. Grey shaded area shows a variation of the pH in the model by 0.5. (×) Measurement, (—) model.

Table 67: Measured concentration of the liquid phase over time for sample No. 29.

t / days	$\tilde{x}_{\text{FA}}^{(m)} / \text{g g}^{-1}$	$\tilde{x}_{\text{FAC}}^{(m)} / \text{g g}^{-1} \cdot 10^{-3}$
0	0.3218	n.a.
30	0.3062	n.a.
64	0.2917	n.a.
228	temperature control failure	
421	0.2658	0.151

n.a. : not available

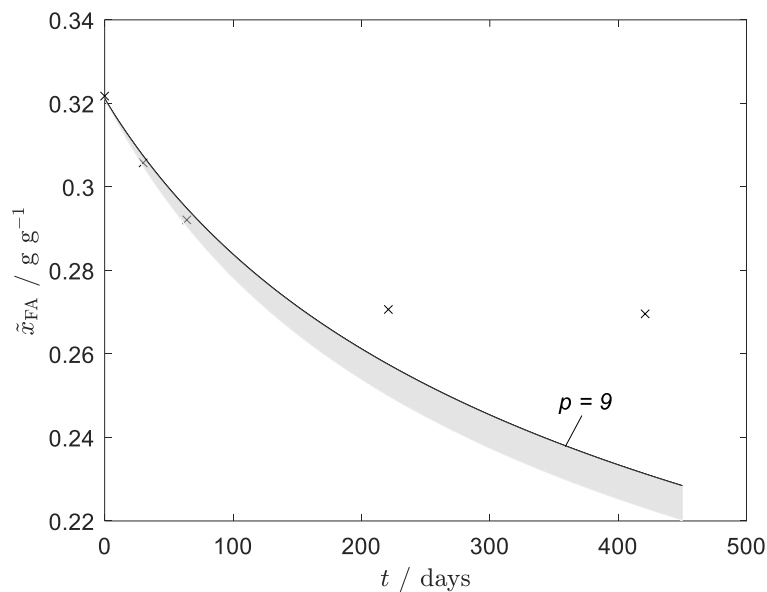


Figure 77: Experimental and calculated overall formaldehyde concentration profile over time for sample No. 30. Grey shaded area shows a variation of the pH in the model by 0.5. (×) Measurement, (—) model.

Table 68: Measured concentration of the liquid phase over time for sample No. 30.

t / days	$\tilde{x}_{\text{FA}}^{(m)} / \text{g g}^{-1}$	$\tilde{x}_{\text{FAc}}^{(m)} / \text{g g}^{-1} \cdot 10^{-3}$
0	0.3218	n.a.
30	0.3058	n.a.
64	0.2921	n.a.
221	0.2707	n.a.
278	Temperature control failure	
421	0.2696	0.569

n.a. : not available

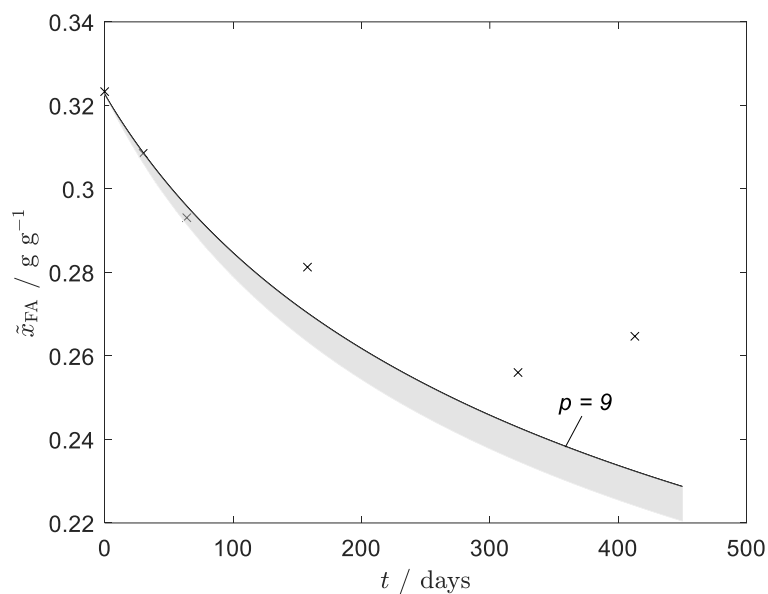


Figure 78: Experimental and calculated overall formaldehyde concentration profile over time for sample No. 31. Grey shaded area shows a variation of the pH in the model by 0.5. (×) Measurement, (—) model.

Table 69: Measured concentration of the liquid phase over time for sample No. 31.

t / days	$\tilde{x}_{\text{FA}}^{(m)} / \text{g g}^{-1}$	$\tilde{x}_{\text{W}}^{(m)} / \text{g g}^{-1}$	$\tilde{x}_{\text{FAc}}^{(m)} / \text{g g}^{-1} \cdot 10^{-3}$
0	0.3233		n.a.
30	0.3085		n.a.
64	0.2931		n.a.
158	0.2813		n.a.
278		Temperature control failure	
322	0.256		0.153
413	0.2647		0.163

n.a. : not available

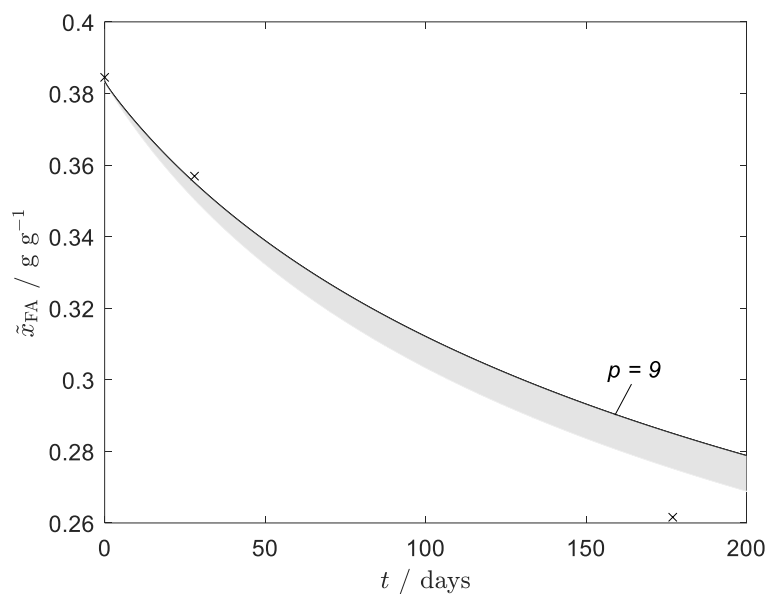


Figure 79: Experimental and calculated overall formaldehyde concentration profile over time for sample No. 32. Grey shaded area shows a variation of the pH in the model by 0.5. (×) Measurement, (—) model.

Table 70: Measured concentration of the liquid phase over time for sample No. 32.

t / days	$\tilde{x}_{\text{FA}}^{(m)} / \text{g g}^{-1}$	$\tilde{x}_{\text{W}}^{(m)} / \text{g g}^{-1}$	$\tilde{x}_{\text{FAc}}^{(m)} / \text{g g}^{-1} \cdot 10^{-3}$
0	0.3845		n.a.
28	0.3569		n.a.
177	0.2616		0.183

n.a. : not available

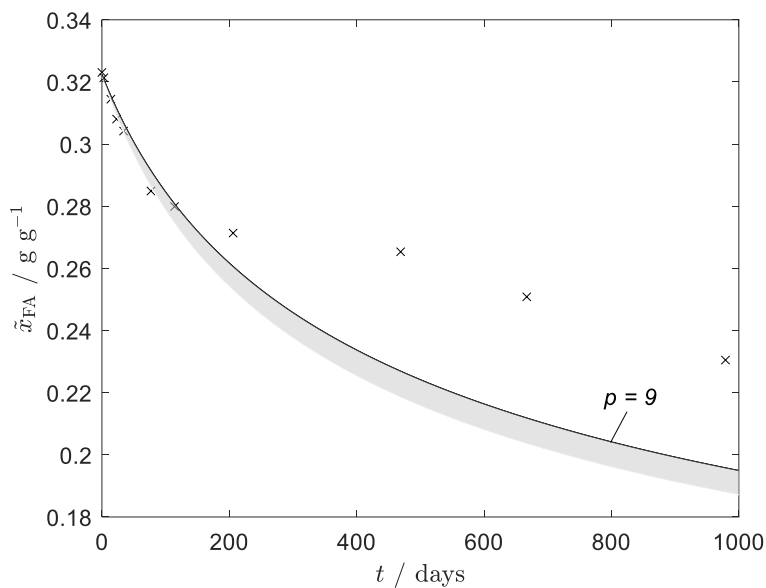


Figure 80: Experimental and calculated overall formaldehyde concentration profile over time for sample No. 33. Grey shaded area shows a variation of the pH in the model by 0.5. (×) Measurement, (—) model.

Table 71: Measured concentration of the liquid phase over time for sample No. 33.

t / days	$\tilde{x}_{FA}^{(m)} / \text{g g}^{-1}$	$\tilde{x}_W^{(m)} / \text{g g}^{-1}$	$\tilde{x}_{FAc}^{(m)} / \text{g g}^{-1} \cdot 10^{-3}$
0	0.3231		n.a.
3	0.3214		n.a.
14	0.3145		n.a.
23	0.3081		n.a.
34	0.3042		n.a.
77	0.2849		n.a.
114	0.2799		0.461
206	0.2714		n.a.
326		Temperature control failure	
469	0.2654		0.575
667	0.2509		0.558
979	0.2305		0.540

n.a. : not available

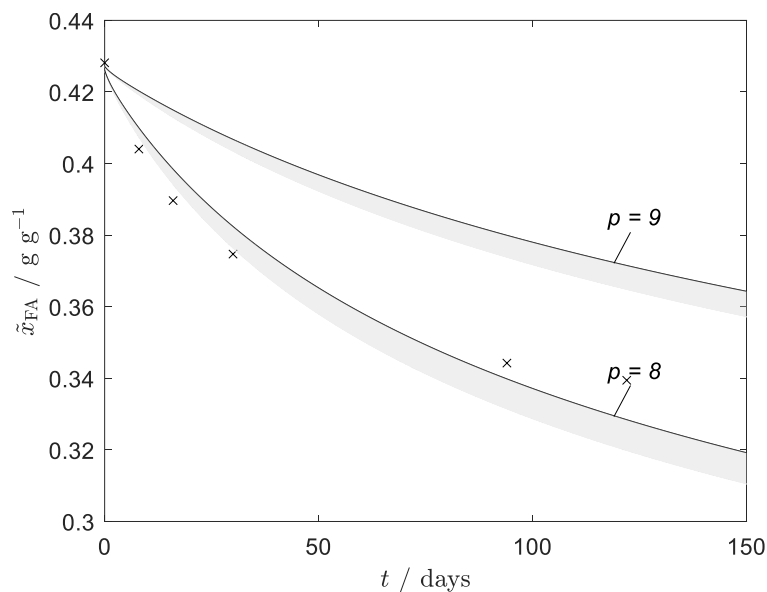


Figure 81: Experimental and calculated overall formaldehyde concentration profile over time for sample No. 34. Grey shaded area shows a variation of the pH in the model by 0.5. (×) Measurement, (—) model.

Table 72: Measured concentration of the liquid phase over time for sample No. 34.

t / days	$\tilde{x}_{\text{FA}}^{(m)} / \text{g g}^{-1}$	$\tilde{x}_{\text{W}}^{(m)} / \text{g g}^{-1}$	$\tilde{x}_{\text{FAc}}^{(m)} / \text{g g}^{-1} \cdot 10^{-3}$
0	0.4282	0.4973	n.a.
8	0.4041	0.5269	n.a.
16	0.3897	0.5326	n.a.
30	0.3747	0.5543	n.a.
94	0.3443	0.5893	n.a.
122	0.3395	0.599	n.a.

n.a. : not available

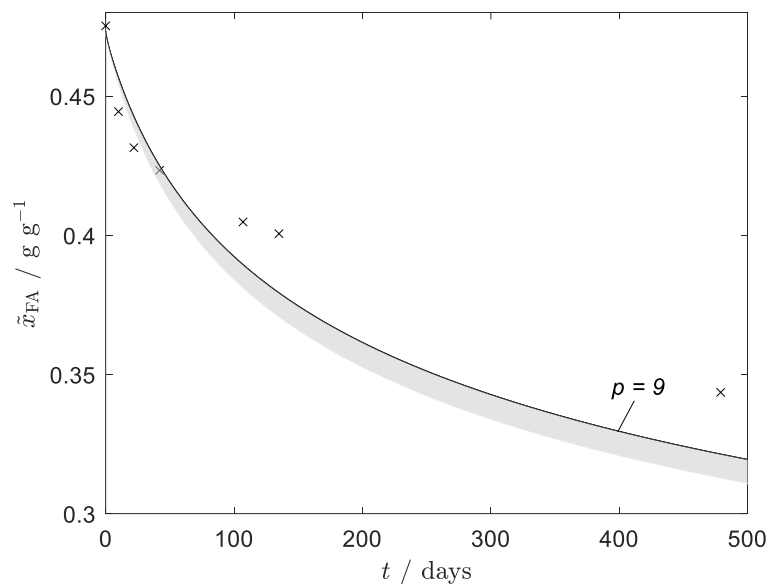


Figure 82: Experimental and calculated overall formaldehyde concentration profile over time for sample No. 35. Grey shaded area shows a variation of the pH in the model by 0.5. (×) Measurement, (—) model.

Table 73: Measured concentration of the liquid phase over time for sample No. 35.

t / days	$\tilde{x}_{\text{FA}}^{(m)} / \text{g g}^{-1}$	$\tilde{x}_{\text{W}}^{(m)} / \text{g g}^{-1}$	$\tilde{x}_{\text{FAc}}^{(m)} / \text{g g}^{-1} \cdot 10^{-3}$
0	0.4752	0.454	n.a.
10	0.4444	0.4817	n.a.
22	0.4315	0.4959	n.a.
42	0.4233	0.506	n.a.
107	0.4048	0.5303	n.a.
135	0.4006	0.5318	n.a.
347		Temperature control failure	
479	0.3436	0.5471	0.258

n.a. : not available

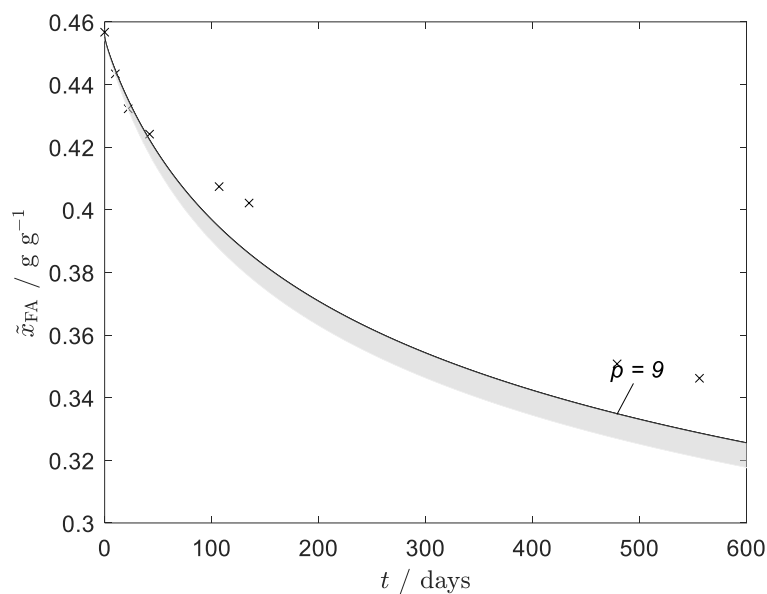


Figure 83: Experimental and calculated overall formaldehyde concentration profile over time for sample No. 36. Grey shaded area shows a variation of the pH in the model by 0.5. (×) Measurement, (—) model.

Table 74: Measured concentration of the liquid phase over time for sample No. 36.

t / days	$\tilde{x}_{\text{FA}}^{(m)} / \text{g g}^{-1}$	$\tilde{x}_{\text{W}}^{(m)} / \text{g g}^{-1}$	$\tilde{x}_{\text{FAc}}^{(m)} / \text{g g}^{-1} \cdot 10^{-3}$
0	0.4567	0.4564	n.a.
10	0.4434	0.4842	n.a.
22	0.4323	0.4979	n.a.
42	0.4242	0.5042	n.a.
107	0.4074	0.5272	n.a.
135	0.4022	0.543	n.a.
479	0.3508	0.537	0.230
556	0.3462	nm	n.a.

n.a. : not available

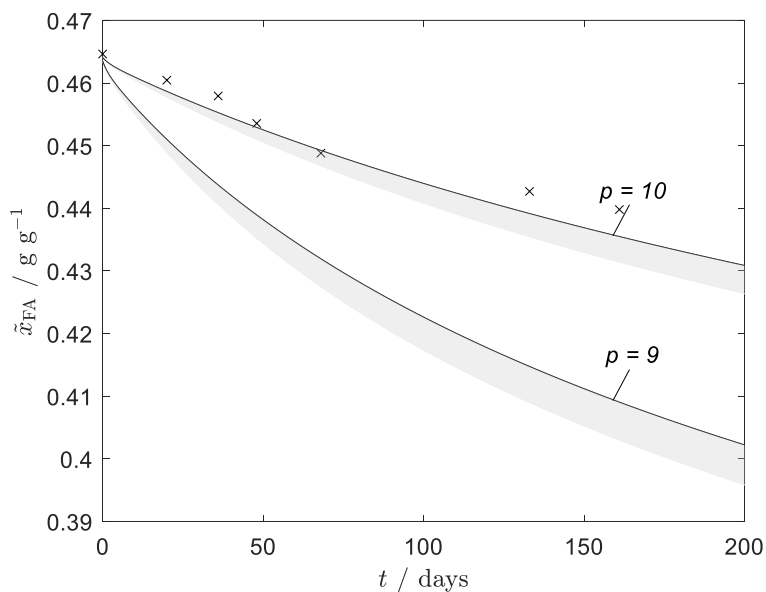


Figure 84: Experimental and calculated overall formaldehyde concentration profile over time for sample No. 37. Grey shaded area shows a variation of the pH in the model by 0.5. (×) Measurement, (—) model.

Table 75: Measured concentration of the liquid phase over time for sample No. 37.

t / days	$\tilde{x}_{\text{FA}}^{(m)} / \text{g g}^{-1}$	$\tilde{x}_{\text{W}}^{(m)} / \text{g g}^{-1}$	$\tilde{x}_{\text{FAc}}^{(m)} / \text{g g}^{-1} \cdot 10^{-3}$
0	0.4646	0.4026	n.a.
20	0.4605	0.406	n.a.
36	0.4579	0.3927	n.a.
48	0.4536	0.3983	n.a.
68	0.4488	0.4011	n.a.
133	0.4427	0.3965	n.a.
161	0.4398	0.4281	0.230

n.a. : not available

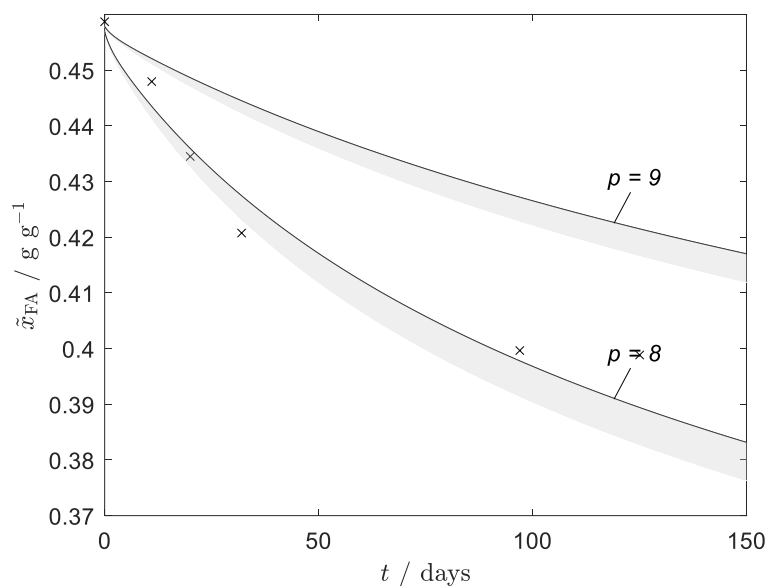


Figure 85: Experimental and calculated overall formaldehyde concentration profile over time for sample No. 38. Grey shaded area shows a variation of the pH in the model by 0.5. (×) Measurement, (—) model.

Table 76: Measured concentration of the liquid phase over time for sample No. 38.

t / days	$\tilde{x}_{\text{FA}}^{(m)} / \text{g g}^{-1}$	$\tilde{x}_{\text{W}}^{(m)} / \text{g g}^{-1}$	$\tilde{x}_{\text{FAC}}^{(m)} / \text{g g}^{-1} \cdot 10^{-3}$
0	0.4587	0.3897	n.a.
11	0.448	0.3975	n.a.
20	0.4345	0.4058	n.a.
32	0.4208	0.3992	n.a.
97	0.3997	0.4497	n.a.
125	0.3989	0.4531	n.a.

n.a. : not available

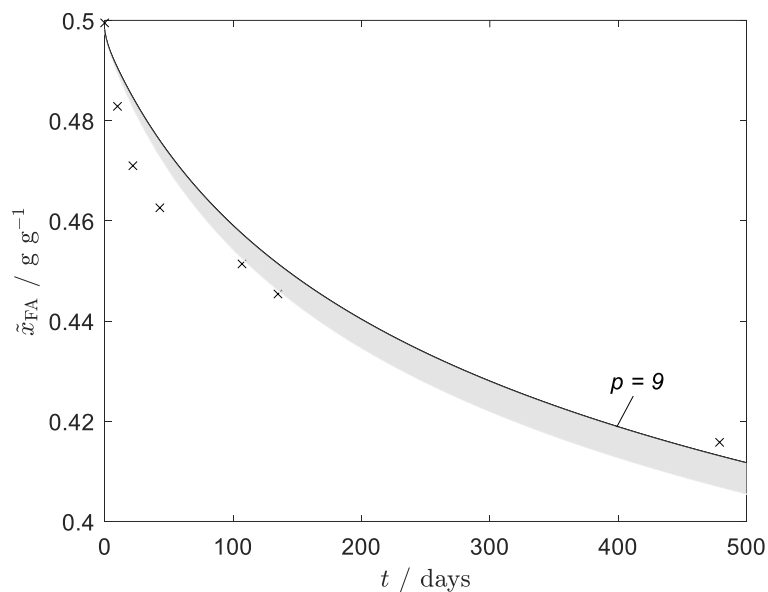


Figure 86: Experimental and calculated overall formaldehyde concentration profile over time for sample No. 39. Grey shaded area shows a variation of the pH in the model by 0.5. (×) Measurement, (—) model.

Table 77: Measured concentration of the liquid phase over time for sample No. 39.

t / days	$\tilde{x}_{\text{FA}}^{(m)} / \text{g g}^{-1}$	$\tilde{x}_{\text{W}}^{(m)} / \text{g g}^{-1}$	$\tilde{x}_{\text{FAc}}^{(m)} / \text{g g}^{-1} \cdot 10^{-3}$
0	0.4995	0.3208	n.a.
10	0.4829	0.3665	n.a.
22	0.471	0.3948	n.a.
43	0.4626	0.395	n.a.
107	0.4514	0.4157	n.a.
135	0.4454	0.4287	n.a.
347		Temperature control failure	
479	0.4158	0.4128	0.298

n.a. : not available

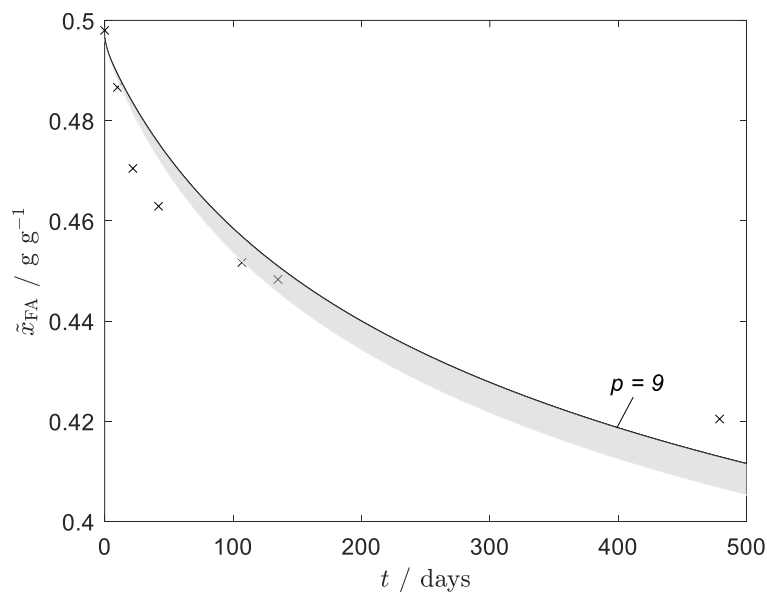


Figure 87: Experimental and calculated overall formaldehyde concentration profile over time for sample No. 40. Grey shaded area shows a variation of the pH in the model by 0.5. (×) Measurement, (—) model.

Table 78: Measured concentration of the liquid phase over time for sample No. 40.

t / days	$\tilde{x}_{\text{FA}}^{(m)} / \text{g g}^{-1}$	$\tilde{x}_{\text{W}}^{(m)} / \text{g g}^{-1}$	$\tilde{x}_{\text{FAc}}^{(m)} / \text{g g}^{-1} \cdot 10^{-3}$
0	0.498	0.317	n.a.
10	0.4866	0.3435	n.a.
22	0.4705	0.3835	n.a.
42	0.4629	0.3964	n.a.
107	0.4517	0.4169	n.a.
135	0.4483	0.431	n.a.
347		Temperature control failure	
479	0.4205	0.4088	0.302

n.a. : not available

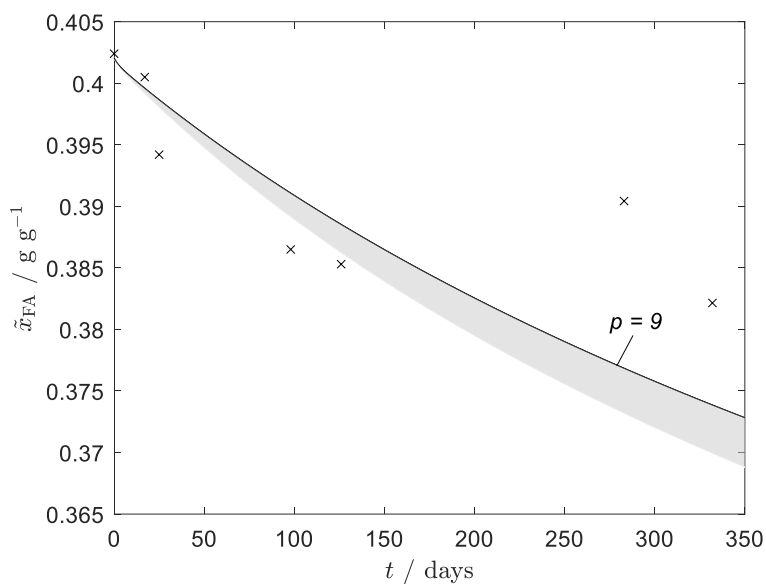


Figure 88: Experimental and calculated overall formaldehyde concentration profile over time for sample No. 41. Grey shaded area shows a variation of the pH in the model by 0.5. (×) Measurement, (—) model.

Table 79: Measured concentration of the liquid phase over time for sample No. 41.

t / days	$\tilde{x}_{\text{FA}}^{(m)} / \text{g g}^{-1}$	$\tilde{x}_{\text{W}}^{(m)} / \text{g g}^{-1}$	$\tilde{x}_{\text{FAC}}^{(m)} / \text{g g}^{-1} \cdot 10^{-3}$
0	0.4024	0.435	n.a.
17	0.4005	0.4389	n.a.
25	0.3942	0.4399	n.a.
98	0.3865	0.4608	n.a.
126	0.3853	0.4678	n.a.
221		Temperature control failure	
283	0.3904	0.4437	0.546
332	0.3822	0.4494	0.519

n.a. : not available

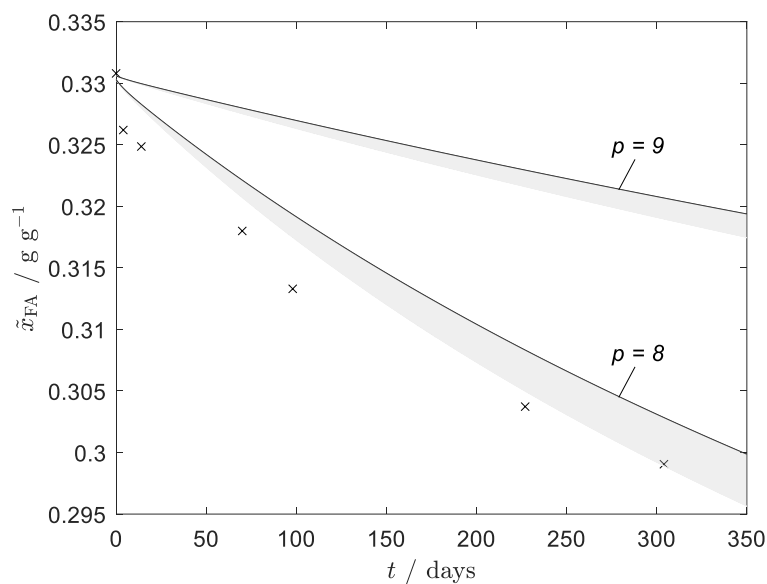


Figure 89: Experimental and calculated overall formaldehyde concentration profile over time for sample No. 42. Grey shaded area shows a variation of the pH in the model by 0.5. (×) Measurement, (—) model.

Table 80: Measured concentration of the liquid phase over time for sample No. 42.

t / days	$\tilde{x}_{\text{FA}}^{(m)} / \text{g g}^{-1}$	$\tilde{x}_{\text{W}}^{(m)} / \text{g g}^{-1}$	$\tilde{x}_{\text{FAC}}^{(m)} / \text{g g}^{-1} \cdot 10^{-3}$
0	0.3308	0.5836	n.a.
4	0.3262	0.5902	n.a.
14	0.3249	0.6043	n.a.
70	0.318	0.6077	0.172
98	0.3133	0.6163	n.a.
227	0.3037	0.607	0.160
304	0.2991	0.6078	0.151

n.a. : not available

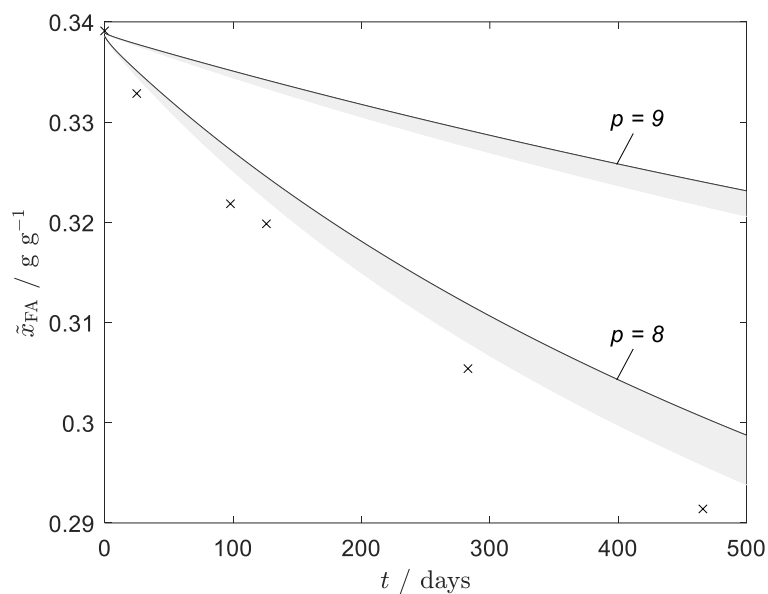


Figure 90: Experimental and calculated overall formaldehyde concentration profile over time for sample No. 43. Grey shaded area shows a variation of the pH in the model by 0.5. (×) Measurement, (—) model.

Table 81: Measured concentration of the liquid phase over time for sample No. 43.

t / days	$\tilde{x}_{\text{FA}}^{(m)} / \text{g g}^{-1}$	$\tilde{x}_{\text{W}}^{(m)} / \text{g g}^{-1}$	$\tilde{x}_{\text{FAc}}^{(m)} / \text{g g}^{-1} \cdot 10^{-3}$
0	0.3308	0.5836	n.a.
4	0.3262	0.5902	n.a.
14	0.3249	0.6043	n.a.
70	0.318	0.6077	0.172
98	0.3133	0.6163	n.a.
227	0.3037	0.607	0.160
304	0.2991	0.6078	0.151

n.a. : not available

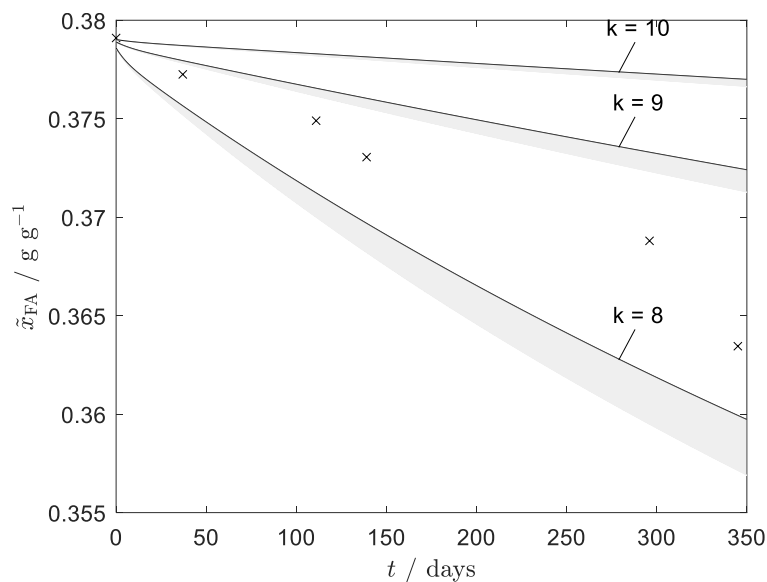


Figure 91: Experimental and calculated overall formaldehyde concentration profile over time for sample No. 44. Grey shaded area shows a variation of the pH in the model by 0.5. (×) Measurement, (—) model.

Table 82: Measured concentration of the liquid phase over time for sample No. 44.

t / days	$\tilde{x}_{\text{FA}}^{(m)} / \text{g g}^{-1}$	$\tilde{x}_{\text{W}}^{(m)} / \text{g g}^{-1}$	$\tilde{x}_{\text{FAC}}^{(m)} / \text{g g}^{-1} \cdot 10^{-3}$
0	0.3791	0.4525	n.a.
37	0.3773	0.4594	n.a.
111	0.3749	0.4699	n.a.
139	0.3731	0.4756	n.a.
296	0.3688	0.4621	0.509
345	0.3635	0.4636	0.479

n.a. : not available

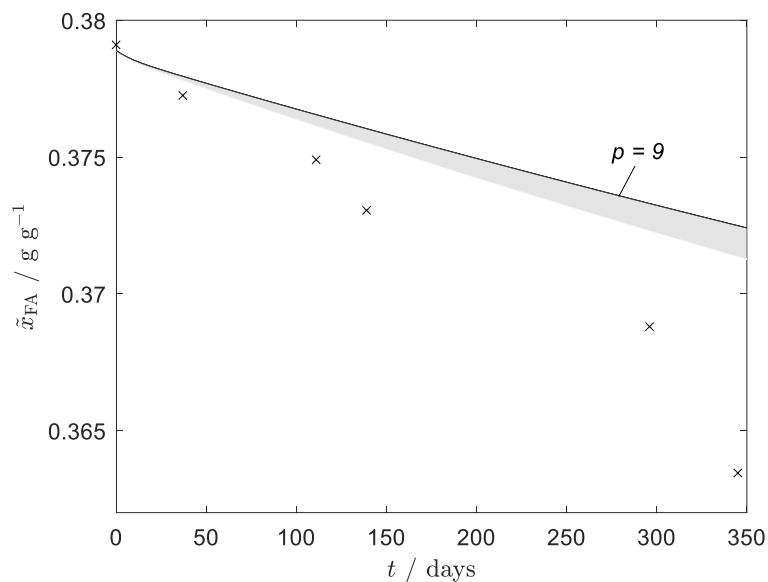


Figure 92: Experimental and calculated overall formaldehyde concentration profile over time for sample No. 45. Grey shaded area shows a variation of the pH in the model by 0.5. (×) Measurement, (—) model.

Table 83: Measured concentration of the liquid phase over time for sample No. 45.

t / days	$\tilde{x}_{\text{FA}}^{(m)} / \text{g g}^{-1}$	$\tilde{x}_{\text{W}}^{(m)} / \text{g g}^{-1}$	$\tilde{x}_{\text{FAC}}^{(m)} / \text{g g}^{-1} \cdot 10^{-3}$
0	0.4092	0.4293	n.a.
42	0.4071	0.4309	n.a.
56	0.4056	0.4362	n.a.
105	0.3977	0.4591	n.a.
308	0.3755	0.4566	0.542
357	0.371	0.4596	0.528

n.a. : not available

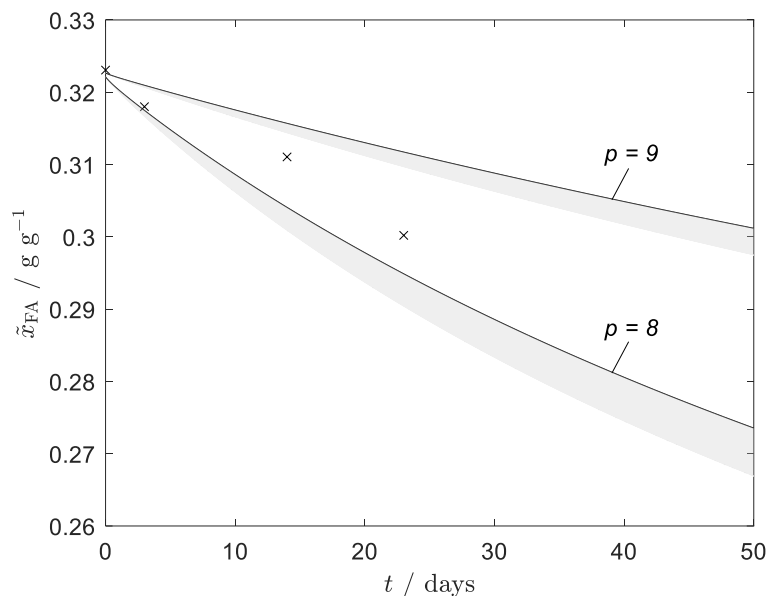


Figure 93: Experimental and calculated overall formaldehyde concentration profile over time for sample No. 46. Grey shaded area shows a variation of the pH in the model by 0.5.(\times) Measurement, (—) model.

Table 84: Measured concentration of the liquid phase over time for sample No. 46.

t / days	$\tilde{x}_{\text{FA}}^{(m)} / \text{g g}^{-1}$	$\tilde{x}_{\text{W}}^{(m)} / \text{g g}^{-1}$	$\tilde{x}_{\text{FAC}}^{(m)} / \text{g g}^{-1} \cdot 10^{-3}$
0	0.3231		n.a.
3	0.3180		n.a.
14	0.3111		n.a.
23	0.3002		n.a.

n.a. : not available

A.9 Experimental data for the systems (formaldehyde + water + OME) and (formaldehyde + water + methanol + OME)

In Table 85 an overview of all measurements of this work is given. In Table 86 to Table 117 the numerical results for the measurements are given. Each Table corresponds to one experiment according to the number given in Table 85. In Figure 94 to Figure 116 for every experiment, which could be evaluated with the kinetic model, the concentration profile of the measurement and the model is shown like in Figure 16 in the main part. Beside the best fitting value also the model results for $p=9$ is given. The samples with two liquid phases were not evaluated.

Table 85: Overview of the experiments carried out in this work.

Experiment	T K	OME_n	ternary / quaternary	SLE / SLLE	$\tilde{\chi}_{OME,sol}^{(m)}$ $g\ g^{-1}$	$\frac{\tilde{\chi}_{MeOH}^{(m)}}{\tilde{\chi}_W^{(m)}}$	$\tilde{\chi}_{NaOH}^{(m)}$ $g\ g^{-1}$	Best fitting p	
OME-1	273.2	2	ternary	SLE	0.1562	0	0.0018	7	
OME-2						0.2935		0.0017	7
OME-3					SLLE	0.4150		0.0018	n.e.
OME-4	283.0				SLE	0.1569			≤ 8
OME-5						0.2932			8
OME-6	293.3					0.1569			≤ 8
OME-7						0.2939			≤ 9
OME-8					SLLE	0.4162			n.e.
OME-9	303.4				SLE	0.1528			≤ 12
OME-10	273.2	4	ternary		0.1561		0.0017	7	
OME-11					SLLE	0.2937			n.e.
OME-12						0.4164		0.0018	
OME-13	283.0				SLE	0.1566			8
OME-14					SLLE	0.2930			n.e.
OME-15						0.4162			
OME-16	293.3				SLE	0.1584			≤ 9
OME-17					SLLE	0.2929		0.0018	n.e.
OME-18						0.4167		0.0017	
OME-19	303.4	4		SLE	0.1574	0	0.0017	11	
OME-20					0.2939		0.0018		
OME-21			quaternary	SLLE	0.4167			n.e.	
OME-22	273.2	2			SLE	0.1615	0.1573		8
OME-23						0.3024	0.1576		
OME-24						0.1705	0.3904		≤ 7
OME-25		4				0.1685	0.1579		
OME-26						0.3020	0.1580		
OME-27						0.1701	0.3901		
OME-28						0.3164	0.3924		
OME-29	293.3					0.1613	0.1576		10
OME-30						0.3021	0.1588		≤ 10
OME-31						0.1705	0.3898		11
OME-32						0.3159	0.3896		≤ 10

n.e.: not evaluated

Table 86: Measured concentration of the liquid phase over time for Experiment OME-1.

t / days	$\tilde{x}_{\text{FA}}^{(m)} / \text{g g}^{-1}$	$\tilde{x}_{\text{W}}^{(m)} / \text{g g}^{-1}$	$\tilde{x}_{\text{FAC}}^{(m)} / \text{g g}^{-1}$
0	0.3571	0.5405	n.a.
11	0.1226	0.7508	0.00074
92	0.1091	0.7553	0.00182
122	0.1081	0.7589	0.00185
196	0.1074	0.7547	0.00226
590	0.1064	0.7564	n.a.

n.a. : not available

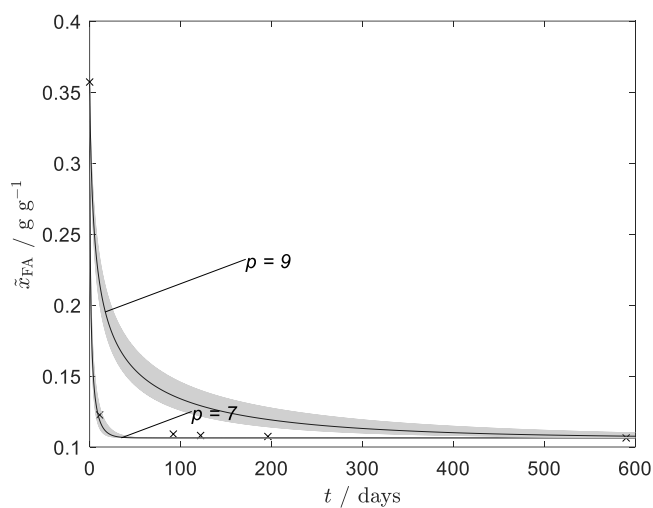


Figure 94: Experimental and calculated overall formaldehyde concentration in the liquid phase for Experiment OME-1. (×) Experimental data, (—) model. The line is for pH value 11, the shaded area indicates the influence a variation of the pH in the model by ± 1.5 .

Table 87: Measured concentration of the liquid phase over time for Experiment OME-2.

t / days	$\tilde{x}_{\text{FA}}^{(m)} / \text{g g}^{-1}$	$\tilde{x}_{\text{W}}^{(m)} / \text{g g}^{-1}$	$\tilde{x}_{\text{FAC}}^{(m)} / \text{g g}^{-1}$
0	0.3182	0.4797	n.a.
11	0.1055	0.6510	0.00073
92	0.0941	0.6473	0.00172
122	0.0939	0.6538	0.00182
196	0.0935	0.6462	0.00213
590	0.0926	0.6456	n.a.

n.a. : not available

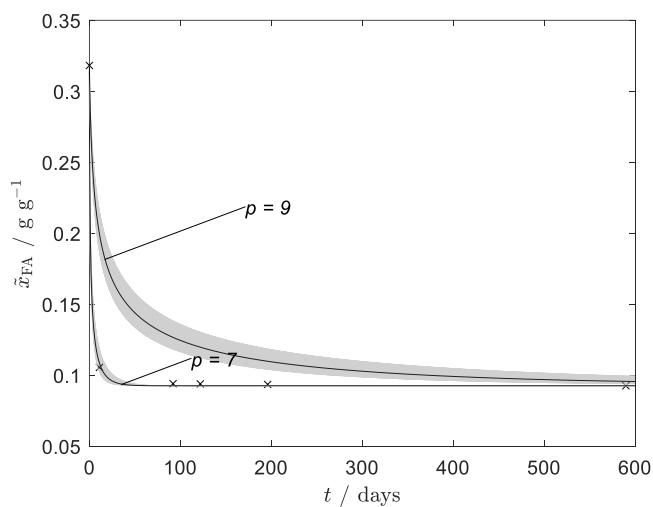
**Figure 95:** Experimental and calculated overall formaldehyde concentration in the liquid phase for Experiment OME-2. (×) Experimental data, (—) model. The line is for pH value 11, the shaded area indicates the influence a variation of the pH in the model by ± 1.5 .

Table 88: Measured concentration of the liquid phase over time for Experiment OME-3.

t / days	$\tilde{x}_{\text{FA}}^{(m)} / \text{g g}^{-1}$	$\tilde{x}_{\text{W}}^{(m)} / \text{g g}^{-1}$	$\tilde{x}_{\text{FAC}}^{(m)} / \text{g g}^{-1}$
0	0.2783	0.4202	n.a.
11	0.1039	0.6230	0.00076
92	0.0911	0.6109	0.00193
122	0.0912	0.6146	0.00210

n.a. : not available

Table 89: Measured concentration of the liquid phase over time for Experiment OME-4.

t / days	$\tilde{x}_{\text{FA}}^{(m)} / \text{g g}^{-1}$	$\tilde{x}_{\text{W}}^{(m)} / \text{g g}^{-1}$	$\tilde{x}_{\text{FAC}}^{(m)} / \text{g g}^{-1}$
0	0.3576	0.5395	n.a.
11	0.1387	0.7324	0.00108
28	0.1366	0.7408	0.00221
87	0.1332	0.7391	0.00271
120	0.1329	0.7380	0.00288

n.a. : not available

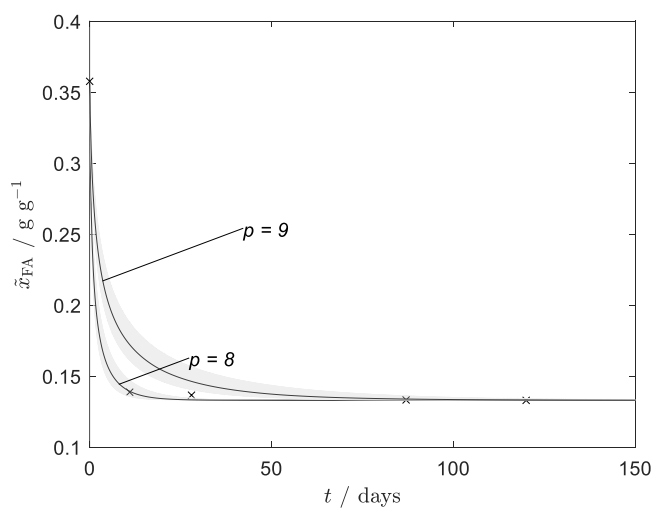
**Figure 96:** Experimental and calculated overall formaldehyde concentration in the liquid phase for Experiment OME-4. (×) Experimental data, (—) model. The line is for pH value 11, the shaded area indicates the influence a variation of the pH in the model by ± 1.5 .

Table 90: Measured concentration of the liquid phase over time for Experiment OME-5.

t / days	$\tilde{x}_{\text{FA}}^{(m)} / \text{g g}^{-1}$	$\tilde{x}_{\text{W}}^{(m)} / \text{g g}^{-1}$	$\tilde{x}_{\text{FAC}}^{(m)} / \text{g g}^{-1}$
0	0.3179	0.4801	n.a.
11	0.1242	0.6288	0.00102
28	0.1178	0.6440	0.00205
120	0.1186	0.6337	0.00273

n.a. : not available

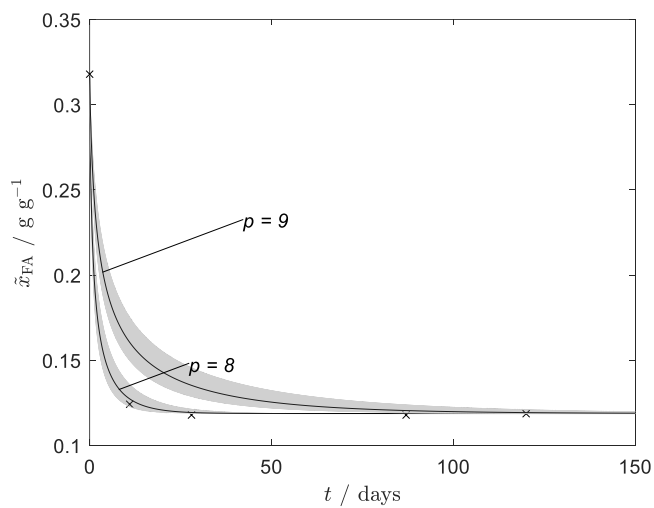
**Figure 97:** Experimental and calculated overall formaldehyde concentration in the liquid phase for Experiment OME-5. (×) Experimental data, (—) model. The line is for pH value 11, the shaded area indicates the influence a variation of the pH in the model by ± 1.5 .

Table 91: Measured concentration of the liquid phase over time for Experiment OME-6.

t / days	$\tilde{x}_{\text{FA}}^{(m)} / \text{g g}^{-1}$	$\tilde{x}_{\text{W}}^{(m)} / \text{g g}^{-1}$	$\tilde{x}_{\text{FAC}}^{(m)} / \text{g g}^{-1}$
0	0.3573	0.5397	n.a.
11	0.1646	0.7161	0.00226
28	0.1642	0.7138	0.00283
94	0.1643	0.7125	0.00283
150	0.1655	0.6927	0.00284

n.a. : not available

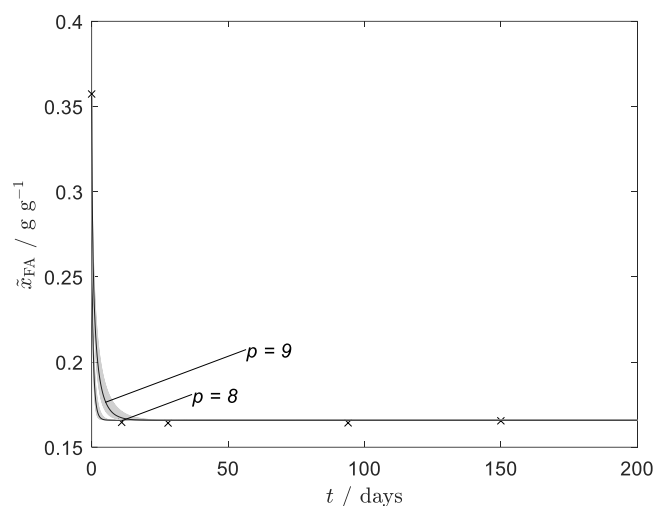
**Figure 98:** Experimental and calculated overall formaldehyde concentration in the liquid phase for Experiment OME-6. (×) Experimental data, (—) model. The line is for pH value 11, the shaded area indicates the influence a variation of the pH in the model by ± 1.5 .

Table 92: Measured concentration of the liquid phase over time for Experiment OME-7.

t / days	$\tilde{x}_{\text{FA}}^{(m)} / \text{g g}^{-1}$	$\tilde{x}_{\text{W}}^{(m)} / \text{g g}^{-1}$	$\tilde{x}_{\text{FAC}}^{(m)} / \text{g g}^{-1}$
0	0.3178	0.4797	n.a.
28	0.1499	0.6175	0.00253
94	0.1483	0.6225	0.00266
122	0.1470	0.6176	0.00261

n.a. : not available

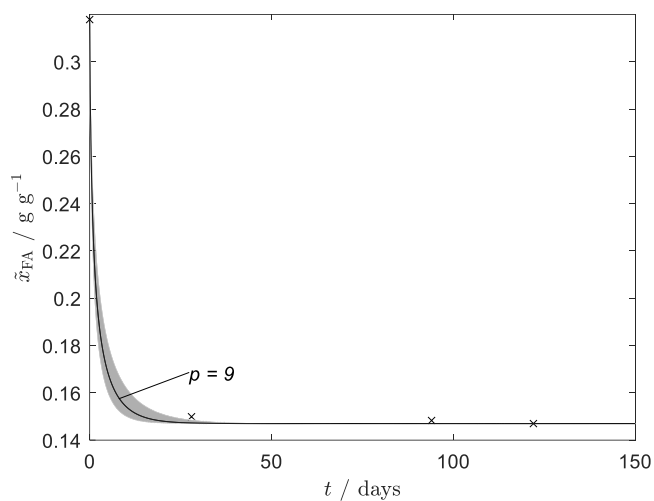
**Figure 99:** Experimental and calculated overall formaldehyde concentration in the liquid phase for Experiment OME-7. (×) Experimental data, (—) model. The line is for pH value 11, the shaded area indicates the influence a variation of the pH in the model by ± 1.5 .

Table 93: Measured concentration of the liquid phase over time for Experiment OME-8.

t / days	$\tilde{x}_{\text{FA}}^{(m)} / \text{g g}^{-1}$	$\tilde{x}_{\text{W}}^{(m)} / \text{g g}^{-1}$	$\tilde{x}_{\text{FAC}}^{(m)} / \text{g g}^{-1}$
0	0.2782	0.4194	n.a.
11	0.1376	0.5629	0.00214
28	0.1375	0.5691	0.00270
94	0.1373	0.5576	0.00266

n.a. : not available

Table 94: Measured concentration of the liquid phase over time for Experiment OME-9.

t / days	$\tilde{x}_{\text{FA}}^{(m)} / \text{g g}^{-1}$	$\tilde{x}_{\text{W}}^{(m)} / \text{g g}^{-1}$	$\tilde{x}_{\text{FAC}}^{(m)} / \text{g g}^{-1}$
0	0.3465	0.5519	n.a.
128	0.2023	0.6856	n.a.
215	0.2039	0.6837	n.a.

n.a. : not available

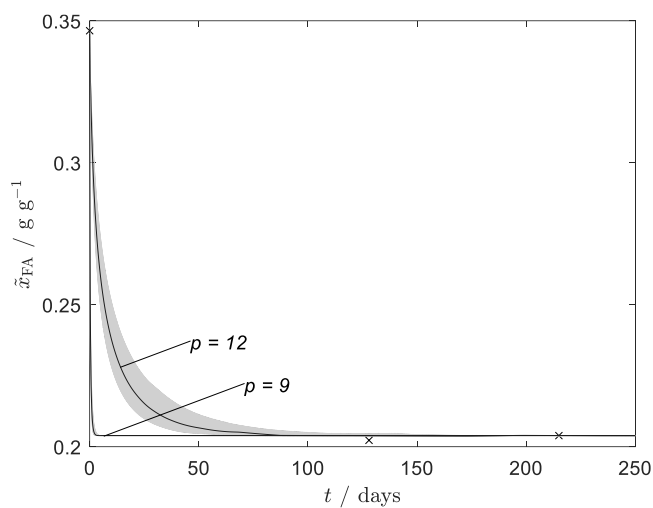
**Figure 100:** Experimental and calculated overall formaldehyde concentration in the liquid phase for Experiment OME-9. (×) Experimental data, (—) model. The line is for pH value 11, the shaded area indicates the influence a variation of the pH in the model by ± 1.5 .

Table 95: Measured concentration of the liquid phase over time for Experiment OME-10.

t / days	$\tilde{x}_{\text{FA}}^{(m)} / \text{g g}^{-1}$	$\tilde{x}_{\text{W}}^{(m)} / \text{g g}^{-1}$	$\tilde{x}_{\text{FAC}}^{(m)} / \text{g g}^{-1}$
0	0.3577	0.5401	n.a.
11	0.1295	0.7529	0.00074
26	0.1199	0.7628	0.00081
92	0.1140	0.7615	0.00175
220	0.1125	0.7512	0.00199

n.a. : not available

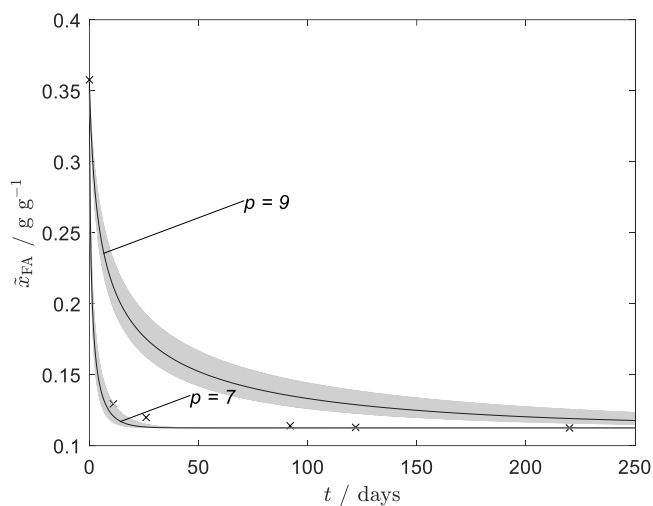
**Figure 101:** Experimental and calculated overall formaldehyde concentration in the liquid phase for Experiment OME-10. (×) Experimental data, (—) model. The line is for pH value 11, the shaded area indicates the influence a variation of the pH in the model by ± 1.5 .

Table 96: Measured concentration of the liquid phase over time for Experiment OME-11.

t / days	$\tilde{x}_{\text{FA}}^{(m)} / \text{g g}^{-1}$	$\tilde{x}_{\text{W}}^{(m)} / \text{g g}^{-1}$	$\tilde{x}_{\text{FAC}}^{(m)} / \text{g g}^{-1}$
0	0.3179	0.4798	n.a.
11	0.1237	0.6758	0.00067
26	0.1105	0.6780	0.00078
92	0.1102	0.6744	0.00160
150	0.1082	0.6539	0.00183
455	0.1020	0.6515	n.a.

n.a. : not available

Table 97: Measured concentration of the liquid phase over time for Experiment OME-12.

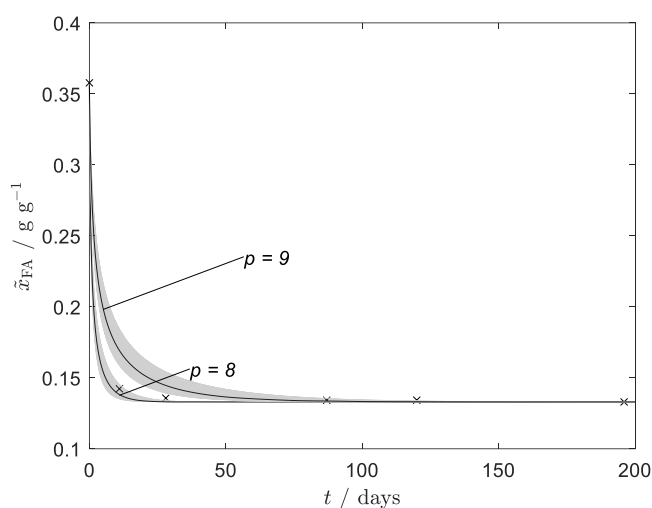
t / days	$\tilde{x}_{\text{FA}}^{(m)} / \text{g g}^{-1}$	$\tilde{x}_{\text{W}}^{(m)} / \text{g g}^{-1}$	$\tilde{x}_{\text{FAC}}^{(m)} / \text{g g}^{-1}$
0	0.2781	0.4193	n.a.
11	0.1258	0.6782	0.00080
26	0.1145	0.6897	0.00097
92	0.1076	0.6865	0.00206
122	0.1065	0.6888	0.00219
455	0.1022	0.6621	n.a.

n.a. : not available

Table 98: Measured concentration of the liquid phase over time for Experiment OME-13.

t / days	$\tilde{x}_{\text{FA}}^{(m)} / \text{g g}^{-1}$	$\tilde{x}_{\text{W}}^{(m)} / \text{g g}^{-1}$	$\tilde{x}_{\text{FAC}}^{(m)} / \text{g g}^{-1}$
0	0.3578	0.5397	n.a.
11	0.1423	0.7309	0.00109
28	0.1357	0.7434	0.00216
87	0.1342	0.7419	0.00271
120	0.1343	0.7427	0.00282
196	0.133	0.7303	0.00272

n.a. : not available

**Figure 102:** Experimental and calculated overall formaldehyde concentration in the liquid phase for Experiment OME-13. (×) Experimental data, (—) model. The line is for pH value 11, the shaded area indicates the influence a variation of the pH in the model by ± 1.5 .**Table 99:** Measured concentration of the liquid phase over time for Experiment OME-14.

t / days	$\tilde{x}_{\text{FA}}^{(m)} / \text{g g}^{-1}$	$\tilde{x}_{\text{W}}^{(m)} / \text{g g}^{-1}$	$\tilde{x}_{\text{FAC}}^{(m)} / \text{g g}^{-1}$
0	0.3181	0.4800	n.a.
11	0.1293	0.6630	0.00107
28	0.1230	0.6575	0.00220
87	0.1228	0.6718	0.00278
150	0.1260	0.6390	0.00274
193	0.1255	0.6347	0.00278
490	0.1249	0.6306	n.a.

n.a. : not available

Table 100: Measured concentration of the liquid phase over time for Experiment OME-15.

t / days	$\tilde{x}_{\text{FA}}^{(m)} / \text{g g}^{-1}$	$\tilde{x}_{\text{W}}^{(m)} / \text{g g}^{-1}$	$\tilde{x}_{\text{FAC}}^{(m)} / \text{g g}^{-1}$
0	0.2778	0.4195	n.a.
11	0.1300	0.6631	0.00128
28	0.1234	0.6591	0.00259
87	0.1232	0.6684	0.00332
196	0.1221	0.6494	0.00324

n.a. : not available

Table 101: Measured concentration of the liquid phase over time for Experiment OME-16.

t / days	$\tilde{x}_{\text{FA}}^{(m)} / \text{g g}^{-1}$	$\tilde{x}_{\text{W}}^{(m)} / \text{g g}^{-1}$	$\tilde{x}_{\text{FAC}}^{(m)} / \text{g g}^{-1}$
0	0.3571	0.5390	n.a.
11	0.1652	0.7073	0.00214
28	0.1636	0.7008	0.00270
94	0.1636	0.7161	0.00276
150	0.1639	0.7083	0.00272
193	0.1636	0.7030	0.00272

n.a. : not available

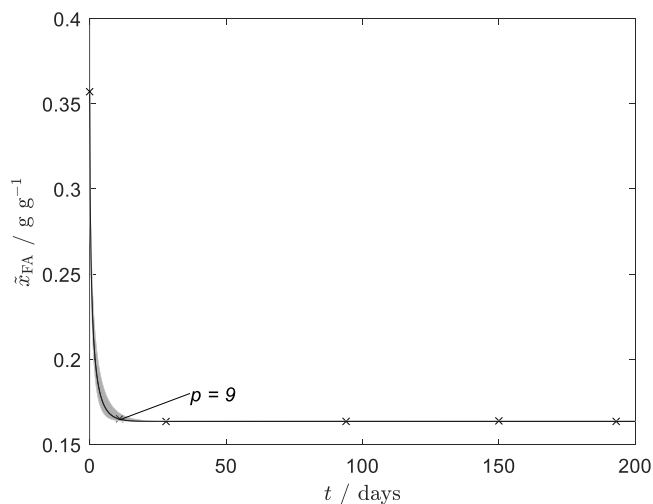
**Figure 103:** Experimental and calculated overall formaldehyde concentration in the liquid phase for Experiment OME-16. (×) Experimental data, (—) model. The line is for pH value 11, the shaded area indicates the influence a variation of the pH in the model by ± 1.5 .

Table 102: Measured concentration of the liquid phase over time for Experiment OME-17.

t / days	$\tilde{x}_{\text{FA}}^{(m)} / \text{g g}^{-1}$	$\tilde{x}_{\text{W}}^{(m)} / \text{g g}^{-1}$	$\tilde{x}_{\text{FAC}}^{(m)} / \text{g g}^{-1}$
0	0.3177	0.4805	n.a.
11	0.1500	0.6240	0.00216
94	0.1478	0.6337	0.00269
193	0.1478	0.6118	0.00267

n.a. : not available

Table 103: Measured concentration of the liquid phase over time for Experiment OME-18.

t / days	$\tilde{x}_{\text{FA}}^{(m)} / \text{g g}^{-1}$	$\tilde{x}_{\text{W}}^{(m)} / \text{g g}^{-1}$	$\tilde{x}_{\text{FAC}}^{(m)} / \text{g g}^{-1}$
0	0.2779	0.4191	n.a.
11	0.1504	0.6366	0.00248
28	0.1490	0.6391	0.00311
94	0.1483	0.6402	0.00306
150	0.1492	0.6027	0.00303
193	0.1486	0.6035	0.00303

n.a. : not available

Table 104: Measured concentration of the liquid phase over time for Experiment OME-19.

t / days	$\tilde{x}_{\text{FA}}^{(m)} / \text{g g}^{-1}$	$\tilde{x}_{\text{W}}^{(m)} / \text{g g}^{-1}$	$\tilde{x}_{\text{FAC}}^{(m)} / \text{g g}^{-1}$
0	0.3573	0.5395	n.a.
11	0.2430	0.6429	0.00248
28	0.1989	0.6825	0.00254
87	0.1991	0.6919	0.00253
120	0.1991	0.6891	0.00275
196	0.1989	0.6789	0.00256

n.a. : not available

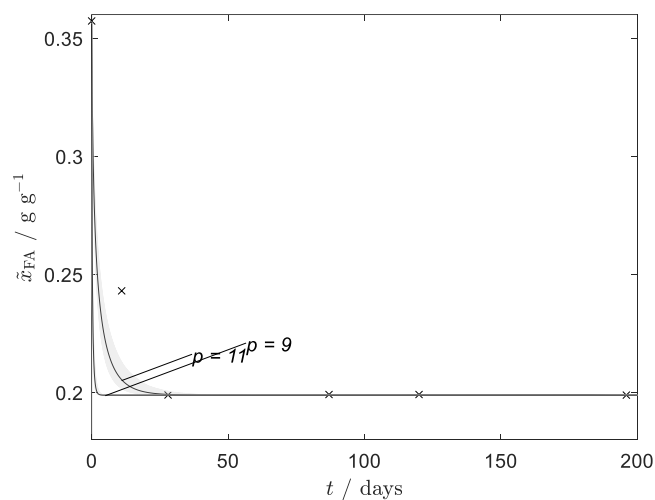


Figure 104: Experimental and calculated overall formaldehyde concentration in the liquid phase for Experiment OME-19. (×) Experimental data, (—) model. The line is for pH value 11, the shaded area indicates the influence a variation of the pH in the model by ± 1.5 .

Table 105: Measured concentration of the liquid phase over time for Experiment OME-20.

t / days	$\tilde{x}_{\text{FA}}^{(m)} / \text{g g}^{-1}$	$\tilde{x}_{\text{W}}^{(m)} / \text{g g}^{-1}$	$\tilde{x}_{\text{FAC}}^{(m)} / \text{g g}^{-1}$
0	0.3178	0.4796	n.a.
11	0.2360	0.5439	0.00152
28	0.1790	0.5958	0.00260
87	0.1801	0.603	0.00258
120	0.1796	0.5999	0.00283
196	0.1796	0.5855	0.00261

n.a. : not available

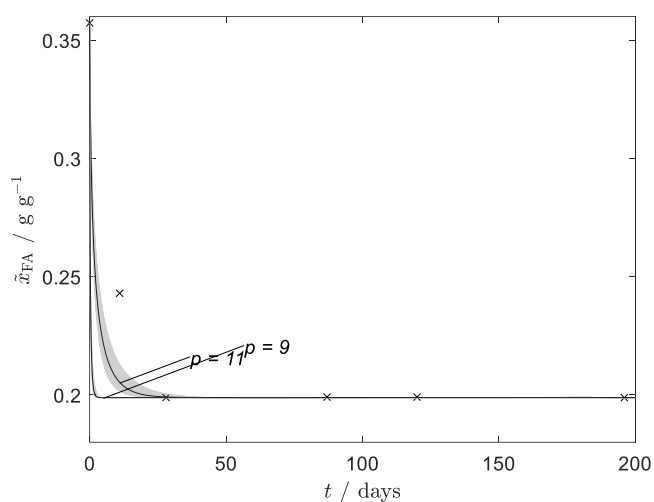
**Figure 105:** Experimental and calculated overall formaldehyde concentration in the liquid phase for Experiment OME-20. (×) Experimental data, (—) model. The line is for pH value 11, the shaded area indicates the influence a variation of the pH in the model by ± 1.5 .

Table 106: Measured concentration of the liquid phase over time for Experiment OME-21.

t / days	$\tilde{x}_{\text{FA}}^{(m)} / \text{g g}^{-1}$	$\tilde{x}_{\text{W}}^{(m)} / \text{g g}^{-1}$	$\tilde{x}_{\text{FAC}}^{(m)} / \text{g g}^{-1}$
0	0.2777	0.4192	n.a.
28	0.1776	0.5899	0.00301
87	0.1768	0.5923	0.00300
150	0.1670	0.5706	0.00299

n.a. : not available

Table 107: Measured concentration of the liquid phase over time for Experiment OME-22.

t / days	$\tilde{x}_{\text{FA}}^{(m)} / \text{g g}^{-1}$	$\tilde{x}_{\text{W}}^{(m)} / \text{g g}^{-1}$	$\tilde{x}_{\text{MeOH}}^{(m)} / \text{g g}^{-1}$	$\tilde{x}_{\text{FAC}}^{(m)} / \text{g g}^{-1}$
0	0.3783	0.4452	0.07029	n.a.
64	0.1730	0.5742	0.11454	
215	0.1718	0.6040	0.07441	
314	0.1698	0.5956	0.09664	

n.a. : not available

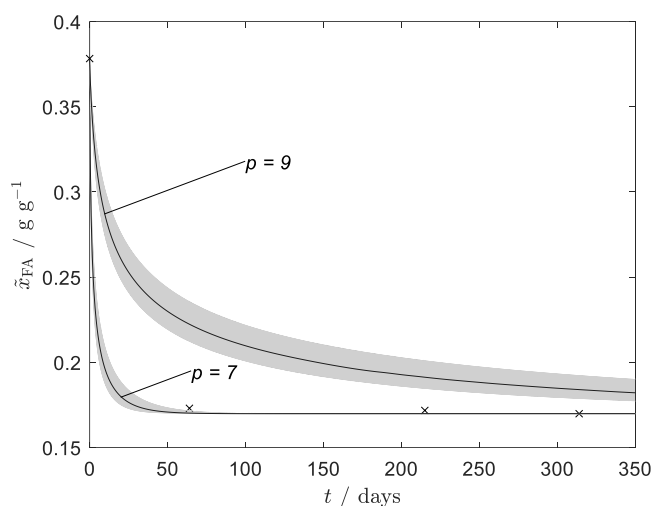
**Figure 106:** Experimental and calculated overall formaldehyde concentration in the liquid phase for Experiment OME-22. (×) Experimental data, (—) model. The line is for pH value 11, the shaded area indicates the influence a variation of the pH in the model by ± 1.5 .

Table 108: Measured concentration of the liquid phase over time for Experiment OME-23.

t / days	$\tilde{x}_{\text{FA}}^{(m)} / \text{g g}^{-1}$	$\tilde{x}_{\text{W}}^{(m)} / \text{g g}^{-1}$	$\tilde{x}_{\text{MeOH}}^{(m)} / \text{g g}^{-1}$	$\tilde{x}_{\text{FAC}}^{(m)} / \text{g g}^{-1}$
0	0.3374	0.3982	0.0629	n.a.
64	0.1559	0.4929	0.0982	n.a.
215	0.1539	0.5162	0.0513	n.a.
314	0.1516	0.5119	0.0825	n.a.

n.a. : not available

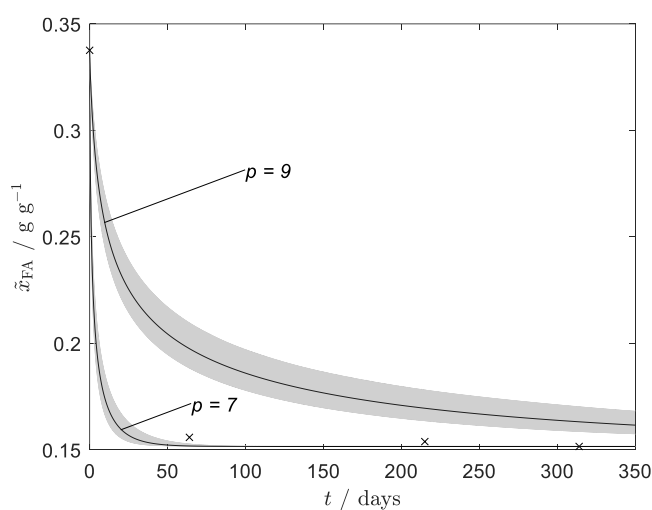
**Figure 107:** Experimental and calculated overall formaldehyde concentration in the liquid phase for Experiment OME-23. (×) Experimental data, (—) model. The line is for pH value 11, the shaded area indicates the influence a variation of the pH in the model by ± 1.5 .

Table 109: Measured concentration of the liquid phase over time for Experiment OME-24.

t / days	$\tilde{x}_{\text{FA}}^{(m)} / \text{g g}^{-1}$	$\tilde{x}_{\text{W}}^{(m)} / \text{g g}^{-1}$	$\tilde{x}_{\text{MeOH}}^{(m)} / \text{g g}^{-1}$	$\tilde{x}_{\text{FAC}}^{(m)} / \text{g g}^{-1}$
0	0.4118	0.3499	0.1366	n.a.
64	0.2372	0.4395	0.1977	
128	0.2369	0.4596	0.1626	
215	0.2362	0.4600	0.1631	
314	0.2370	0.4506	0.1811	

n.a. : not available

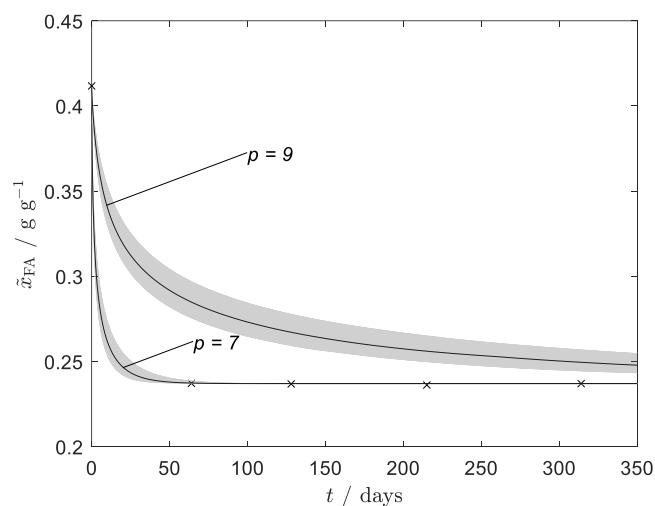
**Figure 108:** Experimental and calculated overall formaldehyde concentration in the liquid phase for Experiment OME-24. (x) Experimental data, (—) model. The line is for pH value 11, the shaded area indicates the influence a variation of the pH in the model by ± 1.5 .

Table 110: Measured concentration of the liquid phase over time for Experiment OME-25.

t / days	$\tilde{x}_{\text{FA}}^{(m)} / \text{g g}^{-1}$	$\tilde{x}_{\text{W}}^{(m)} / \text{g g}^{-1}$	$\tilde{x}_{\text{MeOH}}^{(m)} / \text{g g}^{-1}$	$\tilde{x}_{\text{FAC}}^{(m)} / \text{g g}^{-1}$
0	0.3656	0.3106	0.1219	n.a.
64	0.2093	0.3757	0.1738	0.00125
215	0.2082	0.3953	0.1330	n.a.
314	0.2069	0.3975	0.1495	n.a.

n.a. : not available

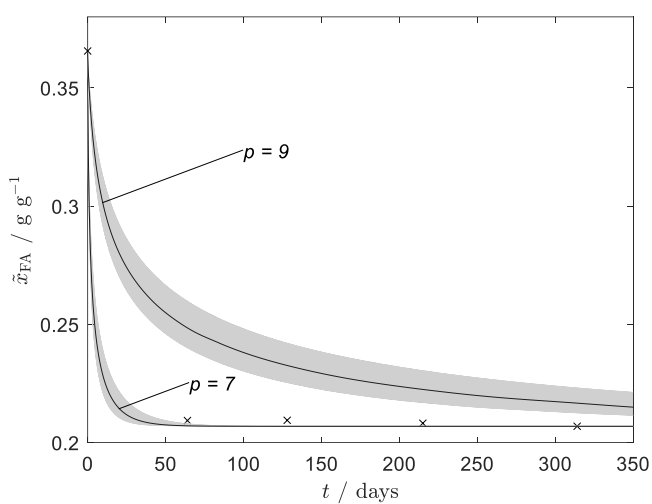
**Figure 109:** Experimental and calculated overall formaldehyde concentration in the liquid phase for Experiment OME-25. (×) Experimental data, (—) model. The line is for pH value 11, the shaded area indicates the influence a variation of the pH in the model by ± 1.5 .

Table 111: Measured concentration of the liquid phase over time for Experiment OME-26.

t / days	$\tilde{x}_{\text{FA}}^{(m)} / \text{g g}^{-1}$	$\tilde{x}_{\text{W}}^{(m)} / \text{g g}^{-1}$	$\tilde{x}_{\text{MeOH}}^{(m)} / \text{g g}^{-1}$	$\tilde{x}_{\text{FAC}}^{(m)} / \text{g g}^{-1}$
0	0.3803	0.4477	0.0706	n.a.
64	0.2365	0.5340	0.0985	
128	0.2319	0.5577	0.0739	
215	0.2337	0.5553	0.0803	
314	0.2328	0.5572	0.0893	

n.a. : not available

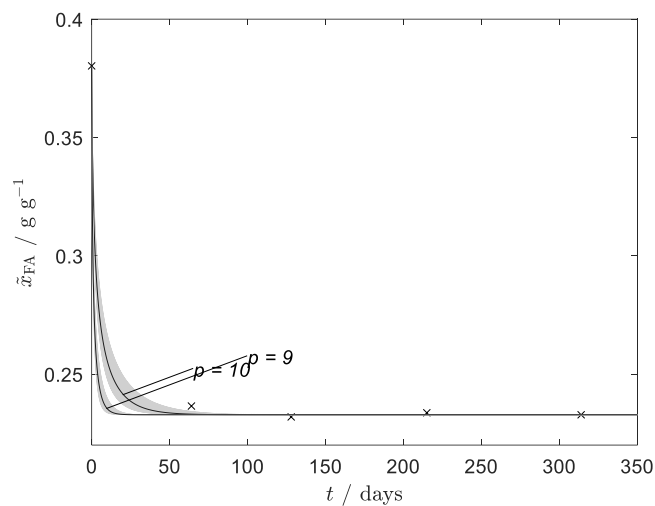
**Figure 110:** Experimental and calculated overall formaldehyde concentration in the liquid phase for Experiment OME-26. (×) Experimental data, (—) model. The line is for pH value 11, the shaded area indicates the influence a variation of the pH in the model by ± 1.5 .

Table 112: Measured concentration of the liquid phase over time for Experiment OME-27.

t / days	$\tilde{x}_{\text{FA}}^{(m)} / \text{g g}^{-1}$	$\tilde{x}_{\text{W}}^{(m)} / \text{g g}^{-1}$	$\tilde{x}_{\text{MeOH}}^{(m)} / \text{g g}^{-1}$	$\tilde{x}_{\text{FAC}}^{(m)} / \text{g g}^{-1}$
0	0.3377	0.3978	0.0632	n.a.
64	0.2070	0.4584	0.0857	n.a.
314	0.2057	0.4786	0.0779	n.a.

n.a. : not available

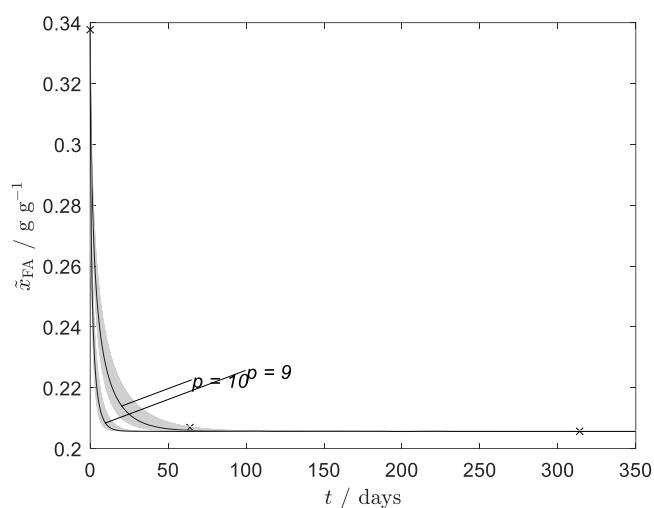
**Figure 111:** Experimental and calculated overall formaldehyde concentration in the liquid phase for Experiment OME-27. (×) Experimental data, (—) model. The line is for pH value 11, the shaded area indicates the influence a variation of the pH in the model by ± 1.5 .

Table 113: Measured concentration of the liquid phase over time for Experiment OME-28.

t / days	$\tilde{x}_{\text{FA}}^{(m)} / \text{g g}^{-1}$	$\tilde{x}_{\text{W}}^{(m)} / \text{g g}^{-1}$	$\tilde{x}_{\text{MeOH}}^{(m)} / \text{g g}^{-1}$	$\tilde{x}_{\text{FAC}}^{(m)} / \text{g g}^{-1}$
0	0.4117	0.3500	0.1365	n.a.
64	0.3084	0.3983	0.1672	0.00235
215	0.3024	0.4200	0.1509	n.a.
314	0.2989	0.4219	0.1616	n.a.

n.a. : not available

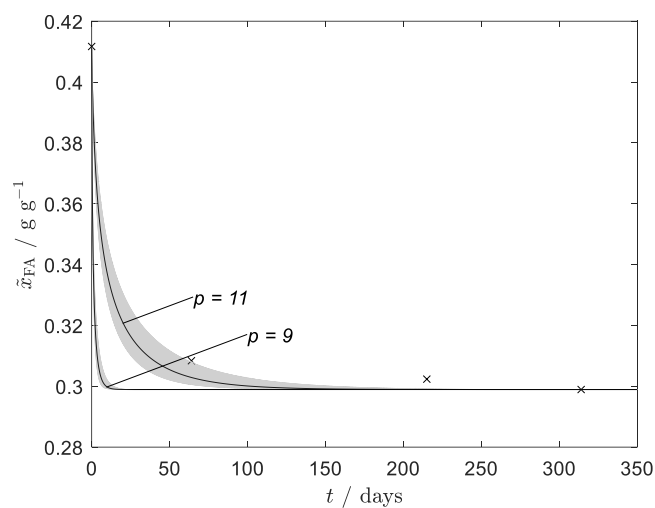


Figure 112: Experimental and calculated overall formaldehyde concentration in the liquid phase for Experiment OME-28. (×) Experimental data, (—) model. The line is for pH value 11, the shaded area indicates the influence a variation of the pH in the model by ± 1.5 .

Table 114: Measured concentration of the liquid phase over time for Experiment OME-29.

t / days	$\tilde{x}_{\text{FA}}^{(m)} / \text{g g}^{-1}$	$\tilde{x}_{\text{W}}^{(m)} / \text{g g}^{-1}$	$\tilde{x}_{\text{MeOH}}^{(m)} / \text{g g}^{-1}$	$\tilde{x}_{\text{FAC}}^{(m)} / \text{g g}^{-1}$
0	0.3655	0.3115	0.1214	n.a.
64	0.2544	0.3528	0.1493	
215	0.2532	0.3709	0.1214	
314	0.2534	0.3706	0.1425	

n.a. : not available

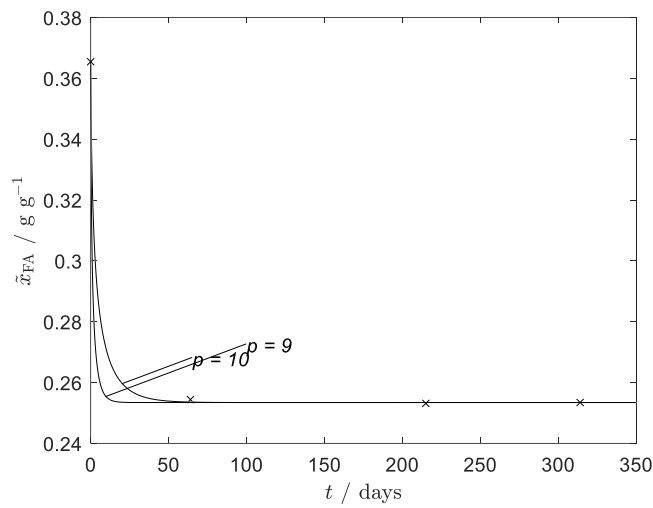


Figure 113: Experimental and calculated overall formaldehyde concentration in the liquid phase for Experiment OME-29. (×) Experimental data, (—) model. The line is for pH value 11, the shaded area indicates the influence a variation of the pH in the model by ± 1.5 .

Table 115: Measured concentration of the liquid phase over time for Experiment OME-30.

t / days	$\tilde{x}_{\text{FA}}^{(m)} / \text{g g}^{-1}$	$\tilde{x}_{\text{W}}^{(m)} / \text{g g}^{-1}$	$\tilde{x}_{\text{MeOH}}^{(m)} / \text{g g}^{-1}$	$\tilde{x}_{\text{FAC}}^{(m)} / \text{g g}^{-1}$
0	0.3801	0.4478	0.07043	n.a.
64	0.1839	0.5350	0.13764	
128	0.1736	0.6004	0.09411	
215	0.1721	0.6027	0.10045	
350	0.1710	0.5977	0.09934	

n.a. : not available

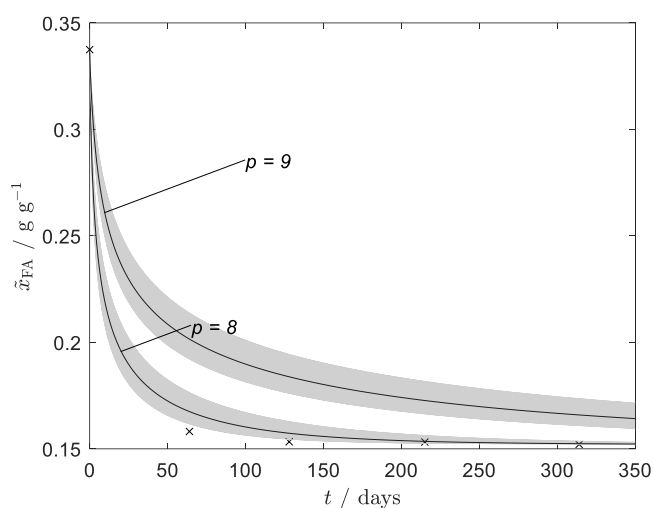
**Figure 114:** Experimental and calculated overall formaldehyde concentration in the liquid phase for Experiment OME-30. (x) Experimental data, (—) model. The line is for pH value 11, the shaded area indicates the influence a variation of the pH in the model by ± 1.5 .

Table 116: Measured concentration of the liquid phase over time for Experiment OME-31.

t / days	$\tilde{x}_{\text{FA}}^{(m)} / \text{g g}^{-1}$	$\tilde{x}_{\text{W}}^{(m)} / \text{g g}^{-1}$	$\tilde{x}_{\text{MeOH}}^{(m)} / \text{g g}^{-1}$	$\tilde{x}_{\text{FAC}}^{(m)} / \text{g g}^{-1}$
0	0.3374	0.3982	0.06275	n.a.
64	0.1582	0.4712	0.10097	
128	0.1533	0.5108	0.08853	
215	0.1532	0.5082	0.08258	
314	0.1521	0.5123	0.08325	

n.a. : not available

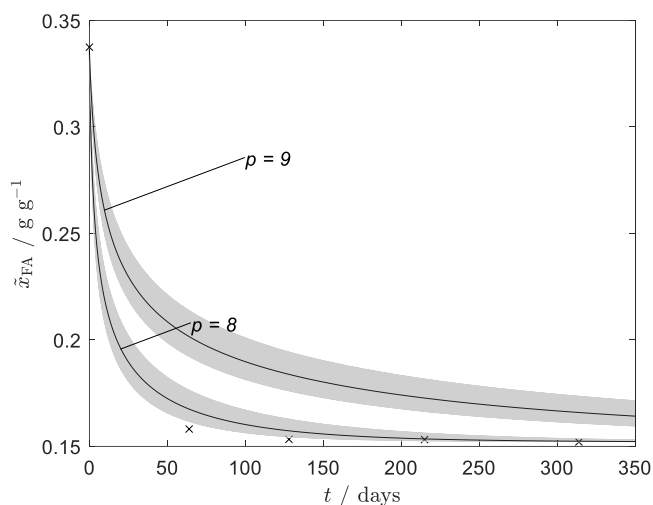
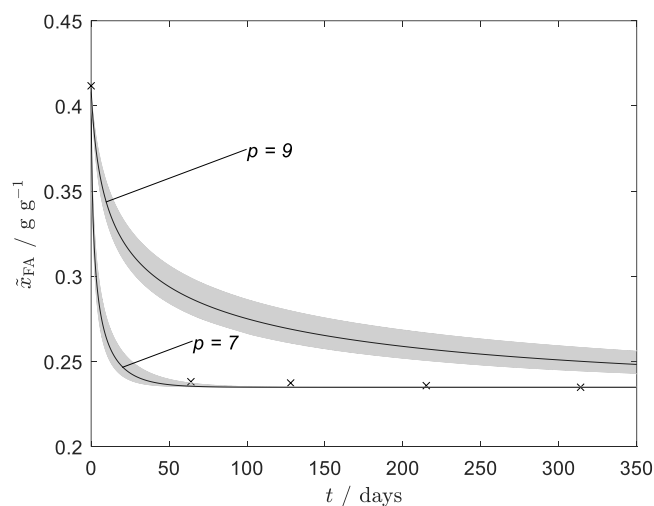
**Figure 115:** Experimental and calculated overall formaldehyde concentration in the liquid phase for Experiment OME-31. (×) Experimental data, (—) model. The line is for pH value 11, the shaded area indicates the influence a variation of the pH in the model by ± 1.5 .

Table 117: Measured concentration of the liquid phase over time for Experiment OME-32.

t / days	$\tilde{x}_{\text{FA}}^{(m)} / \text{g g}^{-1}$	$\tilde{x}_{\text{W}}^{(m)} / \text{g g}^{-1}$	$\tilde{x}_{\text{MeOH}}^{(m)} / \text{g g}^{-1}$	$\tilde{x}_{\text{FAC}}^{(m)} / \text{g g}^{-1}$
0	0.4118	0.3501	0.13655	n.a.
64	0.2382	0.4387	0.19389	
128	0.2374	0.4589	0.18117	
215	0.2359	0.4546	0.17993	
314	0.2349	0.4558	0.18094	

n.a. : not available

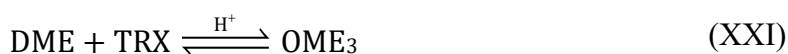
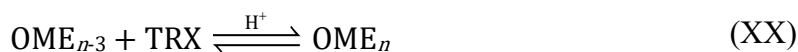
**Figure 116:** Experimental and calculated overall formaldehyde concentration in the liquid phase for Experiment OME-32. (×) Experimental data, (—) model. The line is for pH value 11, the shaded area indicates the influence a variation of the pH in the model by ± 1.5 .

B Supporting information for Chapter 3

B.1 Discussion of alternative reactions mechanisms of the OME formation

Only one reaction mechanism leading from DME and FA to OME was discussed in Chapter 3.2 for brevity. Alternatives have been described in the literature, which are briefly discussed here.

Some authors [31,32,37,77] suggest, in contrast to the reaction mechanism of this work, a direct reaction of TRX with MAL and OME according to Reactions (XIX) and (XX). The corresponding reaction with DME is Reaction (XXI)



The equilibrium constants of Reactions (XIX) to (XXI) can be calculated from the information presented in Chapter 3. Based on the results from the present work, Reactions (XIX) and (XX) are expected to be fast compared to Reaction (XXI). As the experimental evidence for the direct insertion of trioxane is scarce in literature [33,36,77], and also the present study gives no indications pointing at such a mechanism, it was refrained from using it in the model.

Haltenort et al.[31] describe a transacetalisation as a mechanism for forming OME. Thereby two OME molecules of some initial chain lengths m_0 and n_0 react to form two OMEs of different chain lengths m_1 and n_1



It is assumed that the reaction proceeds by cleavage of the educts and a cross-exchange of the different parts. Haltenort et al.[31] showed the occurrence of this exchange of end-groups by experiments with mixtures of methylal and ethylal ($\text{CH}_3\text{-CH}_2\text{-O-CH}_2\text{-O-CH}_2\text{-CH}_3$) in which

ethoxymethoxymethane was formed. Also, the equilibrium constants of the transacetalisation reactions can be calculated from those presented in the present work. As the transacetalisation only relates to the formation of different OME, i.e., to reactions which are assumed to be in equilibrium at any time in our experiments, introducing transacetalisation in our model would lead to no difference.

As methanol and HF_n are present in the acidic reaction mixture, in principle, OME_n can be formed also, according to Equation (XXIII) [22,27,59]. Due to the small amounts of HF_n and methanol, it is not expected that Reaction (XXIII) is important here. Furthermore, as it is assumed that the chain elongation reactions are in equilibrium at all times, introducing reaction (XXIII) would not alter the model.



The reverse Reaction (XXIII) can be interpreted as a hydrolysis of OME_n. In the same way, a hydrolysis of DME could occur, as described by Reaction (XXIV).



Reaction (XXIII) and (XXIV) in connection with the formation of hemiformals HF_n from formaldehyde and methanol provide another pathway for the formation of OME_n from DME and formaldehyde. Since water is present only in traces here, it cannot be expected that this pathway plays a significant role.

B.2 Operating procedures of the experiments

In the following, an extended description of the experimental procedure of the different experiments in Chapter 3 is given.

B.2.1 Type A experiments

The reactor was evacuated and flushed with nitrogen. The reactor was opened, and the trioxane was filled in. The catalyst reservoir was filled with catalyst. The reactor was closed, cooled down with liquid nitrogen, and evacuated to a pressure of $p = 0.2$ bar. The liquid DME was filled in. The reactor was heated to the reaction temperature. When the reaction mixture temperature reached 343 K (Which is 6 K above the melting temperature of trioxane to avoid mixing of solids), the stirrer was switched on. The catalyst reservoir was pressurized to 31 bar with nitrogen. The valve of the catalyst reservoir was opened for a few seconds. This procedure was carried out twice to ensure that the complete mass of the catalyst is blown into the reactor. The catalyst mass in the

reactor was determined by weighing the full reservoir before and after the experiment (uncertainty ± 0.05 g). The time of the insertion of the catalyst was taken as starting time of the reaction.

B.2.2 Type B experiments

The reactor was evacuated and flushed with nitrogen. The reactor was opened, and the liquid OMEs were filled in together with the catalyst. The reactor was closed, and cooled down with liquid nitrogen. Subsequently, the liquid DME was filled in. Then the reactor was heated to the reaction temperature within 30 minutes. When the reaction mixture temperature reached 293 K (at this temperature the mixture is complete fluid), the stirrer was switched on. The start of the reaction was formally defined to be the time when the reactor had reached the desired temperature.

B.3 Peak assignment of the components in the NMR spectra

In Table 118 the peak assignment of the components in the ^{13}C NMR-spectra is given. In Figure 117 a typical ^{13}C NMR spectrum of a sample from the reaction experiments is given.

Table 118: Structural formula and peak assignment of the measured components. Tetramethylsilane was used as reference with a chemical shift of 0 ppm.

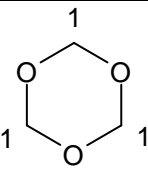
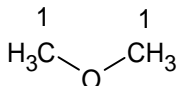
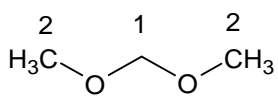
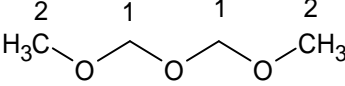
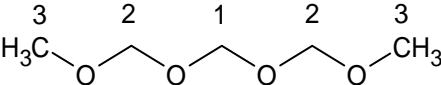
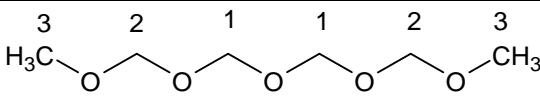
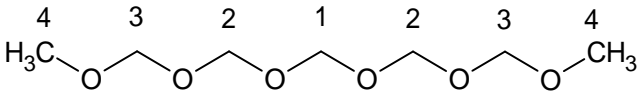
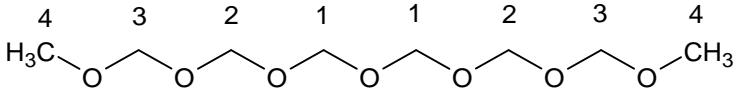
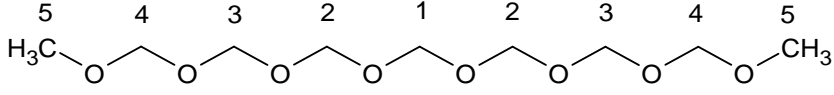
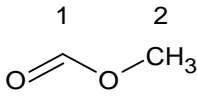
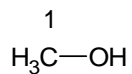
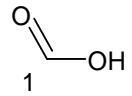
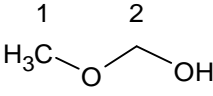
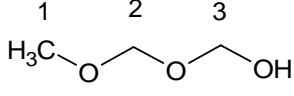
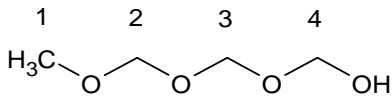
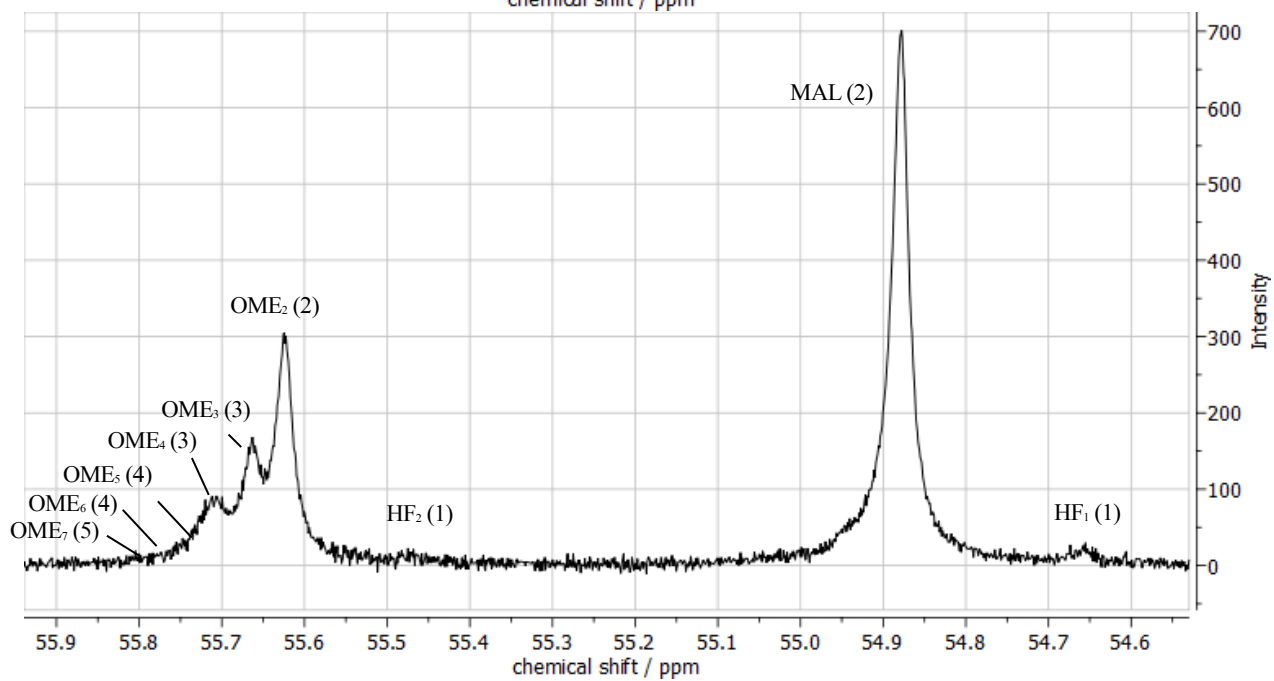
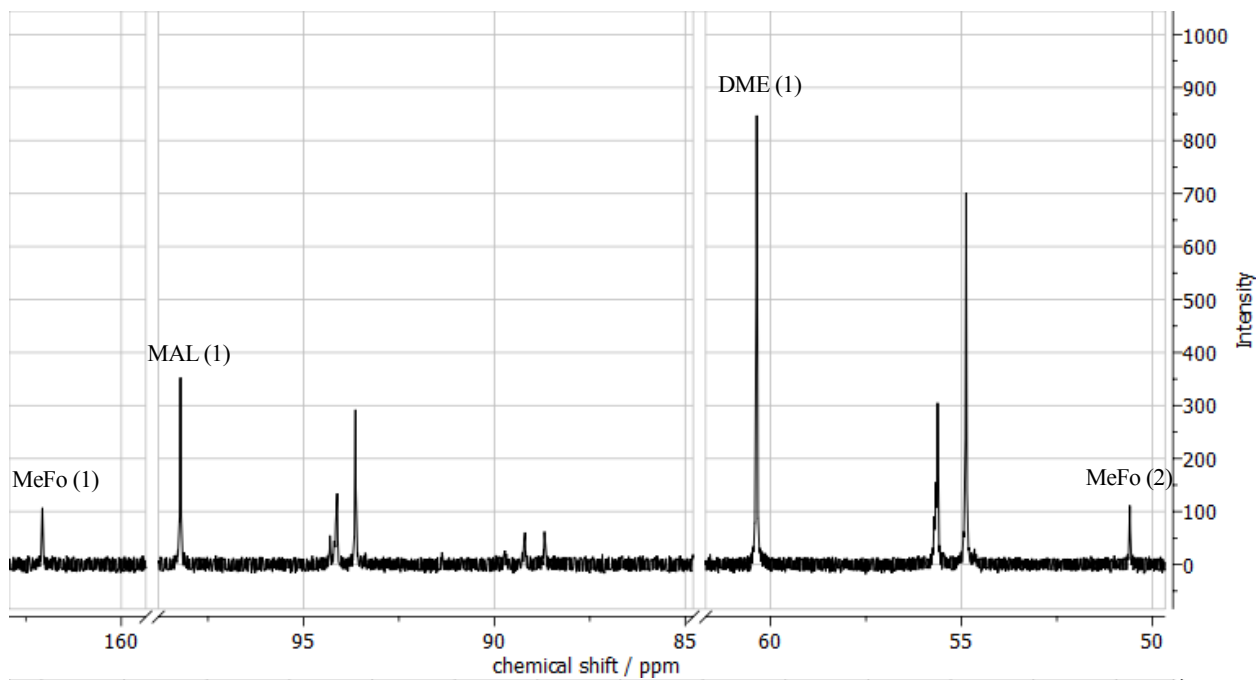
Component <i>i</i>	Structure	chemical shift / ppm
TRX		(1) 94,31
DME		(1) 60,36
MAL		(1) 98,20 (2) 54,86
OME ₂		(1) 93,67 (2) 55,65
OME ₃		(1) 88,67 (2) 94,14 (3) 55,69

Table 118 continued

OME ₄		(1) 89,24 (2) 94,18 (3) 55,73
OME ₅		(1) 89,27 (2) 89,73 (3) 94,20 (4) 55,75
OME ₆		(1) 89,31 (2) 89,75 (3) 94,21 (4) 55,76
OME ₇		(1) 89,33 (2) 89,76 (3) 94,22 (4) 94,30 (5) 55,77
MeFo		(1) 162,12 (2) 50,65
MeOH		(1) 49,85
FAc		(1) 162,58
HF ₁		(1) 54,68 (2) 91,38
HF ₂		(1) 55,6 (2) 86,58 (3) 93,27
HF ₃		(1) 55,63 (2) 86,94 (3) 93,83 (4) 93,84



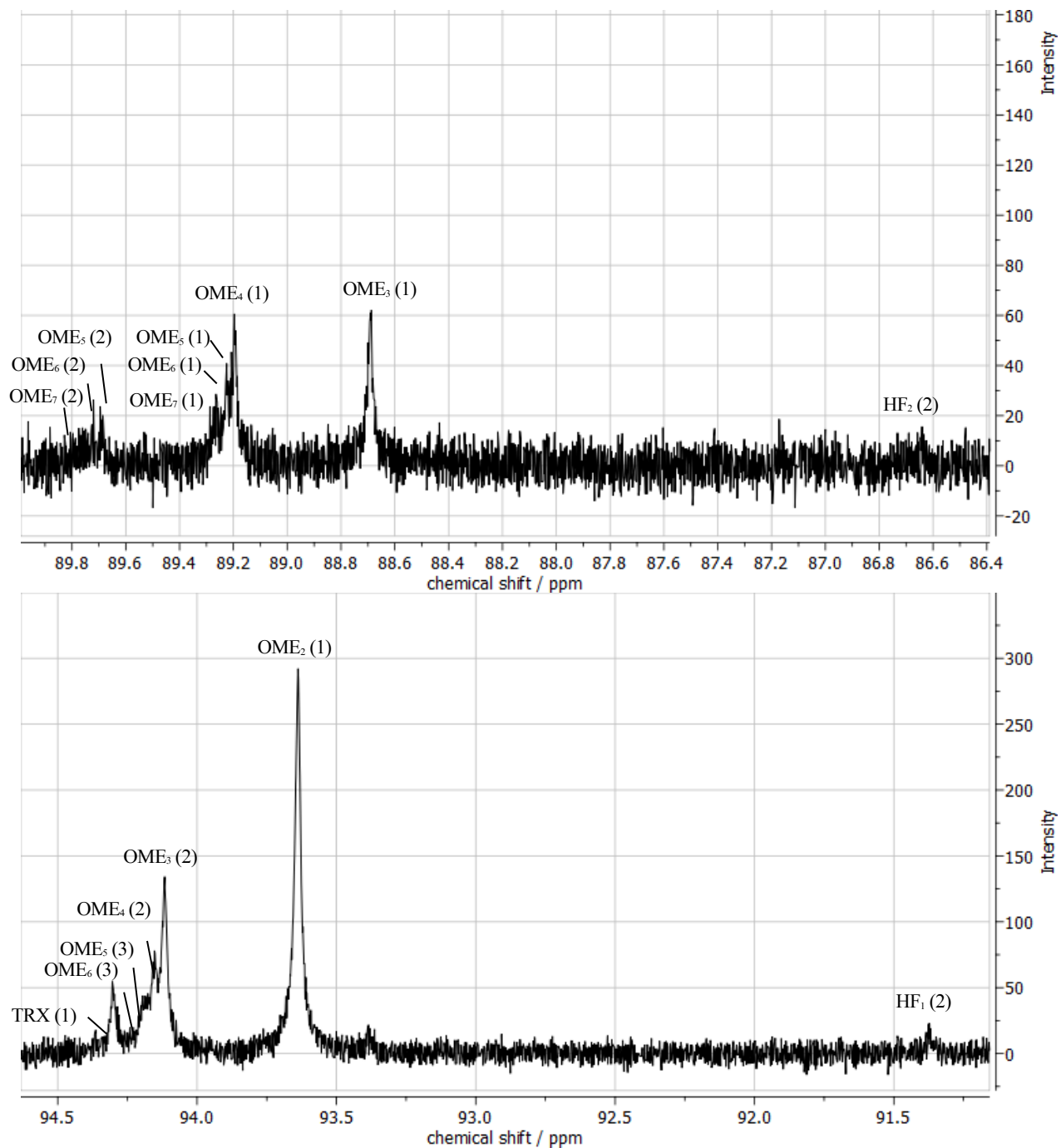


Figure 117: NMR spectrum of a typical sample from the experiments. For peak assignment see Table 118.

B.4 Pure component properties

The correlation used for describing pure component vapor pressures that was used in Chapter 3 is given in Equation (39). The corresponding parameters are given in Table 119. The amount of hemiformals with $n > 1$ in the gas phase can be neglected [55].

$$p_i^{LV} / \text{Pa} = 10^{F_i} \cdot \exp\left(A_i + \frac{B_i}{T/\text{K} + C_i} + D_i \cdot \ln(T/\text{K}) + E_i(T/\text{K})^2\right) \quad (39)$$

Table 119: Parameters for the calculation of the vapor pressure according to Equation (39).

Comp. i	A_i	B_i	C_i	D_i	E_i	F_i	Ref.
FA	14.4625	-2204.13	-30.15	0	0	3	[110]
TRX	14.3796	-3099.47	-68.92	0	0	3	[111]
DME	44.7040	-3525.60	0	-3.4444	0	0	[72]
MAL	9.6420	-2640.84	-41.22	0	0	5	[29]
OME ₂	68.1040	-7223.44	0	-8.2522	0	5	[29]
OME ₃	63.6820	-8042.31	0	-7.4100	0	5	[29]
OME ₄	81.2140	-10017.28	0	-9.7511	0	5	[29]
OME ₅	86.9390	-11323.17	0	-10.3994	0	5	[29]
OME ₆	93.4940	-12720.00	0	-11.1491	0	5	[29]
OME ₇	99.8120	-14090.90	0	-11.8697	0	5	[29]
MeFo	77.1840	-5606.10	0	-8.3920	$7.6468 \cdot 10^{-6}$	0	[72]
MeOH	16.5725	-3625.55	-34.29	0	0	3	[110]
FAc	15.4167	-3899.10	-12.94	0	0	3	[110]
HF ₁	19.5736	-5646.71	0	0	0	3	[110]

For describing the molar volume of the pure components, the correlation given in Equation (40) was used; the corresponding parameters are given in Table 120. The critical temperatures are given in Table 121. The parameters A_i , B_i , C_i for OME₅ are fitted to the experimental data of Kang et al.[147]. For the longer OME these parameters are adopted.

$$v_{i,\text{pure}} / (\text{m}^{-3} \cdot \text{kmol}) = \frac{B_i^{1 + \left(1 - \frac{T/\text{K}}{T_{\text{crit},i}/\text{K}}\right)^{C_i}}}{A_i} \quad (40)$$

Table 120: Parameters for the calculation of the molar volume according to Equation (40).

Component i	A_i	B_i	C_i
FA	1.9415 ^a	0.2231 ^a	0.2857 ^a
TRX	1.1590 ^a	0.2594 ^a	0.2857 ^a
DME	1.5693 ^b	0.2679 ^b	0.2882 ^b
MAL	1.4355 ^a	0.3058 ^a	0.3176 ^a
OME ₂	0.9005 ^a	0.2778 ^a	0.2857 ^a
OME ₃	0.7039 ^a	0.2725 ^a	0.2857 ^a
OME ₄	0.5506 ^a	0.2626 ^a	0.2857 ^a
OME ₅₋₇	0.5392 ^c	0.2791 ^c	0.3170 ^c
MeFo	1.5250 ^a	0.2634 ^a	0.2806 ^a
MeOH	2.3267 ^b	0.2707 ^b	0.2471 ^b
FAc	1.938 ^b	0.2423 ^b	0.2444 ^b
HF ₁	1.321 ^d	0.2390 ^d	0.2857 ^d
HF ₂	0.969 ^d	0.2469 ^d	0.2857 ^d
HF ₃	0.749 ^d	0.2464 ^d	0.2857 ^d

^(a)Burger et al.[29], ^(b) DIPPR-database[72] ^(c) fitted to data of Kang et al.[147] ^(d) Dyga et al.[148]

B.5 PSRK equation of state

Parameters needed for calculations with the PSRK EoS [86] are summarized in Table 121 (critical data) and Table 122 (Mathias-Copeman parameters). For the OME and HF the Mathias-Copeman parameters were not available, and the generalized form using the acentric factor was used.

Table 121: Critical temperature and pressure of the components.

Comp. i	$T_{c,i} / \text{K}$	$p_{c,i} / \text{bar}$
FA	408.0 ^a	65.90 ^b
TRX	604.0 ^a	58.20 ^b
DME	400.1 ^b	53.70 ^b
MAL	480.6 ^a	39.50 ^b
OME ₂	552.2 ^a	35.65 ^d
OME ₃	603.4 ^a	30.60 ^d
OME ₄	646.9 ^a	26.74 ^d
OME ₅	683.7 ^a	23.72 ^d
OME ₆	714.8 ^a	21.31 ^d
OME ₇	743.0 ^a	19.36 ^d
MeFo	487.2 ^a	60.00 ^b
MeOH	512.5 ^b	80.84 ^b
FAc	588.0 ^b	58.10 ^b

Table 121 continued

HF ₁	517.2 ^c	56.90 ^c
HF ₂	571.0 ^c	46.00 ^c
HF ₃	614.1 ^c	38.20 ^c

(^a) Burger et al.[²⁹] (^b) DIPPR[72] (^c) Dyga et al.[148] (^d) estimated with Marrero and Gani[149]

Table 122: Mathias-Copeman parameters adopted from Horstmann et al.[86].

Comp. <i>i</i>	$c_{1,i}$	$c_{2,i}$	$c_{3,i}$
FA	0.86009	-	-
TRX	0.94346	1.66560	-3.36300
DME	0.77572	0.04503	-0.17891
MAL	0.82106	-	-
MeFo	0.86547	-0.22908	0.86272
MeOH	1.42970	-0.66558	-0.12578
FAc	1.08545	-0.88879	0.81290

B.6 UNIFAC-based activity coefficient model

In Table 123 the group assignment for the components is given together with the size (R) and surface (Q) parameters of the groups. The interaction parameters are summarized in Table 124. The basis for this parameter table is taken from Schmitz et al.[56]. Parameters for MeFo and formic acid had to be integrated from literature. The split into functional groups and their parameters for methyl formate and formic acid were adopted from Kuhnert [110].

Table 123: Group assignment and size and surface parameters of the groups for the UNIFAC-based activity coefficient model.

Comp. <i>i</i>	group	count	R_i	Q_i	Ref.
FA	FA	1	0.9183	0.7800	[56]
TRX	TRX	1	2.7540	3.3000	[56]
DME	DME	1	2.0461	1.9360	[115]
MAL	MAL	1	2.9644	2.7160	[56]
OME _{<i>n</i>}	MAL	1			[56]
	FA _{OME}	(<i>n</i> -1)	0.9183	0.7800	[56]
MeFo	MeFo	1	2.2024	2.0720	[110]
MeOH	MeOH	1	1.4311	1.4320	[56]
FAc	FAc		1.5280	1.5320	[110]
HF _{<i>n</i>}	CH ₃ O	1	1.1450	1.0880	[56]
	CH ₂ OH	1	1.2044	1.1240	[56]
	FA	(<i>n</i> -1)			

Table 124: Interaction parameters of the groups for the UNIFAC-based activity coefficient model.

group j →	FA	TRX	DME				MeOH	FAC	CH ₃ O	CH ₂ OH
group i ↓			MAL	FA _{OME}	MeFo	MeOH	FAC	CH ₃ O	CH ₂ OH	
FA	-	554.9-2.476 · (T/K) ^a	0 ^a	0 ^a	0 ^b	238.4 ^a	0 ^b	0 ^a	238.4 ^a	
TRX	16980-39.47 · (T/K) ^a	-	0 ^a	0 ^a	0 ^g	239.6 ^a	0 ^g	0 ^a	392.2 ^a	
DME	0 ^f	0 ^e	0 ^e	26 ^e	113.42 ^d	410 ^f	0 ^g	0 ^f	0 ^f	
MAL	0 ^a	0 ^a	-	26 ^a	133.175 ^c	410 ^a	0 ^g	0 ^a	0 ^a	
FA _{OME}	0 ^a	0 ^a	141.5 ^a	-	0 ^h	141.96 ^a	0 ^h	0 ^a	3297 ^a	
MeFo	0 ^b	0 ^g	-81.789 ^c	0 ^h	-	299.7 ^b	-714.7 ^b	0 ^b	0 ^b	
MeOH	-128.6 ^a	-16.67 ^a	-71.21 ^a	128.59 ^a	6 ^b	-	-1426.9 ^b	-128.6 ^a	0 ^a	
FAC	0 ^b	0 ^g	0 ^g	0 ^h	-277.7 ^b	-13.3 ^b	-	0 ^b	0 ^b	
CH ₃ O	0 ^a	0 ^a	0 ^a	0 ^a	0 ^b	238.4 ^a	0 ^b	-	238.4 ^a	
CH ₂ OH	-128.6 ^a	-187.7 ^a	0 ^a	1022 ^a	0 ^b	0 ^a	0 ^b	-128.6 ^a	-	

^(a)Schmitz et al.[56], ^(b)Kuhnert[111], ^(c)Lee et al.[152], ^(d)Sundberg et al.[116], ^(e)cf. Chapter 4.2.4.2 ^(f)adopted from methylal, ^(g)set to zero, ^(h)adopted from formaldehyde

B.7 Experimental data

B.7.1 Experiments described in the main text

The numerical results of the experiments E1 – E10 are reported in Table 125 to Table 134. In Figure 118 to Figure 127 the experimental concentration profiles are compared to the results obtained with the model. Some of these Figures are repetitions from the main part which were included here for completeness. The parameters from Table 9 were used for the calculations.

Table 125: Results from experiment E1: component mass fractions and total mass in the reactor as a function of time. Temperature 363.15 K; catalyst: 9.8 g A36.

t / h	0	20.16	46.16	46.50	111.83	112.16	143	143.33	166.33	166.66	190.66	191
m / g	308.71	293.91	280.22	279.22	265.80	264.80	250.89	249.89	236.32	235.32	221.82	220.82
	$x_i / \text{mol mol}^{-1}$											
TRX	0.2081	0.0968	0.0573	0.0482	0.0138	0.0128	0.0036	0.0056	0.0021	0.0012	0.0023	0.0053
DME	0.7919	0.7903	0.7353	0.7462	0.6160	0.6227	0.5873	0.5830	0.5716	0.5807	0.5666	0.5698
MAL	0.0000	0.0154	0.0523	0.0534	0.1487	0.1541	0.1900	0.1909	0.2089	0.1969	0.2172	0.2012
OME ₂	0.0000	0.0132	0.0351	0.0360	0.0652	0.0625	0.0581	0.0586	0.0493	0.0489	0.0361	0.0366
OME ₃	0.0000	0.0052	0.0225	0.0244	0.0286	0.0319	0.0189	0.0179	0.0128	0.0117	0.0063	0.0073
OME ₄	0.0000	0.0430	0.0245	0.0305	0.0133	0.0121	0.0081	0.0070	0.0006	0.0027	0.0008	0.0026
OME ₅	0.0000	0.0073	0.0211	0.0151	0.0074	0.0063	0.0014	0.0028	0.0031	0.0001	0.0003	0.0027
OME ₆	0.0000	0.0009	0.0113	0.0014	0.0044	0.0022	0.0005	0.0026	0.0010	0.0001	0.0003	0.0013
OME ₇	0.0000	0.0004	0.0036	0.0021	0.0060	0.0025	0.0001	0.0008	0.0004	0.0006	0.0001	0.0006
MeFo	0.0000	0.0206	0.0312	0.0373	0.0833	0.0851	0.1143	0.1148	0.1364	0.1381	0.1515	0.1614
MeOH	0.0000	0.0000	0.0000	0.0000	0.0000	0.0000	0.0000	0.0000	0.0000	0.0000	0.0000	0.0000
FAc	0.0000	0.0000	0.0000	0.0000	0.0071	0.0064	0.0043	0.0054	0.0050	0.0070	0.0044	0.0022
HF ₁	0.0000	0.0043	0.0044	0.0032	0.0055	0.0006	0.0087	0.0058	0.0067	0.0076	0.0097	0.0030
HF ₂	0.0000	0.0026	0.0013	0.0023	0.0006	0.0009	0.0047	0.0049	0.0022	0.0044	0.0045	0.0058
HF ₃	0.0000	0.0000	0.0000	0.0000	0.0000	0.0000	0.0000	0.0000	0.0000	0.0000	0.0000	0.0000

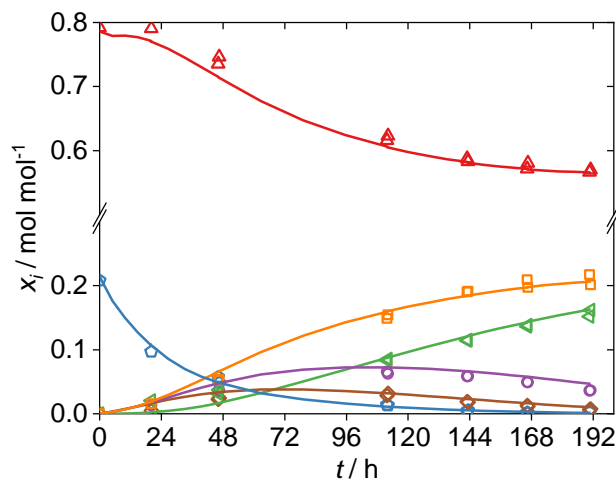


Figure 118: Experimental and calculated mole fraction profiles over time for experiment E1. Symbols are experimental data, and lines are calculated with the model. Parameters were fitted to the experimental data and are given in Table 9. (\square) trioxane (\triangleleft) methyl formate (\triangle) dimethyl ether (\square) methylal (\circ) OME₂ (\diamond) OME₃.

Table 126: Results from experiment E2: component mass fractions and total mass in the reactor as a function of time. Temperature 363.15 K; catalyst: 9.92 g A36.

t/h	0	0.1	4	8	25.7	48	75.8	169.7
m/g	225.04	208.87	197.39	184.73	171.29	157.86	144.42	130.98
$x_i / \text{mol mol}^{-1}$								
TRX	0.2207	0.2451	0.2561	0.2022	0.1403	0.0606	0.0359	0.0045
DME	0.7792	0.7548	0.7438	0.7977	0.7316	0.7747	0.6757	0.5616
MAL	0.0000	0.0000	0.0000	0.0000	0.0170	0.0334	0.0777	0.1862
OME ₂	0.0000	0.0000	0.0000	0.0000	0.0170	0.0236	0.0480	0.0561
OME ₃	0.0000	0.0000	0.0000	0.0000	0.0086	0.0177	0.0305	0.0165
OME ₄	0.0000	0.0000	0.0000	0.0000	0.0100	0.0089	0.0187	0.0047
OME ₅	0.0000	0.0000	0.0000	0.0000	0.0164	0.0106	0.0129	0.0008
OME ₆	0.0000	0.0000	0.0000	0.0000	0.0150	0.0161	0.0125	0.0011
OME ₇	0.0000	0.0000	0.0000	0.0000	0.0000	0.0000	0.0000	0.0000
MeFo	0.0000	0.0000	0.0000	0.0000	0.0313	0.0330	0.0644	0.1402
MeOH	0.0000	0.0000	0.0000	0.0000	0.0000	0.0000	0.0000	0.0000
FAc	0.0000	0.0000	0.0000	0.0000	0.0123	0.0209	0.0231	0.0278
HF ₁	0.0000	0.0000	0.0000	0.0000	0.0000	0.0000	0.0000	0.0000
HF ₂	0.0000	0.0000	0.0000	0.0000	0.0000	0.0000	0.0000	0.0000
HF ₃	0.0000	0.0000	0.0000	0.0000	0.0000	0.0000	0.0000	0.0000

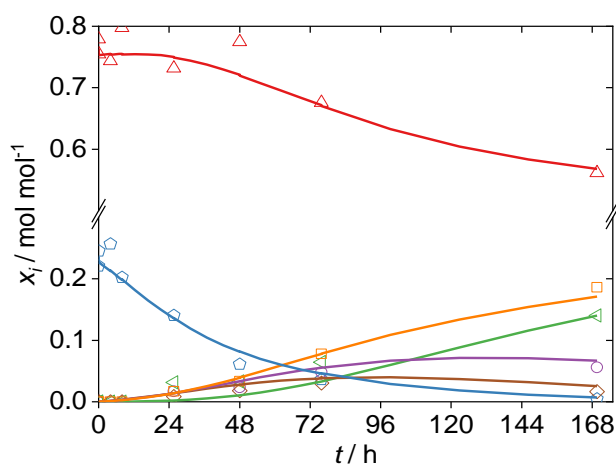


Figure 119: Experimental and calculated mole fraction profiles over time for experiment E2. Symbols are experimental data, and lines are calculated with the model. Parameters were fitted to the experimental data and are given in Table 9. (\diamond) trioxane (\triangleleft) methyl formate (\triangle) dimethyl ether (\square) methylal (\circ) OME₂ (\diamond) OME₃.

Table 127: Results from experiment E3: component mass fractions and total mass in the reactor as a function of time. Temperature 363.15 K; catalyst: 9.8 g A36.

t/h	0	0.1	12.42	20.82	43.38	66.15	85.78	119.5	144	192
m/g	471.16	456.81	439.48	424.45	408.56	391.81	377.34	364.38	350.43	336.48
	$x_i / \text{mol mol}^{-1}$									
TRX	0.0131	0.0156	0.0193	0.0197	0.0104	0.0079	0.0043	0.0018	0.0028	0
DME	0.2739	0.2636	0.2446	0.2539	0.3184	0.3051	0.3522	0.3633	0.3677	0.4195
MAL	0.3732	0.3453	0.3339	0.3174	0.2946	0.2912	0.2738	0.2611	0.2654	0.2155
OME ₂	0.1591	0.1763	0.1608	0.1480	0.1162	0.1040	0.0798	0.0558	0.0566	0.0234
OME ₃	0.0829	0.0875	0.0705	0.0632	0.0468	0.0371	0.0255	0.0145	0.0155	0.0051
OME ₄	0.0395	0.0516	0.0341	0.0331	0.0183	0.0133	0.0074	0.0036	0.0025	0.0001
OME ₅	0.0235	0.0204	0.0189	0.0173	0.0086	0.0105	0.0054	0.0001	0.0008	0.0001
OME ₆	0.0087	0.0139	0.0109	0.0146	0.0046	0.0003	0.0002	0.0002	0.0001	0.0002
OME ₇	0.0000	0.0000	0.0000	0.0000	0.0000	0.0000	0.0000	0.0000	0.0000	0.0000
MeFo	0.0002	0.0007	0.0744	0.1072	0.1598	0.2052	0.2320	0.2627	0.2658	0.3085
MeOH	0.0000	0.0000	0.0000	0.0000	0.0000	0.0000	0.0000	0.0000	0.0000	0.0000
FAc	0.0005	0.0021	0.0017	0.0003	0.0089	0.0070	0.0079	0.0237	0.0120	0.0230
HF ₁	0.0152	0.0102	0.0192	0.0152	0.0082	0.0125	0.0069	0.0090	0.0092	0.0028
HF ₂	0.0095	0.0120	0.0110	0.0095	0.0048	0.0054	0.0039	0.0036	0.0009	0.0014
HF ₃	0.0000	0.0000	0.0000	0.0000	0.0000	0.0000	0.0000	0.0000	0.0000	0.0000

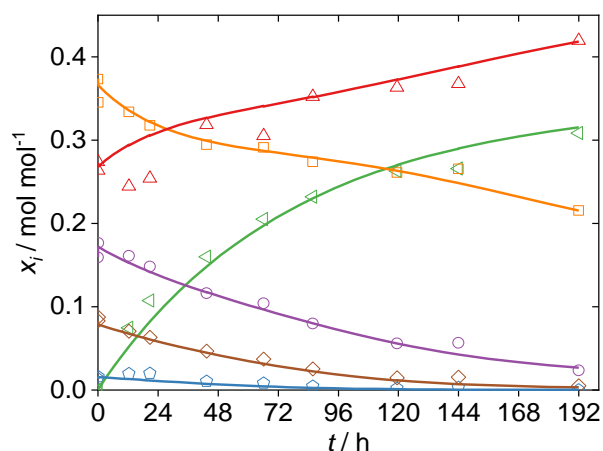
**Figure 120:** Experimental and calculated mole fraction profiles over time for experiment E3. Symbols are experimental data, and lines are calculated with the model. Parameters were fitted to the experimental data and are given in Table 9. (\diamond) trioxane (\triangleleft) methyl formate (\triangle) dimethyl ether (\square) methylal (\circ) OME₂ (\diamond) OME₃.

Table 128: Results from experiment E4: component mass fractions and total mass in the reactor as a function of time. Temperature 363.15 K; catalyst: 12.12 g A36.

t/h	0	0.1	13	21.50	43.75	64.50	86	109.50	187.50
m/g	417.76	406.01	389.53	372.04	357.52	341.36	324.97	310.02	293.91
$x_i / \text{mol mol}^{-1}$									
TRX	0.0087	0.0113	0.0190	0.0160	0.0087	0.0045	0.0055	0.0019	0.0014
DME	0.2590	0.2514	0.2562	0.2464	0.2935	0.3255	0.3357	0.3412	0.3758
MAL	0.3560	0.3738	0.3447	0.3248	0.3088	0.2897	0.2855	0.2708	0.2420
OME ₂	0.1861	0.1809	0.1625	0.1520	0.1236	0.0936	0.0742	0.0578	0.0390
OME ₃	0.0921	0.0897	0.0775	0.0663	0.0541	0.0342	0.0187	0.0125	0.0080
OME ₄	0.0451	0.0523	0.0372	0.0360	0.0210	0.0113	0.0057	0.0049	0.0044
OME ₅	0.0229	0.0167	0.0197	0.0147	0.0085	0.0047	0.0052	0.0001	0.0001
OME ₆	0.0104	0.0153	0.0111	0.0102	0.0062	0.0018	0.0003	0.0001	0.0001
OME ₇	0.0000	0.0000	0.0000	0.0000	0.0000	0.0000	0.0000	0.0000	0.0000
MeFo	0.0053	0.0010	0.0533	0.0992	0.1558	0.2175	0.2308	0.2784	0.2981
MeOH	0.0000	0.0000	0.0000	0.0000	0.0000	0.0000	0.0000	0.0000	0.0000
FAc	0.0000	0.0000	0.0000	0.0000	0.0000	0.0048	0.0111	0.0188	0.0208
HF ₁	0.0094	0.0071	0.0121	0.0234	0.0089	0.0075	0.0223	0.0117	0.0097
HF ₂	0.0045	0.0000	0.0062	0.0104	0.0104	0.0044	0.0045	0.0014	0.0001
HF ₃	0.0000	0.0000	0.0000	0.0000	0.0000	0.0000	0.0000	0.0000	0.0000

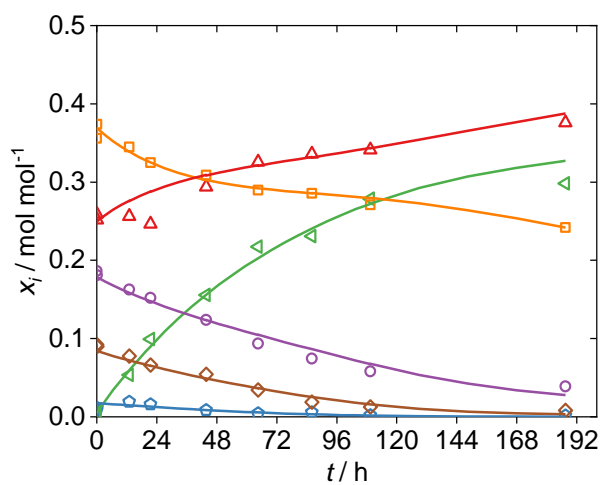


Figure 121: Experimental and calculated mole fraction profiles over time for experiment E4. Symbols are experimental data, and lines are calculated with the model. Parameters were fitted to the experimental data and are given in Table 9. (\square) trioxane (\triangleleft) methyl formate (\triangle) dimethyl ether (\square) methylal (\circ) OME₂ (\diamond) OME₃.

Table 129: Results from experiment E5: component mass fractions and total mass in the reactor as a function of time. Temperature 363.15 K; catalyst: 11.74 g A36.

t / h	0	0.1	23	48	71.5	95.5	171.5
m / g	473.85	467.87	452.73	438.94	424.77	416	401.63
	$x_i / \text{mol mol}^{-1}$						
TRX	0.0187	0.0164	0.0158	0.0106	0.0075	0.0042	0.0031
DME	0.2075	0.1903	0.2218	0.2439	0.2806	0.2975	0.3013
MAL	0.3991	0.4005	0.3491	0.3191	0.3079	0.3077	0.2917
OME ₂	0.1808	0.1907	0.1539	0.1275	0.1063	0.0917	0.0716
OME ₃	0.0936	0.0926	0.0671	0.0533	0.0371	0.0284	0.0199
OME ₄	0.0474	0.0446	0.0312	0.0238	0.0135	0.0072	0.0044
OME ₅	0.0221	0.0223	0.0107	0.0163	0.0051	0.0014	0.0016
OME ₆	0.0112	0.0162	0.0083	0.0048	0.0028	0.0000	0.0002
OME ₇	0.0000	0.0000	0.0000	0.0000	0.0000	0.0000	0.0000
MeFo	0.0000	0.0004	0.1019	0.1635	0.1974	0.2273	0.2672
MeOH	0.0000	0.0003	0.0036	0.0026	0.0014	0.0000	0.0012
FAc	0.0000	0.0000	0.0075	0.0127	0.0144	0.0174	0.0198
HF ₁	0.0103	0.0165	0.0202	0.0158	0.0199	0.0162	0.0148
HF ₂	0.0089	0.0085	0.0082	0.0054	0.0055	0.0074	0.0025
HF ₃	0.0000	0.0000	0.0000	0.0000	0.0000	0.0000	0.0000

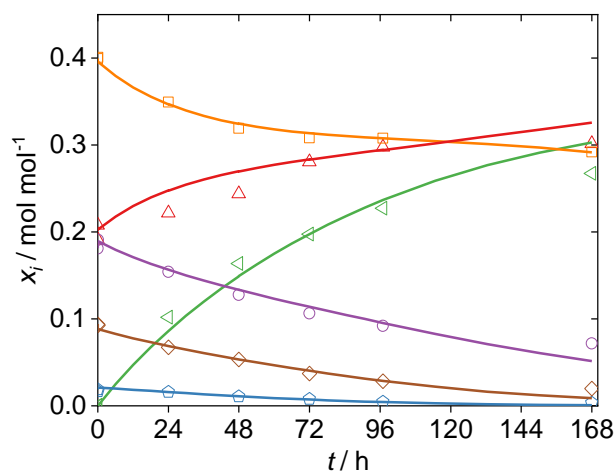


Figure 122: Experimental and calculated mole fraction profiles over time for experiment E5. Symbols are experimental data, and lines are calculated with the model. Parameters were fitted to the experimental data and are given in Table 9. (\diamond) trioxane (\triangleleft) methyl formate (\triangle) dimethyl ether (\square) methylal (\circ) OME₂ (\diamond) OME₃.

Table 130: Results from experiment E6: component mass fractions and total mass in the reactor as a function of time. Temperature 363.15 K; catalyst: 7.53 g A36.

t / h	0	0.1	5	23.50	31.50	48	72	151.25
m / g	422.06	408.22	390.41	362.92	349.21	336.20	318.86	301.52
	$x_i / \text{mol mol}^{-1}$							
TRX	0.0226	0.0187	0.0205	0.0168	0.0156	0.0096	0.0100	0.0094
DME	0.5584	0.5423	0.5341	0.5230	0.5169	0.5115	0.5012	0.5048
MAL	0.1933	0.1987	0.2081	0.2175	0.2261	0.2310	0.2446	0.2445
OME ₂	0.0984	0.1079	0.1037	0.0995	0.1011	0.0903	0.0958	0.0938
OME ₃	0.0508	0.0508	0.0503	0.04544	0.0457	0.0246	0.0369	0.0358
OME ₄	0.0265	0.0251	0.0303	0.0249	0.0252	0.0324	0.0176	0.0142
OME ₅	0.0114	0.0176	0.0092	0.0112	0.0137	0.0183	0.0064	0.0089
OME ₆	0.0130	0.0079	0.0005	0.0050	0.0004	0.0128	0.0012	0.0000
OME ₇	0.0000	0.0023	0.0010	0.0003	0.0011	0.0021	0.0001	0.0000
MeFo	0.0038	0.0063	0.0130	0.0235	0.0292	0.0414	0.0636	0.0626
MeOH	0.0022	0.0000	0.0000	0.0000	0.0000	0.0000	0.0000	0.0000
FAc	0.0011	0.0000	0.0000	0.0000	0.0000	0.0023	0.0047	0.0045
HF ₁	0.0153	0.0129	0.0214	0.0183	0.0156	0.0130	0.0127	0.0152
HF ₂	0.0034	0.0097	0.0081	0.0145	0.0094	0.0108	0.0053	0.0065
HF ₃	0	0	0	0	0	0	0	0

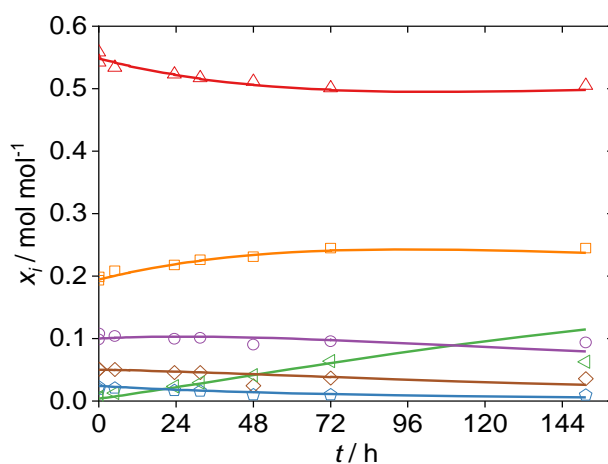


Figure 123: Experimental and calculated mole fraction profiles over time for experiment E6. Symbols are experimental data, and lines are calculated with the model. Parameters were fitted to the experimental data and are given in Table 9. (\square) trioxane (\triangle) methyl formate (\triangle) dimethyl ether (\square) methylal (\circ) OME₂ (\diamond) OME₃.

Table 131: Results from experiment E7: component mass fractions and total mass in the reactor as a function of time. Temperature 363.15 K; catalyst: 15.01 g A36.

t/h	0	21	21.50	46	46.50	117.25	117.75	142	142.50	166.66	167.16
m/g	446.57	431.36	416.54	402.35	387.72	373.49	359.47	345.04	330.93	317.29	303.08
	$x_i / \text{mol mol}^{-1}$										
TRX	0.0149	0.0117	0.0108	0.0060	0.0069	0.0027	0.0027	0.0003	0	0.0075	0.0053
DME	0.3650	0.3793	0.3819	0.3727	0.3774	0.3713	0.3605	0.4006	0.3998	0.4113	0.4151
MAL	0.3014	0.2779	0.2747	0.2778	0.2773	0.2648	0.2733	0.2598	0.2659	0.2510	0.2520
OME ₂	0.1544	0.1088	0.1085	0.0909	0.0930	0.0586	0.0534	0.0422	0.0378	0.0347	0.0327
OME ₃	0.0777	0.0436	0.0418	0.0293	0.0315	0.0133	0.0095	0.0087	0.0096	0.0057	0.0025
OME ₄	0.0362	0.0164	0.0161	0.0076	0.0118	0.0012	0.0033	0.0035	0.0004	0.0002	0.0012
OME ₅	0.0165	0.0073	0.0064	0.0032	0.0040	0.0021	0.0005	0.0001	0.0006	0.0012	0.0011
OME ₆	0.0078	0.0023	0.0044	0.0027	0.0010	0.0010	0.0014	0.0005	0.0004	0.0013	0.0010
OME ₇	0.0064	0.0023	0.0003	0.0006	0.0011	0.0002	0.0031	0.0003	0.0003	0.0007	0.0002
MeFo	0.0000	0.1220	0.1227	0.1691	0.1630	0.2350	0.2504	0.2440	0.2533	0.2583	0.2621
MeOH	0.0000	0.0000	0.0000	0.0000	0.0000	0.0000	0.0000	0.0000	0.0000	0.0000	0.0000
FAc	0.0000	0.0074	0.0066	0.0125	0.0165	0.0239	0.0210	0.0163	0.0133	0.0133	0.0129
HF ₁	0.0123	0.0146	0.0157	0.0173	0.0103	0.0170	0.0163	0.0154	0.0142	0.0133	0.0112
HF ₂	0.0068	0.0059	0.0093	0.0098	0.0056	0.0082	0.0041	0.0075	0.0039	0.0009	0.0021
HF ₃	0.0000	0.0000	0.0000	0.0000	0.0000	0.0000	0.0000	0.0000	0.0000	0.0000	0.0000

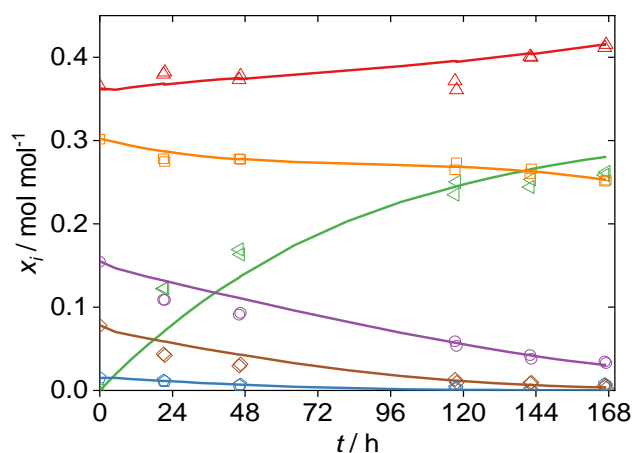
**Figure 124:** Experimental and calculated mole fraction profiles over time for experiment E7. Symbols are experimental data, and lines are calculated with the model. Parameters were fitted to the experimental data and are given in Table 9. (\diamond) trioxane (\triangleleft) methyl formate (\triangle) dimethyl ether (\square) methylal (\circ) OME₂ (\diamond) OME₃.

Table 132: Results from experiment E8: component mass fractions and total mass in the reactor as a function of time. Temperature 363.15 K; catalyst: 7.40 g A36.

t / h	0	15.83	37.50	64.75	86.75	157.75
m / g	452.42	424.48	410.15	395.77	381.21	367.23
$x_i / \text{mol mol}^{-1}$						
TRX	0.0045	0.0105	0.0072	0.0033	0.0031	0.0002
DME	0.3551	0.3180	0.2711	0.3267	0.2807	0.2847
MAL	0.1290	0.1470	0.1548	0.1680	0.1675	0.1692
OME ₂	0.0550	0.0600	0.0572	0.0452	0.0430	0.0296
OME ₃	0.0286	0.0235	0.0212	0.0137	0.0099	0.0066
OME ₄	0.0136	0.0111	0.0074	0.0034	0.0045	0.0005
OME ₅	0.0081	0.0054	0.0045	0.0005	0.0009	0.0004
OME ₆	0.0030	0.0025	0.0013	0.0004	0.0001	0.0001
OME ₇	0.0000	0.0000	0.0000	0.0000	0.0000	0.0000
MeFo	0.3939	0.3947	0.4182	0.4126	0.4446	0.4678
MeOH	0.0000	0.0000	0.0000	0.0000	0.0000	0.0000
FAc	0.0001	0.0164	0.0431	0.0201	0.0289	0.0266
HF ₁	0.0052	0.0073	0.0104	0.0052	0.0132	0.0116
HF ₂	0.0032	0.0031	0.0029	0.0003	0.0031	0.0020
HF ₃	0.0000	0.0000	0.0000	0.0000	0.0000	0.0000

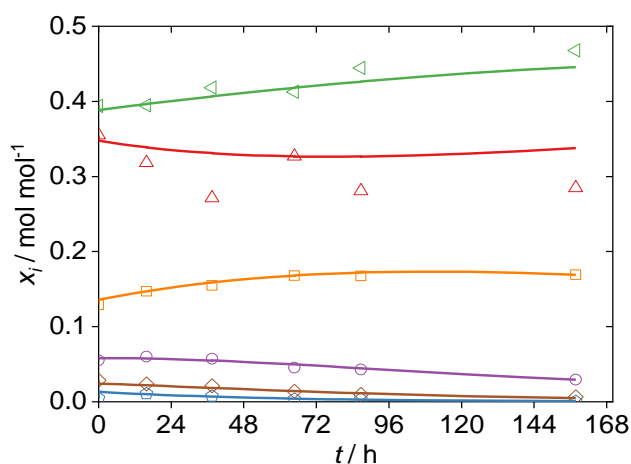


Figure 125: Experimental and calculated mole fraction profiles over time for experiment E8. Symbols are experimental data, and lines are calculated with the model. Parameters were fitted to the experimental data and are given in Table 9. (\square) trioxane (\triangleleft) methyl formate (\triangle) dimethyl ether (\square) methylal (\circ) OME₂ (\diamond) OME₃.

Table 133: Results from experiment E9: component mass fractions and total mass in the reactor as a function of time. Temperature 353.15 K; catalyst: 14.70 g A36.

t/h	0	20.66	21.16	45.41	45.91	117.75	118.08	141.08	141.58	168.25	168.58
m/g	450.31	434.63	419.47	404.51	388.95	374.43	359.58	345.14	330.08	315.29	300.55
	$x_i / \text{mol mol}^{-1}$										
TRX	0.0145	0.0141	0.0152	0.0119	0.0066	0.0058	0.0060	0.0056	0.0052	0.0019	0.0039
DME	0.3649	0.3538	0.3285	0.3575	0.3498	0.3674	0.3664	0.3595	0.3391	0.3675	0.3417
MAL	0.3114	0.3101	0.3096	0.3025	0.3040	0.2978	0.2970	0.2982	0.3071	0.2968	0.3061
OME ₂	0.1498	0.1345	0.1382	0.1214	0.1247	0.0959	0.0952	0.0940	0.0972	0.0780	0.0868
OME ₃	0.0754	0.0612	0.0629	0.0490	0.0536	0.0314	0.0294	0.0307	0.0335	0.0260	0.0259
OME ₄	0.0351	0.0350	0.0268	0.0279	0.0265	0.0111	0.0174	0.0162	0.0121	0.0120	0.0091
OME ₅	0.0160	0.0145	0.0206	0.0198	0.0177	0.0063	0.0032	0.0085	0.0037	0.0023	0.0021
OME ₆	0.0076	0.0038	0.0106	0.0022	0.0083	0.0034	0.0027	0.0003	0.0004	0.0013	0.0005
OME ₇	0.0062	0.0036	0.0012	0.0032	0.0008	0.0005	0.0004	0.0000	0.0000	0.0000	0.0000
MeFo	0.0000	0.0559	0.0547	0.0820	0.0870	0.1620	0.1616	0.1602	0.1731	0.1934	0.1960
MeOH	0.0000	0.0000	0.0000	0.0000	0.0000	0.0000	0.0000	0.0000	0.0000	0.0000	0.0000
FAc	0.0000	110746	0.0014	0.0000	0.0015	0.0059	0.0059	0.0062	0.0075	0.0053	0.0085
HF ₁	0.0119	0.0109	0.0203	0.0150	0.0115	0.0113	0.0112	0.0156	0.0193	0.0116	0.0160
HF ₂	0.0066	0.0022	0.0095	0.0071	0.0074	0.0006	0.0028	0.0044	0.0010	0.0032	0.0028
HF ₃	0.0000	0.0000	0.0000	0.0000	0.0000	0.0000	0.0000	0.0000	0.0000	0.0000	0.0000

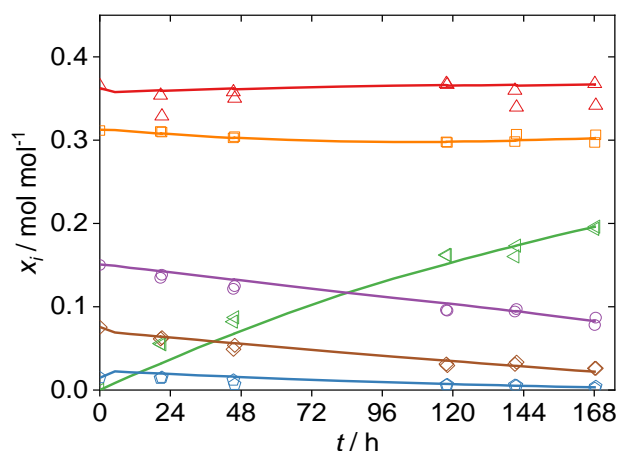
**Figure 126:** Experimental and calculated mole fraction profiles over time for experiment E9. Symbols are experimental data, and lines are calculated with the model. Parameters were fitted to the experimental data and are given in Table 9. (\square) trioxane (\triangleleft) methyl formate (\triangle) dimethyl ether (\square) methylal (\circ) OME₂ (\diamond) OME₃.

Table 134: Results from experiment E10: component mass fractions and total mass in the reactor as a function of time. Temperature 373.15 K; catalyst: 9.80 g A36.

t / h	0	21.50	22	46.50	47	119	119.50	143.50	144	169	169.50
m / g	422.38	408.04	394.08	380.65	366.79	353.13	339.76	326.68	313.04	299.68	286.32
	$x_i / \text{mol mol}^{-1}$										
TRX	0.0113	0.0058	0.0055	0.0023	0.0019	0.0008	0.0023	0.0013	0.0056	0.0010	0.0019
DME	0.4768	0.4865	0.4880	0.4802	0.4837	0.4905	0.5084	0.5378	0.5296	0.5140	0.5481
MAL	0.3192	0.2447	0.2454	0.2458	0.2518	0.2180	0.2086	0.1866	0.1958	0.1839	0.1775
OME ₂	0.1057	0.0775	0.0769	0.0533	0.0478	0.0280	0.0194	0.0167	0.0158	0.0128	0.0127
OME ₃	0.0392	0.0271	0.0306	0.0142	0.0120	0.0047	0.0039	0.0007	0.0011	0.0041	0.0012
OME ₄	0.0166	0.0140	0.0114	0.0035	0.0022	0.0003	0.0023	0.0011	0.0002	0.0021	0.0000
OME ₅	0.0073	0.0023	0.0015	0.0010	0.0001	0.0000	0.0000	0.0000	0.0000	0.0000	0.0000
OME ₆	0.0025	0.0001	0.0000	0.0005	0.0001	0.0000	0.0000	0.0000	0.0000	0.0000	0.0000
OME ₇	0.0020	0.0000	0.0001	0.0000	0.0002	0.0000	0.0000	0.0000	0.0000	0.0000	0.0000
MeFo	0.0171	0.1286	0.1288	0.1723	0.1840	0.2292	0.2290	0.2329	0.2329	0.2548	0.2416
MeOH	0.0000	0.0000	0.0000	0.0000	0.0000	0.0000	0.0000	0.0000	0.0000	0.0000	0.0000
FAc	0.0000	0.0067	0.0055	0.0060	0.0041	0.0129	0.0073	0.0081	0.0063	0.0194	0.0096
HF ₁	0.0018	0.0061	0.0058	0.0117	0.0106	0.0149	0.0150	0.0079	0.0115	0.0076	0.0072
HF ₂	0.0000	0.0000	0.0000	0.0086	0.0007	0.0002	0.0033	0.0062	0.0008	0.0000	0.0000
HF ₃	0.0000	0.0000	0.0000	0.0000	0.0000	0.0000	0.0000	0.0000	0.0000	0.0000	0.0000

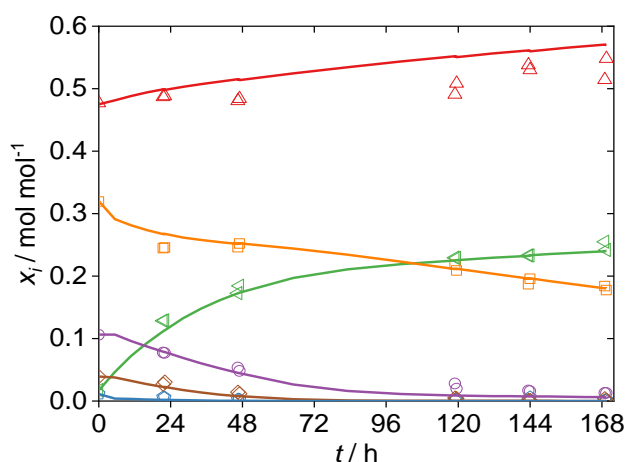


Figure 127: Experimental and calculated mole fraction profiles over time for experiment E10. Symbols are experimental data, and lines are calculated with the model. Parameters were fitted to the experimental data and are given in Table 9. (\square) trioxane (\triangleleft) methyl formate (\triangle) dimethyl ether (\square) methylal (\circ) OME₂ (\diamond) OME₃.

B.7.2 Experiment with zeolite catalyst

The zeolite catalyst CP 814E was bought in its dried form from Zeolyst International. It was calcined at 773 K for 5 hours and dried at 383 K and pressure below 30 mbar for 24 hours. The catalyst was then tabletted, ground, and sieved. The fraction with a particle size of 250 to 355 μm was then used for the experiment.

B.8 Comparison of the mechanisms for methyl formate formation

For the formation of methyl formate two mechanisms are described. In this work, a new mechanism according to Reaction (VII) is used as it enables a much better fit of the experimental data. Figure 129 shows the same experiments as Figure 22 in Chapter 3.5.3 but, this time, the mechanism for the formation of methyl formate regarding to Reaction (VI) is used for the fit. It can be seen that the concentration profile of methyl formate is not well described for experiment E1 in Figure 129 a). For experiment E4 (cf. Figure 129 b)) a good description of the methyl formate concentration is possible but a adequate description of the concentration of DME and methylal is not possible. This weakness of the mechanism can be seen in all experiments. Due to this the alternative mechanism was chosen as it allows a much better description of the experimental data.

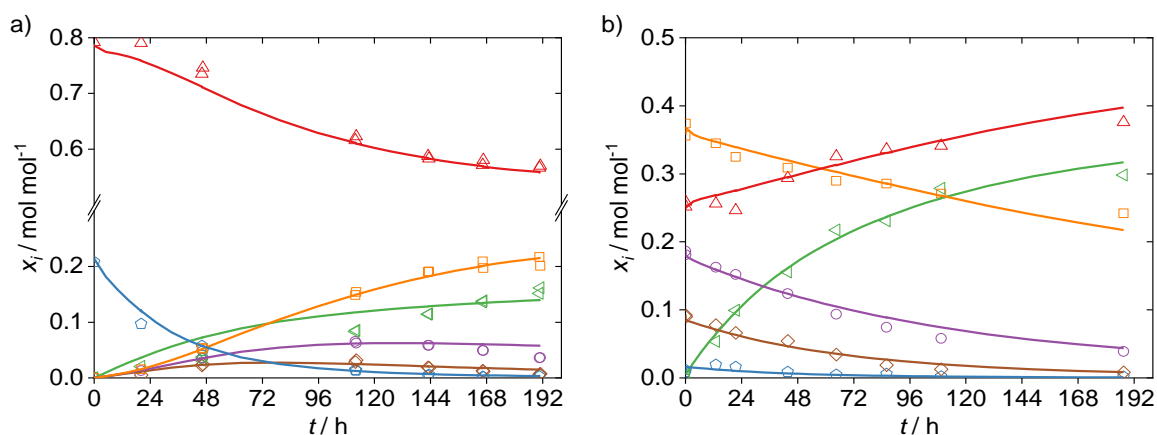


Figure 129: Experimental and calculated mole fraction profiles over time for experiments a) E1 and b) E5. Symbols are measured concentrations, and lines are calculated with a modified version of model A. In this the methyl formate formation according to Equation 8 is implemented. Parameters were fitted to the experimental data: a) $K_{\text{DME}} = 150.88$, $K_{\text{TRX}} = 7.43 \cdot 10^{-6}$, $k_{\text{DME}} = 0.21$, $k_{\text{MeFo}} = 7.43$ b) $K_{\text{DME}} = 223.61$, $K_{\text{TRX}} = 1.21 \cdot 10^{-5}$, $k_{\text{DME}} = 14.25$, $k_{\text{MeFo}} = 48.05$. (\square) trioxane (\triangleleft) methyl formate (\triangle) dimethyl ether (\square) methylal (\circ) OME₂ (\diamond) OME₃.

B.9 Activity-based and mole-fraction based equilibrium constants

To enable the direct comparison of the activity-based equilibrium constants determined in Chapter 3.5.4 with equilibrium constants from the literature and Chapter 4.2, that were reported in a mole-fraction based form, the latter were converted using Equation (41):

$$K_a = \prod_{i=1}^{N_C} a_i^{v_i} = \prod_{i=1}^{N_C} x_i^{v_i} \cdot \prod_{i=1}^{N_C} \gamma_i^{v_i} = K_x \cdot K_\gamma \quad (41)$$

In Equation (41) the problem arises that both K_x and K_γ depend on the composition of the mixtures. It was started with a constant value for K_x adopted from some source from the literature and want to convert it to a constant value of K_a . This requires choosing a constant value of K_γ . This value was obtained, separately for each experiment by averaging the instantaneous values over the entire experiment, as described by Equation (42).

$$\overline{K_\gamma} = \frac{1}{t_{\text{exp}}} \int_0^{t_{\text{exp}}} \prod_{i=1}^{N_C} \gamma_i^{v_i} dt \quad (42)$$

Therein is t_{exp} the total time of the experiment. The numbers of the activity coefficients were obtained with the model from Chapter 3. The calculated values were fitted with Equation (18) and the result of the fit is shown in Figure 25. For the temperature of 363 K the mean of the experiments E3 to E8 and for the other temperatures the values of the corresponding experiments were used.

C Supporting information for Chapter 4

C.1 Supporting information for Chapter 4.1

C.1.1 Process Model

In the following, a detailed description of the process model used in Chapter 4.1 is given. The model is based on the works of Kuhnert[110] and Albert[111] and is equal to the one used by Grützner[91], except for the description of the crystallizer. First, the apparatus models for the calculation of chemical equilibria and vapor-liquid equilibria are presented. Second, the enthalpy model is described, which is essential for the calculation of process heats. Sidecomponents, such as formic acid, methanol, or methyl formate, were not considered in the modeling.

Evaporator S1 and distillation columns C1, C2, and C3

An equilibrium stage model was used for these apparatuses. The liquid phase was treated as a non-ideal mixture of formaldehyde (CH₂O, FA), water (H₂O, WA), trioxane ((CH₂O)₃, TR), and polyoxymethylene glycols (HO(CH₂O)_nH, MG_n) with $n \leq 15$. Grützner[91] only considered oligomers with a maximum chain length of $n \leq 10$. However, for large overall formaldehyde concentrations, as appear in the processes discussed in Chapter 4.1, oligomers with more CH₂O segments are also present in significant amounts and have to be taken into account. The effect of pressure on the chemical potentials in the liquid phase was neglected. The vapor phase was treated as a mixture of ideal gases consisting of formaldehyde, water, trioxane, and MG₁. MG_n with $n \geq 2$ were considered nonvolatile. The vapor-liquid equilibrium was calculated with the extended Raoult's law:

$$p_i^S \cdot x_i \cdot \gamma_i = p \cdot y_i \quad (43)$$

where i stands for a component, x_i and y_i are the true mole fractions of component i in the liquid and vapor phase, respectively, and p_i^S its pure component vapor pressure. p is the total pressure. The temperature dependence of the pure component vapor pressure was calculated with the extended Antoine equation. The Antoine parameters used in Chapter 4.1 are given in Table 136.

Table 136: Antoine parameters for the calculation of pure component vapor pressures p_i^S .
 $\ln(p_i^S/\text{kPa}) = A_i + B_i / ((T/\text{K}) + C_i)$.

Comp. i	A_i	B_i	C_i	Ref.
FA	14.4625	-2204.13	-30.15	[110]
WA	16.2886	-3816.44	-46.13	[110]
TRX	14.3796	-3099.47	-68.92	[111]
MG ₁	17.4364	-4762.07	-51.21	[110]

γ_i is the activity coefficient of component i , normalized according to Raoult's law. The activity coefficients were calculated with a modified version of the UNIFAC model [112]. The UNIFAC group assignment, the UNIFAC size (R) and surface (Q) parameters and the interaction parameters $a_{k,l}$ as used in Chapter 4.1 are given in Table 137 and Table 138.

Table 137: UNIFAC group assignment.

Comp.	group assignment
FA	1 CH ₂ O
WA	1 H ₂ O
TRX	1 (CH ₂ O) ₃
MG ₁	1 HOCH ₂ OH
MG _{<i>n</i>}	(<i>n</i> -1) CH ₂ O, 2 OH, 1 CH ₂

Table 138: UNIFAC size (*R*) and surface (*Q*) parameters.

group	group label	<i>R</i>	<i>Q</i>	Ref.
CH ₂ O	1	0.9183	0.780	[110]
H ₂ O	2	0.9200	1.400	[110]
HOCH ₂ OH	3	2.6744	2.940	[110]
OH	4	1.0000	1.200	[110]
CH ₂	5	0.6744	0.540	[110]
(CH ₂ O) ₃	6	2.7540	3.300	[111]

Table 139: UNIFAC interaction parameters $a_{k,l}/K$. Group labelling according to Table 137.

group <i>k</i>	group <i>l</i>					
	1	2	3	4	5	6
1	-	867.8 ^b	189.2 ^b	237.7 ^b	83.4 ^b	$a_{1,6}(T)^a$
2	-254.5 ^b	-	189.5 ^b	-229.1 ^b	300 ^b	80.63 ^a
3	59.2 ^b	-191.8	-	-229.1 ^b	300 ^b	80.63 ^a
4	28.1 ^b	353.5	353.5 ^b	-	156.4 ^b	28.06 ^a
5	251.5 ^b	1318	1318 ^b	986.5 ^b	-	251.5 ^a
6	$a_{6,1}(T)^a$	379.4 ^a	379.4 ^a	237.7 ^a	83.36 ^a	-

$a_{1,6}(T) = 554.9 - 2.476 \cdot (T/K) = 16980 - 39.47 \cdot (T/K)$; ^(a) adopted from Albert[111]; ^(b) adopted from Kuhnert[110]

For the calculation of the vapor-liquid equilibria in the apparatuses, the true species distribution in the vapor and liquid phase had to be taken into account, i.e., all species, including the oligomers of formaldehyde and water. Therefore, the oligomerization reactions of formaldehyde and water had to be taken into account at all times. The oligomerization reactions are given in Chapter 2.3 by Reaction (I) and (II).

Trioxane was considered inert such that it did not participate in any reaction. The reactions (I) and (II) take place under all conditions, even without any catalyst, and were considered instantaneous equilibrium reactions. The chemical equilibria of the oligomerization reactions in the liquid phase

were modeled by temperature-dependent, activity-based equilibrium constants like described in Chapter 2.5.1.2.

For the calculation of the species distribution in the chemical equilibrium, besides the chemical equilibrium conditions according to Equation (1), also mole balances according to the Equations (44) to (47) had to be satisfied. These mole balances link the overall to the true mole fractions.

$$\tilde{x}_{\text{FA}} = \frac{1}{s} (x_{\text{FA}} + \sum_{n=1}^{15} n \cdot x_{\text{MG}_n}) \quad (44)$$

$$\tilde{x}_{\text{WA}} = \frac{1}{s} (x_{\text{WA}} + \sum_{n=1}^{15} x_{\text{MG}_n}) \quad (45)$$

$$\tilde{x}_{\text{TRX}} = \frac{1}{s} x_{\text{TRX}} \quad (46)$$

$$s = 1 + \sum_{n=1}^{15} n \cdot x_{\text{MG}_n} \quad (47)$$

where \tilde{x}_{FA} , \tilde{x}_{WA} , and \tilde{x}_{TRX} are the overall mole fractions of formaldehyde, water, and trioxane. n is the number of CH_2O segments in the respective oligomer.

Reactor R1

The reactor was modeled as an equilibrium stage. The stream leaving the reactor was specified as a boiling liquid at $p = 1$ bar so that no vapor phase had to be considered. In addition to the formaldehyde and water oligomerization Reactions (I) and (II), following Grützner[91], also the formation of trioxane according to Reaction (XXV) was allowed, i.e., it was considered that a heterogeneous catalyst was present in the reactor.



All reactions were considered instantaneous equilibrium reactions, which can technically be achieved, e.g., by using large amounts of heterogeneous acid catalysts. This circumvented the necessity to select a reaction mechanism that correctly describes the reaction kinetics of the trioxane formation, which is still subject of ongoing research, see for example [96,99].

As described earlier, the equilibrium of the oligomerization Reactions (I) and (II) was modeled using activity-based equilibrium constants. In contrast, the equilibrium of Reaction (XXV) was modeled using a mole fraction-based approach:

$$K_{x,(XXV)} = \frac{x_{\text{TRX}} \cdot x_{\text{WA}}}{x_{\text{MG3}}} \quad (48)$$

where $K_{x,(XXV)}$ is the mole fraction-based equilibrium constant of Reaction (XXV). The temperature dependence of $K_{x,(XXV)}$ was modeled with the integrated van't Hoff equation. The van't Hoff parameters were taken from Grützner[91] and are given in Table 140.

Table 140: Parameters for the calculation of chemical equilibrium constants K_j .
 $\ln(K_j) = A_j + B_j / (T / \text{K}) + C_j \ln(T / \text{K}) + D_j (T / \text{K})$.

reaction	A	B	C	D	Ref.
X	4.556	-2350	0	0	[91]

The use of a mole fraction-based equilibrium constant made the model thermodynamically inconsistent. This was unproblematic here, as only liquid phase reactions were considered in the reactor. However, the inconsistency would have undesirable effects on the calculation of reactive vapor-liquid equilibria, see for example [113].

For the calculation of the species distribution in the chemical equilibrium, in addition to the chemical equilibrium conditions, also the following mole balances had to be satisfied:

$$\tilde{x}_{\text{FA}} = \frac{1}{S} (x_{\text{FA}} + \sum_{n=1}^{15} n \cdot x_{\text{MGn}} + 3 x_{\text{TRX}}) \quad (49)$$

$$\tilde{x}_{\text{WA}} = \frac{1}{S} (x_{\text{WA}} + \sum_{n=1}^{15} x_{\text{MGn}}) \quad (50)$$

$$S = 1 + \sum_{n=1}^{15} n \cdot x_{\text{MGn}} + 2 x_{\text{TRX}} \quad (51)$$

Crystallizer X1

The crystallizer was modeled as a combination of a heat exchanger, in which the feed stream was cooled to the crystallization temperature, and a stream splitter, in which the pure trioxane was separated from the feed stream. During the cooling process, the oligomerization Reactions (I) and (II) were always considered in equilibrium. Trioxane was considered inert. Therefore, the same model for the calculation of the chemical equilibrium as for the evaporator step S1 and the distillation columns C1, C2, and C3 was employed, see above.

The amount of pure trioxane that could be obtained in the crystallization step was determined by the solubility of trioxane in the liquid supernatant. The dependence of the solubility on the crystallization temperature was correlated with a second-order polynomial:

$$\tilde{x}_{\text{TRX}}^{(m)} / \text{g g}^{-1} = 4.1033 \cdot 10^{-5} \cdot (T / K)^2 - 1.9686 \cdot 10^{-2} \cdot (T / K) + 2.4008 \quad (52)$$

where $\tilde{x}_{\text{TRX}}^{(m)}$ is the overall mass fraction of trioxane in the liquid supernatant. The parameters of Equation (52) were fitted to the results of the solid-liquid equilibrium experiments of this thesis, which are described in Chapter 4.1. This approach is purely empirical and is only considered viable for ratios of $\tilde{x}_{\text{FA}}^{(m)}$ to $\tilde{x}_{\text{WA}}^{(m)}$ that are close to the ratio during the solid-liquid equilibrium experiments of this work, where $\tilde{x}_{\text{FA}}^{(m)}$ and $\tilde{x}_{\text{WA}}^{(m)}$ are the overall mass fractions of formaldehyde and water in the liquid supernatant. This ratio was about 0.29 g g⁻¹ in the solid-liquid equilibrium experiments and about 0.37 g g⁻¹ in the simulations performed in this thesis, which is considered close enough for Equation (52) to be valid. A thermodynamically consistent modeling of the solid-liquid equilibrium in the system (formaldehyde + water + trioxane) based on activities was also considered. The approach was as however discarded, as the amount of available experimental data was found to be too low to develop a meaningful model of the studied complex reacting system.

C.1.2 Enthalpy model

Excess enthalpies and the pressure dependence of the enthalpy were neglected. The enthalpies h^L of the pure liquid components formaldehyde and water were normalized to the reference temperature $T^\theta = 273.15$ K:

$$h_i^L(T^\theta = 273.15 \text{ K}) = 0, i = \text{FA, WA} \quad (53)$$

The liquid phase enthalpy of MG₁ at the reference temperature T^θ was then calculated as follows:

$$h_i^L(T^\theta) = \underbrace{h_{\text{WA}}^L(T^\theta)}_{=0} + \underbrace{h_{\text{FA}}^L(T^\theta)}_{=0} + \Delta h_{\text{R,(I)}}^L(T^\theta) = \Delta h_{\text{R,(I)}}^L(T^\theta) \quad (54)$$

where $\Delta h_{\text{R,(I)}}^L(T^\theta)$ is the liquid phase reaction enthalpy of Reaction (I), in which MG₁ is formed. However, Albert[111] only reported the vapor phase reaction enthalpy $\Delta h_{\text{R,(I)}}^V(T^\theta)$.

The liquid phase reaction enthalpy was therefore calculated from:

$$\Delta h_{\text{R,(I)}}^L(T^\theta) = \Delta h_{\text{V,WA}}(T^\theta) + \Delta h_{\text{V,FA}}(T^\theta) - \Delta h_{\text{V,MG1}}(T^\theta) + \Delta h_{\text{R,(I)}}^V(T^\theta) \quad (55)$$

where $\Delta h_{\text{V},i}$ is the enthalpy of vaporization of component i . For water, Albert[111] reported $\Delta h_{\text{V,WA}}$ based on the Watson equation. For all other components, $\Delta h_{\text{V},i}$ was calculated from the pure component vapor pressure correlations using the Clausius-Clapeyron equation:

$$\Delta h_{V,i}(T) = \frac{-RB_i}{\left(1 + \frac{C_i}{T/R}\right)^2}, i = \text{FA, TRX, MG}_1 \quad (56)$$

where R is the universal gas constant and B_i and C_i are parameters of the extended Antoine equation. For formaldehyde and trioxane, these parameters are the same as shown in Table 136. The parameters of MG_1 were taken from the vapor pressure correlation of Albert[111]. The enthalpies of vaporization of all components were correlated with the extended Watson equation (cf. Equation (57)). The parameters of the extended Watson equation used in Chapter 4.1 are given in Table 141.

$$\Delta h_{V,i}(T)/\text{J kmol}^{-1} = A_i \left(1 - \frac{T}{T_{C,i}}\right)^{B_i + C_i \left(\frac{T}{T_{C,i}}\right) + D_i \left(\frac{T}{T_{C,i}}\right)^2 + E_i \left(\frac{T}{T_{C,i}}\right)^3} \quad (57)$$

Table 141: Parameters of the extended Watson equation for the calculation of enthalpies of vaporization. For the critical temperature T_c , a reference is given. MG_n with $n \geq 2$ were considered non-volatile and therefore no enthalpy of vaporization is given.

Comp.	A	B	C	D	E	T_c / K	Ref.
FA	19768445.3	-2.0209	5.8203	-5.9004	2.0856	408.00	[150]
WA	54321385.8	0.33714	0	0	0	647.30	[111]
TRX	99430021.0	2.0972	-1.8104	0	0	604.00	^a
MG_1	60497679.5	0.2453	-0.2127	0	0	570.15	^b

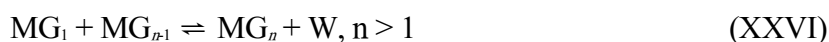
^(a)adopted from DIPPR database (version 23.04.2019) [151]; ^(b)Estimated using the group contribution method of Marrero and Gani[149]

Analogously to MG_1 , the enthalpies of MG_n with $n \geq 2$ and of trioxane at T^θ were calculated using the liquid phase reaction enthalpies $\Delta h_{R,(II)}^L(T^\theta)$ and $\Delta h_{R,(XXV)}^L(T^\theta)$:

$$h_{\text{MG}_n}^L(T^\theta) = h_{\text{MG}_{n-1}}^L(T^\theta) + \underbrace{h_{\text{FA}}^L(T^\theta)}_{=0} + \Delta h_{R,(II)}^L(T^\theta), n \geq 2 \quad (58)$$

$$h_{\text{TRX}}^L(T^\theta) = h_{\text{MG}_3}^L(T^\theta) - \underbrace{h_{\text{W}}^L(T^\theta)}_{=0} + \Delta h_{R,(XXV)}^L(T^\theta), n \geq 2 \quad (59)$$

Note that $\Delta h_{R,(II)}^L(T^\theta)$ depends on the number of CH_2O segments n of the oligomer that is formed in the respective reaction (cf. Table 142). For the oligomerization reactions, Albert[111] only reported the liquid phase reaction enthalpies of the reactions in the following form:



From these reported values of $\Delta h_{R,(XXVI)}^L(T^\theta)$, the reactions enthalpies $\Delta h_{R,(II)}^L(T^\theta)$ of the oligomerization reactions in the form of Reaction (II), as used in Chapter 4.1, were calculated using the reaction enthalpy $\Delta h_{R,(I)}^L(T^\theta)$ of Reaction (I):

$$\Delta h_{R,(II)}^L(T^\theta) = \Delta h_{R,(I)}^L(T^\theta) + \Delta h_{R,(XXVI)}^L(T^\theta) \quad (60)$$

$\Delta h_{R,(XXV)}^L(T^\theta)$ was calculated using the van't Hoff equation as follows:

$$\Delta h_{R,(XXV)}^L(T^\theta) = -RB_{(XXV)} \quad (61)$$

where $B_{(XXV)}$ is the van't Hoff parameter of Reaction (XXV) (cf. Table 140). The reaction enthalpies of all reactions of this work at $T^\theta = 273.15$ K are given in Table 142.

Table 142: Reaction enthalpies at $T^\theta = 273.15$ K.

reaction	Δh_R^L kJ mol ⁻¹
(I)	-20.207
(II), $n = 2$	-27.437
(II), $n \geq 3$	-24.737
(XXV)	19.538

The temperature dependence of the liquid phase enthalpies h_i^L was calculated as follows:

$$h_i^L(T) = h_i^L(T^\theta) + \int_{T^\theta}^T c_{p,i}^L dT^* \quad (62)$$

where $c_{p,i}^L$ is the liquid phase molar isobaric heat capacity. For formaldehyde, water, and trioxane, Albert[111] only reported the vapor phase molar isobaric capacity $c_{p,i}^V$. $c_{p,i}^L$ was therefore calculated according to Equation (63) using the temperature derivative of the enthalpy of vaporization:

$$c_{p,i}^L = c_{p,i}^V - \frac{d\Delta h_{V,i}}{dT}, \quad i = \text{FA, W, TRX} \quad (63)$$

$c_{p, \text{MG1}}^L$ was calculated according to Equation (64) using the temperature derivative of the reaction enthalpy of Reaction (II)

$$c_{p, \text{MG1}}^L = c_{p, \text{W}}^L + c_{p, \text{FA}}^L + \frac{d\Delta h_{R,(I)}^L}{dT} \quad (64)$$

$$\text{with } \frac{d\Delta h_{R,(I)}^L}{dT} = \frac{d\Delta h_{V, \text{W}}}{dT} + \frac{d\Delta h_{V, \text{FA}}}{dT} - \frac{d\Delta h_{V, \text{MG1}}}{dT} + \frac{d\Delta h_{R,(I)}^L}{dT}$$

For MG_n with $n \geq 2$, c_{p, MG_n}^L was calculated from Equation (65) using the temperature derivative of the reaction enthalpy of Reaction (II):

$$c_{p, MG_n}^L = c_{p, MG_{n-1}}^L + c_{p, FA}^L + \frac{d\Delta h_{R, (II)}^L}{dT}, \quad n \geq 2 \quad (65)$$

$$\text{with } \frac{d\Delta h_{R, (II)}^L}{dT} = \frac{d\Delta h_{R, (I)}^L}{dT} + \underbrace{\frac{d\Delta h_{R, (XXVI)}^L}{dT}}_{=0}$$

where $\Delta h_{R, (XXVI)}^L$, as reported by Albert[111], is independent of the temperature. For all components, the temperature dependence of $c_{p,i}^L$ was correlated with a fourth-order polynomial of which the parameters are given in Table 143.

Table 143: Parameters for the calculation of molar liquid phase isobaric heat capacities. $c_{p,i}^L / \text{J kmol}^{-1} \text{K}^{-1} = A_i + B_i \cdot (T/\text{K}) + C_i \cdot (T/\text{K})^2 + D_i \cdot (T/\text{K})^3 + E_i \cdot (T/\text{K})^4$.

Comp.	<i>A</i>	<i>B</i>	<i>C</i>	<i>D</i>	<i>E</i>
FA	144408	-501.9	0.65331	0	0
WA	217788	-1845.3	8.3444	-0.0158	$1.084 \cdot 10^{-5}$
TRX	1781910	-14116.8	45.7042	-0.0659	$3.592 \cdot 10^{-5}$
MG ₁	164483	-1646.5	8.0359	-0.0158	$1.084 \cdot 10^{-5}$
MG _{<i>n</i>} , $n \geq 2$	$-53305n + 217788$	$198.8n - 1845.3$	$-0.3086n + 8.3444$	-0.0158	$1.084 \cdot 10^{-5}$

The enthalpy in the vapor phase was calculated using Equation (66):

$$h_{MG_n}^L(T) = h_i^L(T) + \Delta h_{v,i} \quad (66)$$

Enthalpy in the Crystallizer X1

The indirect calculation of c_p^L from c_p^V and $\Delta h_v(T)$ can lead to serious errors in the description of liquid phase enthalpies [152]. These errors were tolerated here, as the total energy demand of the processes is dominated by the heat duties of the distillation columns, which in turn are mainly dependent on the enthalpies of vaporization rather than on the liquid phase enthalpies. However, for a detailed evaluation of the cooling duty of the crystallizer, an accurate description of the liquid phase enthalpies is essential. Therefore, only for the calculation of the liquid phase enthalpies in the crystallizer, c_p^L was not calculated as described in the section above. Instead, c_p^L was either directly taken from the DIPPR database [151] or estimated using a group contribution method [153]. This approach is considered to provide a more accurate description of the liquid phase enthalpies. The parameters for the calculation of c_p^L in the crystallizer are given in Table 144.

Table 144: Parameters for the calculation of molar liquid phase isobaric heat capacities in the crystallizer X1. $c_{p,i}^L / \text{J kmol}^{-1} \text{K}^{-1} = A_i + B_i \cdot (T/\text{K}) + C_i \cdot (T/\text{K})^2 + D_i \cdot (T/\text{K})^3 + E_i \cdot (T/\text{K})^4$.

Comp.	<i>A</i>	<i>B</i>	<i>C</i>	<i>D</i>	<i>E</i>	<i>Ref.</i>
FA	70077	-661.79	5.9749	-0.01813	$1.983 \cdot 10^{-5}$	^a
WA	276370	-2090.1	8.125	-0.014116	$9.3701 \cdot 10^{-6}$	^a
TRX	94990	-60.319	0.68234	0	0	^a
MG _{<i>n</i>} , <i>n</i> ≥ 1	47556 <i>n</i> - 117907	-1.558 <i>n</i> + 973.968	-0.0796 <i>n</i> - 1.1756	0	0	[153]

^(a) adopted from the DIPPR database (version 23.04.2019) [151]

Furthermore, the cooling duty needed for the precipitation of solid trioxane in the crystallizer was obtained from $\dot{m}^{(10)} \cdot \Delta h_{f,TRX}$, where $\dot{m}^{(10)}$ is the mass flow of the precipitated trioxane and $\Delta h_{f,TRX} = -162.3 \text{ kJ kg}^{-1}$ is the enthalpy of fusion of trioxane at its melting point of 334.65 K as reported in the DIPPR database (version 23.04.2019) [151]. The difference in the molar heat capacities of liquid and solid trioxane was neglected.

C.1.3 Crystallization-based trioxane process with a crystallization temperature of 303 K

The process specifications and the simulation results of the crystallization-based trioxane process with a crystallization temperature of 303 K are given here. For the simulation of this version of the process, the empirical correlation of the trioxane solubility that was developed in this thesis (cf. Equation (52)) had to be extrapolated slightly beyond the range of the experimental data that was used in the development of the correlation. Except for the reflux ratios and the feed stages of the distillation columns, all process specifications were adopted from the process with a crystallization temperature of 288 K. The reflux ratios and the feed stages of the distillation columns were then adjusted during the optimization procedure, which was equal to the one described in Chapter 4.1. The final process specifications of the crystallization-based trioxane process with a crystallization temperature of 303 K are given in Table 145. The streams and the specific heat duties of the process are given in the Table 146 and Table 147.

Table 145: Overview of the process specifications of the crystallization-based trioxane process with a crystallization temperature of 303 K. The reflux ratios and feed stages of the distillation columns C1 and C3 were adjusted during the optimization as described in Chapter 4.1.

apparatus	specification
S1	$\tilde{x}_{\text{FA},1}^{(m)} = 0.49 \text{ g g}^{-1}$ $p = 0.1 \text{ bar}$ $\dot{m}_3 / \dot{m}_2 = 1$
R1	$p = 1.0 \text{ bar}$ boiling state $N = 15$
C1	feed stage = 8 $p = 1.0 \text{ bar}$ $R = 3.180$
X1	$\tilde{x}_{\text{FA},8}^{(m)} = 0.70 \text{ g g}^{-1}$ $T = 303.15 \text{ K}$ $p = 1.0 \text{ bar}$
C3	$\tilde{x}_{\text{TRX},10}^{(m)} = 1 \text{ g g}^{-1}$ $N = 18$ feed stage = 10 $p = 2.5 \text{ bar}$ $R = 1.230$
	$\tilde{x}_{\text{W},13}^{(m)} = 0.99 \text{ g g}^{-1}$

Table 146: Stream tables of the crystallization-based trioxane process with a crystallization temperature of 303 K. The stream numbers are the same as in the Figure 26.

Stream	1	2	3	4	5	6	7	8	9	10	11	12	13
$\dot{m}^{(j)} / \dot{m}^{(10)}$	2.06	1.03	1.03	41.53	41.53	44.09	3.59	40.50	2.59	1.00	3.62	2.56	1.06
$\tilde{x}_{FA}^{(m)} / \text{g g}^{-1}$	0.4900	0.6609	0.3191	0.6990	0.6749	0.6553	0.1505	0.7000	0.2086	0.0000	0.2400	0.3355	0.0100
$\tilde{x}_W^{(m)} / \text{g g}^{-1}$	0.5100	0.3391	0.6809	0.2918	0.2918	0.3014	0.4240	0.2906	0.5877	0.0000	0.6143	0.4583	0.9900
$\tilde{x}_{TRX}^{(m)} / \text{g g}^{-1}$	0.0000	0.0000	0.0000	0.0092	0.0333	0.0433	0.4255	0.0094	0.2037	1.0000	0.1457	0.2062	0.0000

Table 147: Specific reboiler and condenser duties of the distillation columns of the crystallization-based trioxane process at the respective temperatures. The specific cooling duty of the crystallizer X1 is $q = -0.71 \text{ MJ kg}^{-1}$ at the crystallization temperature of 303 K. Specific heat duties are defined as $q = \dot{Q}/\dot{m}^{(10)}$, i.e., as heat duty per mass of the product trioxane.

	reboiler		condenser	
	q MJ kg ⁻¹	T K	q MJ kg ⁻¹	T K
C1	20.89	373.9	21.08	364.8
C3	9.54	400.3	9.52 (0.0 ^a)	393.1
total	30.43 (20.91 ^a)	-	30.60 (21.08 ^a)	-

^(a) required external specific heat duty with heat integration

C.2 Supporting information for Chapter 4.2

C.2.1 Details on the calculation of $K_{(XV)}$

For the estimation of $K_{(XV)}$ Equation (67) is used. Therein g is the molar gibbs energy. R is the ideal gas constant and θ indicates the standard state. T is the absolute temperature. Since the chemical equilibrium in the liquid phase is considered, the enthalpy h_i and entropy s_i in the liquid state have to be calculated from the standard states via Equation (68) and (69).

$$\ln(K_{(XV)}) = \frac{-L_{RG}^{(XV)}}{RT} = \frac{1}{RT} (h_{MAL} - h_{DME} - \frac{1}{3} h_{TRX} - T(s_{MAL} - s_{DME} - \frac{1}{3} s_{TRX})) \quad (67)$$

$$h_i(T) = h_i^\theta + \int_T^T c_{p,i}^{liq} dT^* - L_{vap,i}^\theta + L_{fus,i}^\theta \quad (68)$$

$$s_i(T) = s_i^\theta + \int_T^T \frac{c_{p,i}^{liq}}{T^*} dT^* - L_{vap,i}^\theta + L_{fus,i}^\theta \quad (69)$$

At standard conditions, trioxane is a solid and dimethyl ether is a gas. Thus, the values for enthalpy and entropy of formation of trioxane and dimethyl ether have to be corrected by the values for fusion ($\Delta h_{fus,i}^\theta$, $\Delta s_{fus,i}^\theta$) respectively vaporization ($\Delta h_{vap,i}^\theta$, $\Delta s_{vap,i}^\theta$).

C.2.2 Parameters of the used UNIFAC-based model

The distribution of the components in the system into groups of the UNIFAC-based model is given in Table 123. There can also be seen the volume- and surface-parameter of the groups. In Table 148 the interaction-parameters of the groups can be seen.

Table 148: Interaction-parameters of the group in the UNIFAC-based model.

group	group				
	FA	TRX	DME	MAL	FA _{OME}
FA	-	0 ^a	0 ^c	0 ^b	0 ^b
TRX	0 ^a	-	0 ^d	0 ^d	0 ^d
DME	0 ^c	0 ^d	-	0 ^d	26 ^c
MAL	0 ^b	0 ^d	0 ^d	-	26 ^b
FA _{OME}	0 ^b	0 ^d	141.5 ^c	141.5 ^b	-

^(a) [114]; ^(b) [60]; ^(c) adopted from the group MAL; ^(d) set to zero

D Supporting information for Chapter 5

D.1 NMR spectroscopy

In Figure 130 and Figure 131 typical ¹H NMR spectra of mixtures studied in Chapter 5 are shown and the peaks are assigned to components, without going into details. The individual peaks were assigned only to components and not to the exact positions of the protons in the corresponding molecules. For the evaluation, the signal of each proton was assumed to be equal of strength and that the signal is proportional to the mole fraction in the mixture. For the quantification the peak area of all protons assigned to one molecule was divided by the number of protons of this molecule and this area was set in ratio to the analogously calculated area of the other species. A detailed peak assignment of OME can be found in Schmitz et al.[60]. A detailed assignment of the hydrocarbons and water can be found in [154].

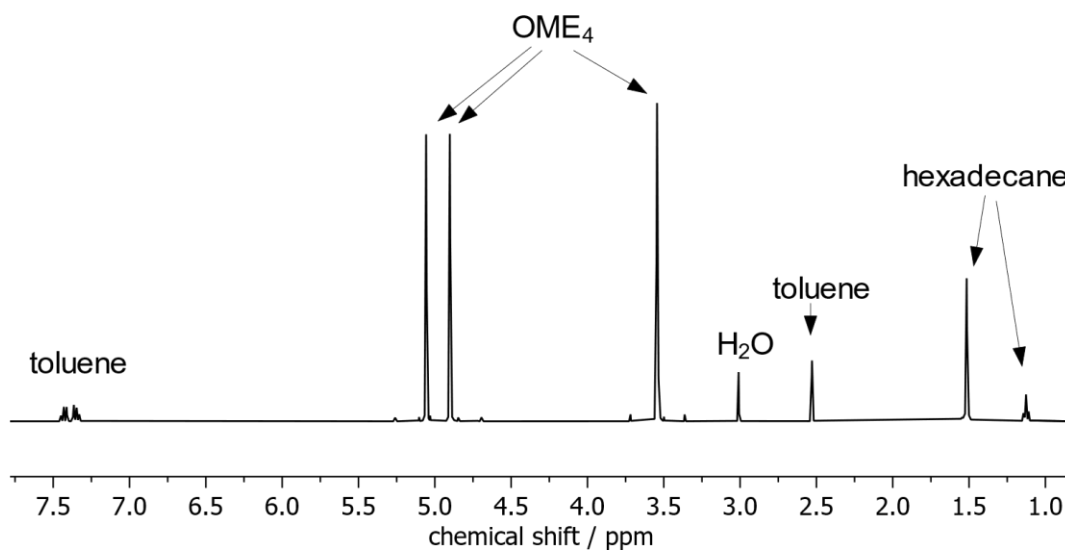


Figure 130: ^1H NMR example spectrum and peak assignment for a mixture of OME₄, water, hexadecane, and toluene.

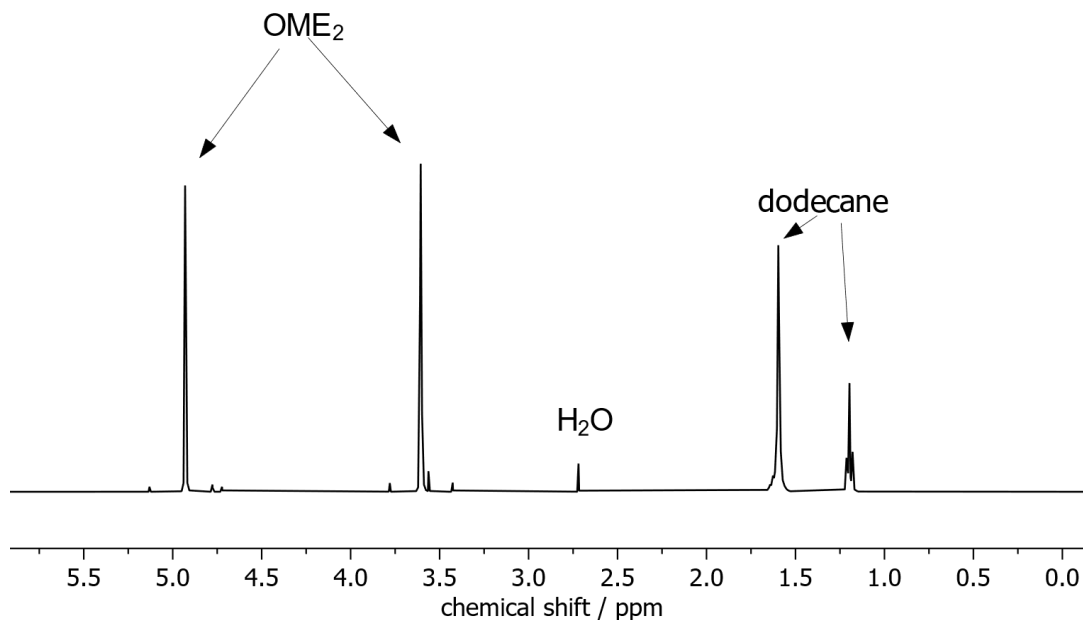


Figure 131: ^1H NMR example spectrum and peak assignment for a mixture of OME₂, water, and dodecane.

D.2 Karl-Fischer titration

For the volumetric Karl-Fischer titration a automatic titrator 870 KF Tritrino plus from Metrohm was used. For the titration dry methanol (Hydranal methanol dry, Honeywell Fluka) was used as solvent and Hydranal Composite 5 (Honeywell Fluka) was as used as titrant.

For the coulometric titration a 831 KF Coulometer from Metrohm was used. A generator electrode with diaphragm was used. The cell was filled with a mixture of 0.8 g g⁻¹ Hydranal-Coulomat AG-H (Honeywell Fluka) and 0.2 g g⁻¹ 1-pentanol (purity >0.99 g g⁻¹, Acros Organics). The pentanol was added to achieve a homogeneous mixture between the unipolar samples and the anolyte. As katholyte in the generator electrode Hydranal Coulomat CG (Honeywell Fluka) was used.

D.3 Interaction parameters of the UNIFAC-model

The interaction parameters of the UNIFAC model were adopted from Schmitz et al.[56] where this was possible. If this was not possible, but parameters could be taken from Gmehling et al.[145], this was done. The remaining parameters were fitted to experimental data from the present work or estimated using analogies. The result is reported in Table 23 in Chapter 5.3. The fitted parameters are those describing interactions between groups in OME and groups in hydrocarbons. They were fitted to data from the measurements in two steps. First the toluene-free systems were considered and the corresponding parameters were fitted, without using the data for the OME-mixture. Then, the model was extended to toluene, using the experimental data for the toluene-containing systems for fitting the corresponding parameters.

The fit was carried out such that the deviations in the isoactivity criterion (cf. Equation (31) in the main text) were minimized using the Matlab software and its “lsqnonlin” routine. The target function is given in Equation (70).

$$\min \sum_{j=1}^{N_S} \left\{ \begin{array}{l} \frac{1}{S_j} \sum_{i=1}^N (x_i' \cdot \gamma_i' - x_i'' \cdot \gamma_i'')^2, p_j = 2 \\ \frac{1}{2 \cdot S_j} \sum_{i=1}^N (x_i' \cdot \gamma_i' - x_i'' \cdot \gamma_i'')^2 + (x_i' \cdot \gamma_i' - x_i''' \cdot \gamma_i''')^2, p_j = 3 \end{array} \right. \quad (70)$$

Therein is N_S the number of different data sets used in the fit, S_j the number of measured equilibria measured within data set j , N the number of components, and p the number of phases in equilibrium in data set j .

D.4 Isothermal flash calculation

After calculating the starting point from the feed point the starting values for the composition of each phase was given into a minimization using the Matlab function “lsqnonlin”. The target function of the minimization is given in Equation (71). The algorithm was always searching for two phases. In case of only two stable phases the composition of two phases was the same.

$$\min \sum_{i=1}^N (x_i' \cdot \gamma_i' - x_i'' \cdot \gamma_i'')^2 + (x_i' \cdot \gamma_i' - x_i''' \cdot \gamma_i''')^2 \quad (71)$$

D.5 Feed compositions

In Table 149 the composition of the feed mixtures of the measurements of this work are given.

Table 149: Composition of the feed mixtures for the equilibrium measurements of this work. The order is the same as in Table 25 to Table 30.

T K	$x_{\text{Tol}}^{(m)}$ g g^{-1}	$x_{\text{C12}}^{(m)}$ g g^{-1}	$x_{\text{C16}}^{(m)}$ g g^{-1}	$x_{\text{OME2}}^{(m)}$ g g^{-1}	$x_{\text{OME3}}^{(m)}$ g g^{-1}	$x_{\text{OME4}}^{(m)}$ g g^{-1}	$x_{\text{OME5}}^{(m)}$ g g^{-1}	$x_{\text{OME6}}^{(m)}$ g g^{-1}
264.37	-	0.61002	-	0.32021	-	-	-	-
278.28	-	0.44988	-	0.15002	-	-	-	-
278.50	-	0.39477	-	0.39955	-	-	-	-
278.71	-	0.15071	-	0.44970	-	-	-	-
293.15	-	0.13338	-	0.66669	-	-	-	-
	-	0.15010	-	0.54996	-	-	-	-
	-	0.29991	-	0.29945	-	-	-	-
	-	0.09997	-	0.20007	-	-	-	-
	-	0.22962	-	0.40889	-	-	-	-
	-	0.43791	-	0.13202	-	-	-	-
	-	-	0.15321	0.50812	-	-	-	-
	-	-	0.14280	0.52375	-	-	-	-
	-	-	0.20982	0.45745	-	-	-	-
	-	-	0.29509	0.37156	-	-	-	-
	-	-	0.41646	0.24970	-	-	-	-
	-	-	0.43825	0.13189	-	-	-	-
264.27	-	0.58551	-	-	-	0.33904	-	-
265.63	-	0.41104	-	-	-	0.58374	-	-
266.71	-	0.41085	-	-	-	0.58703	-	-
266.78	-	0.40988	-	-	-	0.58904	-	-
267.19	-	0.41968	-	-	-	0.57625	-	-
278.41	-	0.40133	-	-	-	0.59368	-	-
278.43	-	0.39900	-	-	-	0.59801	-	-
278.63	-	0.39547	-	-	-	0.39516	-	-
278.84	-	0.39985	-	-	-	0.59212	-	-
278.86	-	0.40011	-	-	-	0.59839	-	-
293.15	-	0.40035	-	-	-	0.39975	-	-
	-	0.39897	-	-	-	0.59802	-	-
	-	0.39800	-	-	-	0.59700	-	-
	-	0.39716	-	-	-	0.59584	-	-
	-	-	0.35015	-	-	0.39972	-	-
	-	-	0.39601	-	-	0.59399	-	-
	-	-	0.39757	-	-	0.59643	-	-
	-	-	0.39907	-	-	0.59893	-	-
	-	-	0.36234	-	-	0.63755	-	-
	0.00735	-	0.34315	-	-	0.39972	-	-
	0.01751	-	0.33264	-	-	0.39812	-	-

Table 149 continued

0.07013	-	0.28012	-	-	0.40000	-	-
-	-	0.19661	-	0.23804	0.11081	0.04515	0.01641
-	0.19862	-	-	0.24473	0.11392	0.04641	0.01688

D.6 Modeling of the organic phase in the system (OME_n + n-alkane + water)

Figure 132 shows the results of the modeling in the system (OME₂ + n-alkane + water) in comparison with the measured data.

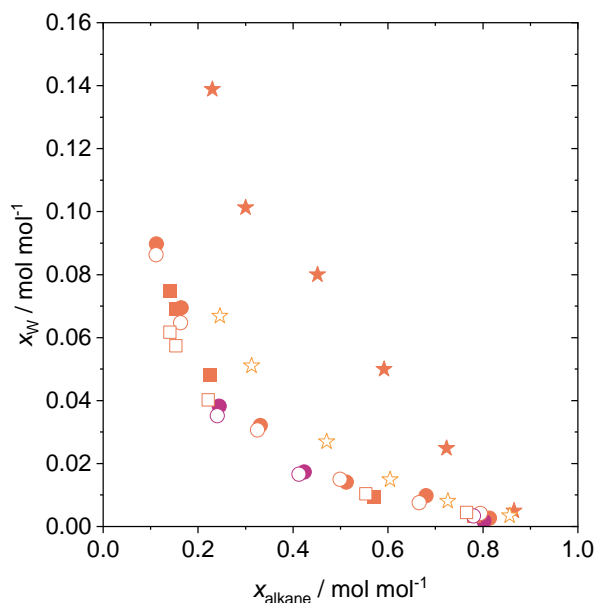


Figure 132: Experimental results (filled symbols) and model results (open symbols) for the LLE in the system (OME₂ + C12 + water, ○) and the system (OME₂ + C16 + water, □). The color represents the temperature: (■) 293 K, (■) 278 K. (☆) experimental results for the data of Zhuang et al.[134] for n-hexane and were modeled in this thesis.

Figure 132 shows that the composition of the organic phase is well described by the model. The model was also used to simulate the experiments of Zhuang et al.[134] that were carried out with n-hexane. Interestingly, the model yields a much lower solubility of water, which is closer to the results from the present work, than that reported by Zhuang et al.[134]. This meets the expectations from the experiments of the present work, that indicate only a weak effect of the chain length of the alkane on the results.

Figure 133 shows the results for the organic phases in the system (OME₄ + n-alkane + water)

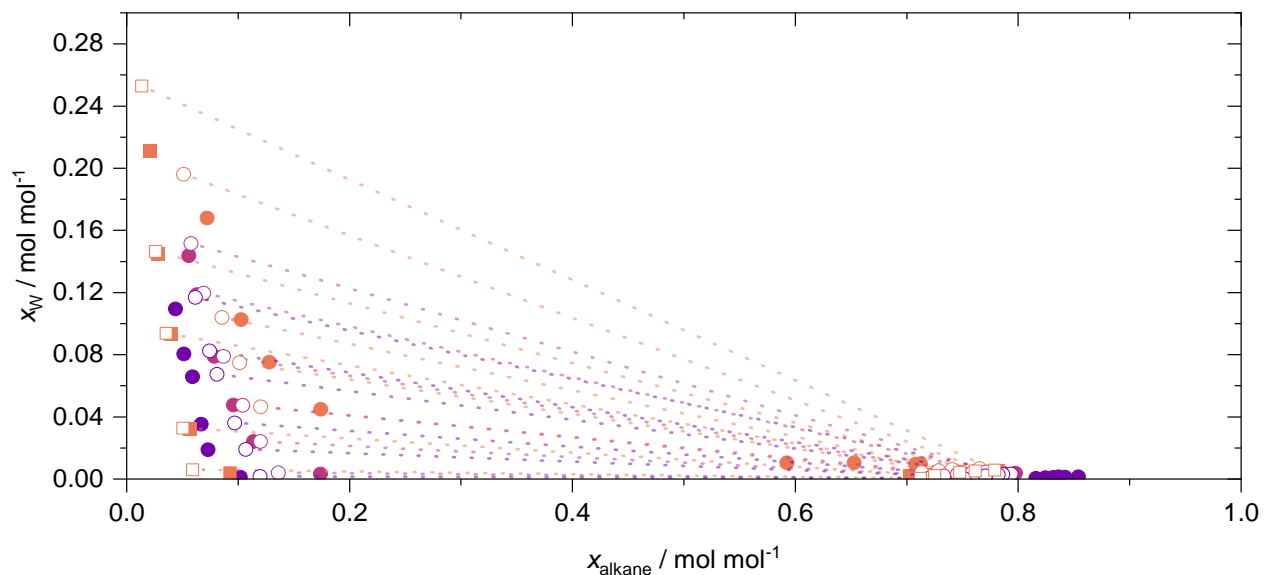


Figure 133: Experimental results (filled symbols) and model results (open symbols) for the LLE in the system (OME₄ + C12 + water, ○) and the system (OME₄ + C16 + water, □) at low water fractions. The color represents the temperature: (■) 293 K, (■) 278 K, (■) 265 K. (.....) tie lines of the modeled results.

The influence of the temperature on the ratio OME/n-alkane in the OME-rich phase in the two-phase area in mixtures with OME₄ is systematically underestimated. For 293 K the calculated alkane concentration in the OME-rich phase is too high, for 265 K it is too low.

Statement on authorship

This dissertation contains material that has been published previously or that is included in submitted publications. In the following, these publications are listed together with a statement on the contributions of the author of the present dissertation.

- C. F. Breitzkreuz, N. Schmitz, E. Ströfer, J. Burger, H. Hasse: Design of a Production Process for Poly(oxymethylene) Dimethyl Ethers from Dimethyl Ether and Trioxane, *Chemie Ingenieur Technik* 90 (2018), 10, 1489-1496
The author performed the simulations and evaluated the results. The author wrote the manuscript.
- C. F. Breitzkreuz, M. Dyga, E. Forte, F. Jirasek, J. de Bont, J. Wery, T. Grützner, J. Burger, H. Hasse: Conceptual Design of a Crystallization-Based Trioxane Production Process, *Chemical Engineering & Processing: Process Intensification* 171 (2022), 108710
The author performed the simulations and evaluated the results. The author wrote the manuscript.
- C. F. Breitzkreuz, J. Burger, H. Hasse: Solid-liquid equilibria and kinetics of the solid formation in binary and ternary mixtures containing (formaldehyde + water + methanol), *Industrial & Engineering Chemistry Research* 61 (2022), 4, 1871-1884
The author carried out or supervised the experiments. The author performed the simulations and evaluated the results. The author wrote the manuscript.
- C. F. Breitzkreuz, N. Hevert, N. Schmitz, J. Burger, H. Hasse: Synthesis of Methylal and Poly(oxymethylene) Dimethyl Ethers from Dimethyl Ether and Trioxane, *Industrial & Engineering Chemistry Research* 61 (2022), 23, 7810-7822
The author carried out or supervised the experiments. The author performed the simulations and evaluated the results. The author wrote the manuscript.
- C. F. Breitzkreuz, J. Burger, H. Hasse: Solubility of formaldehyde in mixtures of water + methanol + poly(oxymethylene) dimethyl ethers, *Fluid Phase Equilibria* (submitted)
The author carried out or supervised the experiments. The author performed the simulations and evaluated the results. The author wrote the manuscript.
- C. F. Breitzkreuz, A. Holzer, T. Fuchs, M. Günthner, H. Hasse: Miscibility in systems containing (poly(oxymethylene) ethers (OME) + hydrocarbons + water), *Fuel* (submitted)
The author carried out or supervised the experiments. The author performed the simulations and evaluated the results. The author wrote the manuscript.

Student theses

The following student theses were prepared under the supervision of the author of the present doctoral thesis in the frame of his research:

- Dyga, M.: Konzeptioneller Verfahrensentwurf zur Herstellung von Polyoxymethylen-dimethylethern aus Dimethylether und Trioxan, Master research thesis, Laboratory of Engineering Thermodynamics (LTD), University of Kaiserslautern (2017).
- Kreußler, J.: Experimentelle Untersuchung des Feststoffausfalls im System Formaldehyd-Wasser-Methanol, Master thesis, Laboratory of Engineering Thermodynamics (LTD), University of Kaiserslautern (2018).
- Selzer, F.: Untersuchung des reaktiven Fest-flüssig Gleichgewichts von Formaldehyd-Wasser-Methanol bei tiefen Temperaturen, Master thesis, Laboratory of Engineering Thermodynamics (LTD), University of Kaiserslautern (2019).
- Schmeckeber, A.: Experimentelle Untersuchung des reaktiven Fest-flüssig Gleichgewichts im System Formaldehyd-Wasser-Methanol, Master research thesis, Laboratory of Engineering Thermodynamics (LTD), University of Kaiserslautern (2020).
- Leicht, J.: Experimentelle Untersuchung von Flüssig-flüssig Gleichgewichten in wasserhaltigen Mischungen synthetischer Dieselmotorenkraftstoffe, Master research thesis, Laboratory of Engineering Thermodynamics (LTD), University of Kaiserslautern (2020).
- Hofmann, M.: Simulation eines Kristallisationsprozesses zur Herstellung von Trioxan, Master research thesis, Laboratory of Engineering Thermodynamics (LTD), University of Kaiserslautern (2020).
- Briodeau, O.: Experimentelle Untersuchung des reaktiven Fest-flüssig Gleichgewichts im System Formaldehyd-Wasser-Poly(oxymethylen)ether (OME), Master research thesis, Laboratory of Engineering Thermodynamics (LTD), University of Kaiserslautern (2020).
- Sterner, P.: Flüssig-flüssig Gleichgewichts in Mischungen synthetischer Kraftstoffe, Master research thesis, Laboratory of Engineering Thermodynamics (LTD), University of Kaiserslautern (2020).

Curriculum vitae

Studium

2011-2017 Studium des Chemieingenieurwesen an der TU Dortmund
Abschluss: Master

Berufliche Tätigkeit

2017-2022 Wissenschaftlicher Mitarbeiter am Lehrstuhl für Thermodynamik
Prof. Dr.-Ing. Hans Hasse
Technische Universität Kaiserslautern